Time-resolved XRD study of size dependence in the photoinduced phase change in transition metal oxides

Ritwika Mandal

COLLEGE SCIENCES DE LA MATIERE
DOCTORAL DES MOLECULES
BRETAGNE ET MATERIAUX

Université de Rennes

THÈSE DE DOCTORAT DE

L'UNIVERSITÉ DE RENNES

ÉCOLE DOCTORALE N° 638
Sciences de la Matière, des Molécules et Matériaux
Spécialité : *Physique*

Par
Ritwika MANDAL

Time-resolved XRD study of size dependance in the photoinduced phase change in transition metal oxides

1 Thèse présentée et soutenue à Rennes, le 21.12.2023
Unité de recherche : Institute de Physique de Rennes UMR 6251
1 **Rapporteurs avant soutenance :**

Kristoffer HALDRUP	Associate professor, Technical University of Denmark, Physics
Renske M. VAN DER VEEN	Professor, Technical University of Berlin

Composition du Jury :

Examinateurs :	Amelie JARNAC	Researcher, ONERA, Palaiseau-France
	Pascal TURBAN	Professor, IPR
Dir. de thèse :	Maciej LORENC	Director of Research, IPR
Co-dir. de thèse :	Celine MARIETTE	Beamline scientist, ESRF

Acknowledgement

I am immensely grateful to everyone who contributed to the success of this project.

First and foremost, I would like to extend my heartfelt gratitude to my supervisor Céline Mariette for her unwavering support and guidance throughout the three years. Her profound knowledge and expertise have been instrumental in shaping the outcome of this thesis. I am thankful to her for not only inspiring me in physics but in all walks of life.

I am equally indebted to my supervisor Maciej Lorenc, whose scientific discussions, coupled with a delightful sense of humour, made this journey even more enjoyable.

I express my sincere gratitude to both Céline Mariette and Maciej Lorenc for believing in me and accepting me as a student in this PhD project.

I would also like to extend my appreciation to the members of my research team and colleagues at Institute of Physics (IPR) in Rennes for their assistance, feedback, and stimulating discussions. Special thanks go to Elzbieta Trzop for her patient teaching of X-ray diffraction, Marius Herve for all the insightful discussions, Gael Privault with whom I have shared the PhD journey, Ernest Pastor for making the beamtimes both educational and enjoyable, Marina Servol, Roman Bertoni, Bertrand Toudic and Philippe Rabillier for their guidance on various concepts.

A heartfelt thanks goes to Etienne Janod from the IMN, Nantes for not only providing the thin films of V_2O_3, but also for engaging in simulating discussions. His positive and energetic attitude towards science have been truly inspiring.

My gratitude extends to the ID09 beamline scientists Matteo Levantino, Marco Cammarata, Serhane Zerdane and Alix Volte for guidance in introducing me to ultra-fast X-ray experiments.

This work would not have been possible without the collaboration of Laurentiu Stoleriu and Christian Enachescu at the University of Iasi, Romania. I deeply appreciate their warm welcome in Iasi and their consistent support in developing the model, which constituted a significant part of my PhD work.

My PhD work involved experiments at the SOLEIL synchrotron radiation facility. I am grateful to the beamline scientist Pierre Fertey for helping during the experiments. Besides, I also performed measurements at the FemtoMAX beamline in Sweden and wish to thank the all the beamline scientists Andrius Jurgilaitis, Van-Thai Pham, David Kroon and Carl Ekström for their hospitality and help during the experiments.

I would like to thank our collaborators Hiroko Tokoro and Marie Yoshikiyo from the University of Tokyo, Japan for generously providing us with the powder sample of Ti_3O_5.

I deeply appreciate the unwavering support and enthusiasm from my parents, Pravat Kumar Mandal and Rupa Mandal, not only during the three years of my PhD but also throughout my life. They have been the guiding force behind my pursuit of higher educa-

tion and their encouragement has helped me overcome the challenges encountered during this endeavor.

Last but not the least, I wish to express my gratitude to Himanshu, a constant pillar of support throughout this journey.

Preface

In recent years with the development of the ultra-fast and intense laser, unprecedented opportunities have emerged to modify the macroscopic properties of materials of different sorts. Literature has been steadily filling up with examples of changing electronic and / or structural orders following excitation, thereby impacting the functionality of the materials. In particular, local electronic or structural rearrangements display dynamics in the femto- or picoseconds time domain, determined by the microscopic interactions. Real time observations of such processes have been possible with the emergence of ultra-fast probing techniques of optical spectroscopy, X-ray or electron diffraction. X-rays are especially suitable tool to follow directly the out-of equilibrium macroscopic structural changes in the photo-excited systems[10].

The core focus of this project revolves around the exploration of photo-induced phase transitions, with particular attention directed toward crystal deformations induced by laser pulses. Our primary interest lies in examining the non-equilibrium changes in crystal volume, a phenomenon occurring on the "acoustic" timescale, which is determined by material dimensions and the speed of sound. This acoustic process is therefore slower than electronic transitions, but remains ultra-fast in the case of nanomaterials[12].

Following on the earlier studies of molecular materials undergoing spin transition[109], our chosen materials for this project are correlated electron systems of transition metal oxides. In particular, we chose Ti_3O_5 with a isostructural semiconductor-metal transition associated with a large volume jump originating from coupling between the lattice parameters and electronic state. With the bistability in nanocrystalline forms [63], polycrystalline powder of Ti_3O_5 has already shown to have reversible phase transition following the strain wave propagation upon laser-irradiation[55].

Our second choice of material is V_2O_3 which exhibits photo-induced insulator to metal transition associated with volume compression as well as symmetry breaking. Our aim was to understand how the propagation of the strain wave would affect the dynamics of the two phenomenon.

This project is guided by two broad objectives. Firstly, if it is possible to achieve some stable and well reproducible states among the transient states during the photo-excitation. This would then have great technological applications like ultra-fast data storage, sensors or as switching devices.

Secondly, the purpose is to study the universality of the strain wave mechanism in correlated electron systems. To explore this idea, we chose two different systems Ti_3O_5 showing volume expansion and V_2O_3 showing a volume contraction. This in turn helps to understand if the sign of volume change across the transition has any effect on the phase transition following the strain propagation.

The manuscript has been divided into 6 different chapters, each with a specific focus.

Chapter 1 gives an introduction to the photo-induced phase transition and using the pump probe techniques to study the precursor states during the transitions. Chapter 2 discusses a general introduction to X-ray diffraction and the experimental technique of time-resolved XRD used to monitor real-time structural changes. Additionally, it explores the different sources of ultra-fast XRD and analysis methods to obtain 1D diffraction patterns from the 2D images collected by the detector. Other complementary experiments that facilitates the understanding of the precursor phases have been mentioned in this chapter. Chapter 3 is dedicated to describe the phase changing correlated electronic systems(Ti_3O_5 and V_2O_3) studied during the thesis. Finally, the results of time-resolved XRD measurements on the polycrystalline pellets of Ti_3O_5 and thin films of V_2O_3 are presented in Chapter 4 and Chapter 5 respectively. Chapter 6 serves as the conclusion of the thesis, summarising the results and provides a broader significance in the context of photo-induced phase transitions.

Table of Contents

1 Introduction **11**
- 1.1 Photo-excitation in semiconductors . . . 11
- 1.2 Strain distribution in photo-excited samples . . . 12
- 1.3 Types of photo-induced strain . . . 14
- 1.4 Themoelastic stress . . . 15
- 1.5 Multiscale process upon photo-excitation . . . 16
- 1.6 Photo-induced phase transition . . . 17
- 1.7 Pump-probe technique . . . 19

2 Experimental Methods to access the structural information **21**
- 2.1 Principle of X-ray diffraction . . . 21
- 2.2 X-ray sources for time-resolved XRD . . . 24
  - 2.2.1 Picosecond sources . . . 25
  - 2.2.2 Sub-picosecond sources . . . 27
- 2.3 Laser pump . . . 33
- 2.4 Experimental geometry . . . 35
  - 2.4.1 Determination of the incidence angle . . . 36
  - 2.4.2 Space-time mapping for temporal resolution . . . 37
- 2.5 Parameters affecting the broadening of Bragg peaks . . . 39
  - 2.5.1 Broadening due to energy dispersion . . . 39
  - 2.5.2 Broadening due to footprint . . . 39
  - 2.5.3 Broadening due to crystallite size . . . 41
- 2.6 Sample Environment . . . 42
  - 2.6.1 Cold finger cryostat at ESRF, ID09 . . . 42
  - 2.6.2 Vacuum chamber at MAX IV, FemtoMAX . . . 42
  - 2.6.3 Diamond Anvil Cells(DAC) at SOLEIL, CRISTAL . . . 43
- 2.7 Method of analysis . . . 45
  - 2.7.1 Generation of 1D diffraction pattern . . . 45
  - 2.7.2 Data reduction of stroboscopic measurements . . . 47
  - 2.7.3 Diffraction pattern refinement . . . 47
- 2.8 Complementary experimental techniques . . . 50
  - 2.8.1 Atomic Force Microscopy . . . 50
  - 2.8.2 Differential Scanning Calorimetry . . . 51

3 Overview of investigated systems **53**
- 3.1 Trititanium pentoxide(Ti_3O_5) : Structure, morphology and characterisation 54
  - 3.1.1 Crystal Structure . . . 54

3.1.2 Polycrystalline powder of Ti_3O_5 . . . 56
3.1.3 Surface characterisation of the pellets using AFM . . . 59
3.1.4 Estimation of transition temperature in pellets using DSC . . . 60
3.1.5 Experimental conditions for TR-XRD . . . 63
3.2 Vanadium Trioxide (V_2O_3): Structure, Morphology and Characterisation . 67
3.2.1 Crystal structure . . . 67
3.2.2 Thin films of V_2O_3 . . . 70
3.2.3 Experimental conditions for TR-XRD . . . 71

4 Photo-induced semiconductor-insulator transition in Ti_3O_5 77
4.1 State of the art . . . 77
4.2 Dynamics of the photo-induced structural changes in Ti_3O_5 measured with TR-XRD at the ID09 beamline . . . 80
4.2.1 Characterisation of phase transition dynamics with various crystallite sizes . . . 88
4.2.2 Influence of incident pump wavelength on the phase transition dynamics . . . 89
4.2.3 Influence of incident pump energy on the phase transition dynamics 91
4.2.4 Influence of incidence angle of the X-rays on the phase transition dynamics . . . 93
4.2.5 Effect of initial λ phase percentage on the phase transition dynamics 94
4.3 Heat Diffusion Model . . . 95
4.3.1 Description of the model . . . 95
4.3.2 Choice of parameters . . . 98
4.4 Results from the model based on the choice of initial conditions . . . 102
4.4.1 Excitation of the whole grain within the first layer . . . 102
4.4.2 Excitation in the form of domains on excited surface but limited by laser penetration depth . . . 106
4.4.3 Excitation in the form of domains limited by the laser penetration depth . . . 108
4.4.4 Domains limited by the crystallite size . . . 110
4.5 Conclusion . . . 114

5 Photo-induced insulator-to-metal transition in V_2O_3 thin films 115
5.1 State of the art . . . 115
5.2 Steady-state study of the pressure induced insulator to metal transition at low temperature . . . 116
5.3 Dynamics of the photo-induced structural changes in V_2O_3 thin films with TR-XRD measurements . . . 122
5.3.1 Propagation of the volume contraction associated with AFI-PM phase transition . . . 128
5.3.2 Propagation of the shear related to AFI-PM symmetry change . . . 130
5.4 Effect of incident laser power on the Photo-induced structural changes . . . 132

5.5 Conclusion 136

6 Conclusion **137**

Bibliography **139**

Chapter 1

Introduction

Phase transition accompanied by electronic, magnetic and structural changes under equilibrium conditions induced by external control parameters such as temperature and pressure have been well studied since several decades. Recently, the manipulation of material properties through photo-induced phase transition driven by ultrashort laser pulses represents an expanding field in condensed matter, materials science and photonics[48]. Most of the early studies have focused on the microscopic changes of chemical bonds in molecules[121] or local structural changes in crystals.

With the application of ultrashort laser pulse, one can drive the system to a new energy landscape that are often not achieved under equilibrium, leading to fascinating technological applications in data storage or signal processing. In recent years, significant progress have been made in understanding and exploiting the efficacy of he strain wave driven photo-induced transitions. Experiments have revealed the efficiency of the femtosecond laser pulses in inducing reversible phase transitions in a wide range of materials including charge transfer crystals[70][22], insulator-metal switching in transition metal oxides[19][27][63], spin crossover complexes[34][40][61], etc. These transitions in physical parameters results from cooperative interactions between the electrons, phonons, magnons, plasmons or polaritons[11]. Here, we have focused on the strain wave feedback mechanism as the driving force of the transitions. The interplay between the lattice distortions and electron -phonon coupling induces and controls phase transitions that are associated with significant volume changes. My PhD work aimed to enhance our understanding of propagation of photo-induced strain waves and their influence on the out-of-equilibrium thermodynamics of these materials, especially during phase transitions.

In this chapter, we will have a brief overview on the key concepts for such a photo induced transition, such as the laser driven electronic excitation, electron -phonon and phonon-phonon coupling and the propagation of strain in systems.

1.1 Photo-excitation in semiconductors

Upon photon absorption in semiconductors, if the energy of the incident photon is greater than the band gap energy, then the electrons in the valence band(VB) can be excited to the conduction band (CB) leaving behind the absence of electron (hole) in the VB. This excited electron relaxes by imparting energy to the phonon energy levels through electron-phonon coupling as shown schematically in Fig. 1.1a.

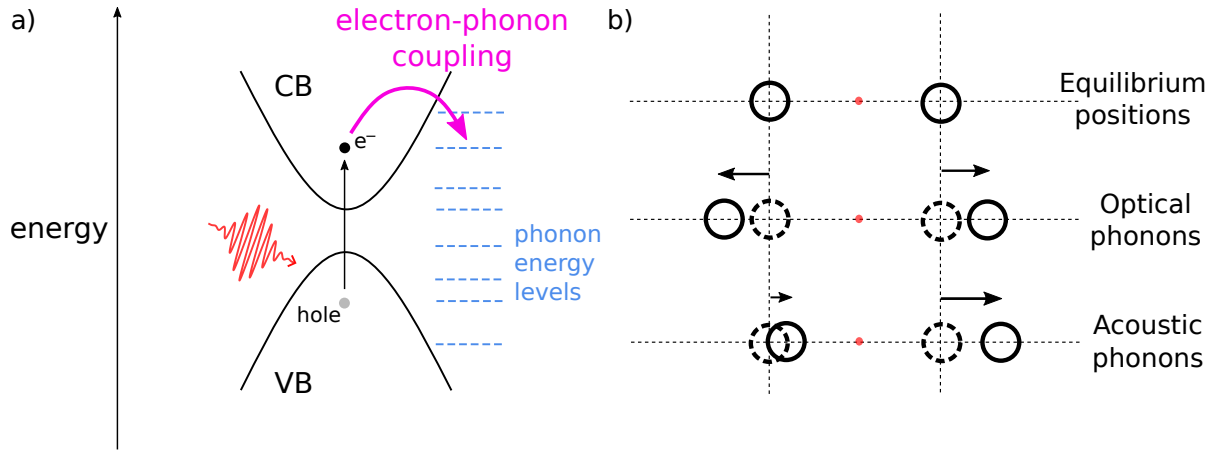

Figure 1.1 – a) Generation of electron-hole pair upon phonon absorption. The electron then relaxes through the electron-phonon coupling. b) The equilibrium positions of the atoms and oscillations due to energy redistribution from the electron to phononic bath.

By imparting energy to the lattice system, there is a disruption of the equilibrium positions of atoms. Fig. 1.1 b is a schematic representation of the atomic positions in a two-atom system before and after photo excitation. With the energy from the electron, if the atoms move such that their mean position is kept constant, then the optical phonon modes[13] are generated. However, when the mean equilibrium position changes, then the acoustic phonons are generated.

The electron-electron collisions takes place quickly within few fs and establishes a local energy equilibrium. Similarly the phonon-phonon relaxation occurs within several 10s of fs[32]. So before the energy redistribution to the phonon bath, two different temperatures can be associated with the electronic and phononic subsystem respectively.

1.2 Strain distribution in photo-excited samples

Photoinduced stress arises from the creation of electron and hole pairs(electronic stress) and the redistribution of the excess electronic energy to the ponon bath(phononic stress). This strain generated from the laser excited free surface to the depth of the sample.

The strain generation in a semi infinite system upon laser irradiation has been initially described by Thomsen et. al.[103]. According to the model, when a short light pulse of energy Q with a penetration depth of μ is incident on the sample surface, the energy deposited per unit volume W(z) at distance of z in depth of the sample is

$$W(z) = (1 - R)\frac{Q}{A\mu}e^{-z/\mu} \tag{1.1}$$

where R is the reflectivity of the sample and A is the area of laser excitation.

As a response to the initial stress profile, a strain wave is launched at the acoustic velocity from the surface to the interior in the sample.

$$\tau = z/v_s \tag{1.2}$$

where v_s is the acoustic velocity in the materials. The typical value of acoustic velocity in inorganic materials is about 6 km/s and in organic materials is about 3 km/s. For example, the time taken to cover a distance of 100 nm is $\sim$ 17 ps with the acoustic velocity of 6 km/s.

In the semi-infinite system, the laser penetration depth(μ) is notably smaller than the thickness of the film(d). As depicted in Fig. 1.2b, the strain distribution at different time units, denoted as $\tau = v_s t/d$ is presented for the shaping factor $\delta = d/\mu >> 1$. In such a configuration, it is important to note the existence of a gradient in both strain and temperature distributions within the sample. Consequently, a continuous process of heat diffusion unfolds within the system, occurring at a temporal scale determined by the thermal diffusivity of the sample.

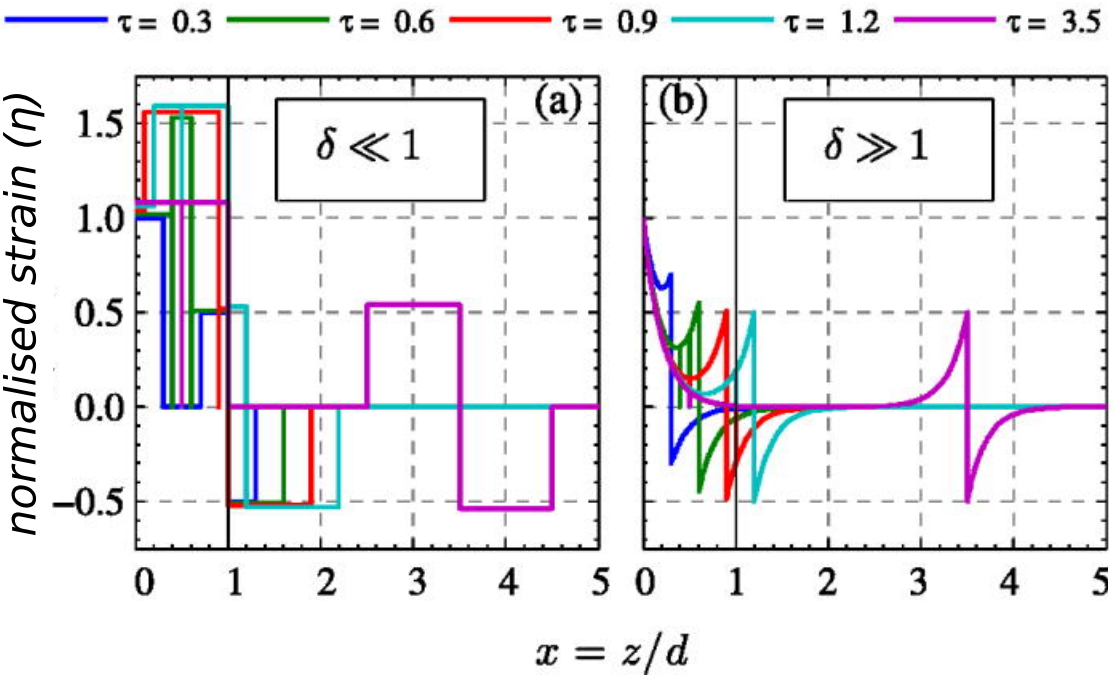

Figure 1.2 – Normalised strain (η) plotted at different time after the laser excitation for the two limiting case of shape parameter ($\delta = d/\mu$). a) shows the photo-induced homogeneous stress profile for $\delta << 1$ and b) shows the inhomogeneous stress profile for $\delta >> 1$ (adapted from [89])

In the context of thin film, the photo-excited stress is homogeneous throughout the depth of the film when the film thickness(d) is less than the laser penetration depth(μ).

The strain propagation has been quantitatively elaborated in [89]. Fig. 1.2a shows the strain distribution for the shaping factor $\delta << 1$ at different time units τ. Under this condition, the lattice dynamics commence at both the laser excited surface and at the film-substrate interface (located at depth z = d) where a notable impedance mismatch is encountered. This initiates the generation of equidistant acoustic echoes at specific time intervals defined by the relationship

$$t = n \times 2d/v_s \tag{1.3}$$

where n is positive integer and v_s is the speed of sound in the system. In this context, the uniform photo-excited stress also implies a consistent temperature distribution within the sample.

An analogous strain distribution is likewise evident along the sample surface, depending on the extent of the laser's footprint on the sample. In a homogeneous medium, for example single crystal, this in-plane stress is effectively constrained, as local volume alterations are confined by the unaltered macroscopic volume. However, this constraint is relaxed in the case of granular films, such as V_2O_3, and in pellets composed of nanocrystals of Ti_3O_5.

1.3 Types of photo-induced strain

In case of a real 3D sample, the strain not only propagates in one direction as has been discussed above. So the strain propagation can be broadly differentiated as
1. **Longitudinal strain:** The strain is generated when the force is perpendicular to the free surface. This strain causes a change in length with respect to its original length. Examples of longitudinal strain are the tensile strain in Ti_3O_5 and compressive strain in V_2O_3.

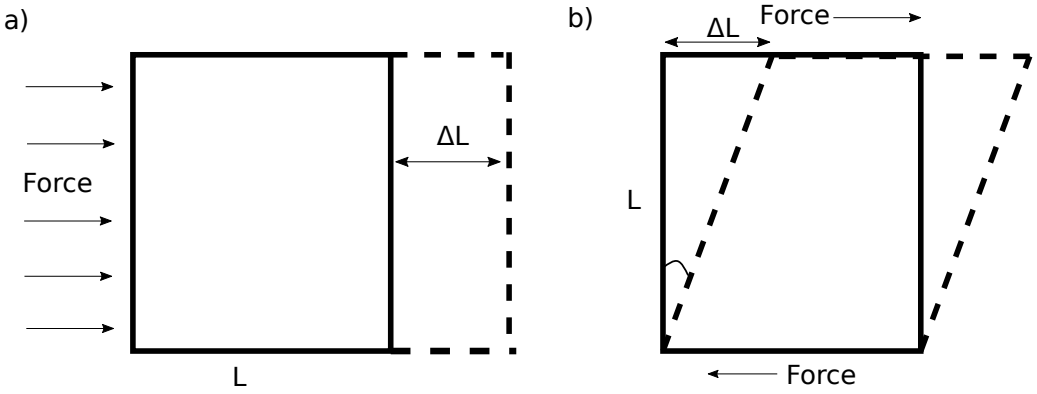

Figure 1.3 – a) Longitudinal strain with the distortion parallel to the force plane. b) Transverse strain with the distortion perpendicular to the force plane.

2. **Transverse strain:** The transverse or shear strain is defined as the ratio of change in length perpendicular to the force plane. This is observed during the symmetry change in V_2O_3.

1.4 Themoelastic stress

The thermoelastic stress rise in the sample when the energy deposited is transferred to the lattice and eventually into heat. The temperature increase in the sample can be extracted from $W(z)$.

$$\Delta T(z) = W(z)/C \tag{1.4}$$

where C is the specific heat per unit volume.

The thermoelastic strain caused by thermal expansion [83] is

$$\eta = \delta V/V = 3\beta B\delta T_L \tag{1.5}$$

where δT_L is the temperature increase in the lattice. Therefore, the thermal stress given by :

$$\sigma_{thermal} = -3B\beta\Delta T(z) \tag{1.6}$$

with β as the linear thermal expansion coefficient and B is the bulk modulus.

In majority of solid materials, the expansion coefficient β is positive resulting in the generation of negative photo-induced stress. When the thermoelastic mechanism is prevailing factor, the strain wave initiated from the surface will consequently leave in its wake a tensile strain, implying an expansion of the volume of the solid.

Such a lattice heating comes from the energy transfer between electrons and phonons during the relaxation of excited electrons. Thermoelastic coupling driven by hot electrons has been observed in metals with weak or strong electron -phonon coupling[116][117][99].

Upon photo excitation in oxides or semiconductors, which have a forbidden energy gap, the electrons absorb the incident laser pulse energy ($h\nu$) and get promoted to higher energy states. Then these excited electrons undergo the relaxation through inter or intra-band process and finally goes back to the ground state as shown in

Intraband relaxation pertains to the electron relaxation within a single band of energy levels in the material. This pathway is governed by electron -phonon scattering and are generally very rapid in time. During this relaxation process, the optical and/or acoustic phonons are emitted in the system. The optical phonons eventually decay into acoustic phonons. Hence, the acoustic phonons generated do not have a phase relationship between them and so they contribute to the incoherent phonon population leading to lattice heating. The ultra-fast lattice heating causes a local temperature rise in the lattice(T_L) by :

$$\Delta T_L = N(h\nu - E_g)/C_L \tag{1.7}$$

where N is the photo-excited carrier concentration, E_g is the band gap and C_L is the lattice heat capacity. This ultra-fast lattice heating can start as soon as few picoseconds

but the heat diffusion in the material takes longer time. So it is hard to decorrelate the heating effect in time. Often, the incident pump energy is chosen such that it is close to the band gap energy, in order to excite the electrons to energy levels close to the gap. This will in turn reduce the incoherent phonon population.

1.5 Multiscale process upon photo-excitation

Upon photo-excitation with ultrashort laser pulse, the molecule or any subunit absorbs photons and undergoes a series of interconnected processes at different rates and length scales. These events include photon absorption, electronic energy distribution, molecular rearrangements, structural changes and relaxation back to the ground state. This constitutes the multi-step process and the different time scales are as follows:

Ultra-fast time scale (femtoseconds): Immediately upon photo-absorption, the electronic excitation takes place. The electrons move from ground state to higher energy levels or electronic states and thermalise through electron-electron coupling, quickly within femtoseconds after the photo-excitation on the materials. This is a very local phenomena, within the penetration depth of the incident laser.

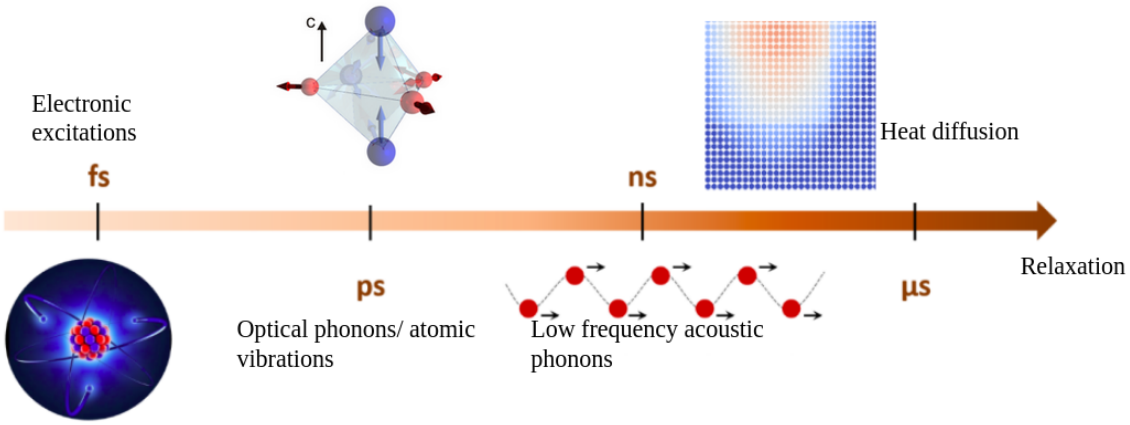

Figure 1.4 – Different processes occurring upon photo-excitation in different length scales. The arrow points in the direction of increasing time scales.

Fast time scale (picosecond): During the electron thermalisation, the excess energy is released in the system through electron-phonon interaction. This also occurs within picosecond timescale. The electron-phonon coupling occurs with the generation of high frequency optical phonons or low frequency acoustic phonons. The thermalisation of the acoustic and optical phonon takes time. During this time scale, structural changes might

start to occur affecting the arrangement of atoms and molecules. This generates an elastic stress in the system coupled with atomic motions[103].

Intermediate time scale (Nano-to microseconds): The strain and thermal gradient still exist in a bulk system at this time scales. The temperature gradient is a result of the finite penetration depth of the laser pulse. The thermal equilibrium takes place within the system governed by the thermal diffusivity. For a material with a thermal diffusivity of the order of 100 nm^2/ns gives the thermal diffusion within 100s of nanoseconds in a 100 nm crystal.

Long time scales (miliseconds): The recovery of the system to its ground state by relaxation of thermal energy with the environment. This step depends on the heat capacity as well as the thermal exchange coefficient of the system with its surrounding.

It is important to note that these time scales vary a lot depending on the conditions of photo-excitation, morphology of the samples and their environment. There is no master equation that is valid over all the time scales.

1.6 Photo-induced phase transition

The phase transitions with changes in external conditions as temperature, pressure, electric and magnetic fields is well known and studied. Since long time, the interplay between light and matter has revealed a captivating phenomenon known as photo-induced phase transitions and has attracted a lot of attention from researchers[59][120]. These transitions, which involve the transformation of a material's structural, electronic, or magnetic properties in response to photon absorption, open new avenues for manipulating and controlling material behavior.

Fig. 1.5 shows a schematic view of photo-induced phase transitions. The photo-excitation can drive the system to a new energy landscape. The excited state upon relaxation, can undergo transient or permanent transition to a new macroscopic state. This state can have a new lattice structure and/or electronic order which is not realised under equilibrium.

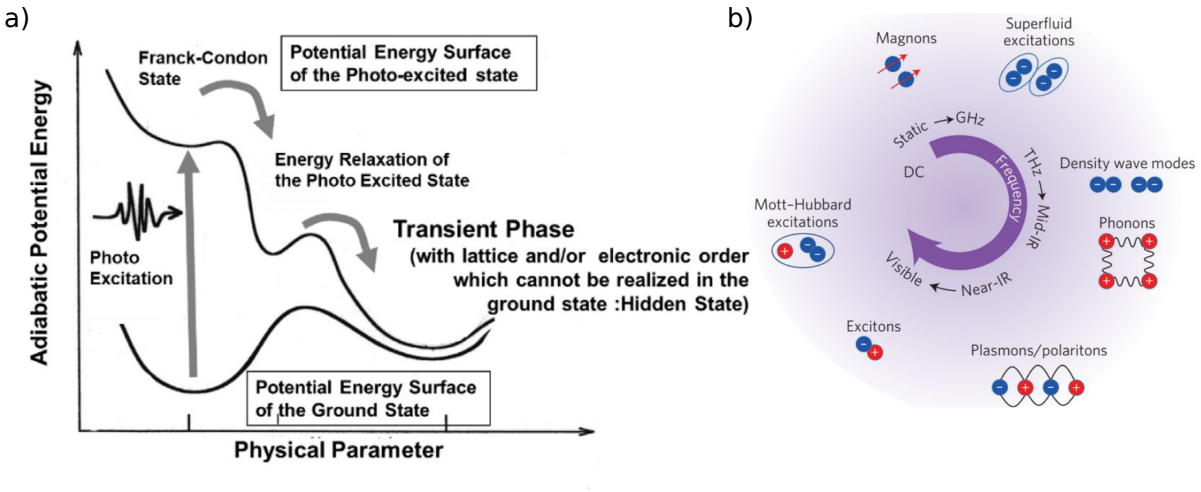

Figure 1.5 – a) Schematic description of the photo-induced phase transitions. Upon photo-excitation, the system can relax in a transient phase (hidden state) during the relaxation(adapted from [48]). b) Schematic representation of the cooperativity between different degrees of freedom (reproduced from [11])

The most common and easy way to achieve a photo-induced transition is heating with the laser. The transition between two macroscopic states can be achieved under continuous photo-irradiation for example in spin crossover systems [14].

However, when the duration of the laser pulse is shorter than the time scale of atomic motions, a coherent excitation occurs prior to the onset of incoherent heating in the sample[16]. The laser is no longer a heat source, but it coherently controls the materials, either by electronic transitions, electronic polarisation with transient fields, or simply by generating impulsive forces (coherent optical and acoustic phonons). Interplay between different degrees of freedoms for instance electron, lattice or spin degrees of freedom leads to strong cooperativity during the photo-induced phase transitions[11]. The field of ultra-fast laser technology[60] has revolutionised our understanding of the material properties at time scales of femto- and picoseconds. The intense laser pulse causes efficient coupling of the electronic excitation with the lattice deformation. This has opened up new avenues for investigating phenomena such as light-matter interactions, phase transitions, structural changes, and electronic dynamics in a wide range of materials. In this thesis, we have explored a new type of cooperativity whereby the strain feedback can lead to efficient transformation in photo-induced phase transition with significant volume change.

The ultrashort light pulse generates coherent motions of atomic wave functions. Resulting strain waves too are coherent propagation of structural deformations within the material, often establishing a new long range order. The nature of coherent strain wave propagation is very different from the incoherent lattice heating, which causes the diffused reflections in XRD. Conversely, the coherent wave results in oscillations of the Bragg peak intensity[96].

The excitation with such ultrashort (fs) laser pulse generates a sequence of events,

which can lead to a non-equilibrium macroscopic phase. The advancement in the field of time resolved X-ray and electron diffraction or optical spectroscopy, enables us to unravel and hopefully understand the transient structural dynamics in non-equilibrium regime.

In this thesis, we have observed two different types of phase transitions:

Isostructural phase transition An isostructural phase transition refers to a distinct category of phase transitions where the crystalline symmetry of a material remains unchanged during the transition. Unlike many phase transitions that involve a change in crystal symmetry, isostructural transitions are characterized by a reorganization of the internal arrangement of atoms within the same crystal symmetry. Examples of such transitions are the Mott transition in V_2O_3 from PI to PM phase, spin transition in Spin Crossover Compounds and the β-λ phase transition in Ti_3O_5. These transitions are associated with a discontinuity of entropy or volume while crossing the transition line in the phase diagram.

Symmetry breaking Symmetry-breaking phase transitions are characterized by a significant alteration in the material's symmetry as it crosses the transition boundary. This shift in symmetry is often accompanied by distinct changes in the material's entropy and volume, rendering the transition of a first-order nature.

What further distinguishes these transitions is the coexistence of both high-symmetry and low-symmetry phases within a finite temperature range around the transition point (thermal hysteresis).

1.7 Pump-probe technique

Pump-probe technique is used to study fast processes in real time and has its application in various fields of chemistry, condensed matter and biology[81]. The short and intense burst of optical pulse acts a pump and initiates electronic and structural change in the system, driving it out of equilibrium. The probe is an ultrashort X-ray or electron pulse or another optical pulse.

The time at which the laser pulse arrives at the sample is considered as time zero. The probe pulse arrives at a defined delay (Δt) after the pump pulse as shown in Fig. 1.6 and helps to study the state of the system at this delay. These changes can be detected and measured using various techniques like spectroscopy and imaging. So a suitable detector is used to track the changes.

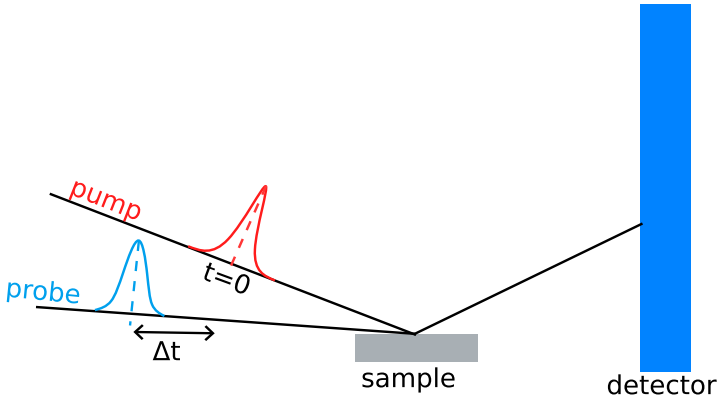

Figure 1.6 – Schematic experimental geometry of the pump-probe technique with the pump pulse arriving at the sample at t = 0, followed by the probe pulse that reaches the sample after a delay of Δt. The photo-induced changes are followed at different delays with a suitable detector.

This set of pump pulse and the subsequent probe pulse at defined delays is repeated several times in stroboscopic manner to have a snapshot of the excited system at different delays. The time resolution of the snapshots depend on the time length of the probe and pump pulses and the corresponding jitter between them.

Pump-probe techniques are used to explore a wide range of phenomena, such as photochemical reactions, charge transfer, phase transitions, and the dynamics of complex materials. These techniques provide invaluable insights into processes that are not accessible through traditional steady-state measurements. By capturing events on extremely short timescales, pump-probe experiments offer a deeper understanding of how materials and molecules respond to sudden changes in their environment.

It's worth noting that there are different variations of pump-probe techniques, including transient absorption spectroscopy[30], time-resolved X-ray diffraction and spectroscopy[10][35][28] and electron pump-probe microscopy and diffraction[106][41], each tailored to investigate specific types of systems and phenomena.

With the recent improvements in the femtosecond X-ray and electron diffraction sources, it has been possible to track the structural changes in the photo-excited systems upon the pump excitation. However, electron diffraction probes very small depth in the sample. Conversely, the penetration depth of X-rays is quite large and the diffraction images give overall information of the penetrated volume in the sample. Hence, X-ray is a good choice of probe to follow the structural changes that are established over macroscopic domains in the sample.

In this manuscript, we have investigated the role of the strain wave pathway in photo-induced phase transition with the help of laser pump and X-ray probe pulses. The X-ray probe pulse investigates the transient structural changes at macroscopic domains in volume changing system of Ti_3O_5 (Chapter 4) and volume plus symmetry changing system of V_2O_3 in Chapter 5.

Chapter 2

Experimental Methods to access the structural information

X-ray diffraction is a powerful analytical technique used in a wide variety of fields including physics, materials science, chemistry, geology and biology to determine the atomic and molecular structure of materials from small crystals to large bio-molecules and complex materials like polymers, ceramics and metals. It is based on the interaction of the X-ray with the crystal lattice, which scatters the beam in the form of diffraction pattern, providing information on the crystal structure.

Upon absorption of photons during laser excitation, the elementary electronic and/or nuclear rearrangements occur in femtoseconds time scales. Often these electronic excitations are coupled with the atomic motions driving the material towards a change of macroscopic properties, electronic and/or structural. The time evolution of photo-induced structural changes can be studied by diffracting ultrashort X-ray pulses at different time delays after pumping the system with femtosecond or picosecond laser pulse. This technique is very useful to study the precursor states during the non-equilibrium pathways of phase transitions.

In this chapter, the principle of time-resolved X-ray diffraction techniques have been discussed in detail with focus on the experiments conducted at the ID09 beamline at ESRF and FemtoMAX beamline at the MAX IV Laboratory, Sweden. In addition, a few experimental techniques that have been used to characterise the samples have been described in the later part of the chapter.

2.1 Principle of X-ray diffraction

Crystalline solids consist of regular arrangement of atoms, ions or molecules with the inter-atomic spacing in the order of Å. X-rays mostly have very short wavelengths (0.1 to 100 Å) comparable to the atomic length scales. Hence X-rays is scattered by crystal lattice and can form diffraction patterns characteristic of the crystal. The diffraction patterns can be used to determine the positions of atoms in the crystal lattice, the distances and angles between the lattice planes. X-rays are used to study a wide range of materials crystalline samples, polycrystalline powders and thin films.

In the following, we have only discussed the elastic scattering of X-rays from the crystals i.e. the energy of the X-rays remains invariant on reflection. An ideal crystal is formed by the infinite repetition of a group of atoms(called 'basis') attached to a set of

points called 'lattice'. In 3D space a lattice is defined by three basis vectors $\vec{a}$, $\vec{b}$ and $\vec{c}$ that define the unit cell. Therefore, the position of any atom j is given in the real space by :

$$\vec{r_j} = x_j\vec{a} + y_j\vec{b} + z_j\vec{c} \tag{2.1}$$

The scattering of the X-rays from the periodic planes of the lattice constructively interfere when the path difference as shown in Fig. 2.1a is an integral multiple(n) of X-ray wavelength(λ) as :

$$2d\ sin\theta = n\lambda \tag{2.2}$$

where d is the distance between the parallel planes of the lattice and θ is the angle of incidence of the X-ray with the plane. This is the Bragg's law which is direct consequence of the periodicity of the lattice.

To the real space of crystal, a reciprocal lattice space can be associated which is identical to the wave-vector($\vec{k}$) space. The three basis vectors $\vec{a^*}$, $\vec{b^*}$ and $\vec{c^*}$ of the reciprocal space are defined as :

$$\vec{a^*} = 2\pi\frac{\vec{b}\times\vec{c}}{V}; \qquad \vec{b^*} = 2\pi\frac{\vec{c}\times\vec{a}}{V}; \qquad \vec{c^*} = 2\pi\frac{\vec{a}\times\vec{b}}{V}; \tag{2.3}$$

where V is the unit cell volume given as $V = \vec{a}.(\vec{b}\times\vec{c})$.

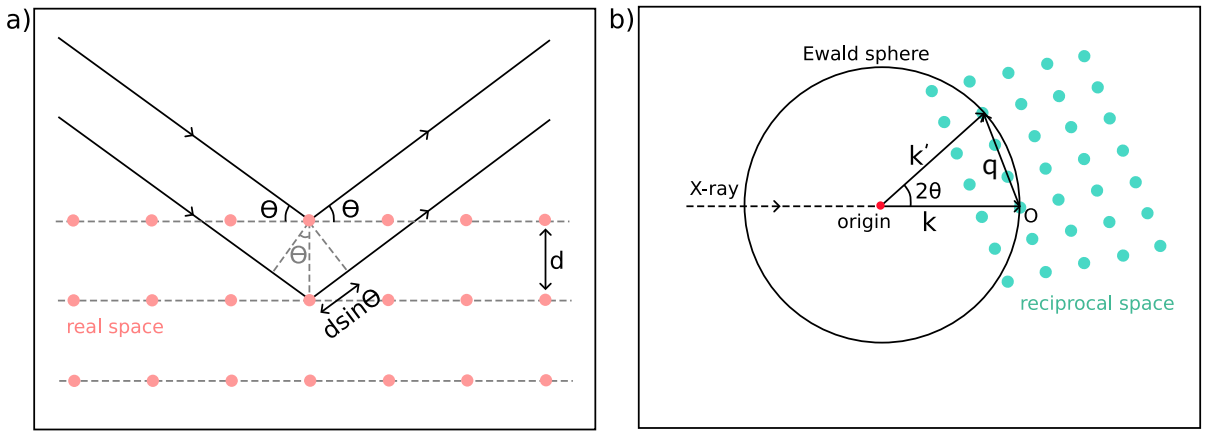

Figure 2.1 – a) Representation of the Bragg's law where d is the spacing between the atomic planes and θ is the incidence angle with respect to the planes. The red points denote atoms in real space. b) Ewald sphere construction in the reciprocal space of the crystal. All the reciprocal lattice points that intercepts with the Ewald sphere gives the diffracted Bragg peaks.

Ewald sphere is a geometric representation that helps us to identify all the possible points in the reciprocal lattice that satisfy the Bragg's condition resulting in the diffraction

spots. The vector $\vec{k}$ is the direction of the incident X-ray beam and its origin is chosen that the $\vec{k}$ terminates at a reciprocal lattice point. The Ewald sphere with the center as the origin of the $\vec{k}$ and radius $k = 2\pi/\lambda$ is shown in Fig. 2.1b for a incident X-ray beam of energy $E = hc/\lambda$. By construction, the terminal point of the incident scattering vector $\vec{k}$ is the origin of the reciprocal space. Any other reciprocal lattice node, such as $\vec{q}$, that lie on the Ewald sphere will give the diffracted peak along $\vec{k'}$.

$$\vec{q} = \vec{k'} - \vec{k} \tag{2.4}$$

The origin of the reciprocal space is indicated by O in Fig. 2.1b and the reciprocal lattice vector $\vec{q}$ is:

$$\vec{q} = h\vec{a^*} + k\vec{b^*} + l\vec{c^*} \tag{2.5}$$

The scattered amplitude in $\vec{k}$ is proportional to the geometrical structure factor:

$$S_G = \sum f_j exp(i\vec{q} \cdot \vec{r}_j) = \sum f_j \, exp[2\pi i(hx_j + ky_j + lz_j)] \tag{2.6}$$

where j runs over the atoms of the basis and f_j is the atomic form factor of the j^{th} atom of the basis.

The atomic form factor is related to Fourier transform of the spatial density distribution $\rho(\vec{r})$,

$$f_j = \int \rho(\vec{r}) exp(i\vec{q}.\vec{r}) d\vec{r} \tag{2.7}$$

The positions of the Bragg peaks ($\vec{q}$) give information on the lattice parameters whereas the intensity tells about the crystal structure and the preferred orientation /texture of the sample.

2.2 X-ray sources for time-resolved XRD

The general technique of time-resolved X-ray diffraction (TR-XRD) involves measuring the diffraction from an excited sample in real time. In the experiments done during my thesis, the sample was excited with an intense laser pulse and the transient structural changes were followed through XRD. So, the time resolution is an important factor in deciding the X-ray or laser source to be used. The time resolution is determined by the duration of the pump and probe pulses and the temporal jitter between them. In the different facilities, typically a Ti:sapphire laser system is used with a pulse width of several femtoseconds, so the resolution is mostly limited by the probe pulse width and jitter. To track the transient structural changes during the photo-induced transitions, high intensity X-ray sources with good time resolutions are required.

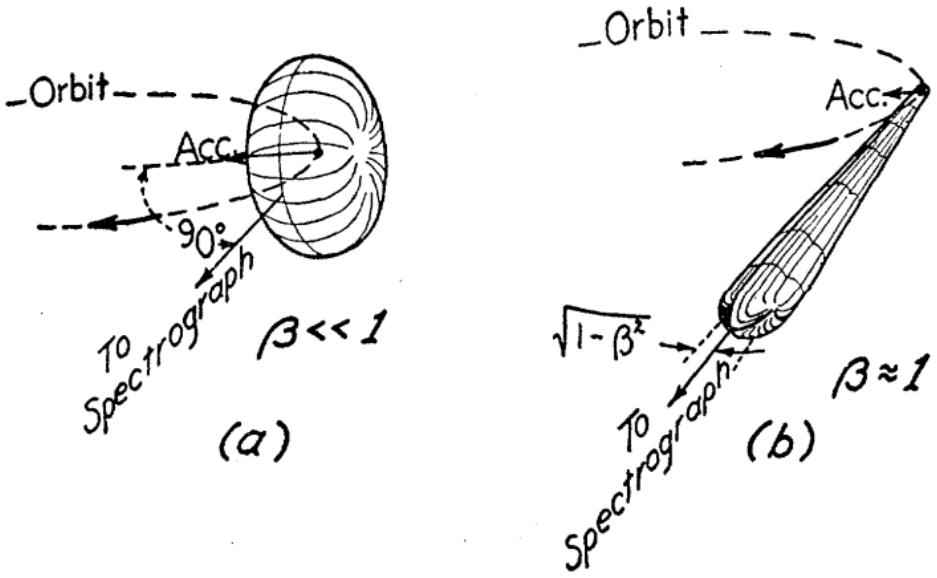

Figure 2.2 – Schematic picture of the radiation from electrons moving in a circular orbit at a)low energy with velocity $v << c$ and b) high energy with velocity $v \approx c$ (adapted from [105])

Synchrotron radiation In synchrotron sources, electrons are circulating in a orbit with velocity v close to the speed of light(c)[54]. A ratio of the velocity of electrons to the speed of light is defined as $\beta = v/c$. The radiation distribution is uniform for $\beta << 1$ as shown in Fig. 2.2a whereas when the electrons are accelerated with the relativistic velocity ($\beta \approx 1$), the radiation emitted is highly collimated (Fig. 2.2b). The angular divergence in the later case is $1/\gamma = \sqrt{1-\beta^2}$ which is very small for the condition where $v \approx c$.

The electrons emitted from the e-gun are accelerated in the LINAC and then injected into the storage rings. Here the electrons are maintained at constant energy with regular

injections from the booster ring. The electron trajectory is deflected by strong magnetic fields produced by dipole magnets and at each turning point X-rays are emitted due to the acceleration of the electrons.

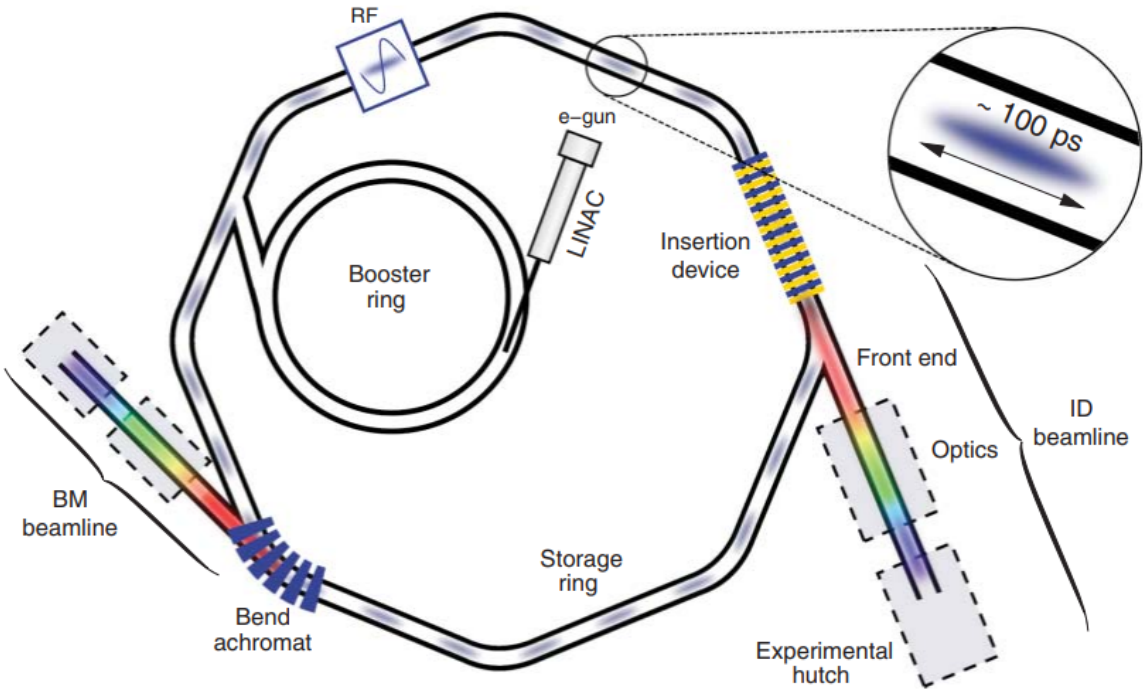

Figure 2.3 – Schematic picture of the components of synchrotron facility as adapted from [114]. Electrons from e-gun are accelerated in a linear accelerator (LINAC) into an evacuated booster ring, where they undergo further acceleration. Then they are injected into the storage ring, where they are maintained with a constant energy. The radiation emitted from the bending magnets and that from the insertion devices are utilised in the beamlines

Based on the temporal resolutions, we have divided the X-ray sources into picosecond and sub-picosecond sources. The flux for each source is also discussed since it is an important factor for grazing angle measurements.

2.2.1 Picosecond sources

Under standard operating conditions, X-ray pulses from synchrotrons have a duration of 30 to 100 ps. Some time resolved experiments in this thesis were done at the ID09 beamline, ESRF. ID09 beamline is an undulator based one, designed to study the ultra-fast structural changes in condensed matter or liquid solutions induced by ultrashort laser pulses. There are two undulators at ID09: in-vacuum U17, and in-air U27. The magnetic fields of the undulators are modulated by changing the gap, thereby changing the intensity

and energy of the X-ray. U17 provides X-ray with minimum energy of $\sim$ 14.5 keV and U27 with minimum energy of $\sim$ 6.5 keV. This corresponds in both case to the maximum intensity. However, the beamline transmission, mainly reduced by optics, windows and travel into air, is very low below 8 keV.

So, the undulator determines the range of X-ray energy, while the monochromators and mirrors determine the energy resolution and spatial shape of the X-ray beam. Energy width contributes in the instrumental broadening of Bragg peaks discussed in detail in Section 2.5.

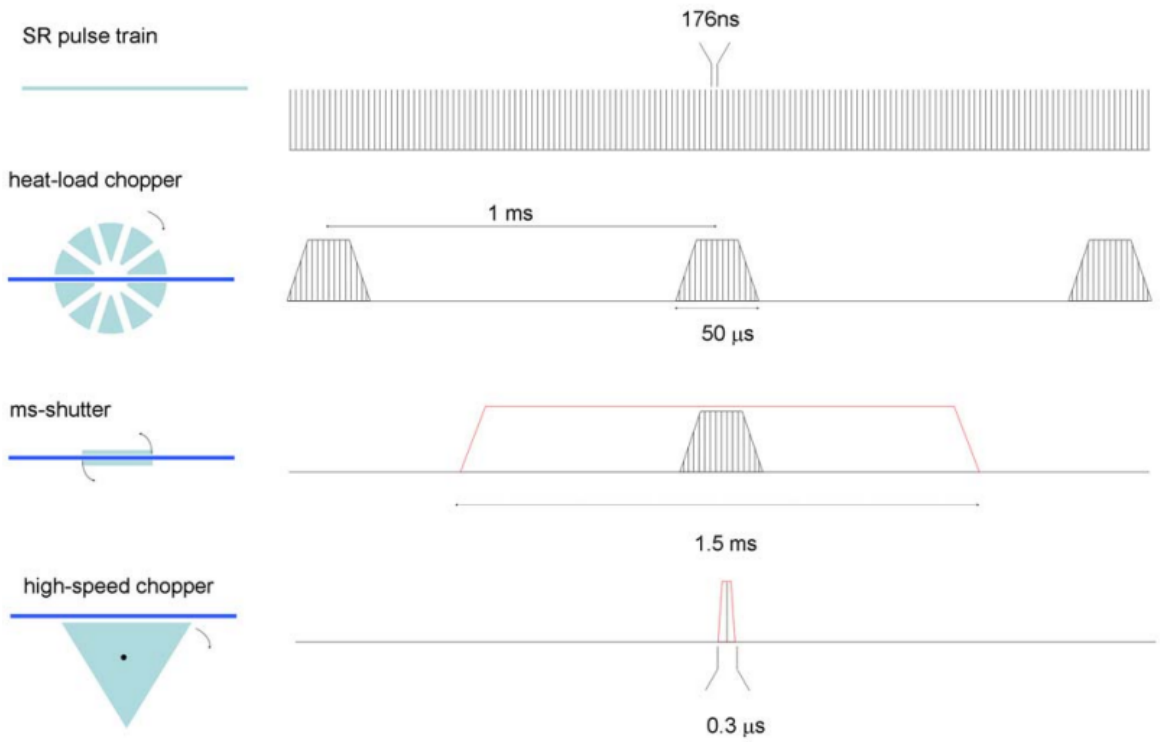

Figure 2.4 – Synchronisation of the choppers and the ms-shutter for choosing a single electron for the time-resolved measurements(adapted from [17])

At ESRF, there are four modes suitable for single pulse experiments- 4 bunch, 16 bunch , the so called hybrid mode and 7/8 + 1 mode. The 7/8 +1 mode has a 352 ns gap with a single bunch in the middle, the low bunch charge in this mode allows the full width of half max of the X-ray pulse duration is $\sim$ 60-80 ps. This is the preferred mode for time resolved experiments. The frequency of the time resolved experiments can vary from single shot experiments (0 Hz) to 1 kHz. Several chopper system as shown in Fig. 2.4 allows for choosing short X-ray pulses out of the X-rays in the ring and also helps to choose the repetition rate of the experiments. The heat load chopper has a window of transmission of 50 µs and helps to reduce the incident power of the X-rays a lot. The high speed chopper plays an important role in choosing a single 100-fs long X-ray pulse from

the synchrotron bunches. A detailed description of the chopper system is given in [17].

A femtosecond Ti:sapphire laser system produces laser pulses of about 100 fs and is synchronised with the X-ray using a N354 timing card, which runs at the radio-frequency(RF) clock of the storage ring. In order to check the time delay between the laser and X-ray pulse, a GaAs detector is used which is sensitive to both X-ray and laser pulse. This fast timing diode is placed in the path of the X-rays. A piece of foam is placed at the sample position so that the diffused light from it gets detected on the GaAs detector. This allows to chose the time zero, at which the X-ray and laser arrives at the same time on the diode and hence on the sample. This in turn, helps to measure time delays of ps to ms (depending on the repetition rate) between the pump and the probe with a jitter of 5 ps, which is much less than the X-ray pulse duration.

The laser beam first excites the sample and then the structural changes are probed with X-rays at different delays ranging from negative to positive. The diffraction images corresponding to each delay are collected using the 2D Rayonix MX170-HS detector with size 3840 × 3840 pixels. Each pixel is 44.3 µm × 44.3 µm. Such large detector are very useful to detect Bragg peaks at high 2θ values of almost 49° at a typical sample-detector distance of 100 mm. With a translation stage at ID09, the sample-detector distance can vary over a wide range from 35 mm to 600 mm.

2.2.2 Sub-picosecond sources

A major drawback of most synchrotron facilities is that they do not provide a time resolution better than 100 ps. Though the study of ultra-fast structural dynamics can be done with such a resolution, but often the phase transitions with acoustic velocity in nanosize objects occur below 100 ps. So there has been a continuous quest in search for a better temporal resolution. There are some modes implemented in several synchrotrons, e.g. the femto-slicing[72], low alpha mode[50]. However, all of them have a low X-ray flux making it very difficult to follow small intensity changes of Bragg peaks during photo-excitation.

Free Electron Laser (FEL) can provide 10 fs pulses with high flux, but the access to these instruments are very restricted and mostly limited to the study of ultra-fast processes in the range of 100 fs.

Ultra-fast hard X-ray pulses using Picoswitch

An attractive alternative has emerged recently to switch the efficiency of Bragg reflection using a laser pulse. It has a advantage that it requires no change to the mode of operation of the synchrotrons, it can be easily added in the X-ray pathways to achieve the temporal resolution.

I am deeply thankful to Daniel Schmidt and Dr. Peter Gaal from TXproducts and Leibniz-Institut für Kristallzüchtung for providing us with the Picoswitch to test it for our TR-XRD experiments. In this section, I would describe the working principle of a

Picoswitch and the results of an experiment performed at ID09, ESRF with a Picoswitch to understand prospect of it to study photo-induced phase transition in oxides.

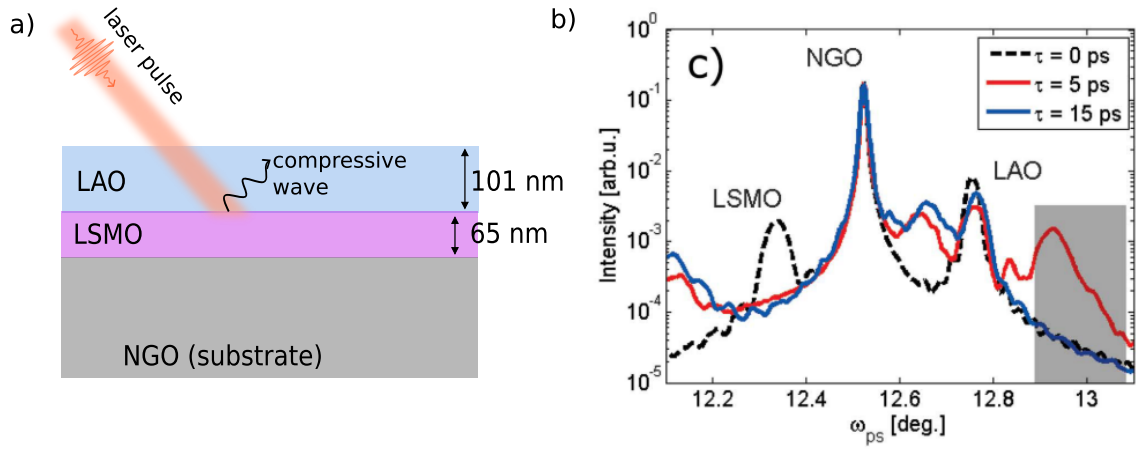

Figure 2.5 – a)Schematic diagram of a Picoswitch showing the different material layers. Upon laser excitation on Picoswitch, a compressive coherent wave is generated in the LAO layer. b) The simulated XRD patterns over a range of incident angle ω_{ps} for different delays[adapted from [87] for a similar Picoswitch of LAO-LSMO-NGO layers with different thickness]. The red curve (at delay = 5 ps) shows the intensity at a higher angle (shown by the grey shaded area) which completely relaxes at 15 ps (blue curve)

Picoswitch is a photo-acoustic device that consists of two layers of thin films epitaxially grown on top of a dielectric substrate using pulsed laser deposition [86]. The uppermost layer of the two is made of a transparent dielectric and the bottom layer is an opaque layer that behaves as a thermoelastic transducer upon optical excitation. Several material combinations can be used to form a Picoswitch. $SrRuO_3$ (SRO) layers on $SrTiO_3$ (STO) substrate Picoswitch has recently been tested at the ID09 beamline at ESRF and has shown a switching time of $\leq$ 5 ps[31]. We had the opportunity to use a Picoswitch consisting of a 101 nm thick $LaAlO_3$ layer (referred to as LAO layer) and 65 nm thick $La_{0.66}Sr_{0.33}MnO_3$ layer (referred to as LSMO layer) grown on $NdGaO_3$ (NGO) substrate which was tested in [87].

Material	q (Å^{-1})	2θ (°)	d_{layer} (nm)	v_{sound} (nm/ps)
LAO	3.355	13.29	101	7.2
LSMO	3.195	12.6	65	7.8
NGO	3.295	13.0	5e5	7.8

Table 2.1 – Theoretical values of the material properties of the Picoswitch sample. The 2θ is calculated at 14.45 KeV.

The working principle relies on the propagation of coherent acoustic phonon. The LAO layer is transparent, so the incident laser pump pulse is absorbed by the underneath LSMO layer which then undergoes expansion. This generates coherent compression waves at the LAO/LSMO interface and also in the substrate layer. This compression wave takes about ~ 14 ps (calculated from d_{layer}/v_{sound} in Table 2.1) to go through the LAO layer and it modulates the lattice parameters resulting in the shift of the diffraction peak towards higher q values.

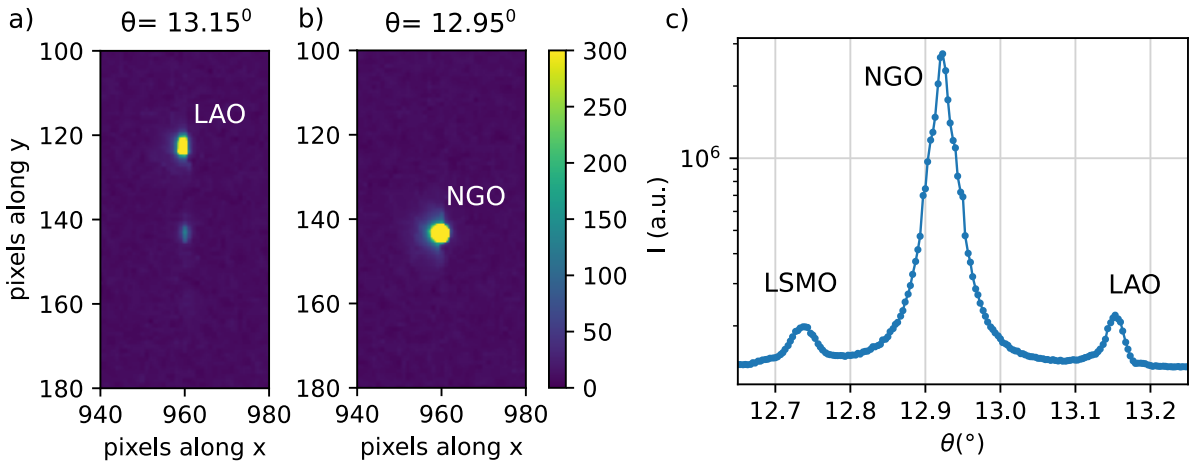

Figure 2.6 – a) Diffraction image showing the most intense peak of LAO at the incidence angle of 13.15° and b) image showing the intense substrate peak (NGO) at the incidence angle of 12.95°. c) The diffracted intensity integrated over the region of interest(ROI) as shown in a and b, is plotted as a function of the incident angle θ showing the Bragg peaks from all the three layers LAO, LSMO and substrate NGO.

X-ray diffraction measurements were performed at the ID09 beamline, ESRF during the filling mode 7/8 th +1. The incident x-rays peak energy of 14.45 keV was chosen to get the maximum flux under the conditions at ID09. The X-ray was monochromatic with the Germanium monochromator to get a smaller bandwidth of 0.034 % to achieve a better switching contrast. Increasing the bandwidth of the x-ray probe gives a higher photon flux, but the switching contrast decreases if the relative bandwidth is too large as was estimated in [87]. At this energy, the x-ray flux is 3e9 photos/sec i.e 3e6 photons/pulse working with the repetition rate of 1 KHz and a single bunch current of around 4 mA (slightly varies from 4.1 to 3.9 depending on the time after the refill). The diffracted signals were recorded on the Rayonix MX170-HS CCD detector in low-noise readout mode.

For the photo-excitation part of the measurements, a synchronized laser at wavelength 800 nm was used to excite the Picoswitch at an angle of about 23°. Laser beam size was (360 µm × 608 µm) leading to a footprint of 1 mm × 0.6 mm. A illustration of the experimental geometry is shown in Fig. 2.9.

Diffraction images (Fig. 2.6a) shows the Bragg peaks of LAO and NGO. The azimuthally integrated intensity i.e. the 1D diffraction patterns are plotted in Fig. 2.6b for

the LAO, NGO and LSMO with the variation of the incidence angle (θ). Fig. 2.7 shows the intensity of the LAO peak at different delays after the laser excitation. The change in intensity at the edge of the LAO peak (shown by the arrow in the Fig. 2.7) is observed at a delay of $\sim$ 20 ps and then it relaxes before 150 ps.

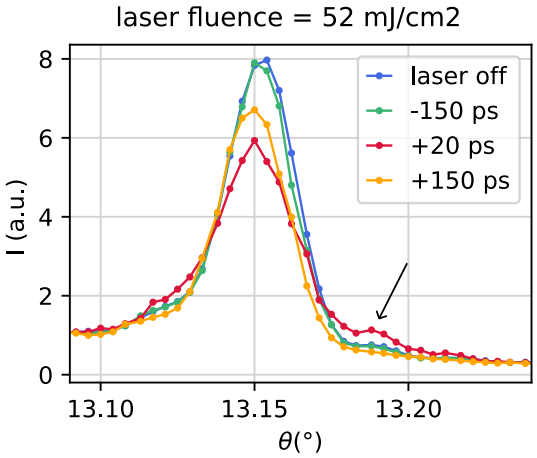

Figure 2.7 – The maximum change in intensity ($\sim$ 48%) is observed on the edge of LAO peak (indicated by the arrow) at a delay of 20 ps and for a laser fluence of 52 mJ/cm^2

The flux obtained at the edge of the LAO peak with an incident laser fluence of 52 mJ/cm^2 is 1000 times less than that without the Picoswitch as seen in Table 2.2.

Flux measured on a pin-diode	**ph/pulse**	**ph/s (at 1 kHz)**
Incident flux at 14.45 keV(without Picoswitch)	$3e^6$	$3e^9$
Flux on the edge of LAO peak (without laser)	$1.45e^3$	$1.45e^6$
Flux on the edge of LAO peak(delay = $-150ps$)	$1.4e^3$	$1.4e^6$
Flux on the edge of LAO peak(delay = $+20ps$)	$2.3e^3$	$2.3e^6$
Flux on the edge of LAO peak(delay = $+150ps$)	$1.3e^3$	$1.3e^6$

Table 2.2 – Flux measured of the X-ray beam at ID09 and that of the shortened beam from the Picoswitch in photons/pulse (ph/pulse) and photons/s (ph/s) with 1 kHz repetition rate.

Thus, Picoswitch helps us to achieve a ps time resolution X-ray probe. The maximum flux that could be extracted from the Picoswitch is 2.3e3 photons/pulse in the configuration we used, making it more suitable for single crystal experiments or experiments with high repetition rate. The flux was a too severe limitation for the polycrystalline samples with small grain size studied in this thesis.

Bunch Compression at MAX IV Laboratory, FemtoMAX beamline

For higher temporal resolution of the TR-XRD studies very short X-ray pulses are required. The FemtoMAX beamline at the MAX IV Laboratory in Lund, Sweden is dedicated to provide ultrashort X-ray pulses (of the order of femtoseconds) for the time resolved pump/probe diffraction experiments[25].

The FemtoMAX beamline utilises the MAX IV linear accelerator as the electron source. The design of the LINAC and short pulse facility (SPF) allows for the electron bunches shorter than 100 fs in duration. These electron bunches when pass through the undulator at the FemtoMAX beamline, they emit femtosecond X-ray pulses with a photon energy ranging from 1.8 keV to 20 keV. The maximum X-ray flux is $\sim 10^7$ photons/pulse around 4 keV. Two kinds of monochromators can be used: double crystal monochromators with InSb and Si crystals with bandwidths in the order of 0.01% and multilayer monochromators with a bandwidth of 1.5%. The multilayer monochromator provides the high flux while suppressing the low energy tails from the undulator spectrum. The beam size is focused to 80 µm with the help of toroidal Si mirrors positioned downstream from the undulators.

An ultra-fast laser system with Ti:sapphire amplifier provides femtosecond optical pulses for optical pump probe experiments. The laser pulses are synchronised to the X-ray pulses by locking the laser oscillator to the 3 GHz radio-frequency (RF) signal from the linear accelerator. This synchronisation gives most of the pulses within the jitter of 1 ps time window in a good dataset. The relative phase between the laser and X-ray is monitored using a fast oscilloscope throughout the measurements. The laser system can run at the repetition rate of 1 kHz and delivers pulses with duration of 50 fs. It also includes the OPA to cover the wavelength range from 0.2 to 10 µm.

The experimental station is equipped with different sample environments, out of which we used the GIXS(Grazing Incidence X-ray scattering) (discussed in detail in Section 2.6.2) end-station for our measurements. A single photon sensitive 2D detector Pilatus3 1.2M detector of size 831 by 1475 pixels (each pixel size is 172 µm × 172 µm) is attached to the GIXS chamber. The detector is designed to be operated in vacuum but can also be operated in air with protective windows.

The repetition rate of experiments is limited by the photo-electron gun developed for 10 Hz. The flux at FemtoMAX is 100 times less compared to that at ID09, ESRF with similar experimental conditions. This is still a severe limitation, but this flux was enough for the studies presented in chapter 5.

Comparison of flux and time-resolution As a summary, the table below gives an overview of the order of magnitude of available flux and time resolution, estimated in the conditions described in the previous paragraphs.

X-ray source	**Flux (polychromatic)** (*photons/pulse*)	**Flux (monochromatic)** (*photons/pulse*)	**Time resolution**
Synchrotron (ID09, ESRF)	10^9 (15 keV, 1.5% *bw*)	10^6 (15 keV, 0.01% *bw*)	100 ps
Synchrotron with Picoswitch	-	2.3*e*3 (15 keV, 0.01% *bw*)	<20 ps*
FemtoMAX	10^7 (4 keV, 1.5% *bw*)	10^4 (4 keV, 0.01% *bw*)	< 1 ps

* depends on the thickness of the Picoswitch layer.

Table 2.3 – Flux and time resolution comparison of the three X-ray sources, where most of the experiments described in this thesis have been performed. The flux is the maximum available at each source for the mentioned X-ray energy(in keV) with the energy bandwidth(*bw*) in percentage.

2.3 Laser pump

In this thesis, the sample were photo-excited using an ultra-short laser pulse. In all cases, we used a laser system with Ti:sapphire amplifier which provides femtosecond optical pulses for pump probe experiments. The laser with wavelength of 800 nm (energy of 1.5 eV) used to excite the Ti_3O_5 pellets can be used directly from the output of the amplifier. The other wavelengths, be it 1550 nm(energy $\sim$ 0.8 eV) for the IR-excitation of Ti_3O_5 pellets or 2300 nm (energy = 0.54 eV) for the V_2O_3 thin films are generated using a Optical Parametric Amplifier(OPA). The laser beam is brought to the sample position by setting up a path of mirrors as shown in Fig. 2.8.

Different optical elements are added in the laser path for various applications. For example, in our measurements, to match the elliptical footprint of the X-ray on the sample, cylindrical lenses are used to focus the laser beam in the direction perpendicular to the X-ray. Often filters are added to reject the contamination of different wavelength from OPA. Absorptive filters are used to reduce the incident laser power on the sample.

Each experiment followed the general laser path with some slight modifications to reach the desired laser footprint on the sample.

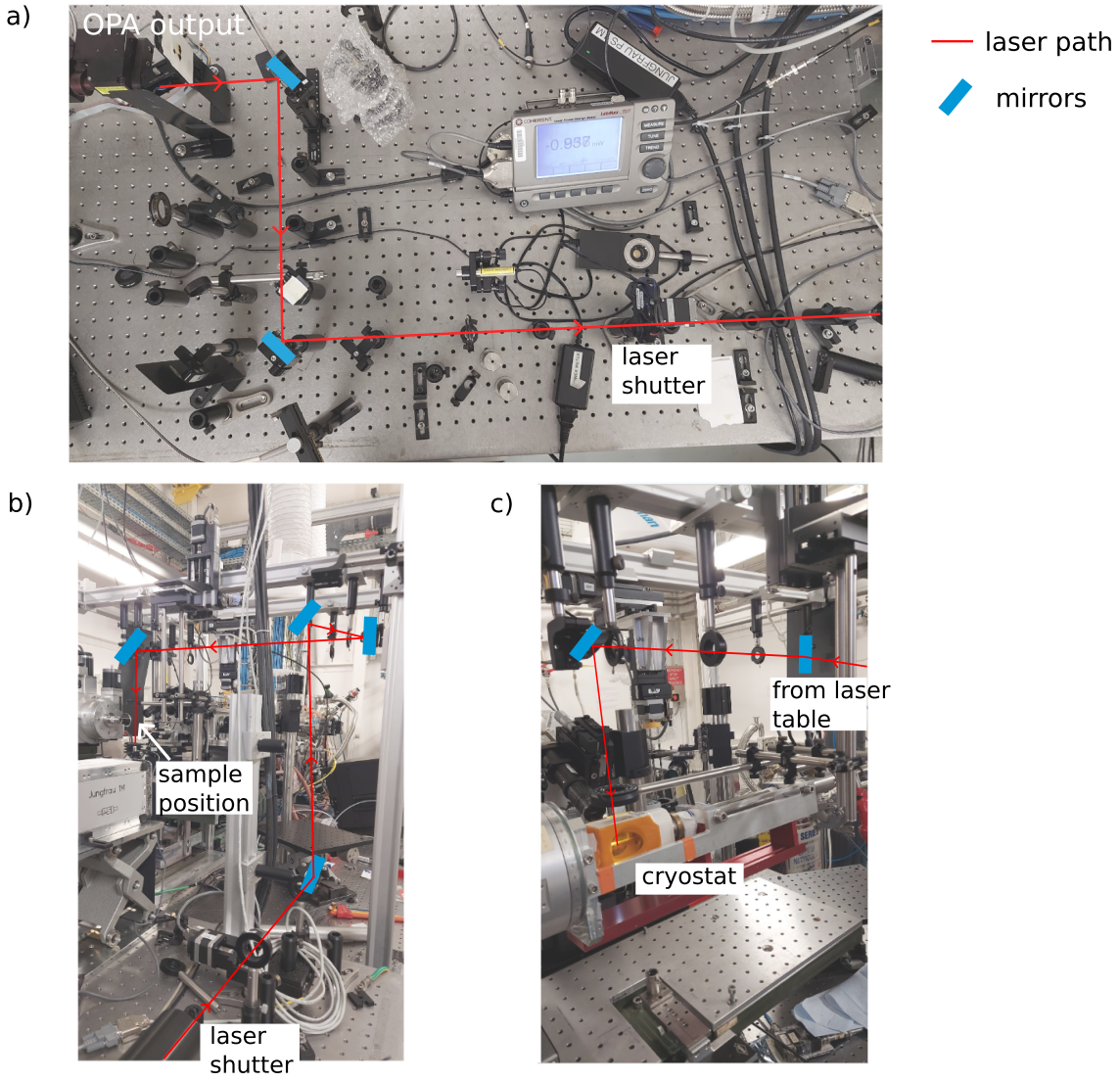

Figure 2.8 – a) Laser path from the output of OPA and guided by a set of suitable mirrors to the laser shutter which is synchronised with the X-ray pulse, so that the laser pulse arrives at desired delays with respect to the X-ray pulse. b) The rest of the laser path from the shutter to the sample position. c) The laser path along with the samples in the cryostat attached to the goniometer. This figure is for the excitation of the laser normal to the sample.

2.4 Experimental geometry

All the time-resolved diffraction measurements discussed in this manuscript have been performed in a reflection geometry. In addition to the laser vs X-ray overlap on the surface of the sample, the overlap in the depth of the material is also essential. The penetration depth of lasers in the photo-excited materials depend of course a lot on the material itself, the selected wavelength and the incident angle. Nevertheless, it is usually quite small, in the order of few 10 nm in the worst cases, and typically less than 1 µm.

On the other hand, X-rays penetrate significant depth in the materials for hard X-ray and depending on the material. For V_2O_3, for instance, the penetration is around 10 µm for 8 keV X-rays, 50 µm for 14 keV and 400 µm for 30 keV. So, X-ray diffraction provides information averaged over a large volume of sample, whereas the laser excites only a limited region below the exposed sample surface.

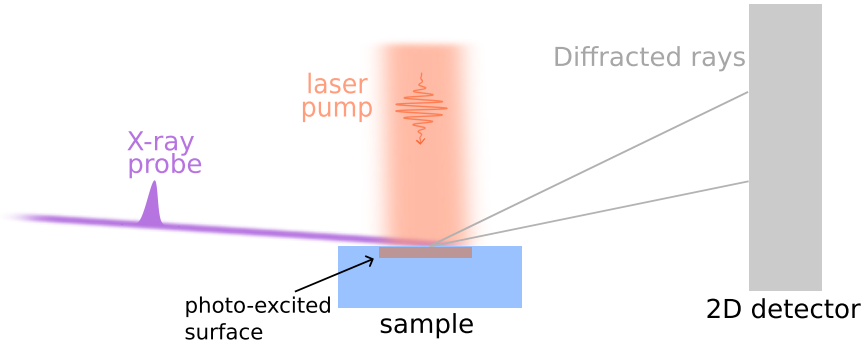

Figure 2.9 – Picture of the laser setup at the ID09 beamline for laser pump excitation perpendicular to the sample surface. A laser shutter is used to select a defined number of pulses. In this geometry, X-ray probe the sample surface with quasi-grazing incidence. X-ray diffraction images are collected by a 2D CCD detector.

In case of a bulk sample, reducing the volume probed by X-rays can be achieved by probing the sample at a grazing incidence. A small angle is chosen in order to increase the effective X-ray penetration depth by increasing the X-ray path below the sample surface. Both energy and angle can be tuned in order to match with the laser penetration. Such grazing incidence results in larger X-ray footprint on the sample, thereby contributing to the broadening of the Bragg peaks as described in the following section.

Another possibility to solve the in-depth overlap problem between X-ray and laser is to prepare the sample as a thin film with a thickness such that the laser penetrates the whole sample layer. In such cases, we don't necessarily have to probe the sample at a grazing incidence, but a small incidence angle is preferred. This is because, we will be able to probe more sample on the surface (since in the depth, the amount of sample is limited) which will increase the diffracted peak intensity. Secondly, having a low incidence angle of X-ray ensures that the X-ray penetrates less into the substrate thereby giving

lesser intense peaks from it. However, a large footprint of X-ray on the sample increases broadening of Bragg peaks and also requires a laser with a comparable footprint, which can be a limitation in some experimental environment. So, a trade-off is made between the q-resolution and the intensity of the Bragg peaks to determine the incidence angle in this case.

2.4.1 Determination of the incidence angle

In order to perform experiments with quasi-grazing X-ray incidence, the sample angle has to be precisely determined. For a ideal perfect surface we can utilise the specular reflection at the small angles to determine the zero angle of the sample, but in case of a rough surface like the Ti_3O_5 pellet we utilise the direct X-ray beam to determine the zero incidence angle. In this process, the sample is scanned along the z-direction in small

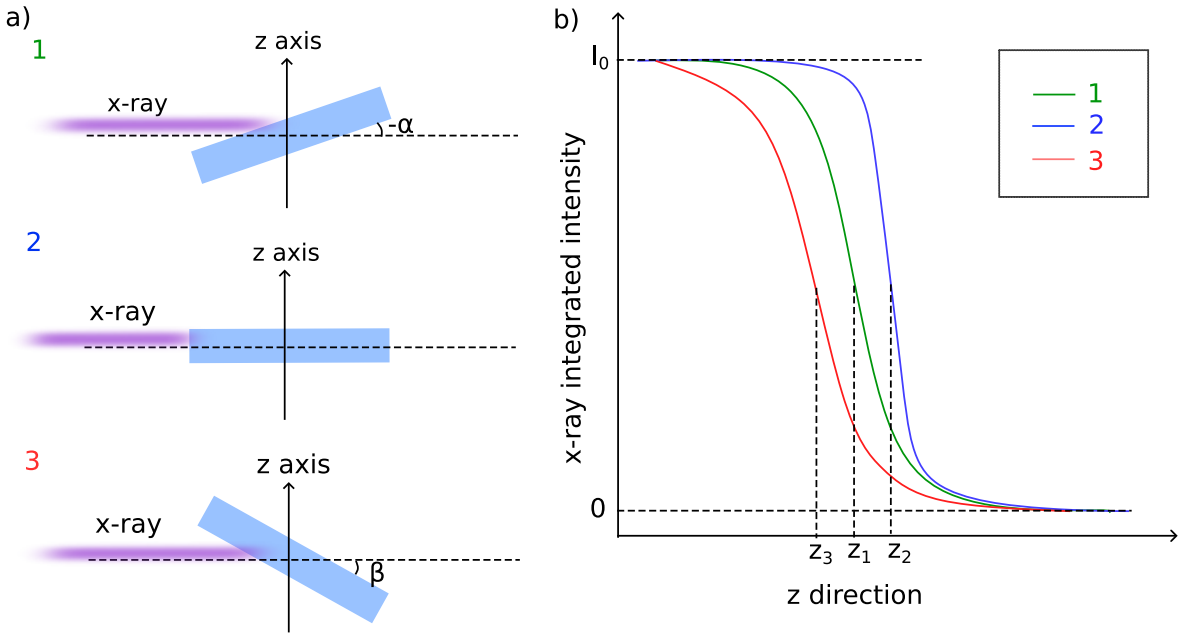

Figure 2.10 – a) The different possible situations of sample misalignment of the angle. b) The X-ray intensity for the three cases with the scan along the z-direction. The angles and the shape of the curves are exaggerated to show the differences in the three situations.

steps, and the total integrated intensity of the X-ray can be measured after the sample using a PIN diode. So when the sample is too low compared to the direct X-ray beam we measure the incident intensity Io uninterrupted by the sample. When the sample is moved in positive z in small steps, the direct beam is partially obstructed and the intensity decreases slowly till it finally goes to zero when the direct beam is completely shadowed by the sample.

Let us consider the situation 1 in Fig 2.10, where the sample is misaligned in angle by α, the the direct beam is obstructed much earlier than in case when the sample is more flat as in situation 2 (the incidence angle is close to zero). The same situation occurs in situation 3 where the sample is misaligned in the other direction by β. The only situation where the beam is obstructed at higher value of z is at the incidence angle of zero, (in the schematic figure $z_2 > z_1 > z_3$ if $\beta > \alpha$). This z-scan repeated for a few small angles around zero helps us to determine the incidence angle of less than a degree.

The choice of the incidence angle for each sample has been discussed in the next Chapter.

2.4.2 Space-time mapping for temporal resolution

For the time resolved experiments described in the thesis, the structural changes are induced by an ultra-fast laser and a series of X-ray diffraction patterns are collected at different time delays relative to the excitation pulse. So, for these kind of measurements, the spacial and temporal overlap of X-ray and laser beam are important parameters.

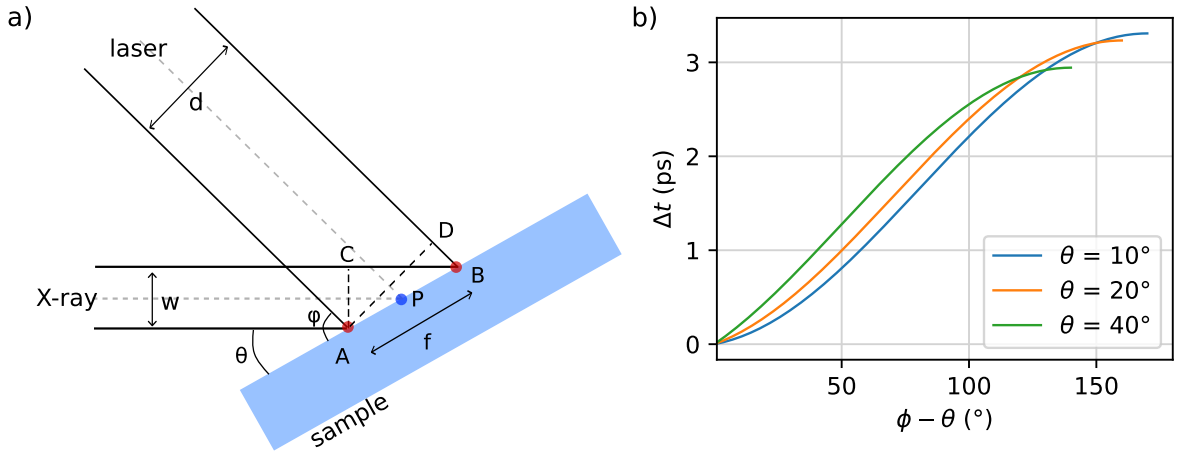

Figure 2.11 – a) Illustration of the spatial overlap of the X-ray with incidence angle of θ and laser beam with an incidence angle of ϕ with a footprint of AB on the sample b) The limitation in time resolution plotted as a function of the relative angle between the X-ray and laser pulse.

In order to achieve spatial overlap, it is a common practise to maintain the laser footprint on the sample larger than that of X-ray. This approach ensures that even in the presence of minor X-ray drifts, the majority of the laser irradiated surface is always probed by the X-rays. Hence, the width of laser beam is larger than that of X-rays. For the temporal overlap only the region that is both excited and probed, indicated by f in Fig. 2.11), is to be taken into account. In our case, f will be limited by the X-ray beam size.

Lets consider that the X-ray of width w is incident on the sample surface at angle of θ and the laser beam of width d is incident at an angle of ϕ to form a footprint of f (from point A to B) on the sample surface. Therefore,

$$f = \frac{w}{sin\theta} = \frac{d}{sin\phi} \tag{2.8}$$

Considering that the X-ray and laser reaches the point P on the sample surface at the same time t_0. X-ray arrives at the point A at time $(t_0 - CB/2v)$ and laser arrives at $(t_0 - BD/2v)$, where v is the velocity of electromagnetic waves. Similarly, to reach the point B, time taken by X-ray is $(t_0 + CB/2v)$ and for the laser is $(t_0 + BD/2v)$. Therefore the waiting time between the X-ray and laser at any point is absolute value of

$$\Delta t = \frac{BD}{2v} - \frac{CB}{2v} = \frac{f}{2v}(cos\phi - cos\theta) \tag{2.9}$$

where v is the velocity of light. For an X-ray pump pulse with different incidence angles, the time resolution possible to achieve for the relative different of the incidence angle of the X-ray and laser. For the 100 ps time resolution, the relative angle between the laser and X-rays is not important because the time resolution due to the geometry is not a limiting factor. Whereas to achieve a picosecond resolution, this geometrical factor is important to consider. As seen in Fig. 2.11, the time resolution can can vary between 0 to as much as 3 ps when the laser is perpendicular to the X-ray beam direction. The exact incidence angle of the laser and X-rays for each experiment have been described in detail in Chapter 3.

2.5 Parameters affecting the broadening of Bragg peaks

Ideally the Bragg peaks are extremely sharp, but in experiments, the peaks have a finite width in q arising from the instrumental broadening and from sample contributions. For example, grazing incidence geometry induces broadening of diffraction peaks thereby losing the q-resolution of them. Broadening of Bragg peaks can also be induced by the instrumental parameter like the energy uncertainty of X-ray or from the crystallite size of samples. The main individual contributions to broadening in the experiments performed during this work have been described below.

2.5.1 Broadening due to energy dispersion

The pink beam at ID09 is preferred because of its high flux, but this introduces a considerable energy width around the peak. The energy spectrum shown in Fig. 2.12 gives an estimation of this width for the polychromatic "pink" beam. It is centered around 12 keV and was measured at the sample position with the primary slits open by 500 µm × 300 µm. An estimation of the energy width of 0.2 keV is made by fitting the peak of the energy flux with a Gaussian function in Fig. 2.12.

$$\frac{\Delta q}{q} = \frac{\Delta E}{E} = \frac{0.2}{12.03} = 0.017 \tag{2.10}$$

Therefore the uncertainty in q due to the broad energy range of the pink beam is 1.7%.

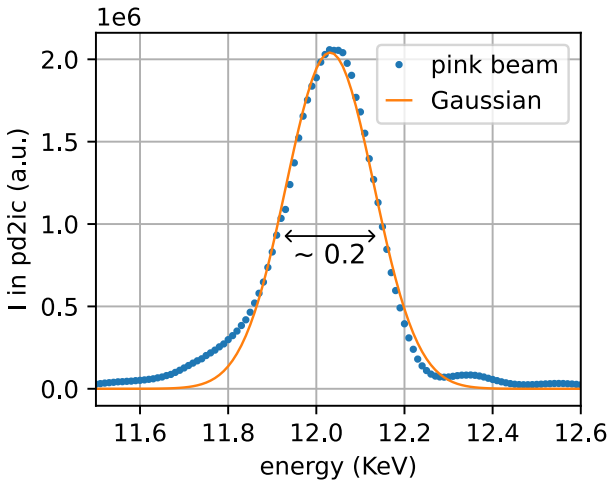

Figure 2.12 – Energy spectrum of the pink-beam centered around 12.03 keV is fitted with a Gaussian curve which gives a rough estimate of FWHM of 0.2 keV

2.5.2 Broadening due to footprint

For a grazing incidence of the X-ray on the sample, the large footprint plays an important role in broadening of the Bragg peaks. Without any X-ray beam width (w), the

diffracted beam will be at the height h on the detector from the position of the direct beam O.

$$h = D\, tan\theta \tag{2.11}$$

where D is the distance from the center of the sample to the detector.

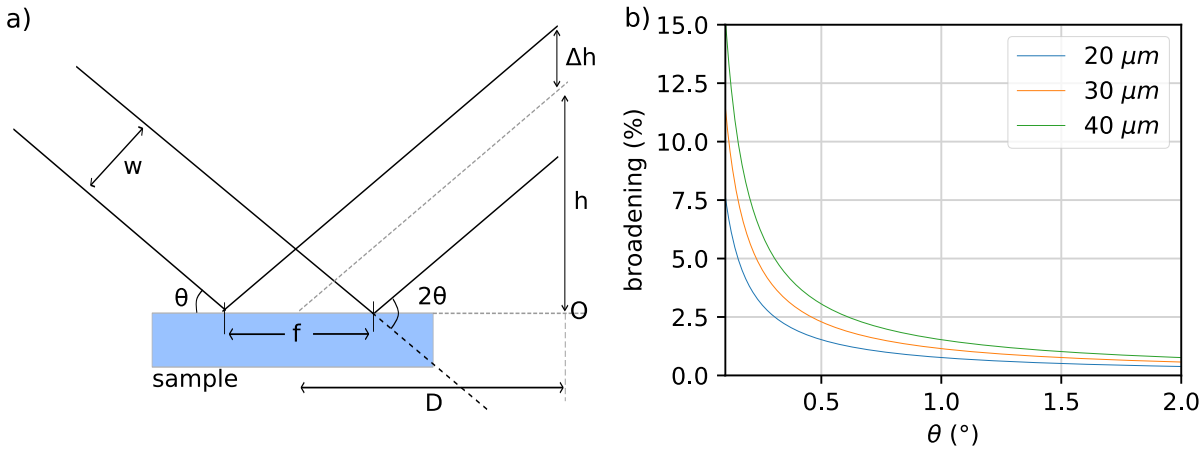

Figure 2.13 – a) Illustration of the experimental geometry showing the finite width of the incident X-ray beam giving rise to broadening in Bragg peaks. b) The percentage of broadening versus the incidence angle θ is plotted for different X-ray beam widths of 20, 30 and 40 µm.

For a finite FWHM of the X-ray footprint (f) on the sample,

$$h + \Delta h = (D + \frac{f}{2})\, tan\theta \tag{2.12}$$

Therefore the broadening of the peaks on the detector :

$$\Delta h = \frac{f}{2}\, tan\theta \tag{2.13}$$

Therefore we can estimate the percentage of broadening as

$$\frac{\Delta q}{q} = \frac{2\Delta h}{h} = \frac{f\, tan\theta}{D\, tan\theta} = \frac{f}{D} \tag{2.14}$$

and is plotted as a function of incidence angle θ for different an X-ray beam width (Fig. 2.13). The larger the footprint of X-ray on the sample, the larger is the broadening of Bragg peaks. This can be either due to small incidence angle or wider X-ray beam as seen from Fig. 2.13b.

2.5.3 Broadening due to crystallite size

The finite size of crystallite causes the broadening of Bragg peaks. The Scherrer equation provides a quantitative relation between the size of sub-micrometer crystallite to the broadening of the Bragg peak. Full width at half maximum(β) of the Bragg peak can be estimated from the equation :

$$\beta = \frac{k\lambda}{\tau cos\theta} \tag{2.15}$$

where τ is the mean size of ordered crystalline domains (maybe equal to or smaller than the grain-size or particle size), λ is the wavelength of the X-ray, θ is diffraction angle and k is a constant factor that depends on the shape of the crystallite. The typical value of k is taken as 0.9.

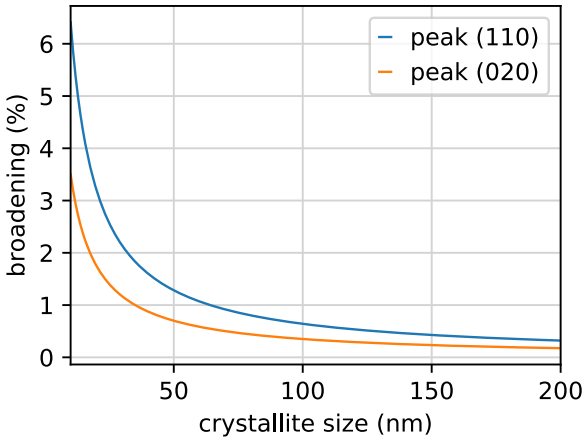

Figure 2.14 – The percentage of increase in FWHM of the two Bragg peaks (110) and (020) of Ti_3O_5 are plotted as a function of crystallite size for an X-ray energy of 12 keV.

For the incident X-ray wavelength of 1.0332 $\mathring{A}$, the broadening of two different peaks (110) at a small q and (020) at a larger q, have been plotted in Fig. 2.14 as a function of the crystallite size of Ti_3O_5. Three different crystallite sizes of Ti_3O_5 (the morphology of the samples has been discussed in details in Chapter 3) have been studied in this thesis. For the smaller crystallites size, the effect of broadening is larger compared to the bigger crystallite sizes.

2.6 Sample Environment

In order to explore the phase diagrams of the studied samples, different samples environments were used. These setups are described below.

2.6.1 Cold finger cryostat at ESRF, ID09

In order to study thin films at low temperature at ESRF, ID09 beamline, a cold finger cryostat was used.The sample holder connected to the cold finger (Fig. 2.15) had a flat surface for the samples to be glued on. This part is made up of Copper for efficient heat conduction to establish a homogeneous temperature over the whole area. The cold finger was provided with a continuous flow of N_2 to keep the temperature at the sample stable around 85 K. However, it is also possible to go to temperatures as low as 10K with He flow in the cold finger. The sample chamber µm Kapton windows for X-ray transmission and UV-fused silica window for the laser beam. The latter transmitted about 90 percents of the intensity of the laser, in a broad range of wavelength between $\sim$ 400 nm and $\sim$ 2.5 µm. Vacuum pump was also connected to the sample chamber to create a vacuum inside of about 10^{-6} mbar. This vacuum was enough to prevent the condensation of water vapour and eventually the formation of ice on the sample.

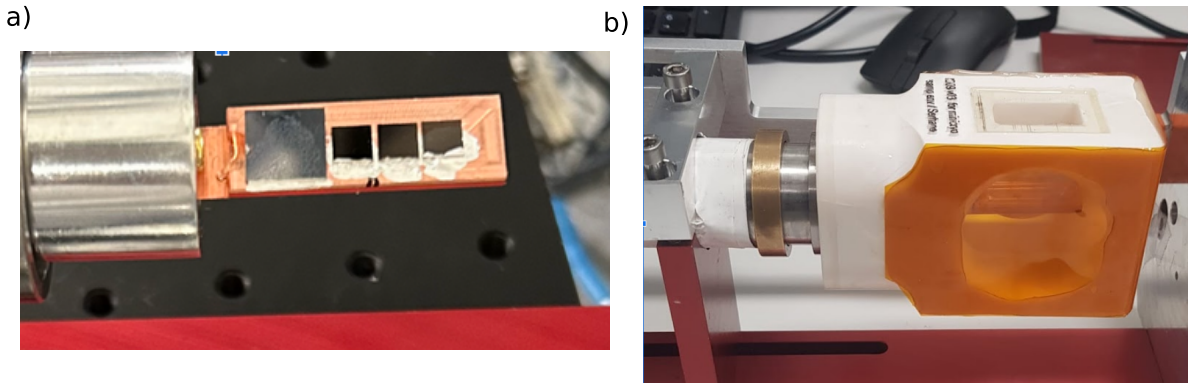

Figure 2.15 – a) Thin films of V_2O_3 and Cr-doped V_2O_3 glued on the copper holder of the cold finger using a Silver paint. b) The sample chamber with the Kapton windows for X-rays and fused silica for the laser beam, specially designed at ESRF.

2.6.2 Vacuum chamber at MAX IV, FemtoMAX

The sample environment at FemtoMAX is a specially designed end-station for Grazing Incidence X-ray Scattering(GIXS). A picture of sample area at the FemtoMAX beamline has been shown in Fig. 2.16 a.

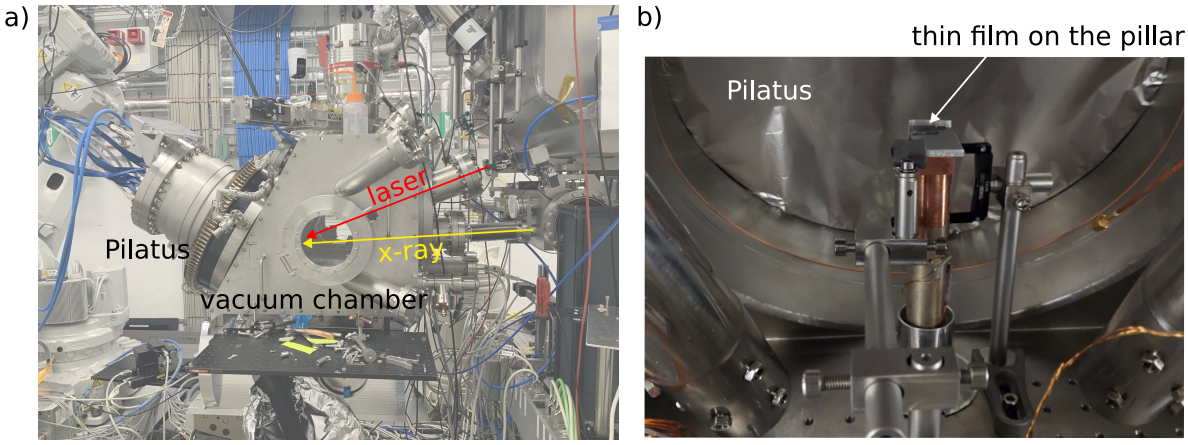

Figure 2.16 – a) The sample area at FemtoMAX showing the GIXS end-station along with the direction of incident X-ray and laser pulses and a 2d Pilatus detector is attached to the chamber. b) Picture inside the GIXS chamber from the direction of incident X-ray, where we see the Copper sample holder along with the Pilatus protected with a layer of Al foil.

The thin films were glued on a Copper pillar (as shown in Fig. 2.16 b) which are previously cut to get the desired incidence angle. A cold finger cryostat is inserted in the sample pillar for cooling the thin films. In general, the cryostat can maintain a broad temperature range from 10 to 500 K. A thermometer is glued to the pillar as close as possible to the sample position to have a good estimate of the temperature of the sample. The GIXS chamber can maintain a ultrahigh vacuum $< 10^{-7}$ mbar and this prevents the condensation of water vapour and the formation of ice on the sample at very low temperatures. It is also equipped with the Pilatus detector to measure the diffraction peaks from the sample.

2.6.3 Diamond Anvil Cells(DAC) at SOLEIL, CRISTAL

In order to understand the structures of out-of equilibrium states during the photo-induced transitions, it is important to understand the equilibrium phase transition induced by temperature but also by pressure.

For this, we have performed steady state diffraction at CRISTAL beamline in SOLEIL synchrotron radiation facility. XRD was performed both on single crystals and powder of pure V_2O_3 of size around 30 to 40 µm with the variation of pressure at room temperature as well as low temperature of 20 K.

The samples were mounted in a diamond anvil cell (DAC). This is the most versatile device to create high pressure on sample and is used widely in geology, engineering, and materials science experiments[94]. DAC creates high pressure by trapping sample in between the point sides (culet faces) of two diamond anvils. A small pressure on the

other face of the diamond puts tremendous pressure on the culet face. The chamber in between the two culet faces is enclosed on the sides with a gasket, which is a metal with a hole in the center. Fig. 2.17a shows the microscope image of the DAC chamber showing the single crystals of different sample, V_2O_3 along with Ruby and Au powder to calibrate the pressure inside the chamber. Fig. 2.17b shows the cross-section of the DAC with different components such as the Diamond Anvils, gasket and the piston to put pressure on the diamond anvils. The X-rays incident on the sample in the DAC chamber and the diffracted beam within the opening angle of the DAC is collected by the detector. High X-ray energy of 29 keV was used in order to increase the accessible q range and decrease the X-rays absorption.

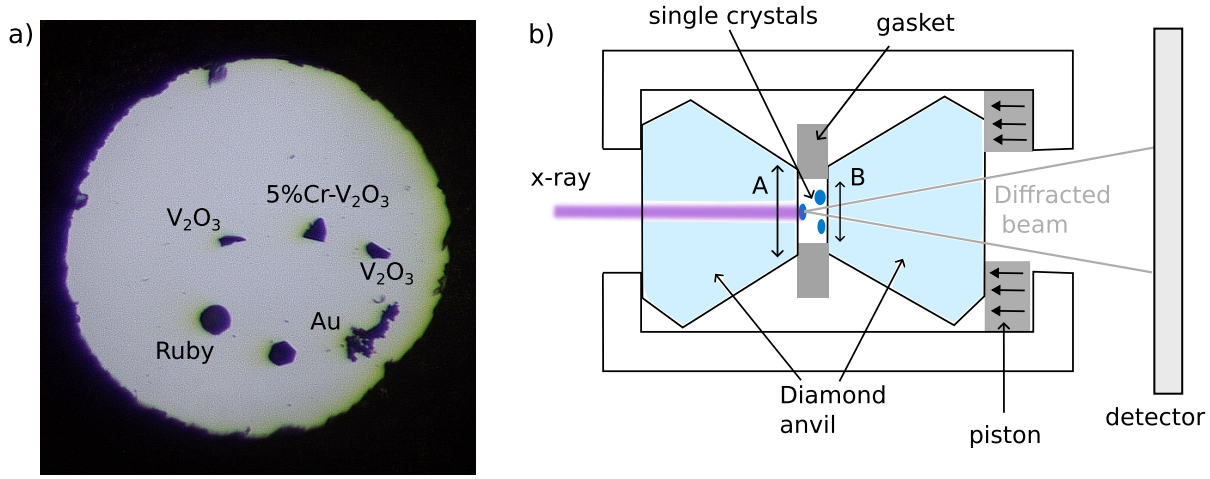

Figure 2.17 – a) Microscope image of the DAC loaded with the single crystals of V_2O_3 along with a single crystal of Ruby and some polycrystalline powder of Au for the pressure calibration inside the cell. b) Illustration of the basic components of the DAC: the anvils with the culet diameter of A, gasket with diameter of B and piston. The DAC has an opening of 30° for the diffracted beam to create an image on the 2D CCD detector

The chamber inside the DAC was filled with He for the low temperature measurements at 10 K. The role of the confining media is to transmit the pressure uniformly to the sample without any stress on them. Liquids provide good hydrostatics measurements, but it is important to check their properties at high pressure. Some liquids crystallizes under high pressure and thereby unable to transport the pressure uniformly throughout the cell. So, it is important to use the pressure transmitting medium in the pressure regime where it is still in liquid phase. Different pressure-transmitting media for the DAC have been tested[101]. Inert gases like nitrogen, Argon and Helium are suitable choices since there is homogeneous strain distribution under pressure in these medium. The high compressibility of helium[52] makes it possible to achieve high pressure inside the DAC.

2.7 Method of analysis

The photo-induced transitions are often associated with small changes in the Bragg peak intensity or position, which is very challenging to follow from the Bragg peak/ rings as collected by the 2D detectors in synchotrons. Consequently, an essential component of large-scale facility experiments is the development of analytical methods for data interpretation.

The data analysis involves reducing the 2D diffraction images from the detectors to 1D diffraction patterns to observe the changes in the position or intensity of Bragg peaks. For the real time visualisations, some python scripts are developed utilising several useful libraries like FABIO[47], pyFAI[46] and txs[38]. The method of quick as well as further analysis involving the pattern refinement are described below.

2.7.1 Generation of 1D diffraction pattern

A powder consists of large number of small crystallites that are randomly oriented with respect to each other. So while the single crystals generate Bragg spots, a powder will produce diffracted rings on the detector called Debye Sherrer rings.

The powder pattern consists of a set of intensities at their corresponding diffracted angles. In the diffraction experiments described, the powder patterns were collected with a two-dimensional detectors. The distribution of diffracted intensity is described with the cylindrical coordinates in reciprocal space: radius q (distance from the center of the rings) and azimuthal angle ψ . In the case of a perfectly randomly oriented polycrystalline sample, diffraction produces homogeneous rings. However, when crystallites show a preferred orientation in the sample, the distribution of diffracted intensity varies across ψ.

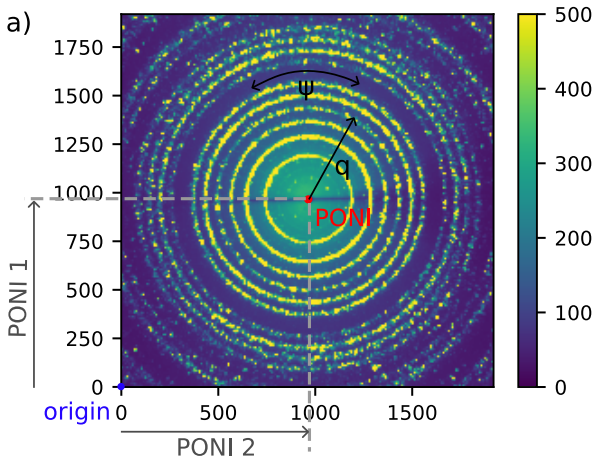

Figure 2.18 – Diffraction image on the Rayonix detector from LaB_6 powder in a capillary, because of transmission geometry

The diffraction images from the 2d area detectors are required to be converted to q

or the diffraction angle 2θ space. A python library have been developed at ESRF since 2011 for that purpose. This library, called pyFAI, for python Fast Azimuthal integration [46], includes tools to determine the geometry of the experimental setup.

The calibration of the detector position is performed using the Debye sherrer rings of a reference pattern. But often the calibration can be done on the sample itself. This step is done using the calibration tool pyFAI-calib2[7]. The rings are extracted either automatically (based on the intensity of each pixel) or using control points chosen manually on the rings or often using both the methods (in case of texture on the sample). The detector is defined in space using 6 coordinates - poni1, poni2, sample detector distance and the three rotations along orthogonal axes around the origin. The geometry used in pyFAI is based on the definition of the point of normal incidence called PONI, which is the normal projection of the direct beam on the detector as seen in Fig. 2.18. The 6 poni parameters defining the geometry are optimized using the known d-spacing of the calibrant or the theoretical values of the sample itself based on the least square difference of 2θ (theoretical - experimental). After the refinement of the geometry, each point on the detector is associated with the reciprocal lattice vector q or diffraction angle 2θ.

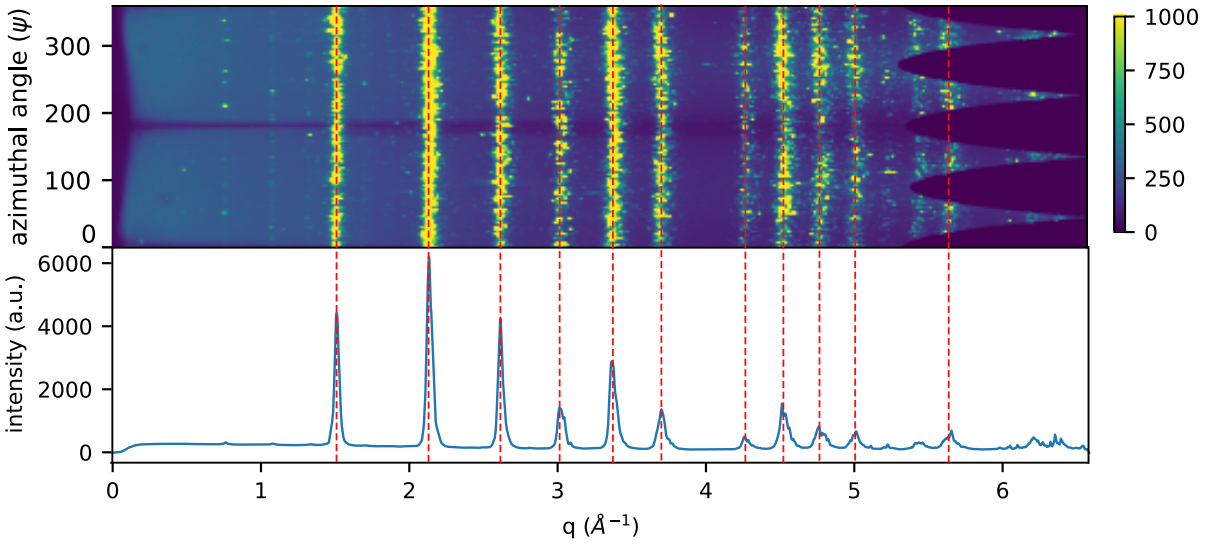

Figure 2.19 – (top) Azimuthal unfolding of the 2d diffraction images. Rings have transformed into lines along the azimuthal angle at different radii from the center(beam position). (bottom) The intensity, integrated along each the azimuthal angle ψ, is plotted with the scattering vector $\vec{q}$ resulting in 1d diffraction pattern.

This calibration process helps to perform 2d or 1d azimuthal integration which represents intensity along the azimuthal angle ψ giving a line of diffraction points in the 2D map or 1d diffraction patterns with the variation of q respectively in top and bottom image of Fig. 2.19.

2.7.2 Data reduction of stroboscopic measurements

The time resolved diffraction patterns are collected for several delays ranging from positive to negative, interleaved with a reference pattern at "laser off" and this set is repeated several times. A data analysis toolbox "txs"[38] have been designed and implemented at the ID09 beamline in order to facilitate the data reduction of such scans. During my thesis work, I have participated in the development and testing of different functionalities of this toolbox for application to measurements on solid polycrystalline samples.

Each diffraction image is integrated using the experimental parameters refined from calibration of the geometry. In the data-reduction step, the 1D pattern at each delay is corrected with the weighted average of nearest consecutive reference patterns[108]. The corrected patterns from different repetitions are then averaged for each delay. This generates differential pattern to track the transient changes in the diffraction patterns and are corrected from any experimental drifts. In addition, the toolbox contains variety of functions useful during the on-flight data analysis and plotting.

2.7.3 Diffraction pattern refinement

In order to extract the time evolution of the structural parameters, the 1D diffraction patterns extracted from the azimuthal integration described above could in some cases be refined following a fundamental parameters approach using TOPAS software[21]. In this thesis, the refinement was performed on the time resolved diffraction patterns of the Ti_3O_5 samples measured at ID09 beamline. The main goal was to extract the evolution of the photo-induced phase fraction. In general, the method involved refining the background and the experimental parameters, such as sample displacement, on the reference pattern. Then these parameters were fixed and only the cell parameters were refined for the patterns at negative and positive delays.

The experimental profile was described using a Gaussian profile of X-ray beam with central energy of 12 keV and FWHM of 17 mÅ. The X-ray beam height(FWHM) at the sample position was fixed to 21 µm and a fixed incidence angle was set depending on the scan. The sample to detector distance was fixed at 151 mm obtained from the refinement in the azimuthal integration process. The background was described by the Chebyshev polynomials with 7 coefficients. The texture were described using spherical harmonics, the coefficients of which were refined on the reference patterns and then kept constant for the patterns at other delays. The refinement was performed within q range from 1.06 $Å^{-1}$ to 4.06 $Å^{-1}$ with a convolution step (number of calculated data points per measured data point) of 4. The atomic positions could not be refined due to limited resolution and q range. These values were fixed at the values from the published structure[67]. Typical R_{wp} values are $5 \pm 1\%$.

Though the powder is biphasic, i.e. the pellets constitute a mixture of the β and λ phases, the Rietveld refinement is efficient to extract the relative weight percentages of each phase in the three types of pellets. The refined patterns along with the differential

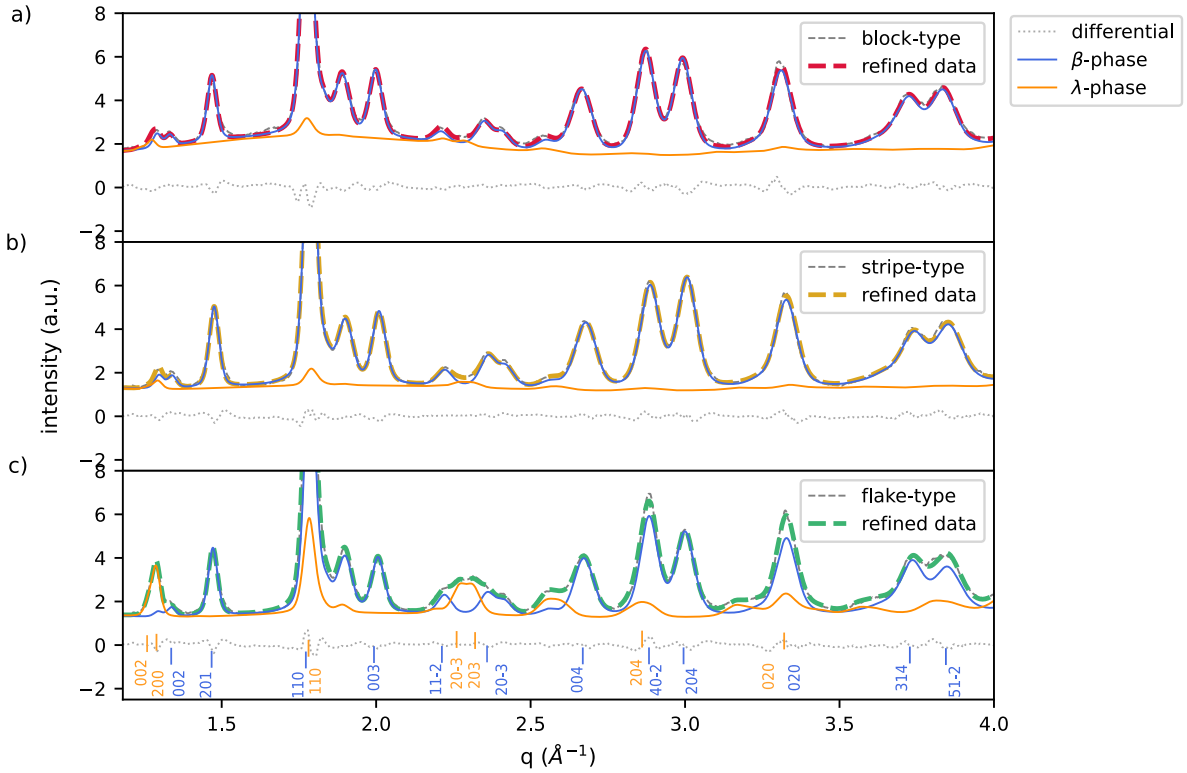

Figure 2.20 – a) to c) Result of the Rietveld refinement of the 1D pattern for the block-, stripe- and flake-type Ti_3O_5 respectively. Measured powder pattern is plotted in gray dashed line, calculated patterns are in red (block-type), yellow(stripe-type) and green (flake-type). Orange and blue curves are the contribution of the λ and β-phase respectively. Labels are shown only for the most intense peaks and not shown when too many peaks overlap. The residual curve is shown in grey dotted line.

.

and relative β/λ patterns have been shown in Fig. 2.20. The initial λ- phase ratio was found as 30%, 5% and 2% for the flake-type, stripe-type and block-type pellet respectively.

The relative changes in X-ray patterns induced by experimental drifts or sample movement can be corrected using essential tools from the txs library as mentioned before. Another possible way is to correct the drifts after refinement of the raw diffraction patterns. The cell parameters or the fraction of individual phases in case of Ti_3O_5, the results of which are discussed in Chapter 4, are extracted from the refinement of individual patterns. Interpolated value between two consecutive references is taken as the reference value and subtracted to extract the change in cell parameters of a given measurement at positive/negative delay. The parameters are then averaged over the repetitions of the time sequence.

For example, the refined weight percentage of the λ-phase (X_λ) for the flake-type Ti_3O_5 pellet has been plotted in Fig. 2.21a with the image number. The sequence

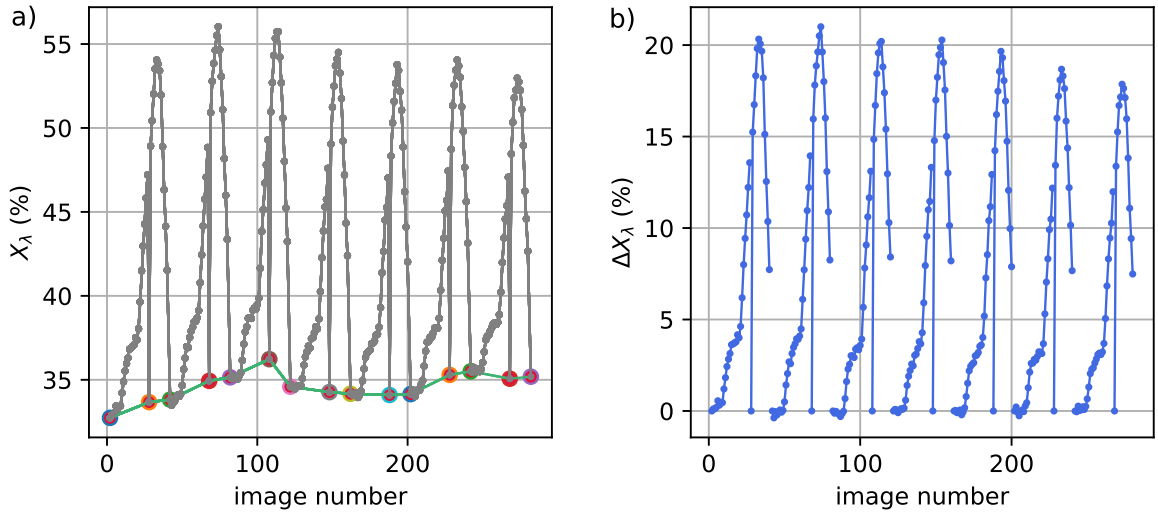

Figure 2.21 – a) The weight percentage of the λ-phase (X_λ) plotted with the image number. The red dots indicate the values from interleaved "laser-off" patterns and the interpolated values between them are indicated by the green lines. b) ΔX_λ after subtracting the interpolated values from the interleaved "laser-off" patterns.

of the time delays were repeated several times in the stroboscopic measurements, with a reference image at "laser-off" measured at the beginning, middle and end of each sequence. The weight percentage at any delay is corrected by interpolating the X_λ in between two consecutive reference "laser-off" patterns. The interpolated values $X^i_{\lambda_{ref}}$ are shown by the green line in Fig. 2.21a. The subtracted values ($\Delta X_\lambda = X_\lambda - X^i_{\lambda_{ref}}$) are shown in Fig. 2.21b. The ΔX_λ has been averaged over the good repetitions plotted as a function of delays in Fig. 4.10.

2.8 Complementary experimental techniques

In the pursuit of understanding the sample morphology and properties under equilibrium, two complementary experimental techniques have been described here that helped us to rationalise the results in chapter 4.

2.8.1 Atomic Force Microscopy

The Atomic Force Microscopy(AFM) allows us to obtain a topographic image of the pellet surface by using the attractive and repulsive forces between a few atoms on the AFM tip and the sample. AFM was done on the Ti_3O_5 pellet surface (Fig. 3.5 in Chapter 3) to understand the quality of the surface and estimate the roughness. The AFM images were taken with the Vecco diInnova system(Fig. 2.22) in the Tapping Mode on a region of 20 x 20 μm^2 on the pellet surface. The tip is an ARROW - NCR from NANO AND MORE and is made up of monolithic Si and is of width 45 µm and length 160 µm, with a thickness of 4.5 µm. The tip is located at the very end of the cantilever and has a height of 10-15 µm with a radius of curvature less than 10 nm. This kind of tips are used for the Tapping mode and is oscillated with resonant frequency to make the contact of the tip with the sample surface. This tapping mode helps us to image the surface without any destruction on the sample. The cantilever is also provided with a 30 nm Al coating on the back surface for the reflection of the laser beam. The reflection of the laser is read by a position sensitive Photo Detector, the output of which goes to the feedback loop to control the vertical position of the AFM tip and maintain the tip to sample interaction at a target value during the scanning.

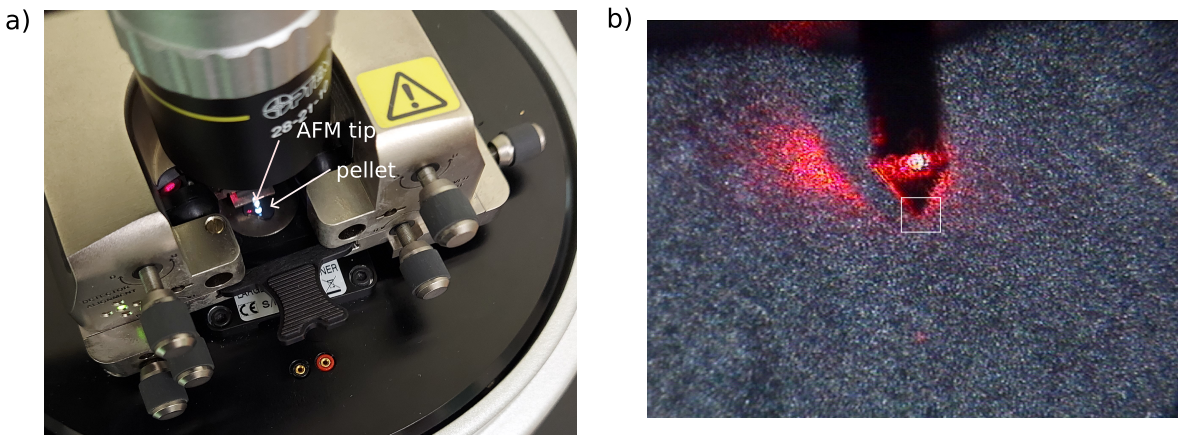

Figure 2.22 – a) The AFM tip on the b) Microscope image of the AFM tip on the pellet surface, with the white box showing an area of 20x20 μm^2 over which the raster scan is performed.

2.8.2 Differential Scanning Calorimetry

Differential Scanning Calorimetry (DSC) was used to understand the thermal characteristics, for example the transition temperature and the latent heat, in the Ti_3O_5 pellets with distinct morphology.

DSC is a standard widely used technique to study the thermal properties of materials by evaluating their transition temperature, enthalpy and specific heat. It is widely used for several applications for determining the structural phase transitions, melting points, heat of fusion, crystallisation kinetics and phase transitions[44][26]. The introduction of differential adiabatic scanning microcalorimeters in 1963 allowed the continuous measurement of heat capacity over a set temperature range [73]. An advantage of DSC over Adiabatic Scanning Calorimetry(ASC) is the ease and speed at which phase transitions can be tracked in materials.

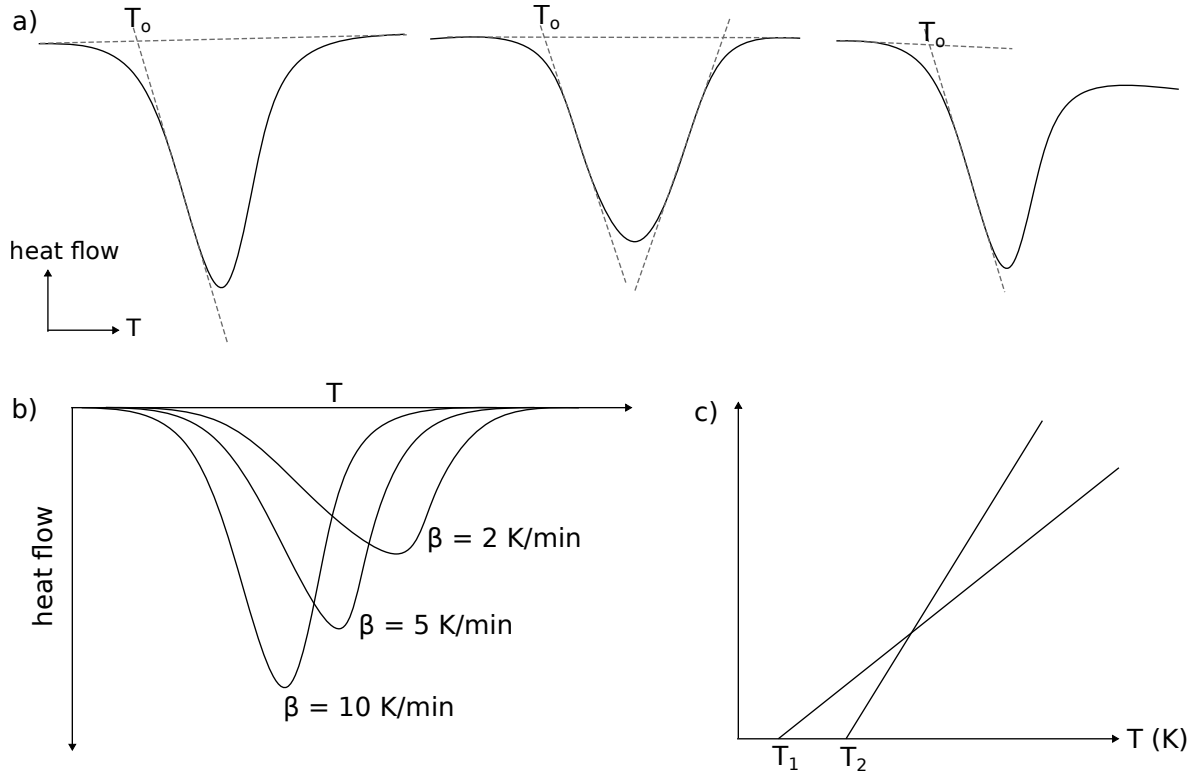

Figure 2.23 – a)A schematic representation of the onset temperatures (T_o) for different situations in the heating cycle. b) Dependence of the peak shape and transition temperature with the heating rate β. c) Mean of T_o for the heating and cooling cycle plotted. The temperature T_1 is the transition temperature and T_2 is the same transition temperature in case of transition with hysteresis (T_2-T_1 would be the thermal hysteresis in this case).

In the heat flux DSC, the sample material is enclosed in a pan and an empty reference pan is placed inside a thermo-electric dish surrounded by a furnace. The furnace is

heated at a linear heating rate and the heat is transferred to the sample and reference pan through the thermo-electric disc. This generates a DSC curves, where heat flow per unit mass of the sample is plotted as a function of Temperature. The curve constitutes of a baseline, which is generally flat showing the heat equilibrium between the sample and the reference. Whenever there is a thermal event like melting, crystallisation, phase transition or chemical reaction, there will be a drift from the baseline often forming a peak in the DSC curves as seen in Fig. 2.23.

To determine the transition temperature of a transition, the sample is allowed to go through a cycle of heating and cooling with different heating rates(β). Fig. 2.23b shows a schematic picture of a heating curve for different β values. An onset temperature is noted for both heating (T_o^h) and cooling (T_o^c) corresponding to the intersection point of tangents of the baseline and the rising edge of heating and cooling curve respectively. Several different conditions to determine this onset temperature has been shown in Fig. 2.23a. The mean of the two onset temperatures T_o^h and T_o^c is plotted as a function of the heating /cooling rate. The extrapolated mean temperature at 0 heating/cooling rate gives the transition temperature. Fig. 2.23c shows two different transitions where T_1 is the temperature without hysteresis and T_2 is the transition temperature of the transition with hysteresis. Sometimes, the peak temperature T_P is also denoted as the transition temperature depending on the specific property we are interested in.

The area under the heat flow versus temperature curves gives an estimation of the latent heat using the density of the sample as

$$latent\,heat = \frac{area}{heating\,rate} \times density \tag{2.16}$$

The area under the DSC curve is measured in WK/g, heating rate is in K/s and density in g/cm^3. The DSC curves of Ti_3O_5 pellets with an estimation of transition temperature and latent heat have been discussed in Chapter 3 (Section 3.1.4).

Chapter 3

Overview of investigated systems

Recent studies have highlighted the crucial role of elastic interactions in stabilizing and enhancing the photo-induced phase transition within spin crossover systems [12, 109, 108]. These molecular systems are characterized by a significant activation energy barrier governing their spin state switching. A distinctive aspect of these systems is the local volume expansion that occurs when the molecules undergo laser excitation. However, this local expansion is not always adequate to induce the desired spin state switching. As a result, threshold laser power becomes a critical parameter, distinguishing whether the local excitation can successfully establish long-range structural and electronic order in the system.

On the other hand, several ultra-fast optical experiments have been performed on correlated electron systems [66][112][76].Mott insulators in particular constitute another family of materials in which phase transitions are accompanied by significant volume change. In these complex systems, a marked departure from the high activation energy barriers is observed. The phase transitions are often facilitated by the propagation of strain waves throughout the material, providing a unique avenue for dynamic transformations.

In this manuscript, we have focused on the laser-induced structural changes in correlated electronic systems. Our broad aim was to observe photo-induced phase transition, propagated by strain waves in these types of materials, delineate those from the local structural changes, and establish connections between sample morphology and laser induced transitions. For the later purpose, we considered two suitable transition metal oxides with different morphology: polycrystalline powder of Trititanium Pentoxide (Ti_3O_5) and the granular thin film of Vanadium Trioxide (V_2O_3). Both the materials show significant volume changes across the transition. This work would not be possible without the fruitful collaboration with the material scientists Hiroko Tokoro from Japan, who thankfully provided us with the polycrystalline powder of Ti_3O_5 and Etienne Janod from IMN, Nantes for providing the V_2O_3 thin films.

In this chapter, we will look into the principles of preparation of these samples along with their atomic structures. The morphology of the samples have been studied by several complementary techniques mentioned in previous chapter. In the later part of this chapter, I have discussed the requirements of TR-XRD for each sample.

3.1 Trititanium pentoxide(Ti_3O_5) : Structure, morphology and characterisation

In recent years, bistable materials have attracted research interests in their application in designing advanced functional systems with varied applications in the fields of sensor, data-storage and information technology, energy harvestors, spintronics, actuators[92][18]. Bistable materials exist in two local minima of potential energy, in two equilibrium states without the application of external stimuli. A good candidate showing bistable metal-semiconductor phase transition is Ti_3O_5[63].

Several oxides of Ti have been studied from binary oxides to suboxides Ti_nO_{2n-1}[4][64]. Since several years, research have been conducted on the structure and properties of several phases of Ti_3O_5 namely, α, β, γ, δ and λ. These phases are closely related in structure and exhibit different properties based on the electric conductivity or magnetism. In this thesis, we will mostly focus on the phase transition between λ and β-phases. The transition between the two phases can be controlled by temperature, pressure, electric field and light irradiation[104].

3.1.1 Crystal Structure

At room temperature, bulk Ti_3O_5 is in a stable phase β with monoclinic symmetry and space group C2/m. This low temperature monoclinic (LM) phase has three different Ti sites based on their link with the neighbouring O - atoms[6] and Ti3- Ti3 pair up to form dimers, forming a charge localization. This makes the β-phase semiconducting with band gap of 0.3 eV[51] [69].

Ti_3O_5 undergoes first order phase transition from the semiconducting β-phase to metallic λ phase at 460 K on heating and 440 K on cooling. $\lambda-Ti_3O_5$ is a high temperature meta-stable phase (HM) with monoclinic symmetry and the same space group C2/m as LM phase[6][62]. This phase transition is isostructural i.e there is no symmetry change between the two phases. As can be seen in the Table 3.1 there is a significant change in volume 349.9 $Å^3$ to 371 $Å^3$ (+6.4%) during this transition. The breakdown of Ti3-Ti3 dimer in the β-phase (indicated in Fig. 3.1) cause the expansion of lattice mostly along the c-axis. The delocalisation of the charge makes the λ-phase to be metallic. The oxygen deficiency and the formation of the Ti-Ti dimers near the E_F makes λ-Ti_3O_5 promising in efficient solar to stem generation technologies[118] .

At much higher temperature (Tc = 500 K) a second order phase transition occurs to a high symmetry orthorhombic α-phase[6].

The phase transition between the β and λ phase involve the structural changes with anisotropic characteristics. In a time resolved pump-probe reflectivity study [84] conducted on a single crystal β-Ti_3O_5, it was observed that the phase transition occurs exclusively when the laser excitation is along the a-b plane. In case where the sample exhibits a macroscopic orientation along the c axis, the lattice changes does not occur, and the absence of the macroscopic deformations prevents the occurrence of the phase

Phase	Crystal system	Space group	a (Å)	b (Å)	c (Å)	beta (°)	V (Å^3)
β-Ti_3O_5	Monoclinic	C2/m	9.7568	3.8007	9.4389	91.547	349.9
λ-Ti_3O_5	Monoclinic	C2/m	9.8261	3.789	9.9694	91.258	371.12
α-Ti_3O_5	Orthorhombic	Cmcm	3.798	9.846	9.988	90	373.5

Table 3.1 – Lattice parameters of the different Ti_3O_5 phases[33][67]

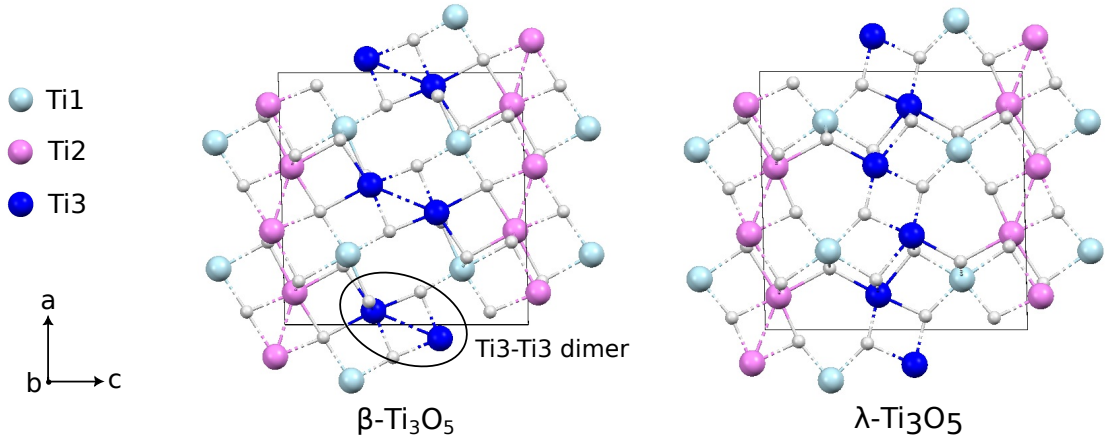

Figure 3.1 – Schematic crystal structures of the Ti_3O_5 showing the Ti3-Ti3 dimer in the β-phase and the absence of it in λ-phase

transition.

A striking feature of the metastable λ-phase is that it is stable at room temperature in the nanocrystals, making the system bi-stable over a wide temperature range. Ohkoshi et al. [63] synthesized nanocrystalline λ-phase in two different morphological forms (Ti_3O_5 nanocrystal in SiO_2 matrix and flake-type Ti_3O_5 nanocrystals) and were the first to obtain a reversible photo-induced phase transition between λ-phase and β-phase at room temperature. Upon laser excitation, there is a transition from the locally trapped λ-phase to the energy minimum state β(Fig. 3.2). The reversibility of this transition depends on the laser fluence. Besides λ-phase could also be achieved with continuous laser irradiation from β to α to λ-phase.

The meta-stable λ-phase can also be stabilised at room temperature by introducing impurity elements in the system. Studies shows that the β to λ transition temperature can be reduced significantly by doping with Mg[111] [33], Li [15] and Al[98]. In case of Al -doping in the single crystals of Ti_3O_5[98], i.e in $Ti_{3-x}Al_xO_5$, the transition temperature largely decreases and the hysteresis widens for increasing x and vanishes for x = 10%. For x = 0.9, the transition temperature is found at 373 K upon heating and 255 K upon cooling. Similarly for the Mg-doping[111], the transition temperature decrease to 335 K for 1%-Mg to the stabilisation of λ-phase at room temperature for 2% Mg. However, in

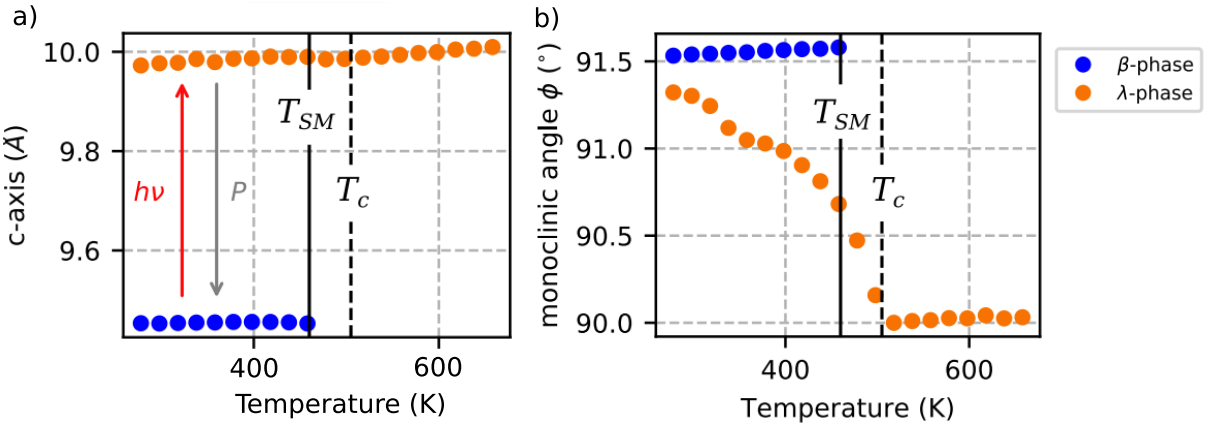

Figure 3.2 – a) Evolution of the lattice parameter $\vec{c}$ and b) Monoclinic angle of Ti_3O_5 plotted for the β and λ phases with temperature[adapted from [55]]. Below $T < T_{SM}$, there is coexistence of the β and λ phases. The angle in λ-phase decreases gradually till it reaches 90° in the α-phase at transition temperature (T_C)

this chapter, we will only focus on the nanocrystallites of pure Ti_3O_5.

3.1.2 Polycrystalline powder of Ti_3O_5

The nanocrystals of Ti_3O_5 can be obtained in different morphological forms namely, flake-type, stripe-type and block-type, by different synthesis methods as has been described in [63][62][104].

Flake-type Ti_3O_5: The flake form of Ti_3O_5 as shown in Fig. 3.3a is obtained by calcinating the anatase form of TiO_2 nanoparticles of 7 nm under hydrogen flow at 1473 K[63]. Initial percentage of λ-phase is 87% as refined from powder X-ray diffraction patterns. The crystallite size was estimated to be 100 ± 40 nm by performing static powder X-ray diffraction in transmission geometry[55]. The pressure at which 25 % λ-phase converts to β-phase is 300 GPa.

Stripe-type Ti_3O_5: Sintering rutile TiO_2 particles in a hydrogen atmosphere at 1390 K followed by a cooling process of approximately 9 hours to room temperature gives a new type of rectangular shaped nanorods of Ti_3O_5[104]. TEM image(Fig. 3.3b(top)) of the obtained sample shows the nanorods are mostly with dimensions 200 nm × 30 nm with the growth direction along $\vec{b}$ lattice axis. The size of these stripe type polycrystalline powder is larger than the flake type Ti_3O_5 prepared from the anastase form of TiO_2.

Block-type Ti_3O_5: Sintering the same polymorph of TiO_2 particles in a hydrogen atmosphere at 1573 K for 2 hours gives another type of λ-Ti_3O_5 with sub-micrometer dimensions.[62]. The morphology of the nanocrystals studied using TEM shows they are

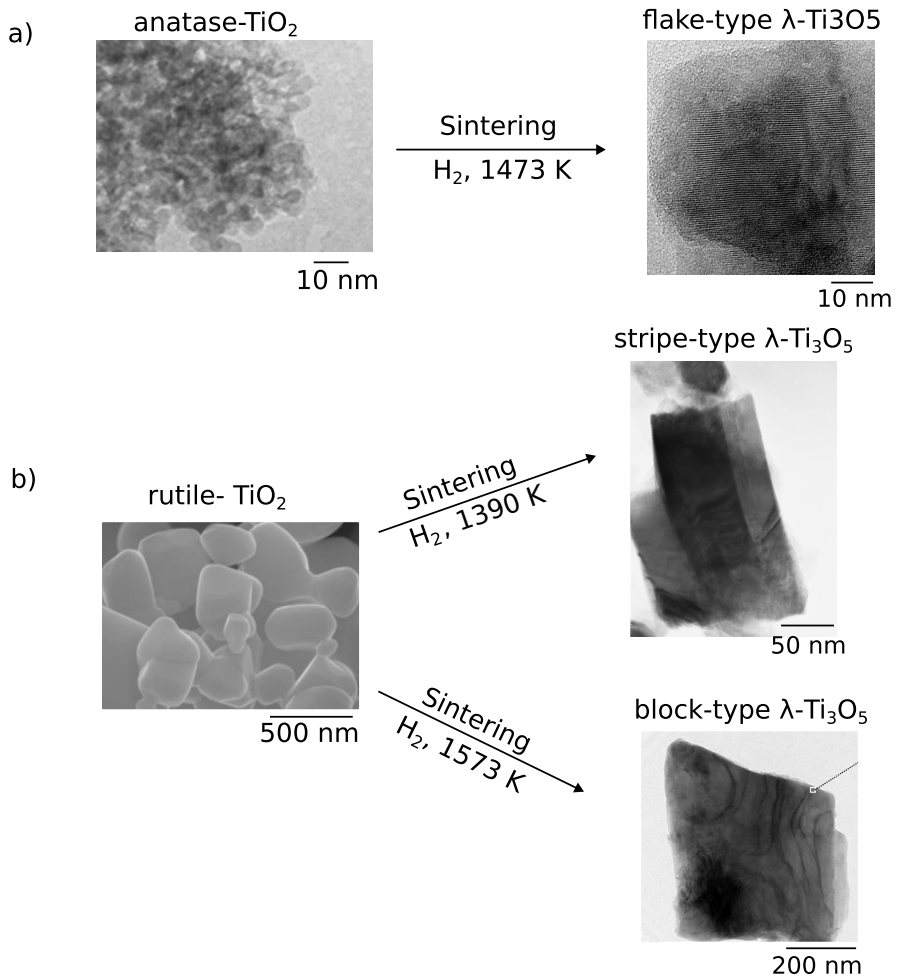

Figure 3.3 – Synthesis routes of Ti_3O_5 showing the three forms flake-type, stripe-type and block-type nanocrystalline powders extracted from different forms of TiO_2. The TEM images show the shape and form of each type.

sub micrometer size, hence named 'block'-type λ-Ti_3O_5 (bottom image of Fig. 3.3 b). The transition pressure (pressure at which the phase fraction of each phase is 50% of the sample) is 7 MPa. The block-type Ti_3O_5 stores a large amount of latent heat 237 kJL^{-1}. With the application of pressure of less than 10 MPa, the thermal hysteresis reduces, transforming λ to β phase and releasing the latent heat.

The polycrystalline powder obtained from the aforementioned processes was grinded to make a finer powder and then compacted into a pellet using a pellet die(Fig. 3.4). Compression is applied on the pellet die in an uniaxial direction of about 50 MPa using a manual hydraulic press. The pellets are of 8 mm in diameter and few mm in width. These pellets were put in a solution of equal parts (1ml each) of water, ethanol and TEOS with 1-2 drops of 37 % HCl and then left to dry for more than 24 hours. The pellets contain a mixture of pressure-induced β- phase and λ- crystallites which depends on the form and

effective pressure applied for pelleting.

Figure 3.4 – a) Polycrystalline powder in the mortar to grind into fine powder b) Parts of the pellet die in which a small amount of powder is added and then pressed under the hydraulic press to form the pellets c) The resulting pellet of Ti_3O_5 under microscope.

In order to understand the area probed by the laser and X-ray in time resolved diffraction experiments, Atomic Force Microscopy (AFM) was performed on the three different pellets flake-type, stripe-type and block-type.

3.1.3 Surface characterisation of the pellets using AFM

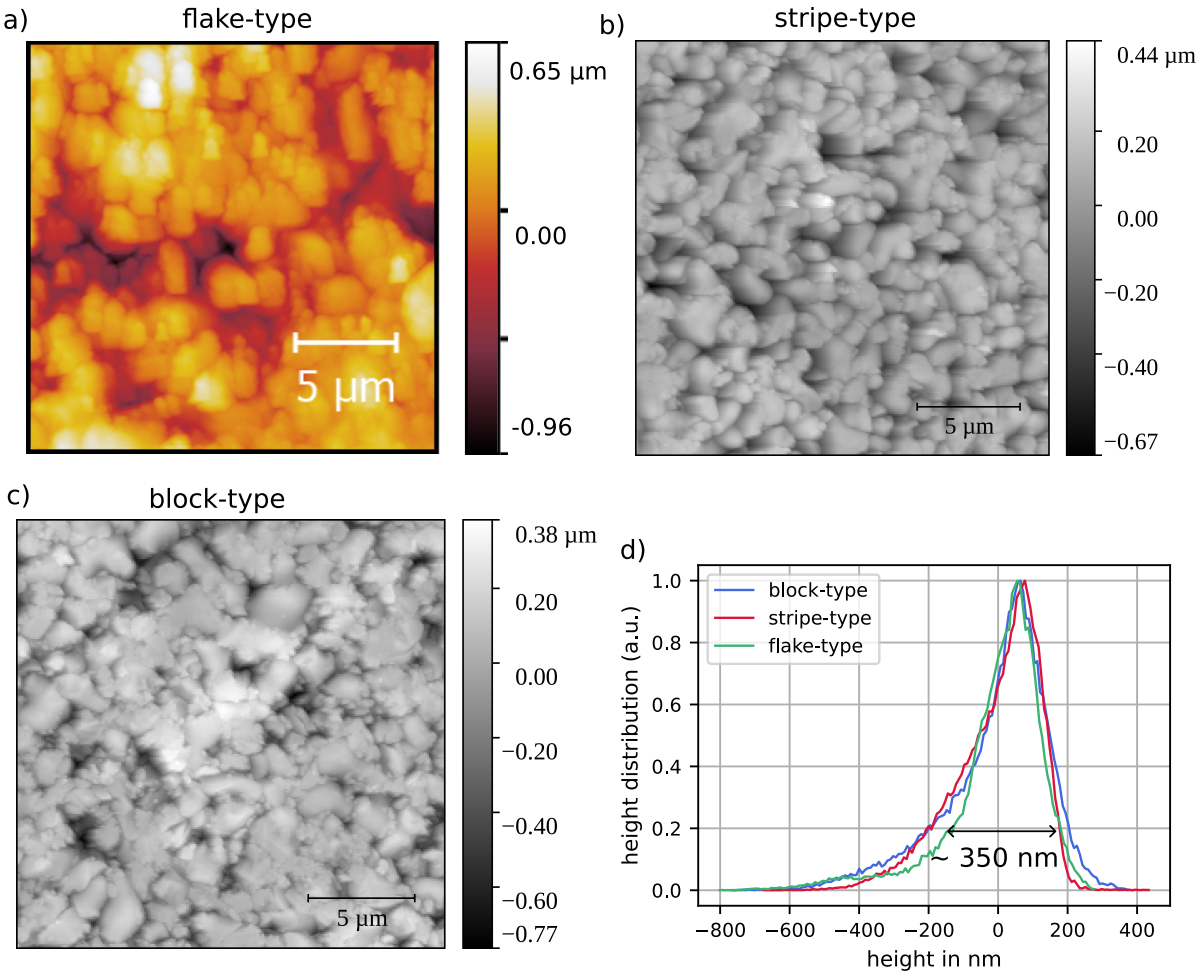

Figure 3.5 – AFM images on the a) flake-type, b) stripe-type and c) block-type Ti_3O_5 pellets. d) Height distribution of the three pellets. The standard deviation of $\sim$ 350 nm of the height distribution indicates similar roughness of the three types of pellets.

The pellets roughness was characterized using Atomic Force Microscopy(AFM). The measurement details have been discussed in previous Chapter. The height distribution image obtained by AFM is first checked for any regions that are duplicated or irregular shaped and these areas are masked to eradicate any effects from instability in tip-sample interaction, surface contamination or any damage in the tips. Then the image is corrected for any tilt by subtracting an average plane and the average height is fixed to zero. The corrected height distribution is plotted over such surface(Fig. 3.5a, b and c) and the standard deviation for such distribution is measured to estimate the roughness of the polycrystalline pellets.

The height distribution for all the three pellets is shown in Fig. 3.5d). Across all pellets, a surface roughness of 350 nm ± 50 nm is measured with no significant variation from sample to sample.

3.1.4 Estimation of transition temperature in pellets using DSC

The β to λ transition temperature T_{SM}^{up} have also been estimated for a single crystal and also the three types of Ti_3O_5 pellets with DSC measurements. This technique has been discussed as the complementary method in previous chapter.

The heat flow in the single crystal of Ti_3O_5 has been plotted in Fig. 3.6 as a function of temperature with a linear heating rate of 5 K/min. From the intercepting tangents of the rising edge of the DSC curves, the onset temperatures for transition have been found to be $T_o^h = 459$ K(during heating) and $T_o^c = 442$ K (during cooling). The transition Temperature T_{SM} for the single crystal can be calculated as the mean of the onset temperatures, making $T_{SM} = 450.5$ K. This heating and cooling cycle is performed with a heating speed (β) of 5 K/min.

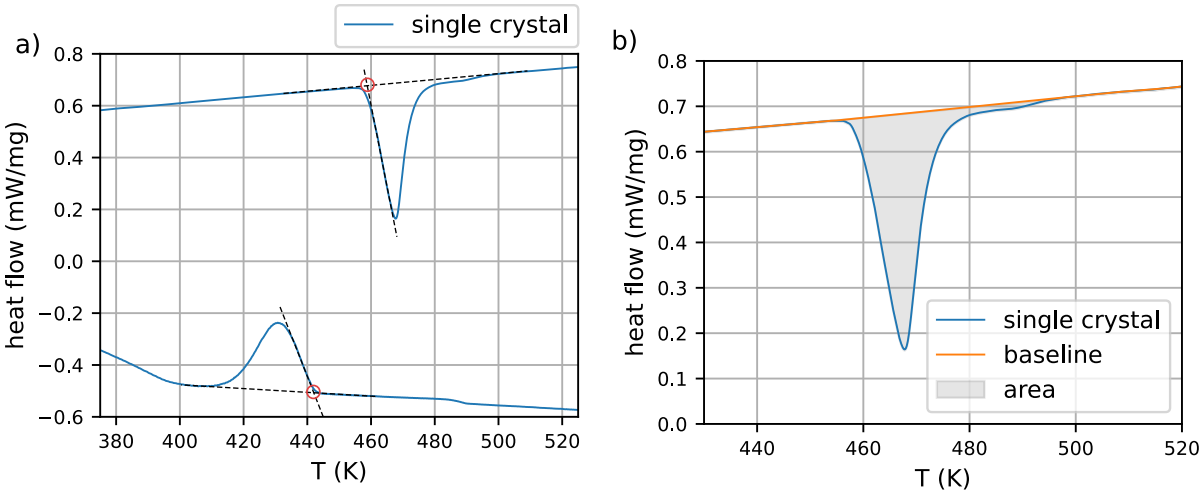

Figure 3.6 – DSC curve on a single crystal of Ti_3O_5 plotted as a function of temperature. The black dashed lines indicate the tangents drawn on the rising edge of the DSC curves and the red circles indicate the intercept of the tangents. The intercept temperatures gives an estimate of the transition temperature.

The area under the DSC curve helps to estimate the latent heat of transition , The area under the curves from Fig. 3.6b is 4.69 WK/g. Therefore the latent heat of the single crystal as calculated from Eqn. 2.16 using the density of 4.19 g/cm^3 for Ti_3O_5 is approximately 235 kJ/l which is in agreement with previous study[104].

However, there is a limitation regarding the DSC technique for the non reversible phase transitions as seen for the polycrystalline Ti_3O_5 pellets as seen in Fig. 3.7. In this figure,

a peak can be observed on the heating cycle with the onset temperatures of 460 K, 468 K and 470 K respectively for the flake-type, stripe-type and block-type λ-Ti_3O_5 pellets. Whereas, on the cooling cycle, no peak is observed, which indicates that the amount of β-phase that transforms to the λ phase does not revert back to the β phase. Hence, the onset temperature during the cooling cycle is not observed, making the calculation of T_{SM} non conclusive. Nevertheless, it is observed that the onset temperatures are quite similar in the three types of pellets, indicating that the T_{SM} would also be quite similar for them. The latent heat calculated for the pellets is similar for the three types and is about 100 J/l. The DSC is a standard method to follow phase transitions in solid/solid phase transition, but it is not a sufficient method for irreversible phase transitions.

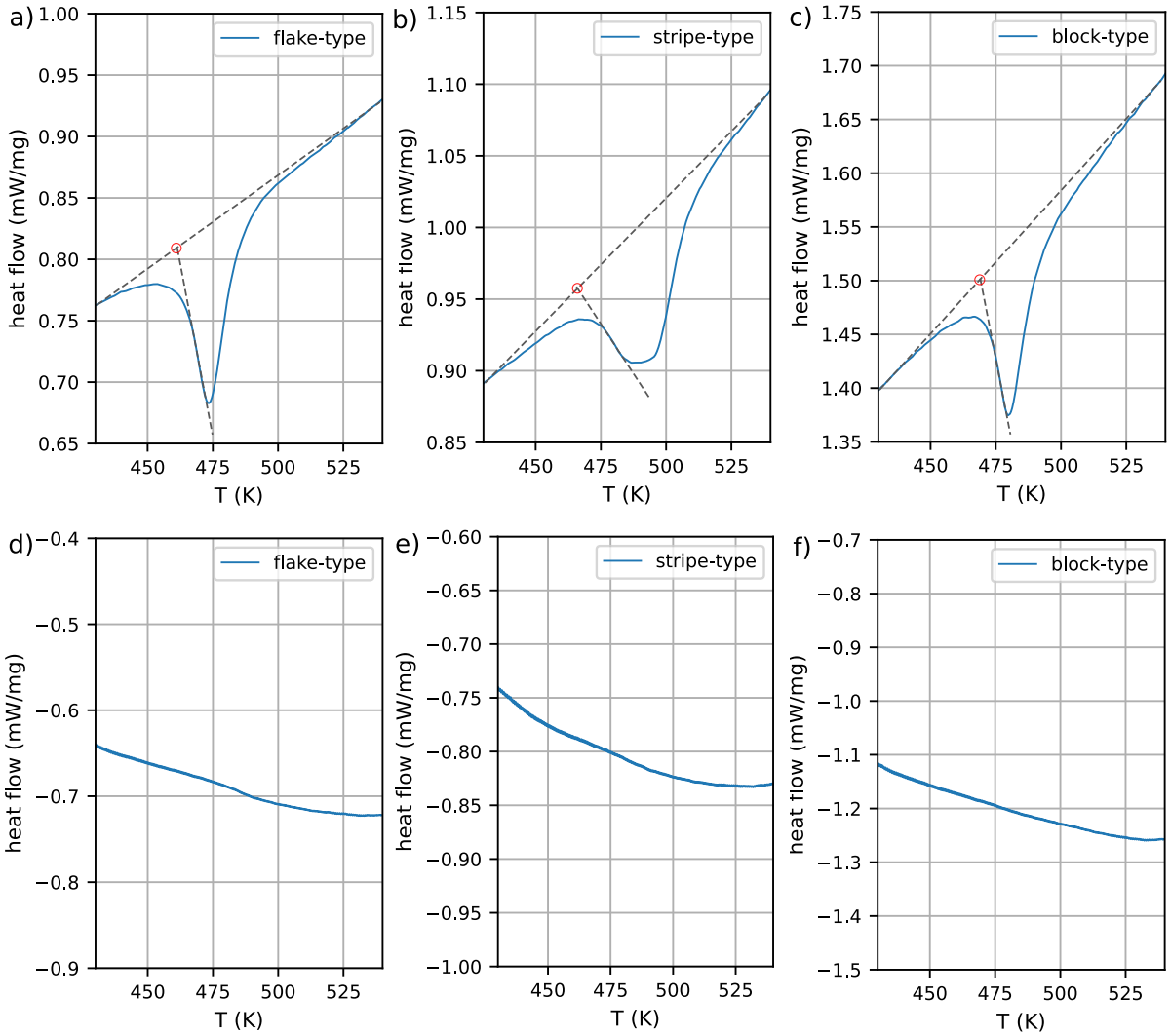

Figure 3.7 – a) to c) The heat flow curve for flake-type, stripe-type and block-type pellets during heating and d) to f) are the curves during cooling respectively. The black dashed line are the tangents of the rising edge of the heating curve and the red circles indicate the intersecting points of tangents. There are no DSC peaks upon cooling because of irreversible transition from β to λ-phase.

3.1.5 Experimental conditions for TR-XRD

The penetration depth of laser in the Ti_3O_5 pellets at the different wavelengths are calculated from the imaginary part of the refractive index of the beta phase for two different polarisation along the lattice parameters $\vec{a}$ and $\vec{c}$(Fig. 3.8a). In the TR-XRD experiments during the thesis, we have used three different wavelengths of 400 nm(energy = 3 eV), 800 nm (energy = 1.55 eV) and 1550 nm(energy = 0.8 eV), the penetration depths of which are indicated in the subfigure a. Similarly the penetration depth of the X-ray in Ti_3O_5 has been calculated for different incidence angle and at three different energies(Fig. 3.8b).

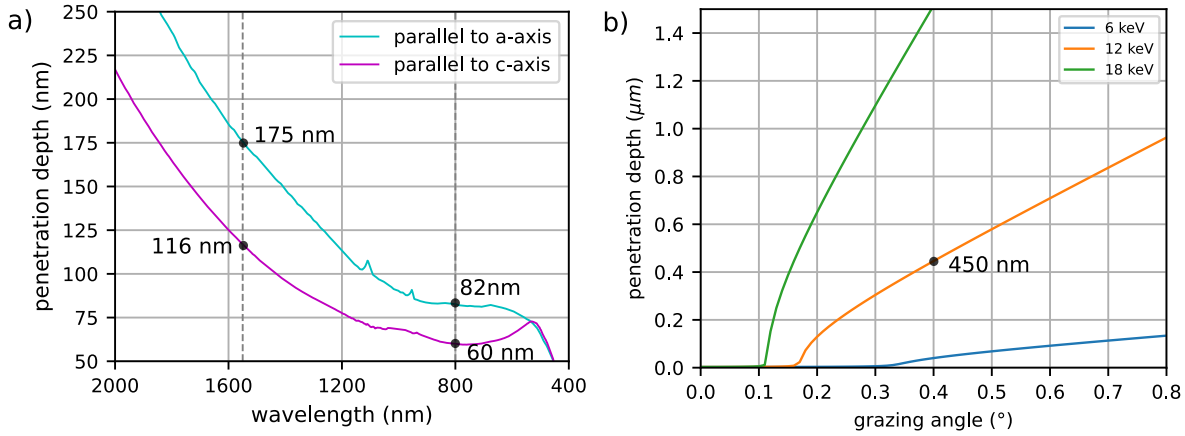

Figure 3.8 – a) The penetration depth of the laser as a function of wavelength calculated from the imaginary component of the refractive index for the β-phase of the single crystal. b) Variation of the penetration depth of the X-rays with the incidence angle as calculated from *https* : *//henke.lbl.gov/optical_constants/atten2.html* for different X-ray energies.

For the time resolved XRD experiments, it is important for the X-ray penetration depth to match the laser penetration depth in order to track the photo-induced structural changes. The laser penetration depth at an wavelength of 800 nm(energy = 1.55 eV) is about 70 nm and that at 1550 nm(energy = 0.8 eV) is $\sim$ 150 nm. All the pellets have a surface roughness of about 350 nm as seen in AFM results. So a low effective penetration depth of the X-ray can be achieved by either decreasing the X-ray energy or decreasing the incidence angle or both(as seen in Fig. 3.8).

Decreasing the X-ray energy can be a problem in synchrotron X-ray sources because we might lose flux(based on the beamline transmission characteristics). On the other hand, lowering the incidence angle of the X-rays is not ideal. First of all, small incidence angle of the X-ray causes total internal reflection. For instance, the values less than 0.32°, 0.16° and 0.12° for the energies 6 keV, 12 keV and 18 keV respectively. Small angles above total internal reflection can be used but this results in a huge footprint on the sample. This in turn, cause broadening of the Bragg peaks(discussed in detail in Section 2.5.2 in

Chapter 2).

For the TR-XRD experiments on the Ti_3O_5 pellets, the results of which are discussed in Chapter 4, a suitable X-ray energy of 12 keV (λ=1.0332 Å) was used with the incidence angle of 0.4°. The effective probed regime at this condition is 800 nm (considering the X-ray penetration depth of 450 nm plus the roughness of pellet surface of $\sim$ 350 nm). Therefore the ratio of excited to non-excited regime is $1/10th$ in case of 800 nm and $1/5th$ in case of 1550 nm laser wavelengths.

X-ray diffraction experiment was performed at ESRF, ID09 beamline during hybrid mode (7/8th continuous filling+1 isolated electron bunch). The X-ray beam size at sample position was 23 (horizontal) x 14 (vertical) µm^2 leading to a footprint of 23 µm x 1.9 mm at 0.4 ° incidence angle. The broadening of the X-rays due to footprint is $\sim$ 1.3% which is less compared to the broadening due to energy 1.7 %.

The pellets are photo-irradiated with a laser pulse of 1-2 ps pulse duration. Laser excitation with quasi-normal incidence lead to measured beam size on sample of 0.13 x 4.2 mm^2. Laser fluences of 0.5 mJ/mm^2 and 0.25 mJ/mm^2 were used.

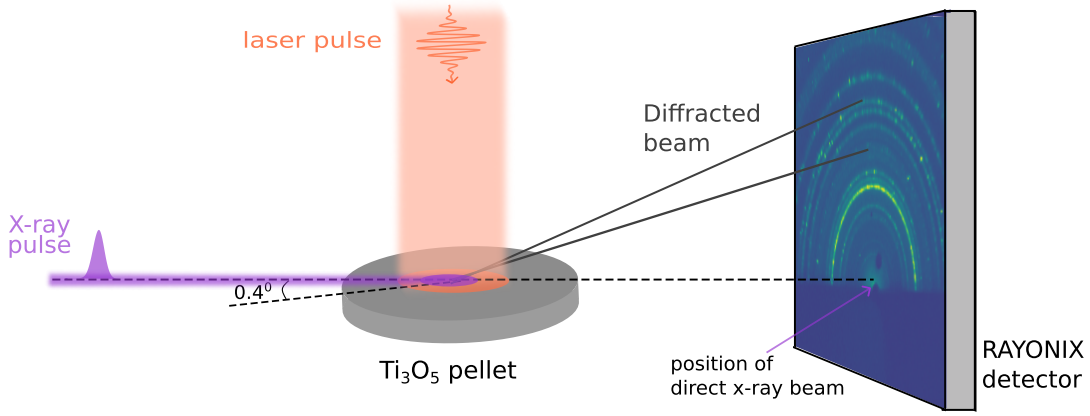

Figure 3.9 – Schematic picture of the experimental geometry at the ID09 beamline, ESRF

Measurements are taken in stroboscopic mode and each image was recorded with 400 shots exposure (i.e, 10 s exposure at 40 Hz). XRD images are measured at different time delays before ("negative" delays) and after ("positive" delays) photo-excitation. The delays sequence is repeated several time to correct for drifts effects and increase the measurement statistics. Reference patterns with no laser excitation are interleaved in the sequence to track X-ray beam/ sample drifts and permanent or long live-time effects.

The typical diffraction images from the different polycrystalline pellets of the flake-type, stripe-type and block-type Ti_3O_5 pellets as collected by the Rayonix detector in the reflection geometry are shown in Fig. 3.10. We can see the shadow from the pellet below 2600 pixels in y. The diffraction peaks are in the form of concentric half-circles with some bright spots on the rings. The bright spots are from the aggregates in the randomly distributed polycrystalline powder. The spotty diffraction is more in the flake-

type compared to the other two types. The intensity of the peaks is more or less similar in all types of pellets.

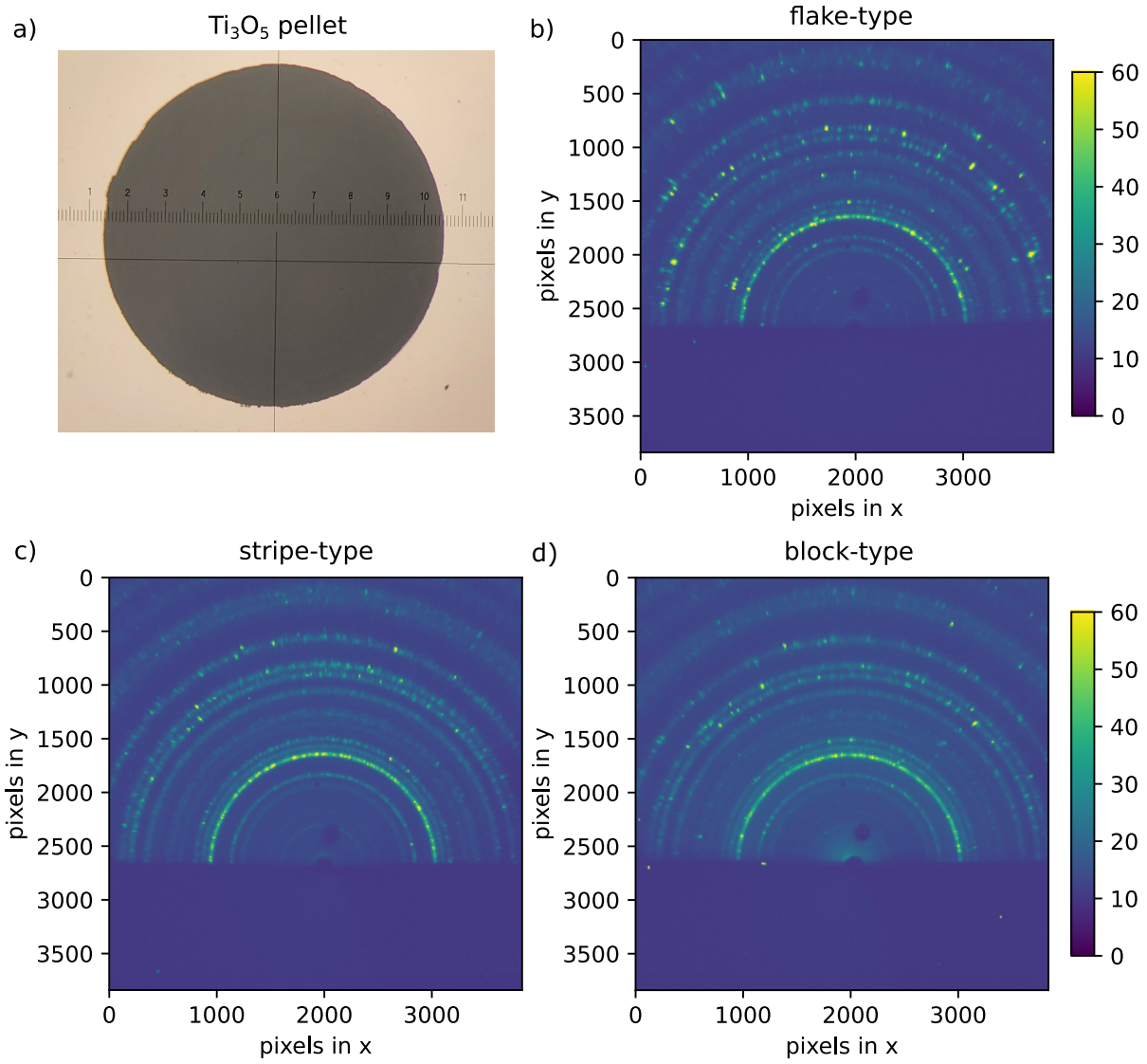

Figure 3.10 – a) Image of the Ti_3O_5 pellet under optical microscope (10 graduations is equivalent to 0.88 mm). b) to d) Diffraction images collected on the Rayonix detector for a) flake-type, b) stripe-type and c) block-type Ti_3O_5 pellet.

Several diffraction rings between q = 1 $Å^{-1}$ to q = 4.5 $Å^{-1}$ are clearly visible with some bigger spots indicating the diffraction from aggregates of crystallites. These spots can be separated from the diffraction rings using the pyFAI library tools and this process does not affect the overall dynamics.

To track the transient changes during the phase transition of semiconducting β to metallic λ phase upon photo-excitation, it is important to understand the structures under equilibrium and the patterns they produce with X-ray diffraction. The diffraction patterns are simulated for the β and λ phase with the same experimental geometry as described in Chapter 3.

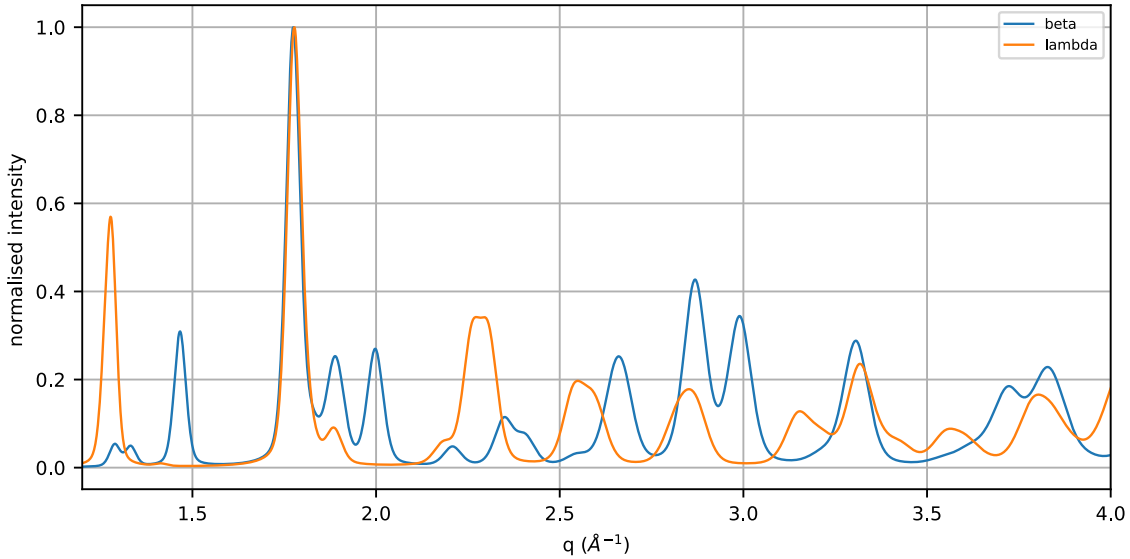

Figure 3.11 – The diffraction patterns simulated from the theoretical cell parameters with incident angle of 0.4 degree and the incident beam height of 25 µm. This is to compare the patterns with the experimental conditions.

Though the symmetry is same for the two phases, but the different lattice parameters result in distinct XRD patterns in the reciprocal space.

The resolution in q for the Bragg peaks are mostly limited by the X-ray energy width of the pink beam and the large footprint on the sample at the grazing incidence of the X-ray. The broadening of Bragg peaks due to crystallite size is small in comparison and the value decreases for the bigger crystallites. So it is not possible to distinguish the type of pellet from the width of the Bragg peaks. The broadening due to different factors have been discussed in detail in Chapter 2.

3.2 Vanadium Trioxide (V_2O_3): Structure, Morphology and Characterisation

Vanadium trioxide (V_2O_3) is a proto-type system for insulator-to-metal phase transition induced by temperature, doping or pressure[56][122]. This system either pure V_2O_3 or substituted by Chromium have been studied intensively over several decades[36][90].

3.2.1 Crystal structure

The schematic phase diagram of V_2O_3 as a function of doping and temperature has been reproduced in Fig. 3.12 [57]. At equilibrium, there are three different known phases: Paramagnetic Metal(PM), Paramagnetic Insulator(PI) and Anti-ferromagnetic Insulator(AFI). At ambient pressure and temperature, the pure V_2O_3 is a paramagnetic metal with a trigonal α-corundum structure. The conventional unit-cell is hexagonal with the cell parameters as in Table 3.2 (with 2 formula units) whereas the primitive cell is rhombohedral (with 2 formula units).

The lattice parameters of PI, PM and AFI phases have been shown in Tab. 3.2 at different temperatures[82][20]. The cell parameters are described in hexagonal unit cell.

Sample	T (K)	Phase	Space group	a (Å)	b (Å)	c (Å)	β (°)	γ (°)	V (Å^3)
V_2O_3	300	PM	$R\bar{3}cH$	4.954	4.954	14.01	90	120	297.76
V_2O_3	15	AFI	$I2/m$	7.266	5.002	5.547	96.76	90	200.25
$(Cr_{0.05}V_{0.95})_2O_3$	300	PI	$R\bar{3}cH$	4.99	4.99	13.919	90	120	301.22

Table 3.2 – Lattice parameters of the different V_2O_3 phases[82][20]

V_2O_3 undergoes a first-order insulator(PI) to metal(PM) transition with increasing pressure. This transition is isostructural, i.e. both the phases have the same space group $R\bar{3}c$ and is accompanied by a volume change. From the Table 3.2, the volume change between the PI-PM phase at room temperature can be calculated to be 1.16%.

Positive or negative pressure in V_2O_3 can be induced by chemical substitution as shown in the phase diagram in Fig. 3.12. The negative (positive) chemical pressure can be created by substituting Vanadium with some smaller(larger) size molecules as Chromium(Titanium).

At low temperature, V_2O_3 undergoes a phase transition from the PM phase to AFI phase. This phase transition is first order and is associated with a monoclinic structural distortion. This is associated with the disappearance of 3-fold symmetry along $\vec{c}$ axis of the hexagonal phase[95](Fig. 3.13) and the creation of 3 equivalent monoclinic domains. The transition temperature was reported at 150-160 K in single crystals[56] and can be lower and broader in polycrystalline thin films due to inhomogeneous strain distribution.

The three equivalent monoclinic unit cells can be derived from hexagonal unit cell[24].

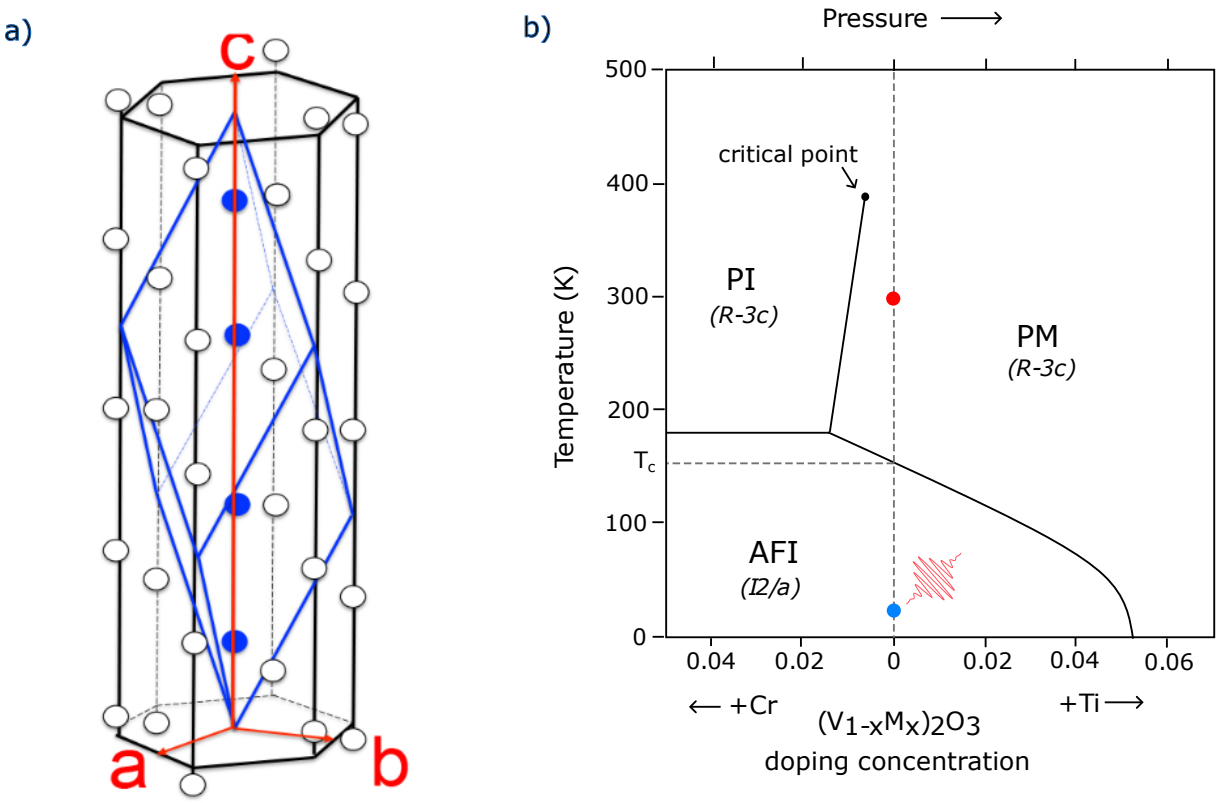

Figure 3.12 – a) V_2O_3 crystal structure showing the hexagonal unit cell (black lines) and the primitive rhombohedral cell (blue lines), with four vanadium atoms (blue circles) in the center b) Phase diagram for the V_2O_3 as a function of temperature, pressure and doping concentration(Cr or Ti). The zero pressure moves with the 0 from the doping concentration scale and the arrow indicates increasing pressure. Each division in pressure is 8 kbar. Cr-doping has the same effect as the negative pressure and Ti-doping as positive pressure. Above Tc = 400 K(shown as the critical point), the system reaches a crossover region between the insulator and metal. The red dot indicates the pure V_2O_3 at ambient temperature and pressure. The blue dot indicates V_2O_3 at 15 K (AFI phase) which is the starting point for our tr-XRD measurement (adapted from [57]).

$$\begin{pmatrix} a_M \\ b_M \\ c_M \end{pmatrix} = M \begin{pmatrix} a_H \\ b_H \\ c_H \end{pmatrix} \tag{3.1}$$

with

$$M = \begin{pmatrix} \frac{2}{3} & \frac{4}{3} & \frac{1}{3} \\ 1 & 0 & 0 \\ \frac{1}{3} & \frac{2}{3} & -\frac{1}{3} \end{pmatrix} ; \begin{pmatrix} -\frac{4}{3} & -\frac{2}{3} & \frac{1}{3} \\ 0 & 1 & 0 \\ -\frac{2}{3} & -\frac{1}{3} & -\frac{1}{3} \end{pmatrix} ; \begin{pmatrix} \frac{2}{3} & -\frac{2}{3} & \frac{1}{3} \\ -1 & -1 & 0 \\ \frac{1}{3} & -\frac{1}{3} & -\frac{1}{3} \end{pmatrix} \tag{3.2}$$

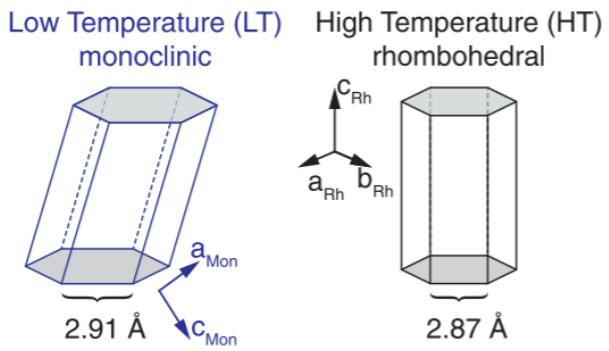

Figure 3.13 – Schematic representation of the ferroelastic distortion at the Low temperature monoclinic phase around the $\vec{c}$ axis of the hexagonal phase(adapted from [95])

So in the rest of the chapter, all the peaks in the diffraction pattern are indicated with the corresponding hexagonal (hkl) peaks as in Fig. 3.14. The diffraction patterns at different temperatures have been simulated using a FWHM of 0.1 °(Fig. 3.14).

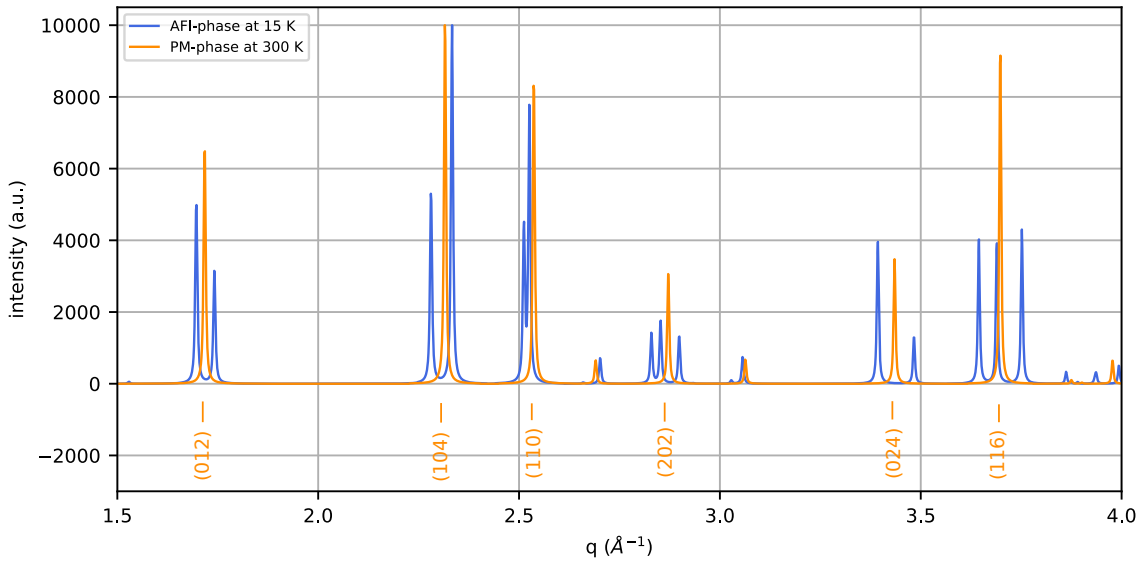

Figure 3.14 – The simulated diffraction patterns using Mercury[53] with the fixed FWHM of the peaks 0.1 °.

One feature from the simulated curves is that group of peaks in the AFI phase merge together in the PM phase, For instance two monoclinic peaks around q = 1.7, 2.3, 2.5 and 3.4 $Å^{-1}$ merge into single peaks of (104), (012) (110) and (024) respectively. Similarly three peaks around q = 2.7 and 3.7 $Å^{-1}$ merge into the peak (202) and (116) in the PM phase. This is because of the symmetry change in the two peaks. In addition to it, there

is an overall shift of the peaks towards higher q values in the PM phase. This is because of the volume contraction upon the AFI to PM transition.

The two phases have different structural parameters and different unit cell volume, which distinguish them in the reciprocal space. These distinguishing features in the X-ray diffraction patterns make TR-XRD a suitable tool to track the structural changes upon photo-excitation in real time.

3.2.2 Thin films of V_2O_3

Polycrystalline thin film of V_2O_3 were provided by our collaborators at the IMN in Nantes, Etienne Janod, Laurent Cario and Benoit Corraze. Most of the samples studied during my PhD were synthesized by Julio Guzman, PhD student in the same team. The films were deposited with reactive magnetron co-sputtering of metallic Vanadium inside a commercial AC450 sputtering chamber. A detailed synthesis procedure has been discussed in [75, 74].

The sample morphologies were characterised using Scanning Electron Microscopy(SEM). The SEM images are made on the surface as well as a cross section of the V_2O_3 thin films. It gives an estimate of the thickness and individual grain size of the nanocrystals.

The SEM image of the cross section of one film shows a thickness of 270 nm and a grain size of roughly 35 nm on the the surface of the film. The layer of V_2O_3 has been deposited on Sapphire substrate.

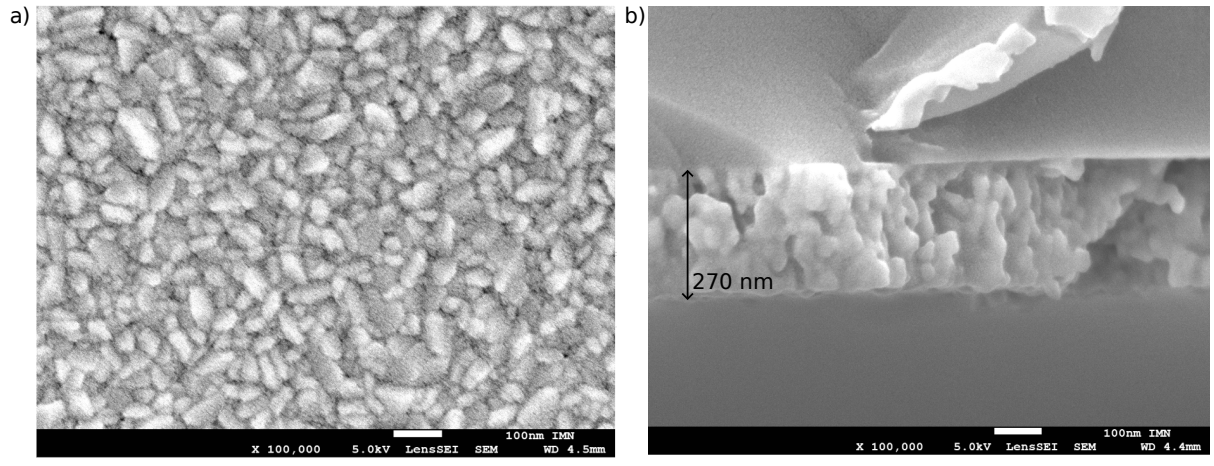

Figure 3.15 – a) SEM image of the thin film surface showing the grain size distribution of about 35 nm b) SEM image of the cross section of the film showing the layer thickness

Another thin film is considered with a thickness 100 nm deposited on Sapphire substrate. The SEM image(Fig. 3.16) of the surface of the film shows a similar grain size of 35 nm as the previous film.

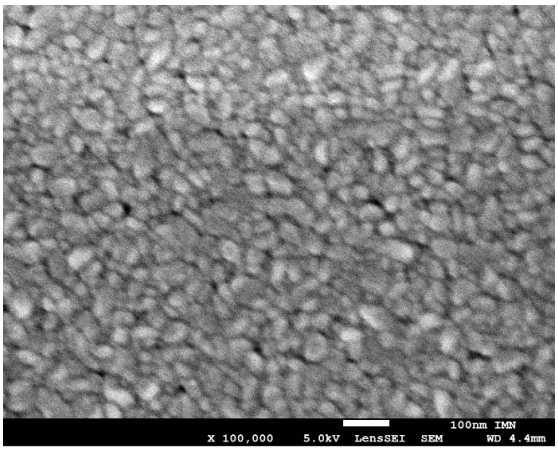

Figure 3.16 – SEM image of the thin film surface indicating the similar distribution of grain size as the previous film

3.2.3 Experimental conditions for TR-XRD

The laser penetration depth of V_2O_3 at 0.9 eV (wavelength $\sim$ 1370 nm) is 500 nm. This penetration depth is larger than the thickness of the thin films used for the measurements. So, in this case, it is not necessary to match the laser irradiated depth to the X-rays. Besides the substrate is a single crystal of sapphire, so it is easy to recognise the Bragg peaks from the substrate compared to the diffraction rings from V_2O_3 sample.

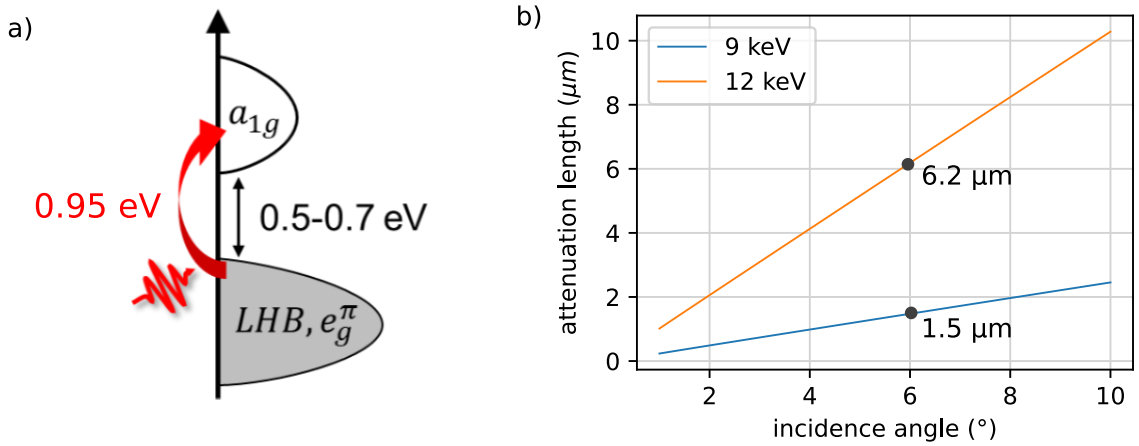

Figure 3.17 – a) Schematic picture of the DOS in V_2O_3 in the AFI phase. Pump laser is 0.95 eV close to the bang gap of 0.5-0.7 eV [adapted from [3]] b) Variation of the penetration depth of the X-rays with the incidence angle calculated for different X-ray energies.

Experimental condition at FemtoMAX beamline

The ultra-fast sub-picosecond time resolved XRD measurements were carried out at the FemtoMAX beamline, at MAXIV Laboratory in Sweden. The experimental geometry is shown schematically in Fig 3.18.

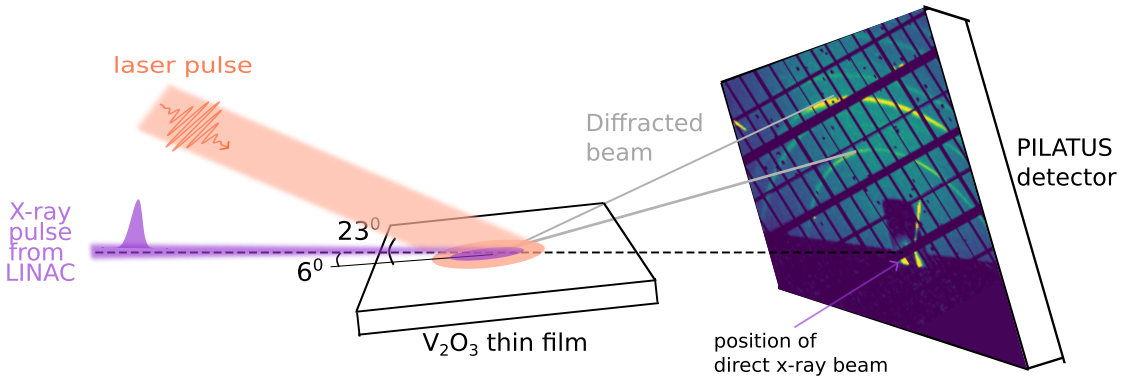

Figure 3.18 – Schematic of the experimental geometry at the FemtoMAX beamline

The thin films were irradiated with a laser pulse of wavelength 1300 nm (energy = 0.95 eV) close to the band gap energy of 0.5-0.7 eV[102]. The laser beam was incident on the films at an angle of 23 ° relative to the sample surface. Such an incidence angle helps to improve the time resolution upto 0.5 ps as seen in Section 2.4.2. The footprint(FWHM) of laser beam on the film was 300 µm (lateral, perpendicular to X-ray direction) and 2.8 mm (longitudinal, parallel to the X-ray direction).

The structural changes upon excitation were probed at different delays using 100 fs long X-rays of energy 9 keV. The $\Delta E/E$ of the X-rays was limited to ∼1.5 % using the multilayer monochromator. The X-rays were incident in the sample at a small angle of 6° with a footprint on the sample of 60 × 570 µm^2. For this, the broadening due to footprint was 0.2% which is much less than the broadening due to energy. A smaller incidence angle might increase the intensity of the Bragg peaks because X-rays will probe more material on surface since the depth is always limited by the thickness of thin film. However an angle $< 6°$ was not used to keep the q -resolution limited by the $\Delta E/E$ only(The quality of diffraction patterns is in Fig. 3.3).

The sample in this case V_2O_3 thin films were placed in the GIXS end-station operated at a high vacuum of $< 10^{-7}$ mbar suitable for such low temperature measurements. The diffracted signal was collected by the Pilatus detector(Fig. 3.19) fixed on the end-station. So, by construction, the sample to detector distance was fixed at 120 mm and detector was also aligned at an angle of 30° from the normal towards the sample.

The diffraction images show the Bragg peaks from V_2O_3 with a preferential orientation. For example, the intensity of the peak (110) is maximum normal to the surface of the

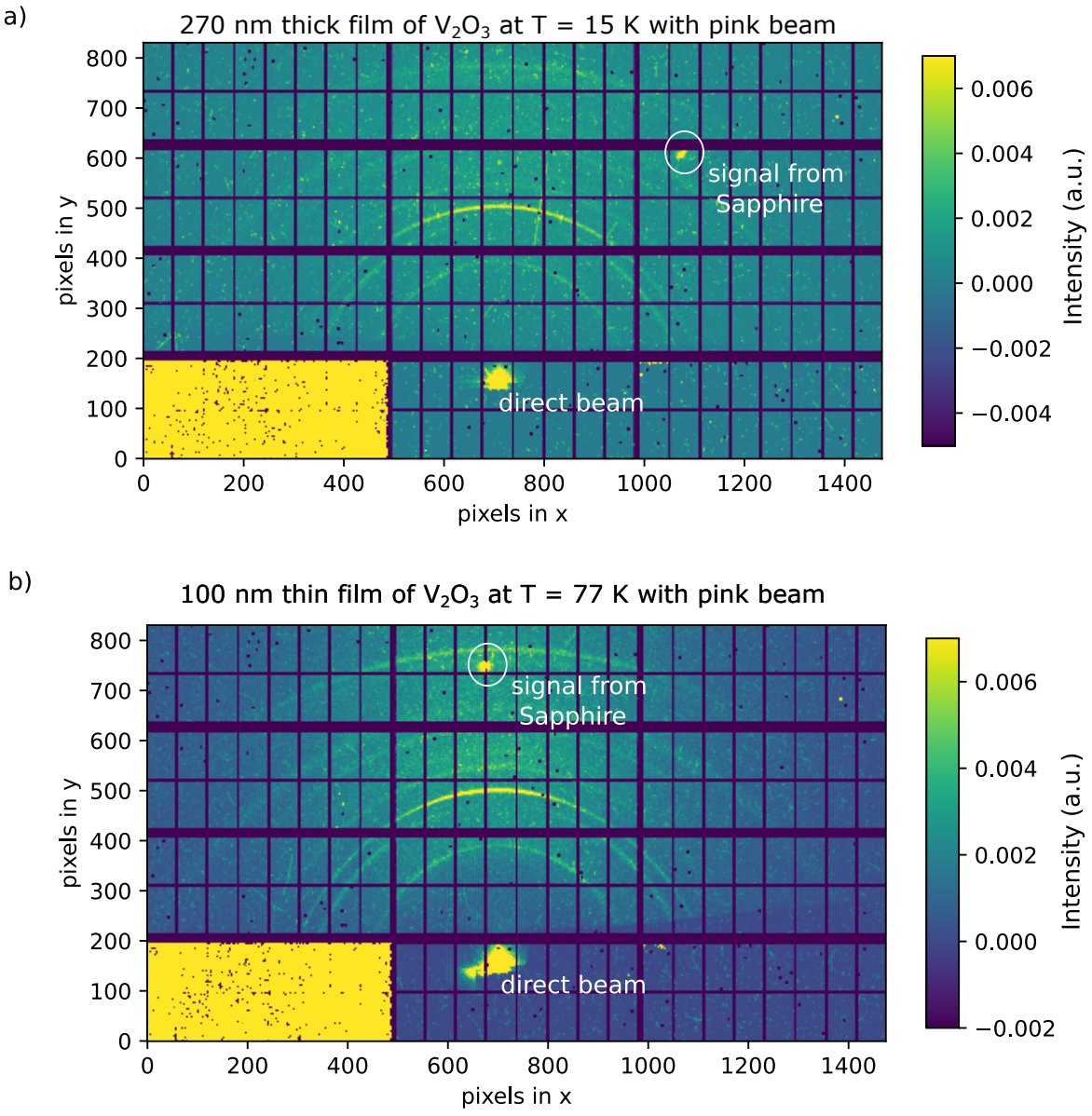

Figure 3.19 – Diffraction image of a) 270 nm thick film and b) 100 nm thin film of V_2O_3 measured with the Pilatus detector at the FemtoMAX beamline. The detector is made up of 16 models and each of them divided into sub-modules. All the bad pixels have been masked before further analysis as been described in the Chapter 2.

sample, whereas intensities of peaks (012) and (116) are mostly on the sides close to the surface with zero intensity along the normal. This is because majority of the crystallites are oriented with the $\vec{a}$ axis predominantly aligned normal to the sample surface as seen in Fig. 3.23. The Bragg rings are semi-elliptical in shape because the detector is aligned at about 60° from the direction of direct X-ray beam as shown in the schematic Fig. 3.18.

We measured the structural changes with the variation of delays between the laser excitation and X-ray probe pulses and at different laser fluence. The delays between the pump pulse and the probe pulse is measured for each image using a monitor developed at the FemtoMAX beamline. The delay uncertainty was taken as half a picosecond for small delays of 10s of picoseconds and 1 ps for the long delays of 100s of picoseconds. The images which have delays lying outside this uncertainty values were rejected while averaging the images during data analysis.

In the experiments, because of the uncertainty in the energy, the q resolution is not good enough to distinguish between the couple or triple peaks in the AFI phase, but it is enough to follow the narrowing of the peaks during the phase transition. (Fig. 3.20)

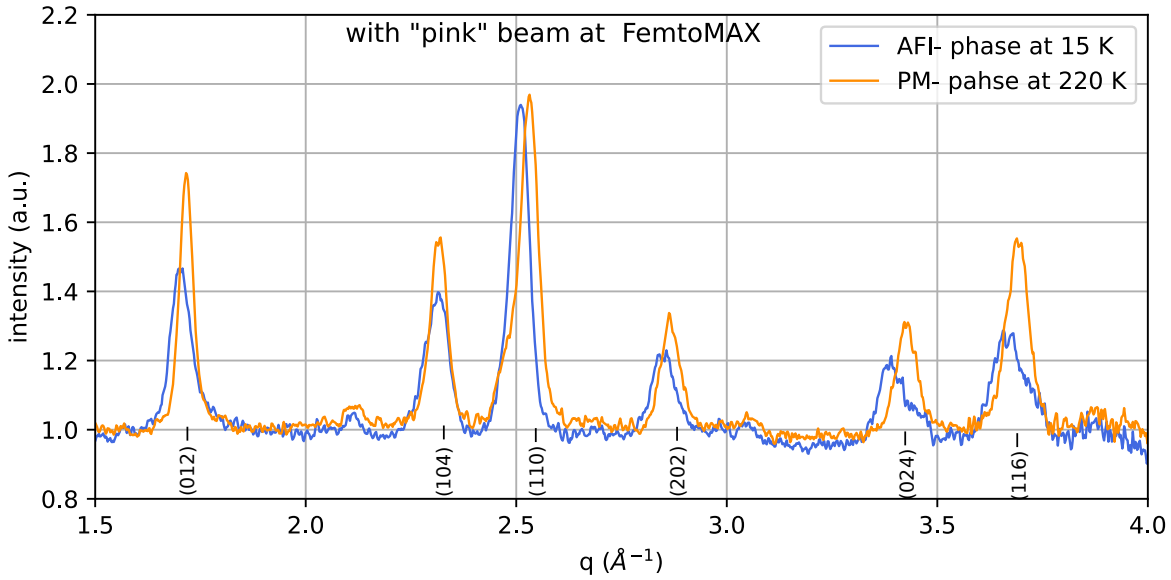

Figure 3.20 – The diffraction patterns obtained at the FemtoMAX beamline for the AFI and PM phases. The intensity is normalised to values around $q = 1.95\ \mathring{A}^{-1}$

Experimental conditions at ID09 beamline, ESRF

The ID09 setup was discussed in detail in Chapter 2. A synchronized laser 1300 nm (energy = 0.95 eV) with 1-2 ps pulse duration was used to excite the sample. Laser excitation with quasi-normal incidence and focused on the sample lead to a beam size of 0.33 x 1.17 mm^2. Different laser fluences ranging from 0.2 mJ/cm^2 to 11 mJ/cm^2 were achieved during the experiment using Optical density (OD) filters in the laser path. The X-rays energy was centered at 15 keV (λ=1.0332 Å) for the maximum flux available.

First series of measurements focused on data measurement as a function of laser fluence, with particular care in the low fluence regime where the photo-induced effects are small. In this case, the pink beam ($\Delta E/E$ = 1.5 %) was used in order to reach good signal over noise. A second series of measurements focused on getting the best possible q resolution in order to distinguish clear the signature of the different phase in the coexistence regime. In this case, the Si monochromator was used ($\Delta E/E = 10^{-4}$). In all cases, the X-ray footprint on the sample was of 50 µm x 250 µm at 6° incidence angle. A schematic representation of the experimental geometry is shown in Fig 3.21. Diffracted X-rays were integrated on a Rayonix MX170-HS CCD detector with pixel size of 44.25 µm. The sample to detector distance was 150 mm.

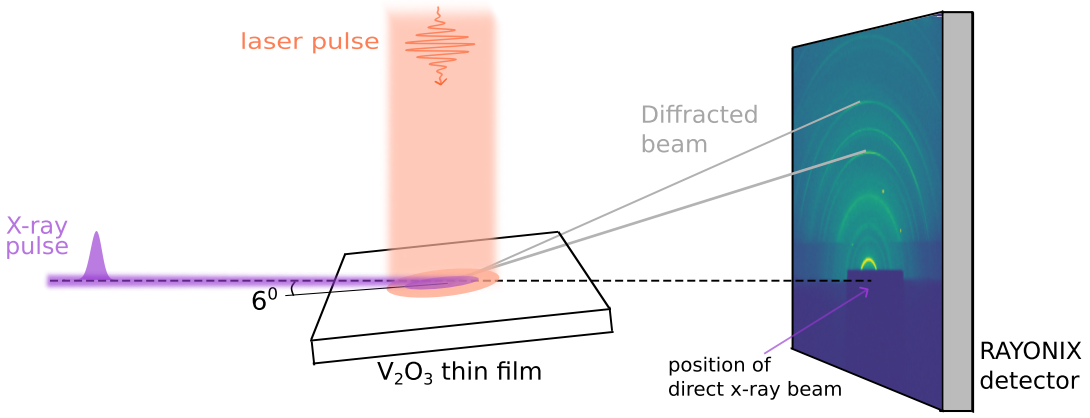

Figure 3.21 – Schematic picture of the experimental geometry at ID09, ESRF. The laser pulse excites the sample at a quasi-normal angle and the X-ray probes at an incidence angle of 6°. The diffraction image is collected by the Rayonix detector.

Measurements were taken in stroboscopic mode and each image was recorded with 1000 shots exposure (i.e, 1 s exposure at the repetition rate of 1 KHz). Diffraction images were measured at different time delays before ("negative" delays) and after ("positive" delays) photo-excitation. The delays sequence was repeated several time with interleaved reference patterns (without any laser excitation) to correct for any drifts in X-rays or permanent changes in the sample and increase the measurement statistics.

It is worth mentioning that the studied V_2O_3 thin films presented a significant pre-

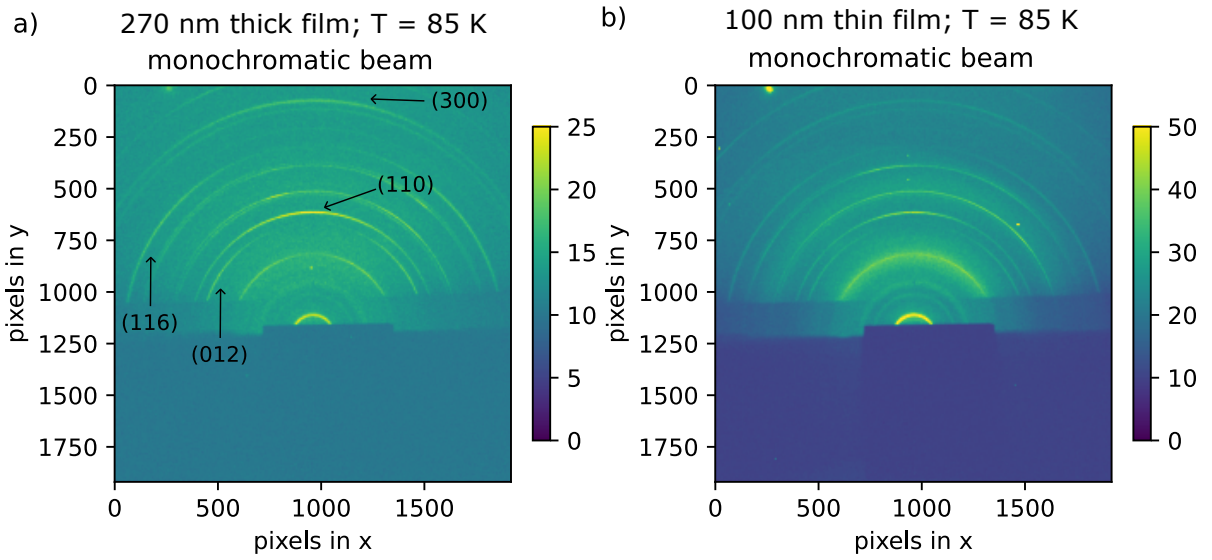

Figure 3.22 – The diffraction images for the thin films of V_2O_3 a) with thickness 270 nm and b) with thickness of 100 nm measured at a temperature of 85 K with monochromatic X-rays at the ID09 beamline, ESRF.

ferred orientation, that could be seen in the diffraction images (Fig. 3.22) which exhibit a noticeable variation in intensity along the the azimuthal angle. Specifically, when we examine the peaks (110) and (300), we observe that their intensities are maximum normal to the surface of the sample, whereas intensities of peaks (012) and (116) are mostly on the sides close to the surface with zero intensity along the normal. This is because majority of the crystallites are oriented with the $\vec{a}$ axis predominantly aligned normal to the sample surface. The $\vec{b}$ and $\vec{c}$ are randomly oriented along the surface as shown in Fig. 3.23.

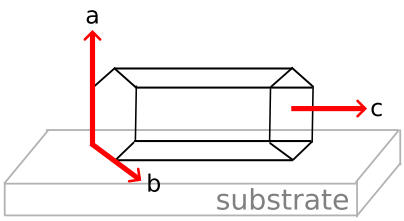

Figure 3.23 – Preferential orientation of majority of the crystallites in the thin films of V_2O_3 with the $\vec{a}$ axis predominantly aligned perpendicular to the substrate. The $\vec{b}$ and $\vec{c}$ axes are aligned along the substrate surface.

Chapter 4

Photo-induced semiconductor-insulator transition in Ti_3O_5

This chapter focuses on the semiconductor to metal phase transition in Ti_3O_5 pellets of different crystallite size upon laser irradiation. In particular, we have focused on the mechanism of thermally induced transition within and across the nanocrystalline grain boundaries and its relationship with the ultra-fast conversion by strain waves. The respective roles of several parameters, such as laser penetration depth, laser fluence and crystallite sizes, are experimentally investigated. The results are rationalised with numerical simulation based on a 2D-model of heat diffusion, which maps the phase distribution of the polycrystalline samples at the nanosecond timescales.

4.1 State of the art

Several studies have been reported on the photo-induced phase transition in nanocrystals of Ti_3O_5 employing a variety of techniques. One such study by Asahara et. al.[5] utilized time-resolved diffused reflection spectroscopy to examine the photo-reversible β to λ -phase transition upon excitation with 800 nm femtosecond laser pulse on the flake-type Ti_3O_5 pellet. Within several hundred femtoseconds, a dispersion of the β-phase charge ordering and transformation to the metastable λ-phase were observed, indicative of a non-thermal phase transition. The whole dynamics from the initial β to λ-phase transition within few hundred fs to the relaxation of meta-stable λ-phase domains in µs were interpreted using the nucleation and growth mechanisms.

Similarly, a time resolved reflectivity study [68] was also done on the flake-type Ti_3O_5 nanocrystals to investigate the β-λ transition through heating with intense ns-laser pulse. The reversible phase transition from β to λ phases was observed within 20 ns whereas the transition from λ to β in about 900 ns. In this study, the phase transition dynamics were predominantly attributed to laser induced heating and the mechanism was explained through nucleation and growth processes.

In 2017, Tasca et.al. [100] observed the photo-induced transition occurring within 10 µs (the resolution of the experiment) of pulsed laser excitation using TR diffused reflectivity and TR X-ray diffraction. The relaxation at delays $>$ 10 µs as seen in Fig. 4.1 was described by thermal diffusion within the nanocrystallites, their aggregates and beyond. However, the morphology of the pellet in this study was not enough to study the effect of particle size on the dynamics of the photo-induced phase transition.

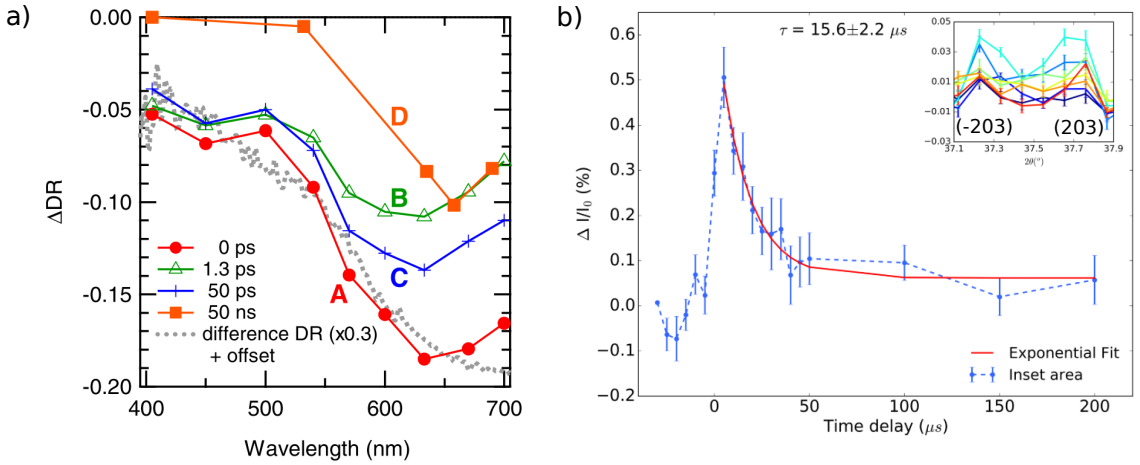

Figure 4.1 – a) ΔDR spectra at different delays 0 ps, 1.3 ps, 50 ps and 50 ns as adapted from [5] b) Temporal evolution of the integrated intensity for the q range of peaks (-203) and (203) as adapted from [100]

A more complete structural study on the flake-type Ti_3O_5 with fs time resolution was performed using laser pump of 800 nm and X-ray probe pulse by Celine Mariette and our research group at IPR[55]. It has been observed that the locally generated electronic and structural precursors upon laser excitation determines a coherent pathway for the

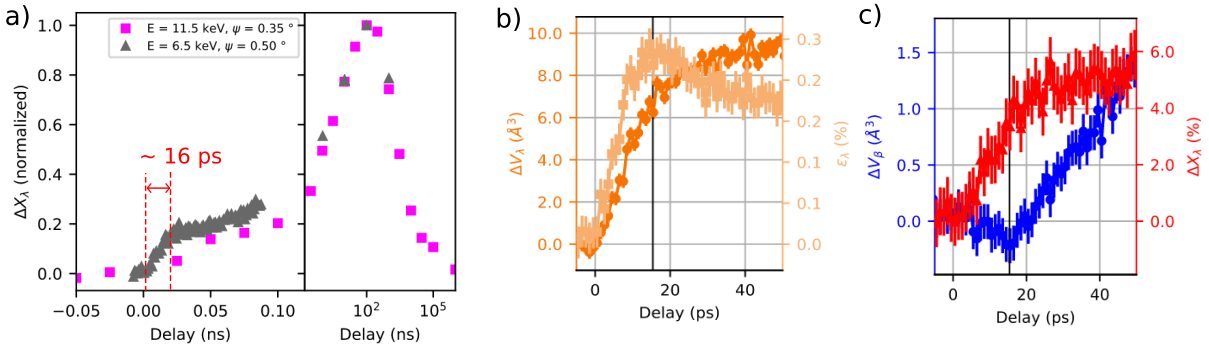

Figure 4.2 – a) Multiscale evolution of the λ-phase fraction (ΔX_λ) in Ti_3O_5 flake-type pellet measured at SwissFEL and ESRF[55]. The grey triangles are from measurement at SwissFEL and the magenta squares are from the measurement at ESRF. The initial β to λ transition occurs within $\sim$ 16 ps followed by another slower transition around 100 ns b) Temporal evolution of the unit cell volume (ΔV_λ) and the strain parameter (E_λ) of the λ phase. c) Evolution of the λ-phase percentage (ΔX_λ) and unit cell volume (ΔV_β) of the β phase with delays.

macroscopic β to λ-phase transition. The λ-phase fraction increases within $\sim$ 16 ps of the laser irradiation as shown in Fig. 4.2a and is accompanied by the volume expansion Fig. 4.2b. The dynamics indicate the phase front starting at the surface propagates in the bulk with acoustic velocity. Unfortunately, it was impossible to determine the limit defining the spatial distribution of transformation, since the laser penetration, the average crystallite size and the phase front limit were very similar, around 100 nm. Nevertheless, an overall multiscale dynamics was achieved: the picosecond switching in nanocrystals by strain wave followed by a thermal switching governed by the heat diffusion in 100s of ns.

A recent study [84] on the effect of polarisation of the incident laser beam on the β to λ transition was done, since the transition is associated with anisotropic migration of atoms in the Ti3-Ti3 dimer. Reflectivity spectra from single crystals of Ti_3O_5 indicated that the transition is favoured only when the pump pulse is along *ab* plane.

A natural question was how the different experimental parameters affect the strain wave pathway and is it possible to decorrelate between the early elastic mechanism and the later thermal induced dynamics? This was the main goal of this part of my work. With this aim, we have investigated the effect of different experimental parameters such as the laser penetration depth, excitation fluence and incidence angle of the probe pulse on different types of Ti_3O_3 nanocrystalline samples.

4.2 Dynamics of the photo-induced structural changes in Ti_3O_5 measured with TR-XRD at the ID09 beamline

In order to track the transient structural changes in the photo-induced Ti_3O_5 with time, TR-XRD measurements were performed on the polycrystalline pellets following the approach discussed in Chapter 3. Fig. 4.3a, 4.4a and 4.5a shows a 2d map of a typical scan on the block-type pellet, stripe-type pellet and flake type pellet, respectively. A series of 30 time delays ranging from negative to positive delays have been repeated several times. The interleave reference patterns at "-10 ns" show that no significant drift or permanent changes occur during the measurement. Transient features show a rise of intensity for all the positive delays at q $\sim$ 1.3 Å^{-1}, q $\sim$ 2.28 Å^{-1} and q $\sim$ 3.18 Å^{-1} and a decrease of intensity at q values of q $\sim$ 2.01 Å^{-1}, q $\sim$ 2.68 Å^{-1}. There is a shift of intensity of peaks at 1.8 Å^{-1} and 3.33 Å^{-1}. These features for the positive delays indicate an increase of λ-phase at the cost of the β-phase in the probed region of X-rays. These changes are well reproduced for the different repetitions.

The same feature are better emphasized in the averaged diffraction patterns and differential signal at different delays as plotted in Fig. 4.3, 4.4, 4.5b and c respectively.

The pure β-phase peaks of Ti_3O_5, for instance (201), (003), (004) and (204) decrease in intensity as shown by the blue arrows in the subfigures b. The corresponding differentials (blue box in subfigures c) shows decreasing signal. Whereas the pure λ-phase peaks (200) and (20-3/203) increase in intensity (indicated by the orange arrows in the absolutes and orange box in the differentials) at the positive time delays and has its maximum between +18 and +56 ns. The intensity of the λ peak (110) increases and β-peak(110) decreases and hence we see a overall shift of the peak (110) to the lower q values(shown by the grey arrow in the absolutes and grey box in the differentials). Similarly, peak shift is also observed for peaks (204)(λ-phase)/(40-2)(β-phase) and (020) (λ/β-phase). Qualitatively, the same signatures are observed for block type, flake type and stripe type pellets. However, the amplitude and dynamics of the changes show slight differences.

As seen in the differentials, the shift of (110) Bragg peak is maximum at around 100 ps ("pure strain") for all the three pellets. A late increase is observed for the peaks which are more sensitive to the phase transition, for example (203)/(20-3) which show a big shift due to the change of both the c parameter and the monoclinic angle, and (201)/(002) for which intensity respectively shrink/increases at the transition from β to λ phase.

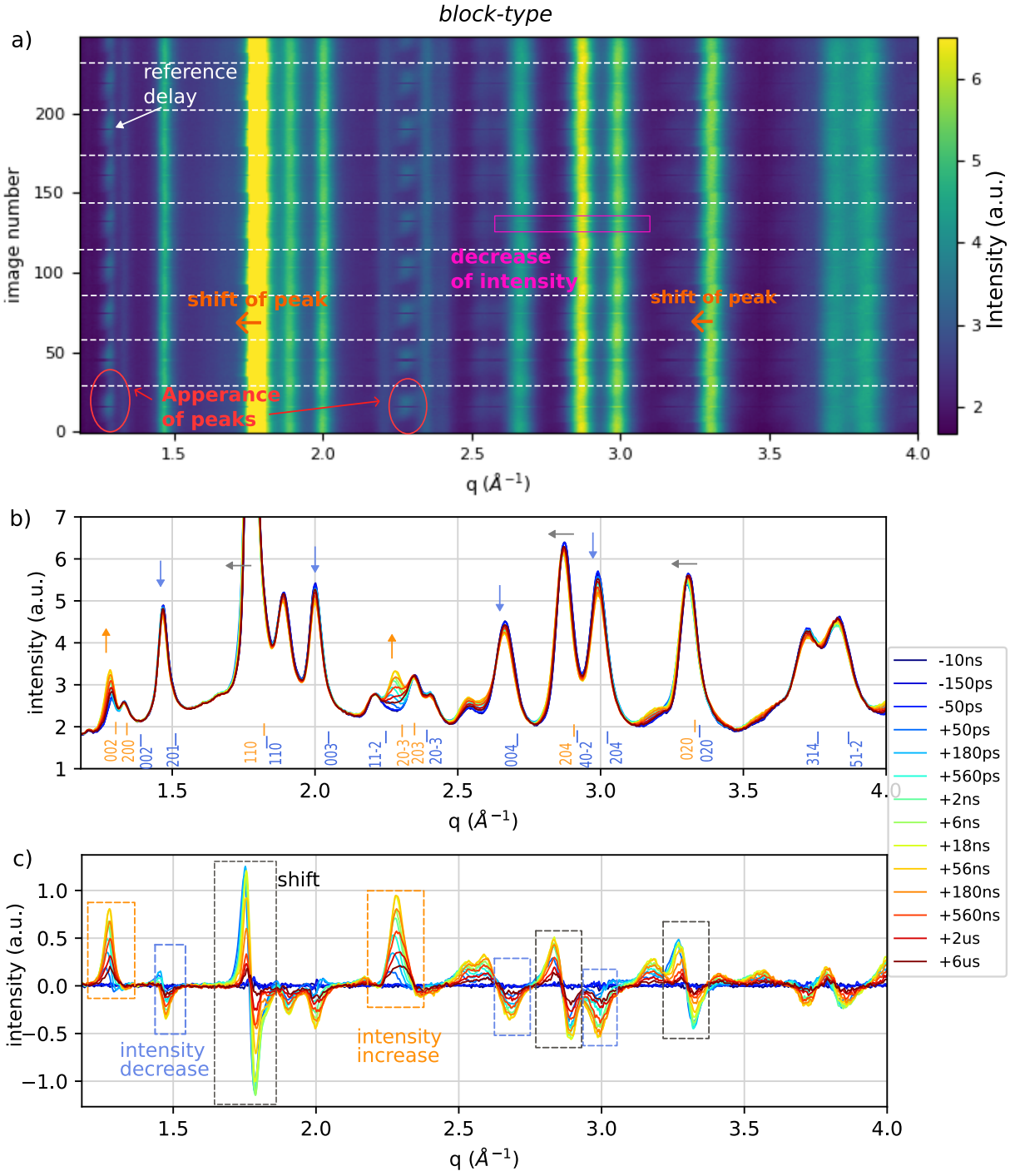

Figure 4.3 – a)A 2D map of intensity of the Bragg peaks plotted for one run measured on the block-type Ti_3O_5 pellet. The diffraction patterns corresponding to each set of delays have been separated with the consecutive white dashed lines. For the positive delays, the intensity increase / decrease or shift of Bragg peaks have been pointed out. b) 1D diffraction patterns measured at different delays from -10 ns to +6 µs on the block-type Ti_3O_5 pellet. c) Differential signal plotted for the same delays set

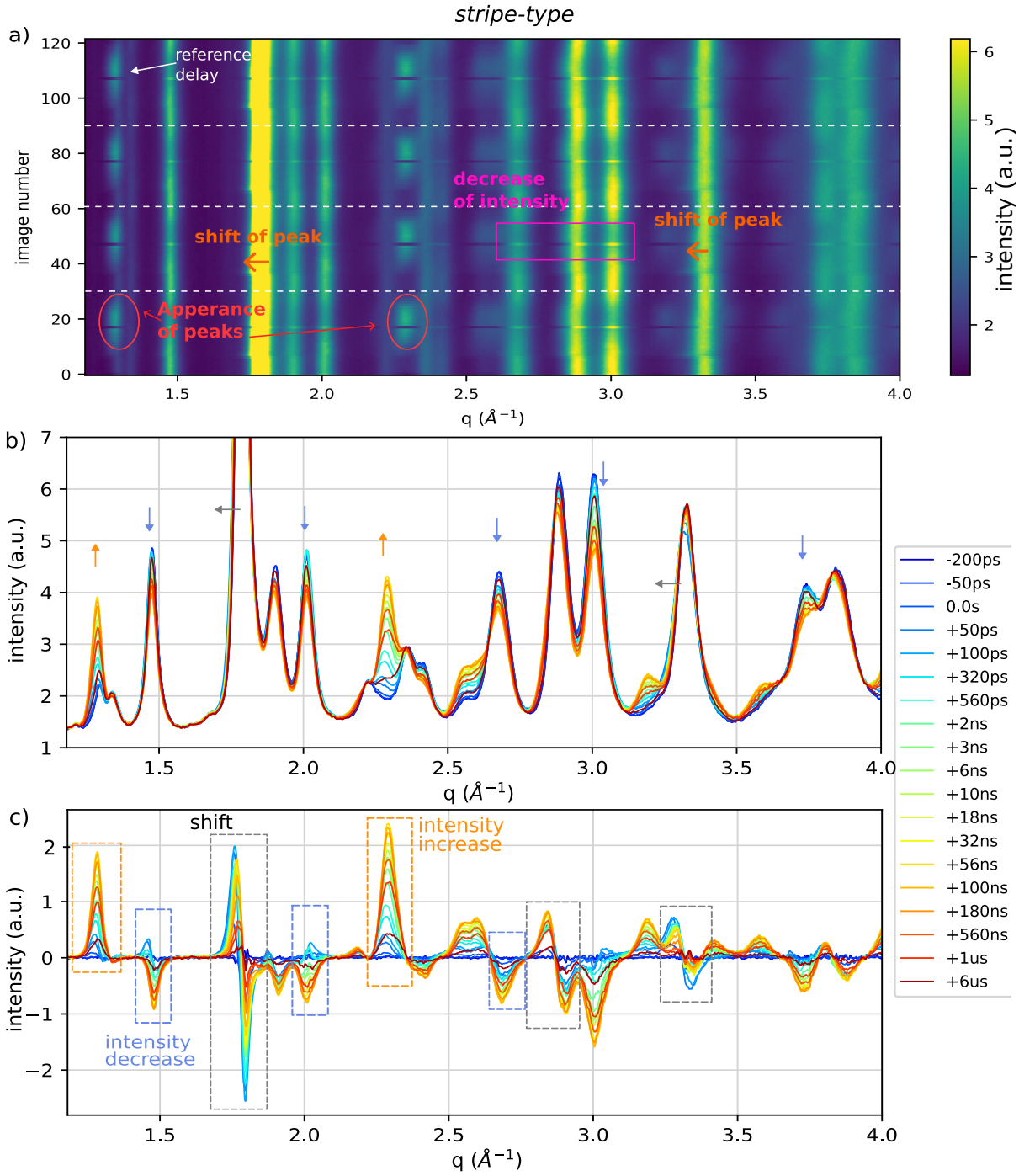

Figure 4.4 – a) A 2D map of intensity of the Bragg peaks plotted at different q values for a typical run measured on the stripe-type Ti_3O_5 pellet. Each set of delays has been repeated 4 times in this run and the diffraction patterns are shown by the consecutive white dashed lines. b) 1D diffraction patterns measured at several delays from -200 ps to +10 µs on the stripe-type Ti_3O_5 pellet. c) The differential signal shows a maximum at +100 ps for the peaks showing shift and at +56 ns for the intensity change.

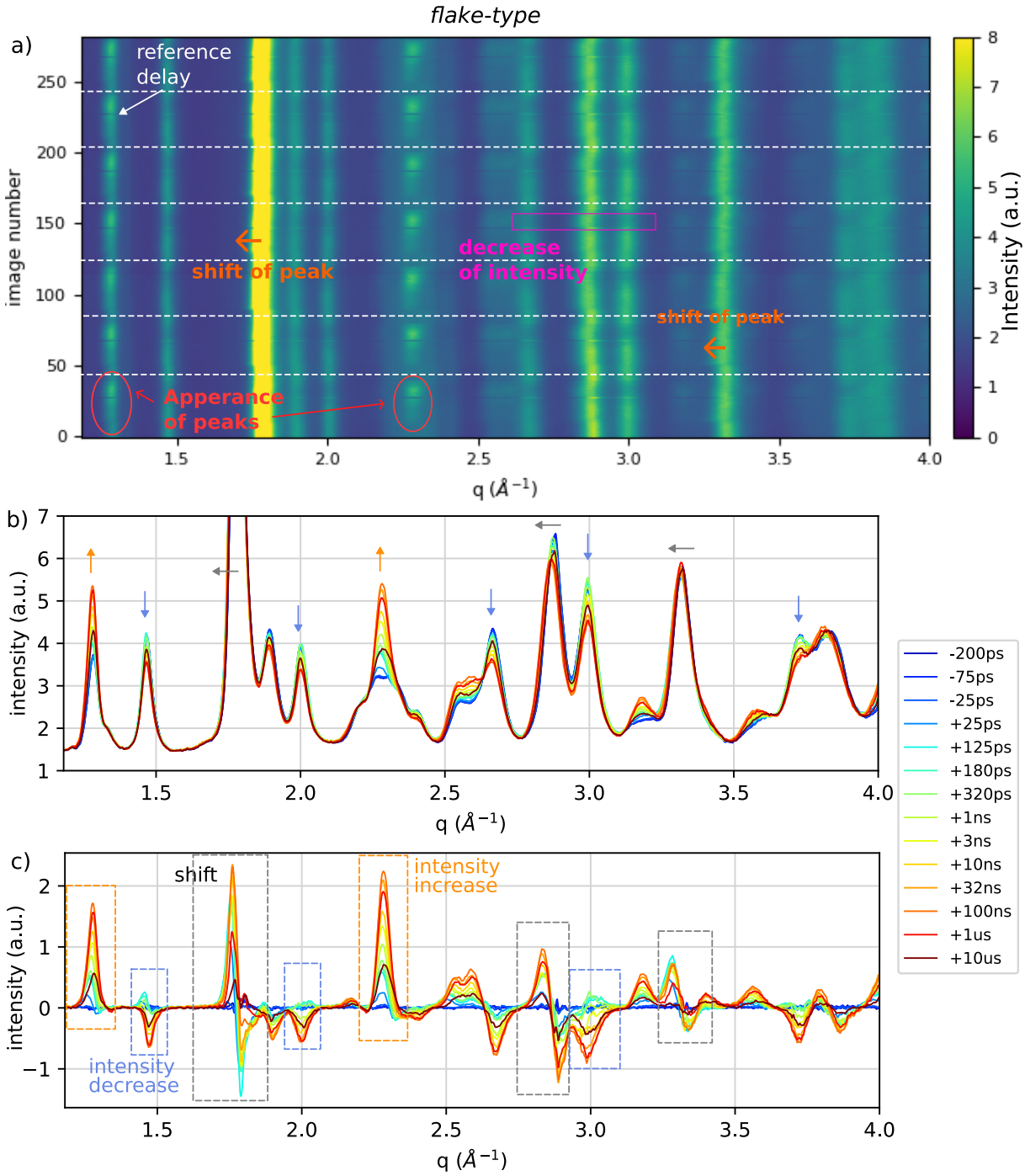

Figure 4.5 – a) A 2D map of intensity of the Bragg peaks plotted for a typical run measured on the flake-type Ti_3O_5 pellet. For the positive delays, the intensity increase / decrease or shift of Bragg peaks have been shown. b) 1D diffraction patterns measured at several delays from -200 ps to +10 µs on the flake-type Ti_3O_5 pellet. b) Differential signal plotted for the same delays

For the three pellets, a full pattern refinement was done for the reference pattern with a laser delay of -10 ns with the same parameters as been described in Section 2.7.3. The refined pattern and the pattern at the delay where maximum phase transition occurs have been plotted for the block-type (Fig. 4.6), stripe-type (Fig. 4.7) and flake-type (Fig. 4.8) pellet.

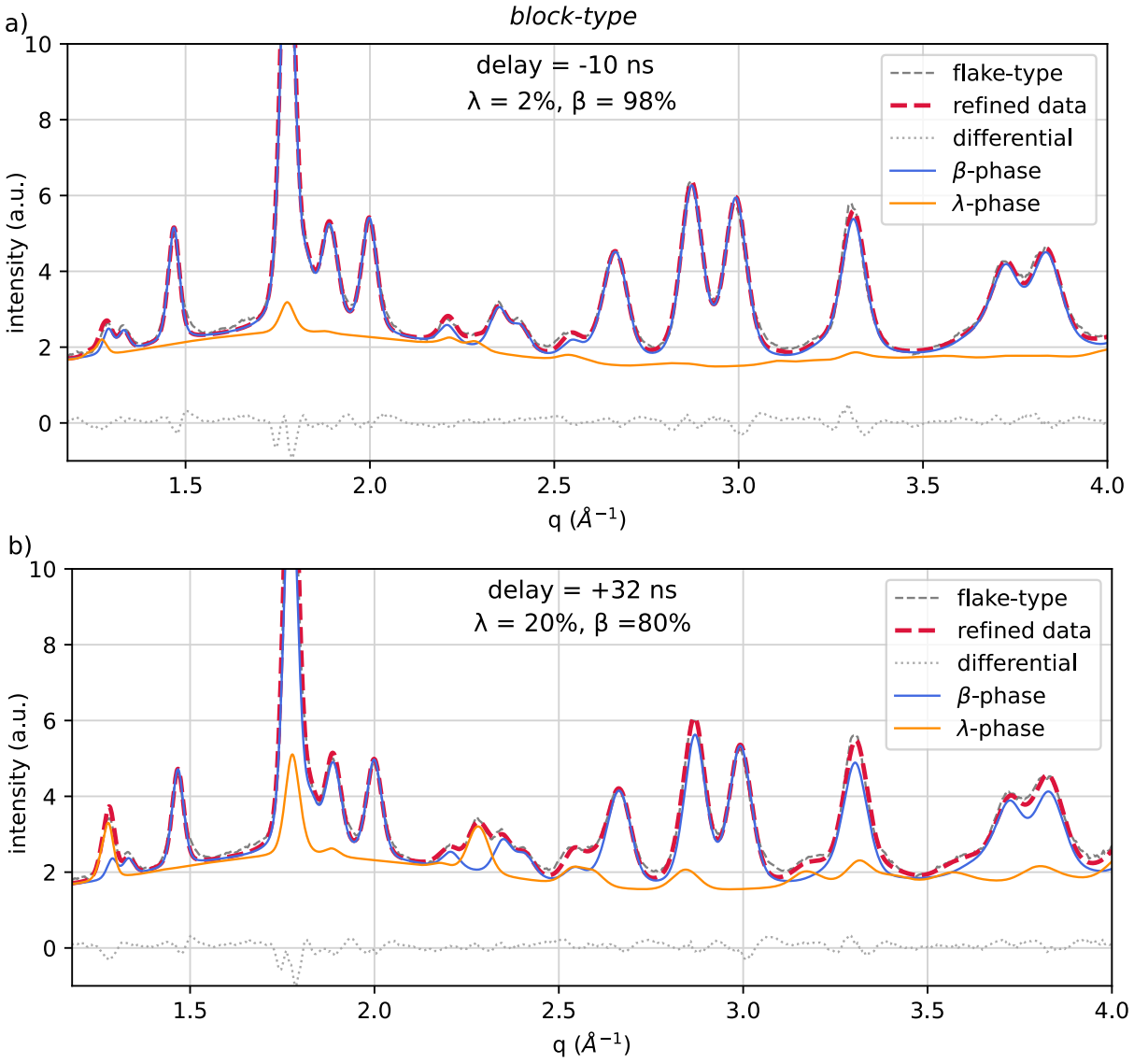

Figure 4.6 – Refined diffraction pattern at a) delay of -10 ns and b) delay at which maximum λ percentage is observed (at 32 ns) measured on the pellet of block-type-Ti_3O_5. The measured pattern is in grey dashed line. The result of the Rietveld refinement is in red line. Blue and orange curves are the contributions of the β and λ-phases respectively. The residual pattern is in dark grey dotted line and shown separately below the curves.

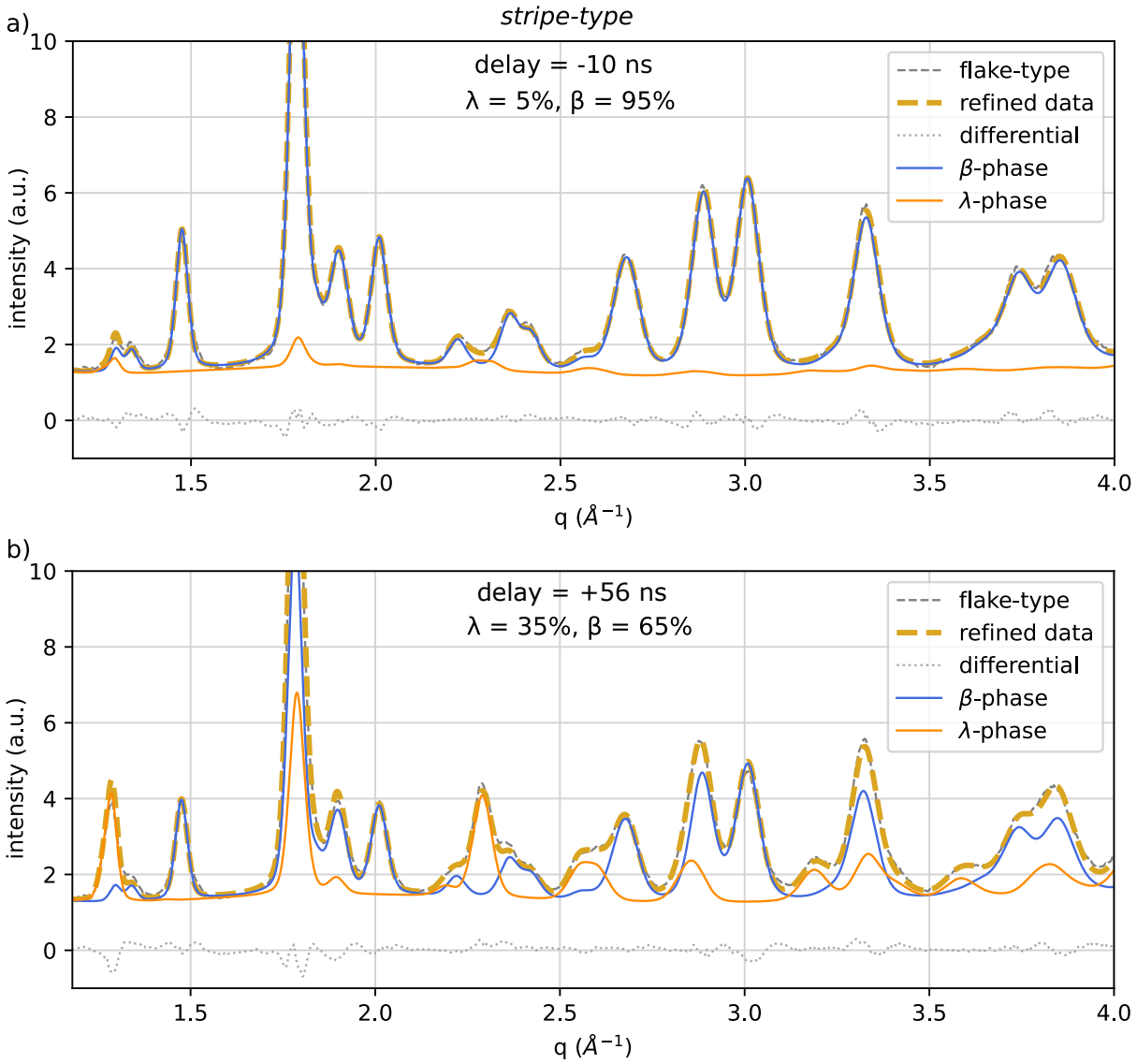

Figure 4.7 – Refined diffraction pattern at a) delay of -10 ns and b) delay at which maximum λ percentage is observed (at 56 ns) measured on the pellet of stripe-type-Ti_3O_5. The measured pattern is in grey dashed line. The result of the Rietveld refinement is in red line. Blue and orange curves are the contributions of the β and λ-phases respectively. The residual pattern is in dark grey dotted line and shown separately below the curves.

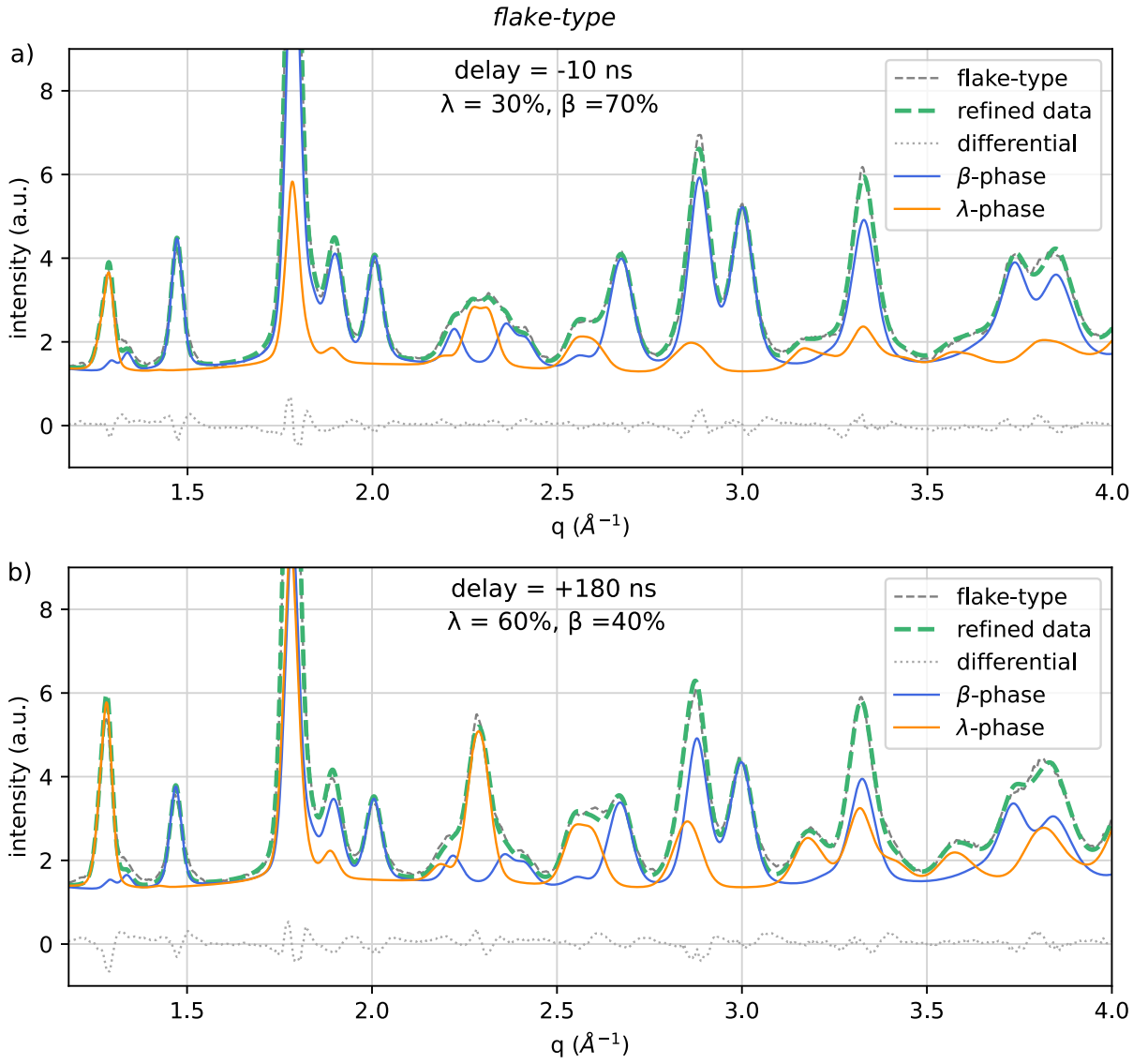

Figure 4.8 – Refined diffraction pattern at a) delay of -10 ns and b) delay at which maximum λ percentage is observed (at 180 ns) measured on the pellet of flake-type-Ti_3O_5. The measured pattern is in grey dashed line. The result of the Rietveld refinement is in red line. Blue and orange curves are the contributions of the β and λ-phases respectively. The residual pattern is in dark grey dotted line and shown separately below the curves.

The evolution of the cell parameters and unit cell volume (Fig. 4.9) was extracted from the Rietveld refinements for different delays. The volume change is maximum around time zero. This is because of high temperature on the surface with the energy deposited on the sample just after the laser irradiation. A temperature change on the sample has been estimated in the later Section 4.3.2 for a laser fluence of 0.5 mJ/mm^2. There is a large uncertainty in the cell parameters of the λ-phase at time zero for the block-type and stripe-type pellets. This is because the λ-phase fraction increases from few percent to several 10s of percent at the point of laser irradiation. For instance, in the block-type pellet, $X_\lambda = 2\%$ in the initial state and it reaches to $\sim 10\%$ upon laser excitation. Hence the points where the fraction changes a lot (at delays 0 and 100 ps or during the relaxation) are not to be trusted in Fig. 4.9.

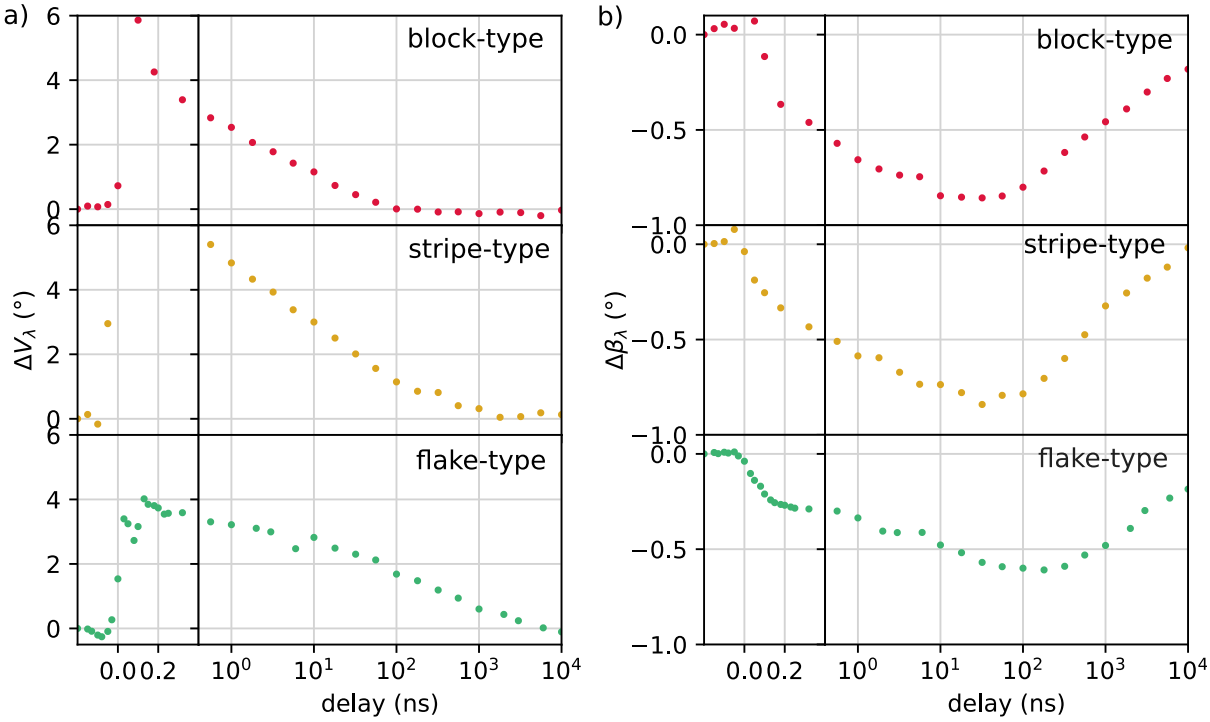

Figure 4.9 – a) Evolution of the change in unit cell volume (ΔV_λ) and b) evolution of the change in angle β ($\Delta\beta_\lambda$) with delays for the flake-type, stripe-type and block-type Ti_3O_5 pellets.

The evolution of the β-angle follows the same dynamics as the phase transition (Fig. 4.10) since the change of the angle is solely because of the transition.

It is important to note here that the change in cell parameters or the weight percentage observed through the XRD measurements is an average over the whole volume (250 µm^2 on surface and 1 µm in depth) probed by the X-rays in the Ti_3O_5 pellet. So it is not possible to know the state of individual crystallites, even in the block-type (with $\sim$ 500 nm crystallites) after the strain propagation or the transition due to heat diffusion.

4.2.1 Characterisation of phase transition dynamics with various crystallite sizes

The time evolution of the weight percentage of the λ-phase (ΔX_λ) is plotted in Fig. 4.10 for the flake-type, stripe type and block-type Ti_3O_5 pellets. The measurements were taken for a laser fluence of 0.5 mJ/mm^2. The multi scale dynamics is in agreement with the previous study [55]. Upon the laser excitation, strain wave propagates in the system establishing a long range order within the system. Because of this, there is an increase of the λ-phase fraction within the 100 ps timescale. The strain and the heat gradient exists in the system and results in the gradual increase of the λ-phase fraction till equilibrium is established in the system.

The early dynamics in the flake-type pellets occurs within 20 ps [55] is beyond the resolution of our TR-XRD experiment at ID09. Even for the block type crystallites, in which the biggest estimated crystallite size is around 500 nm, phase front propagation would be completed after 80 ps (below our time resolution of $\sim$ 100 ps). The slow increase in the ns timescale, on the other hand, can be quantified.

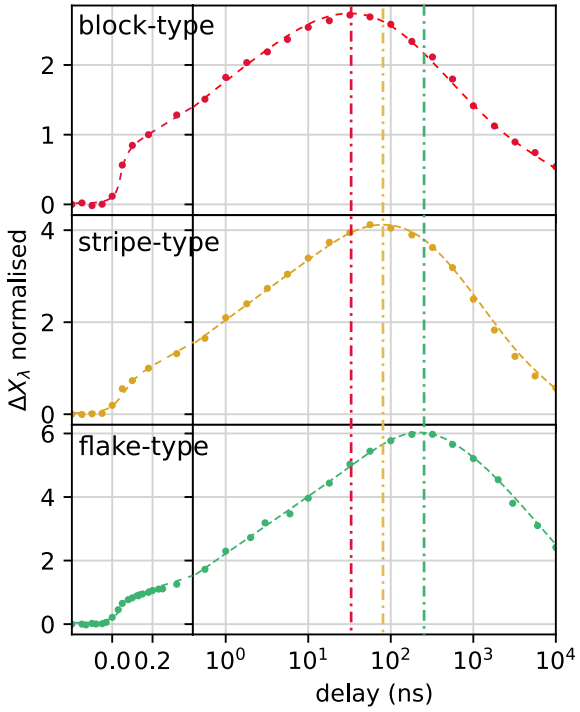

Figure 4.10 – Evolution of λ-phase percentage(ΔX_λ) with delays for a pump wavelength of 800 nm and fluence of 0.5 mJ/mm^2. The values of ΔX_λ have been normalised to its value at $\sim$ 180 ps. The long delays have been plotted in logarithmic scale and the dot-dashed lines are the guide for the eyes.

The primary observation is the influence of the crystallite size on both the amplitude and time evolution of the thermally driven phase transformation. Notably, in Fig. 4.10

the peak of ΔX_λ occurs at different delays: 200 ns for the smallest crystallites ("flake type"), 65 ns for the intermediate size ("stripe type") and 38 ns for the biggest crystallites ("block type"). These time scales match thermal diffusion over 100 nm, 200 nm and 500 nm sizes for the flake-type, stripe-type and block-type crystallites respectively with the thermal diffusivity value of 230 nm^2ns^{-1}[104]. This slow kinetics would thus be associated with thermal equilibrium in the sample, leading to a late transition towards the λ/α (high temperature) phase. The trend is such that the smaller the crystallite size, the longer it takes to reach the peak transformation starting from the state transformed by strain waves.

4.2.2 Influence of incident pump wavelength on the phase transition dynamics

TR-XRD measurements were performed with three different pump wavelengths of 400 nm, 800 nm and 1550 nm, corresponding to the photon energies of 3 eV, 1.5 eV and 0.8 eV respectively. The band gap energy (E_g) of the β-phase is 0.5 eV (Fig. 4.11a). So a part of incident laser photon energy($E_{h\nu}$) goes to excite the electrons from the ground to excited levels while the remaining energy ($E_{h\nu} - E_g$) contributes to incoherent lattice heating. Therefore, the lattice heating is least pronounced for the infrared (IR) pump wavelength of 1550 nm and becomes more substantial for 400 nm.

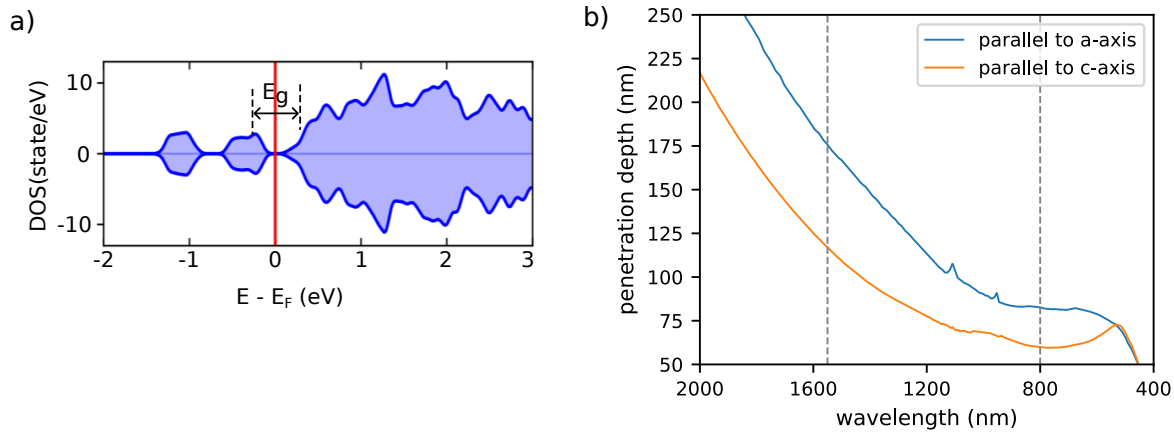

Figure 4.11 – a) Calculated density of states of the β-phase Ti_3O_5 [69] b) Variation of the laser penetration depth with laser wavelength inside Ti_3O_5 for two different polarisations.

The laser penetration depth in the Ti_3O_5 pellet is also wavelength dependent. The penetration depth of the pump laser is determined by considering the imaginary component of the refractive index as measured for single crystals of Ti_3O_5 along different lattice axes $\vec{a}$ and $\vec{c}$[69] (Fig. 4.11b). When the wavelength is 1550 nm, the penetration depth along either axis has a mean value of about 150 nm which is approximately twice of the depth (mean depth of about 70 nm) for wavelength of 800 nm .

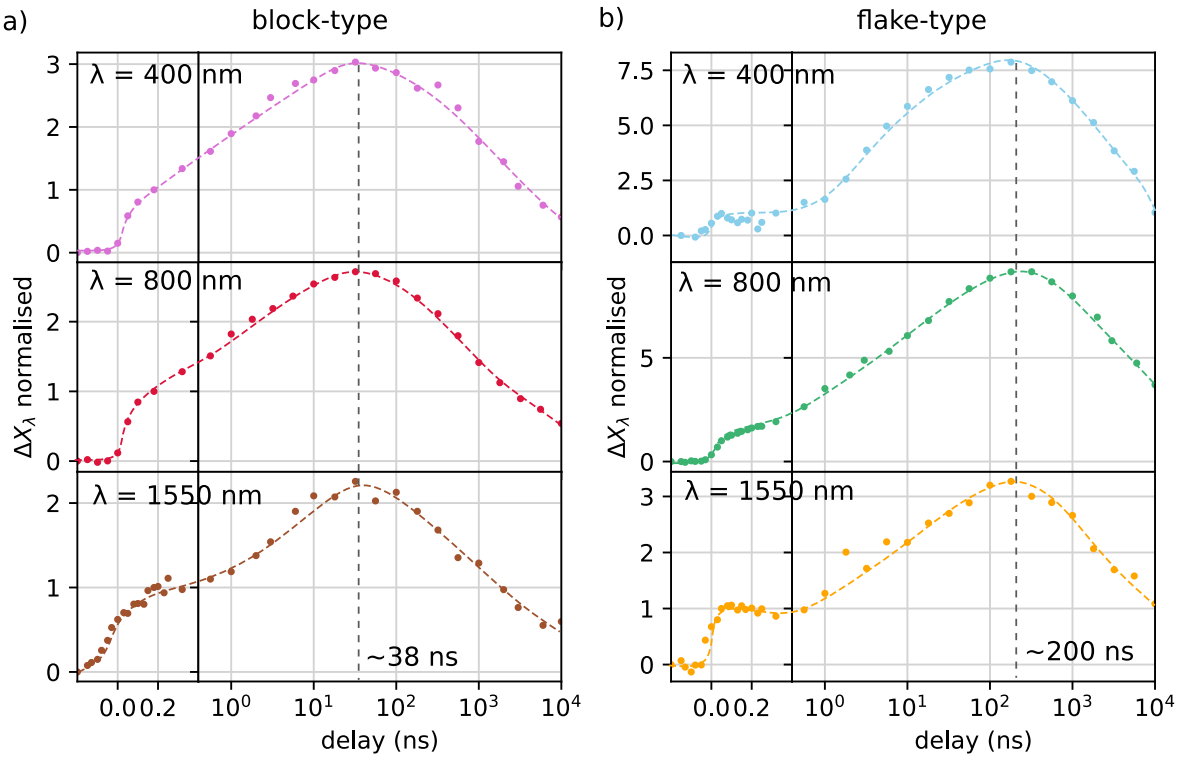

Figure 4.12 – a) λ-phase fraction plotted as a function of delays for three different pump wavelengths 400 nm, 800 nm and 1550 nm with a fluence of 0.5 mJ/mm^2 for the block-type Ti_3O_5 pellet. The values are normalised to its phrase fraction at 180 ps. b)The λ-phase fraction plotted for the pump wavelengths 800 nm and 1550 nm for the flake-type pellet. The values of the phrase fraction is normalised to its value at 200 ps. The dashed lines are guides to the eyes.

The increase in the λ-phase fraction (ΔX_λ) is plotted for the block-type and flake-type pellets in Fig. 4.12 for different excitation wavelengths with a fluence of 0.5 mJ/mm^2. While direct comparisons of the amplitude of thermal transition peak across different wavelengths(correspond to different measurements) may not be valid, the strain-transformed plateau to peak amplitude ratio can be compared. In Fig. 4.12 this ratio is more for the wavelength of 1550 nm compared to that of 400 nm for both types of pellets. This is because the excess energy (3 eV - 0.5 eV) in the 400 nm pulse is much more compared to the energy (0.8 eV - 0.5 eV) for the IR pump pulse and thereby causes more heating in the sample.

The phase transition from β to λ reaches maximum value upon thermal transformation at around 38 ns for the block-type Ti_3O_5 pellet. This peak position is constant irrespective of the laser pump wavelength. For the flake-type Ti_3O_5 pellet, the peak occurs around 200 ns for the different pump laser wavelengths. So, temporal position of the thermal transformation peak is not affected by the laser penetration depth or the incident photon

energies.

4.2.3 Influence of incident pump energy on the phase transition dynamics

The incident laser power imparts energy to the pellet and as the laser fluence increases, more number of β-Ti_3O_5 undergoes transition to the λ-phase due to enhanced heat diffusion within the system. Consequently, the heat diffusion peak appears at longer time delays compared to those observed at lower fluence. Fig. 4.13 shows the changes in λ phase fraction with delays for different laser fluences of 0.25 mJ/mm^2, 0.5 mJ/mm^2 and 0.7 mJ/mm^2 for the block and flake type Ti_3O_5.

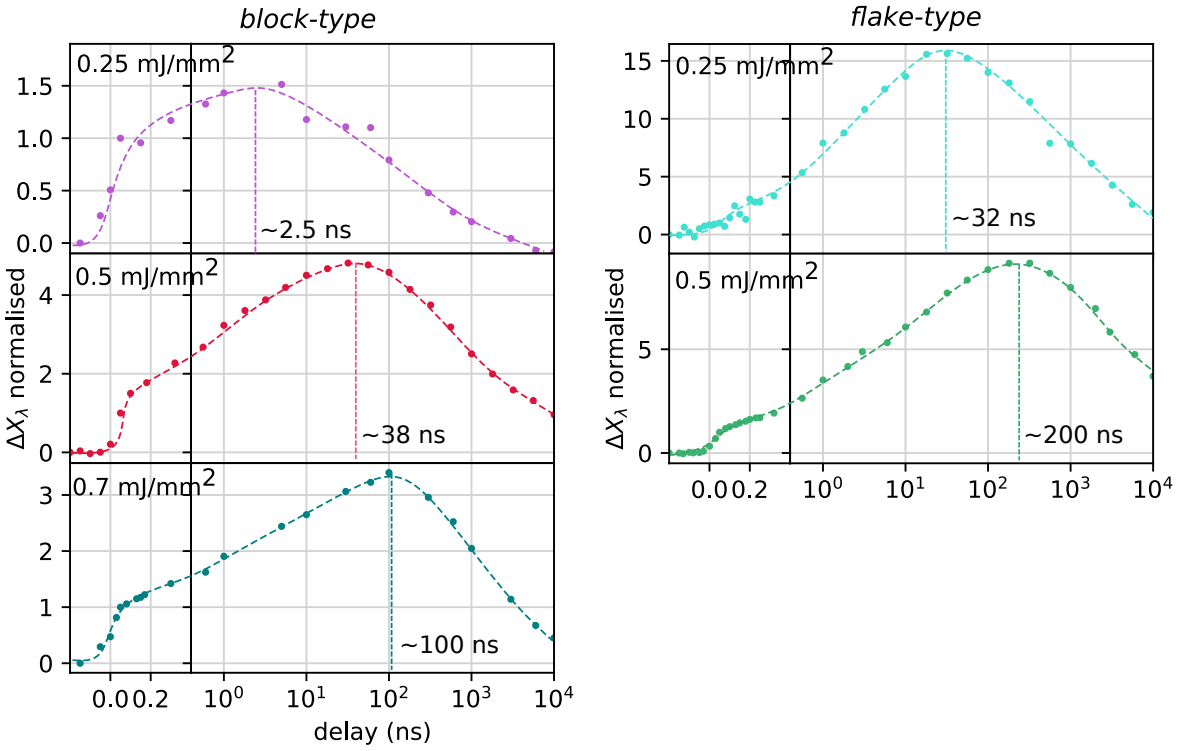

Figure 4.13 – a)λ-phase fraction plotted as a function of delays for the block-type Ti_3O_5 pellet normalised to its value at 180 ps b)λ-phase fraction of the flake-type Ti_3O_5 pellet normalised to its value at 200 ps. The measurements are done at an incident laser wavelength of 800 nm. The dashed lines are guides to the eyes.

For the block-type pellet, the peaks of ΔX_λ for the thermal transformation are observed at different delays of 2.5 ns, 38 ns and 100 ns, corresponding to the fluences of 0.25 mJ/mm^2, 0.5 mJ/mm^2 and 0.7 mJ/mm^2 respectively. In the case of flake-type, the peak occurs at 32 ns and 200 ns for the fluences of 0.25 mJ/mm^2 and 0.5 mJ/mm^2 respectively.

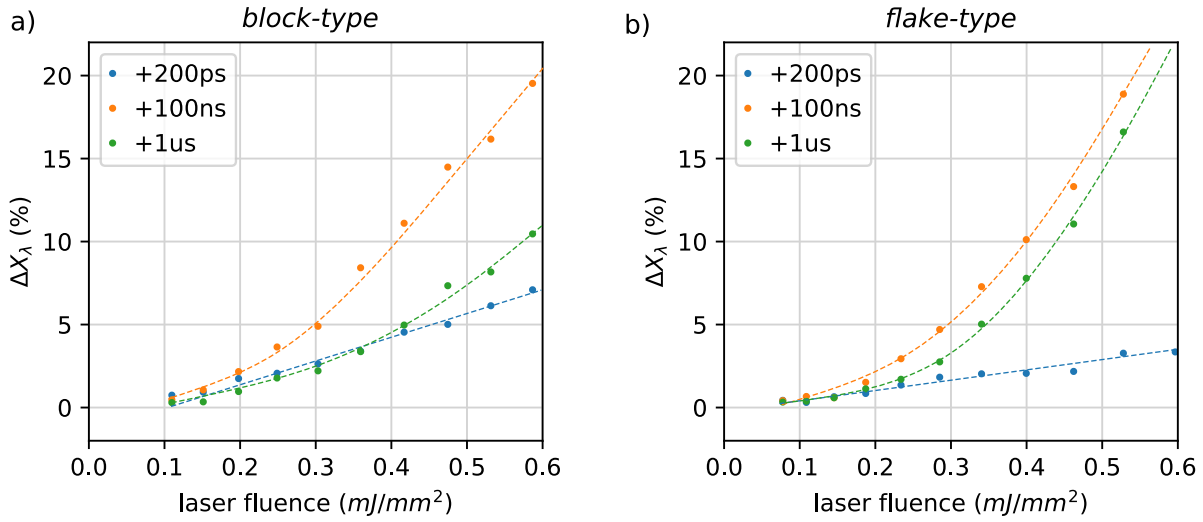

Figure 4.14 – The λ-phase fraction plotted at few notable delays as a function of incident laser fluence for a) the block-type and b) the flake-type Ti_3O_5 pellet. The curves show the linear and non-linear behavior with fluence at 200 ps and 100 ns respectively. The dashed lines are drawn as guides for the eyes.

In order to explore the impact of the incidence laser fluence on the strain driven and heat transformed peaks, the fraction of λ-phase has been plotted in Fig. 4.14 as a function of fluence for a few delays. ΔX_λ at 200 ps time delay shows a linear increase with an increase of laser fluence in both flake and block-type pellets. In contrary, ΔX_λ shows a non-linear increase at 100 ns with the increase of fluence for both types of crystallites. The two contrasting nature of the fluence dependence indicates that the strain wave propagation at picosecond timescale has a different nature compared to the heat diffusion at the nanosecond timescales.

4.2.4 Influence of incidence angle of the X-rays on the phase transition dynamics

With the increase in the incidence angle of X-ray on the pellet, the penetration depth also increases as depicted in Fig. 3.8. This, in turn, leads to a reduction in the ratio of photo-excited region to the probed region in the sample, subsequently causing a decrease in ΔX_λ within the X-ray probed regime as observed in Fig. 4.15.

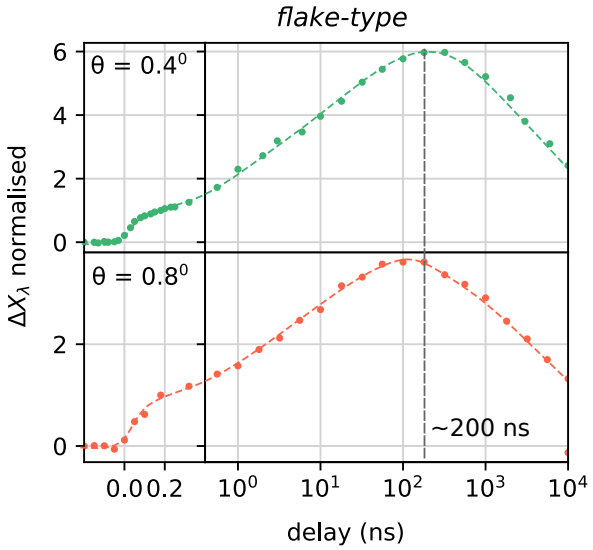

Figure 4.15 – Evolution of ΔX_λ plotted with delays for an incidence angle of 0.4° (top) and 0.8° (bottom) in flake-type pellet. The values of ΔX_λ are normalised to the value at 180 ps. The dashed lines are drawn for guides to the eyes.

This phenomenon manifests through the decrease of the amplitude of the λ-phase fraction in the pellet. The magnitude of these peaks, indicative of the extent of structural changes occurring within the material, is notably affected by the change in the ratio of the photo-excited and probed regions. However, the peak positions are not affected much because of the change in the incidence angle.

4.2.5 Effect of initial λ phase percentage on the phase transition dynamics

We performed the TR-XRD measurements on two different pellets of flake-type crystallites of Ti_3O_5 which had varied initial percentages of the β and λ-phases. One of these flake-type pellet contained 12% λ-phase initially while the other had a higher λ-phase content of 30%.

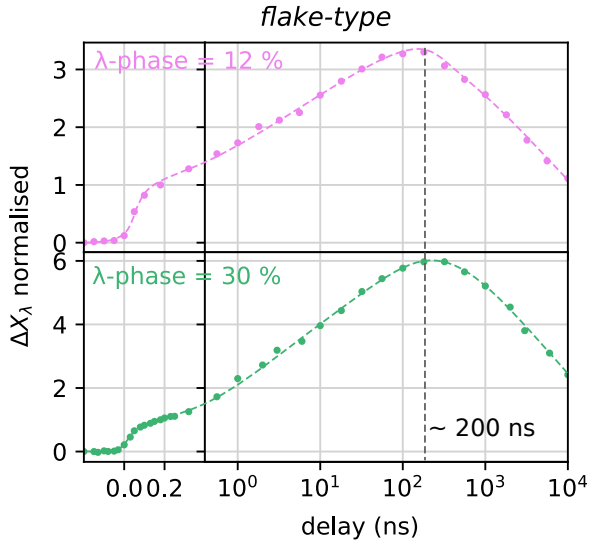

Figure 4.16 – Evolution of ΔX_λ plotted with delays for two different pellets of the same flake-type, with different initial λ-phase content : 12% (top) and 30% (bottom). The dashed lines are guides to the eyes.

From the evolution of the ΔX_λ in Fig. 4.16, we observe that the thermal transition peak occurs at the same delay for both the pellets. This indicates that the dynamics of this peak does not depend on the initial λ/β phase content.

4.3 Heat Diffusion Model

To understand the nanosecond dynamics of phase transition in photo-excited Ti_3O_5 and provide the rationale for the observed size-dependent build up of the high temperature phase, we developed a heat flow model based on finite difference method[78][113]. Similar techniques has been used previously to simulate the heat conduction in composite materials with specific boundary conditions [49].

The most striking observation from the experimental results is that the smaller the crystallite size, the longer it takes to reach the peak thermal transformation starting from the state transformed by strain waves. These two mechanisms not only develop on vastly different timescales but also the dependency on the excitation density points to different physical underpinnings (Fig. 4.14).

4.3.1 Description of the model

In this section, we present a simple 2-dimensional model based on the Fourier theory of heat diffusion to study the dynamics of the photo-excited λ-phase.

The 1 dimensional heat equation[88] is:

$$\frac{\partial T}{\partial t} = \alpha \frac{\partial^2 T}{\partial x^2} \tag{4.1}$$

where $T(x,t)$ is the temperature at position x and time t and α is thermal diffusivity constant. For obtaining the numerical solution of this equation in our sample, we have used finite difference method[78]. In this method, the continuous partial derivatives are approximated with finite differences. So the numerical solutions of this equation can be obtained at a finite number of points and at finite time.

The region of interest for the heat conduction is represented by a network of a set of points (nodes) called 'mesh'. In our case, the region of interest is within the cross section of the laser excited and X-ray probed region as shown by the small box in Fig. 4.17a. For simplicity, we have considered a square shaped simulation box of 500 x 500 nodes out of which 400 nodes on the surface are photo-excited. The nodes (shown in blue dots in Fig. 4.17c) are the points where the discreet solution of the heat equation is obtained.

The nodes represent the photon absorbing centers, the basic units of which corresponding to the Ti-Ti dimers. For simplicity, a square mesh is considered with equal distance ($\Delta x = \Delta y$) between the nodes. Each node has 4 nearest neighbours. To replicate the polycrystallinity in the pellets, subgroups of nodes have been considered as a grain/crystallite (grey shaded area in Fig. 4.17c). So the mesh consists of several crystallites separated by grain boundaries.

Increasing the number of nodes in the mesh increases the spatial resolution of the solutions which in turn increases the accuracy of numerical solution.

The finite difference method involves using discreet approximations like

$$\frac{\partial T}{\partial t} \approx \frac{T_{i+1} - T_i}{\Delta x} \tag{4.2}$$

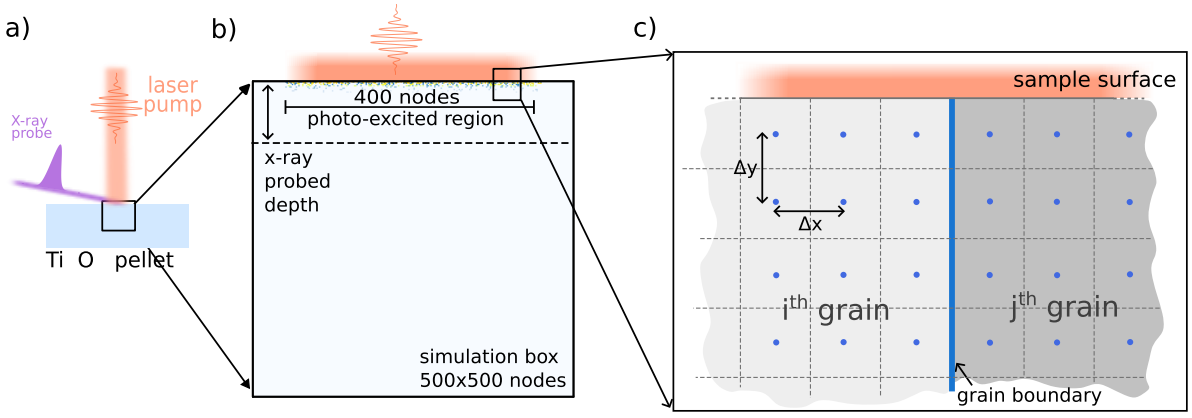

Figure 4.17 – a) Experimental geometry showing the laser pump pulse incident normally on the pellet surface and X-ray probes at an grazing angle (discussed in detail in Chapter 3). b) A section of the laser excited regime of Ti_3O_5 pellet is represented with a simulation box of 500x500 nodes of which 400 nodes on the surface is photo-excited and X-ray probed depth is about 80 nodes. c) A zoomed image on the photo-excited region of the system shows that the simulation box consists of 2D grid of nodes(indicated by the blue dots). Several nodes together form the grain/crystallites(for example, i^{th} and j^{th} grains) and are separated by the grain boundaries.

where the difference $T_{i+1} - T_i$ is calculated at the intermediate points in the mesh. This gives a large number of algebraic equations based on energy balance used to define the relationship between adjacent nodes. At each time step, we can assume the system to be in a steady state. So the heat conduction equation Eqn. 4.3 gives an estimate of the heat flow between the nodes at one time step.

$$q = -kA\frac{dT}{dx} \tag{4.3}$$

Therefore, using discreet approximation, the heat flow between a node *(m, n)* and its 4 surrounding neighbours(Fig. 4.18a) is given by

$$q_{(m-p,n-q)\to(m,n)} = k_{(m-p,n-q)\to(m,n)} A \frac{T_{m-p,n-q} - T_{m,n}}{\Delta x_{(m-p,n-q)\to(m,n)}} \tag{4.4}$$

with $(p, q) = (1, 0), (0, 1), (-1, 0), (0, -1)$ respectively for each of the 4 nearest neighbours as shown in Fig. 4.18a. The heat flow q is in Wm^{-2}, k is the thermal conductivity in $Wm^{-1}K^{-1}$, $T_{m.n}$ are the temperature of the nodes in K and A is the exchange area in m^2. In this square and regular lattice, the exchange area A and the distance $\Delta x_{(m-p,n-q)\to(m,n)}$ between node $(m - p, n - q)$ and node (m, n) are constant.

The temperature change of each node (m, n) is calculated from the heat flux q as:

$$\Delta T_{m,n} = \sum_{(p,q)} q_{(m-p,n-q)\to(m,n)} / C_p^{(m,n)} \tag{4.5}$$

with $(p, q) = (1, 0), (0, 1), (-1, 0), (0, -1)$ for the 4 nearest neighbours and heat capacity $C_p^{(m,n)} = C_p^{\beta} / C_p^{\lambda}$ ($JK^{-1}mol^{-1}$) for λ-phase / β-phase nodes. The specific heat capacities of the β and λ phases are 154.25 J $K^{-1}mol^{-1}$ and 161.82 J $K^{-1}mol^{-1}$ respectively [104]. To each node is associated a temperature which is the sole parameter that distinguishes the two phases. A node with 300 K < T < 470 K is in β-phase and that with T > 470 K is in λ-phase.

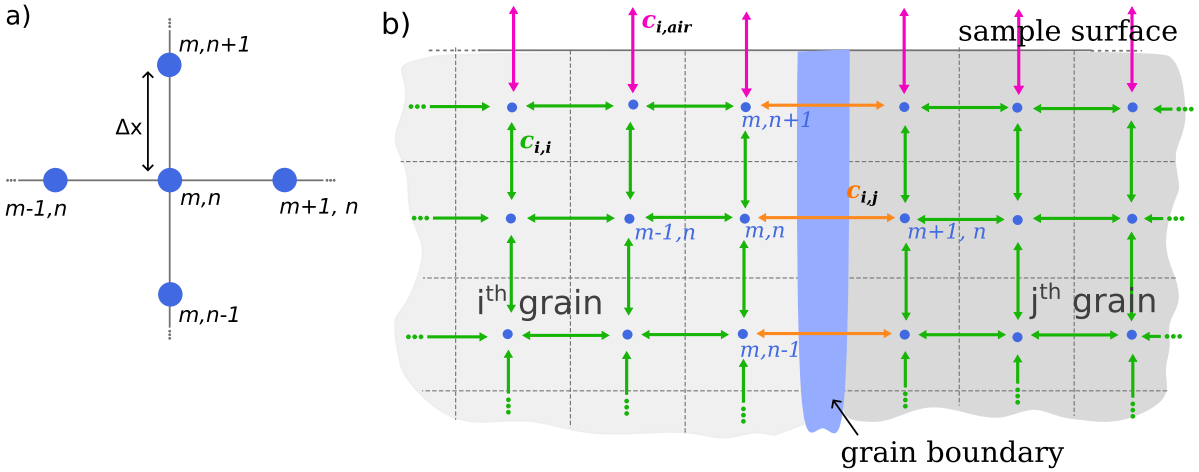

Figure 4.18 – a)A section of the mesh showing the node (m, n) and its 4 nearest neighbours. b) The three different thermal exchange coefficients between the nodes are represented by the green, orange and purple arrows for respectively the intragrain coefficient($c_{i,i}$), intergrain coefficients($c_{i,j}$) and the heat exchange coefficient($c_{i,air}$) with the surrounding air on the sample surface

We define an effective heat exchange coefficient c to compare the heat flow between the different pairs of nodes:

$$c_{(m-p,n-q)\to(m,n)} = \frac{q_{(m-p,n-q)\to(m,n)}}{T_{m-p,n-q} - T_{m,n}} = \frac{1}{R_{(m-p,n-q)\to(m,n)}} \tag{4.6}$$

where $R_{(m-p,n-q)\to(m,n)}$ is the effective thermal resistance between the nodes. The values of this effective heat exchange coefficient has been evaluated for nodes within a crystallite($c_{i,i}$), across the grain boundaries ($c_{i,j}$) and with the surrounding air($c_{i,air}$) (Fig. 4.18) in the following section.

A time step is concluded when the heat exchange is done between the nodes and the phase of each node is checked for transition based on its final temperature. A node with T increasing above 470 K is converted to the λ-phase and a node with T decreasing below 470 is converted to β-phase. At the end of each time step, the λ-phase fraction (ΔX_λ) is calculated as the ratio of the number of λ-nodes to the total number of nodes in the

probed region.

$$\Delta X_\lambda(\%) = \frac{number\ of\ \lambda - phase\ nodes}{number\ of\ nodes\ in\ the\ probed\ depth} \times 100 \tag{4.7}$$

The full relaxation is considered to be achieved when all the nodes are switched back to the low temperature β-phase.

4.3.2 Choice of parameters

Temperature profile in the λ- and β phase nodes

Upon laser excitation, there is local heating on the sample. The deposited heat is proportional to the fluence of the laser pump and the absorption coefficient of the sample. The energy deposited per unit volume on the surface of the pellet can be estimated from Eqn. 1.1 as :

$$W(z=0) = 6.15 \times 10^9 J/m^3 \tag{4.8}$$

for an incident pump fluence of 0.5 mJ/mm^2 and the reflectivity of 0.2 and laser penetration depth of 65 nm. This energy per unit volume gives a surface temperature of about 2500 K.

$$\Delta T = \frac{W(z=0)}{C_v} = 2128\ K \tag{4.9}$$

In order to represent the state of the system after the propagation of the strain wave, the crystallites are partially switched to λ phase. The rest of the nodes are in β-phase. We assume that the β nodes that absorb more heat, transform to the λ phase . So the temperature profile on the λ-nodes is exponentially decreasing in depth from the surface temperature of 2500 K. The β nodes on the surface that absorb less energy stay as a heated β. In our simple model, where the phase is solely based on the temperature of the node, we assume that the "hot" β-nodes on the surface has a temperature of 470 K and it decreases exponentially in depth. The profile follow initial laser excitation in the pellet. The nodes in depth of the pellet beyond the laser penetration stay at the room temperature of 300 K.

The melting point of Ti_3O_5 is about 2073 K. We assume that the surface temperature is close but slightly below the melting point temperature. This is because we have not noticed any changes in the diffraction pattern while the pellet is irradiated with the laser power.

Thermal exchange coefficients and their relations

The different thermal exchange coefficients depend on the phase (λ or β) and crystallite indices (i, j) of the nodes $(m-p, n-q)$ and (m, n). The ratios between the different coefficients are estimated based on the known physical properties of the system.

Heat exchange coefficients inside each crystallites: The heat exchange coefficient within a single crystallite i are estimated based on the reported thermal conductivity values for β and λ phase. The thermal conductivity of the λ- and β phases are respectively 0.2 ± 0.02 $\mathrm{Wm^{-1}K^{-1}}$ and 0.41 ± 0.02 $\mathrm{Wm^{-1}K^{-1}}$ [104].

A global scaling factor is chosen in order to keep the computational time reasonably short. For example, when heat flows between two λ-nodes,

$$c_{i,i}^{\lambda\lambda} = \frac{k_\lambda A}{\Delta x} = \frac{0.2 * (1 \times 10^{-9})^2}{1 \times 10^{-9}} = 0.2 \times 10^{-9}\, WK^{-1} \tag{4.10}$$

We take 0.01 instead, meaning that $c_{i,i}^{\lambda\lambda,sim} = c_{i,i}^{\lambda\lambda} \times 5.10^6$. The factor of 5×10^5 has been used for the heat exchange coefficient between the λ-λ, β-β and λ-β nodes within a single crystallite as well as across the grain boundaries.

$$c_{i,i}^{\beta\beta,sim} = \frac{k_\beta A}{\Delta x} = 2\frac{k_\lambda A}{\Delta x} = 2c_{i,i}^{\lambda\lambda,sim} = 0.02 \tag{4.11}$$

since $k_\beta \approx 2k_\lambda$.

The exchange coefficient between a λ and β node is calculated using the equation for effective thermal resistance(R in Eqn. 4.6) in series.

$$R_{i,i}^{\beta\lambda,sim} = (\frac{1}{k_\beta} + \frac{1}{k_\lambda})\frac{\Delta x/2}{A} = \frac{1}{2}(\frac{1}{c_{i,i}^{\beta\beta,sim}} + \frac{1}{c_{i,i}^{\lambda\lambda,sim}}) = 75 \tag{4.12}$$

Therefore $c_{i,i}^{\beta\lambda,sim} = 0.013$

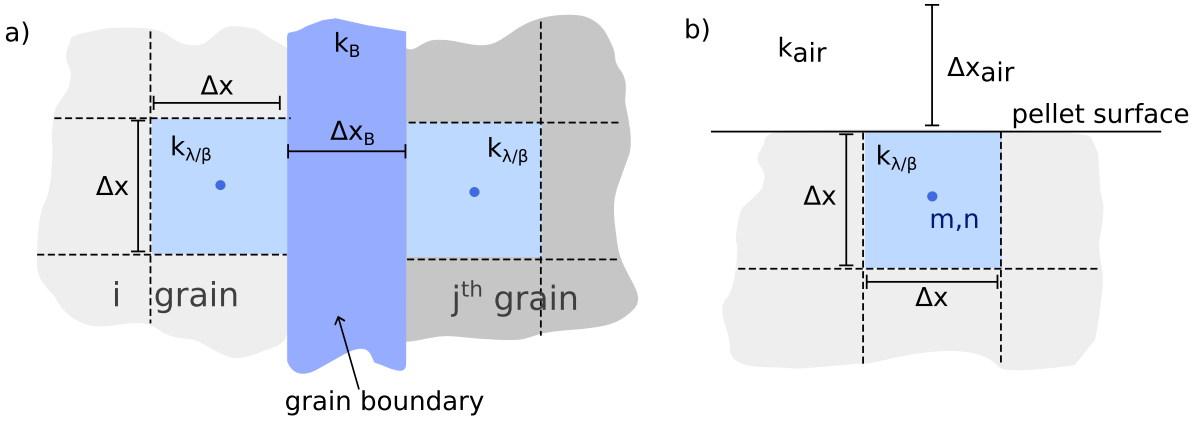

Figure 4.19 – a) Schematic picture of a small part of the system showing the nodes belonging to i^{th} and j^{th} grains separated by a grain boundary layer of thickness Δx_B. The grain boundary has not been assigned any nodes, but the effect of it has been calculated in the heat exchange coefficient using the ratio of B. b) Schematic picture of the node on the surface of the pellet in contact with the air layer of thickness Δx_{air} on top.

Heat exchange coefficients across the grain boundary: The heat exchange between two nodes in neighboring crystallites i and j takes into account a thin polymer layer of few nodes in thickness between the crystallites (Fig. 4.19a).

$$R_{i,j} = \frac{\Delta x/2}{k^i_{\lambda/\beta} A} + \frac{\Delta x_B}{k_B A} + \frac{\Delta x/2}{k^j_{\lambda/\beta} A} \tag{4.13}$$

where $k^i_{\lambda/\beta}$ and $k^j_{\lambda/\beta}$ are the thermal conductivities of nodes belonging to the different grains i and j respectively and the values will be either k_λ or k_β depending on the phase of the corresponding nodes. Δx is the distance between the consecutive nodes within a crystallite and A is the area over which heat exchange takes place. Δx_B is the thickness of the boundary layer with thermal conductivity of k_B. The thermal conductivity of this layer can vary between 0.1 $\mathrm{Wm^{-1}K^{-1}}$ for polymer [39] and 0.025 $\mathrm{Wm^{-1}K^{-1}}$ for the air[43]. Therefore, k_B can vary between $k_\lambda/2$ and $k_\lambda/8$. Therefore,

A ratio(B) of intergrain to intragrain coefficients have been described as

$$B = \frac{c^{x,y}_{i,j}}{c^{x,y}_{i,i}} \tag{4.14}$$

where x,y can be either λ or β phase. Hence, B can vary between 5 and 20.

Heat diffusion across the pellet surface and in the bulk: Similarly the thermal resistivity across the pellet surface can be calculated as :

$$R_{i,air} = \frac{\Delta x/2}{k_{\lambda/\beta} A} + \frac{\Delta x_{air}}{k_{air} A} \tag{4.15}$$

The thermal conductivity of air (k_{air}) is about 0.025 $\mathrm{Wm^{-1}K^{-1}}$ at room temperature of 300 K [43]. Considering that the surface temperature on the pellet upon laser irradiation reaches equilibrium over a distance of about 10 µm thick layer of air,

$$R_{i,air} = \frac{\Delta x}{A}\left(\frac{1}{2k_{\lambda/\beta}} + \frac{\Delta x_{air}/\Delta x}{k_{air}}\right) = \frac{\Delta x}{k_{\lambda/\beta} A}\left(\frac{1}{2} + \frac{10^3}{0.0625}\right) \approx 16000 \frac{\Delta x}{k_{\lambda/\beta} A} \tag{4.16}$$

with the value of $k_{air}/k_\beta = 0.0625$. Therefore, with the value of $c^{\beta\beta}_{i,i} = 0.02$, the value of $c_{i,air}$ is roughly of the order of 1×10^{-8} and is kept the same irrespective of the phase of the node on the surface.

The thermal exchange coefficient with the bulk layer of the pellet beyond the laser and X-ray penetration depth is calculated as in Eqn. 4.15 with by replacing the parameters of air with that of the β-phase.

If we assume that the thickness of Ti_3O_5 bulk layer is 10 µm and majority of the nodes are in β phase,

$$R_{i,bulk} = \frac{\Delta x}{k_{\lambda/\beta} A}\left(\frac{1}{2} + 10^3\right) \approx 1000 \frac{\Delta x}{k_{\lambda/\beta} A} \tag{4.17}$$

Therefore, $c_{i,bulk}$ is of the order of 10^{-5}. Table 4.1 summarises the values of the coefficients considered in the calculation.

coefficient	simulation value	value from thermal conductivities (WK^{-1})
$c_{i,i}^{\lambda\lambda}$	1e-2	2e-9
$c_{i,i}^{\beta\beta}$	2e-2	4e-9
$c_{i,i}^{\beta\lambda}$	1.35e-2	2.7e-9
$c_{i,j}^{\lambda\lambda}$	1e-3	2e-10
$c_{i,bulk}^{\beta}$	1e-5	4.2e-14
$c_{i,air}^{\beta}$	1e-8	2.5e-15

Table 4.1 – The estimated values of the different thermal exchange coefficients that have been considered in the simulation as calculated from the thermal conductivities of two phases of Ti_3O_5 and air.

4.4 Results from the model based on the choice of initial conditions

Different initial conditions with different set of thermal exchange coefficients have been tested for the heat diffusion model. It is important to mention here that the initial state of the simulations is the state achieved in the system after the strain propagation. The amount of transformation within the first crystallite layer after the propagation of the strain wave was estimated to 30% for an pump fluence of 0.5 mJ/mm^2 in the previous study[55]. We have also observed that the transition is favoured when the pump pulse is along *ab* plane[84] showing an optical anisotropy of the randomly oriented crystallites in the pellet. These observations lead to a hypothesis that all crystallites with a favourable orientation gets fully transformed and the rest remains as the β-phase after the strain wave has propagated in the system. The initial conditions are chosen to get initial transformation amount(number of λ-nodes) as close as possible to this observation for the systems.

4.4.1 Excitation of the whole grain within the first layer

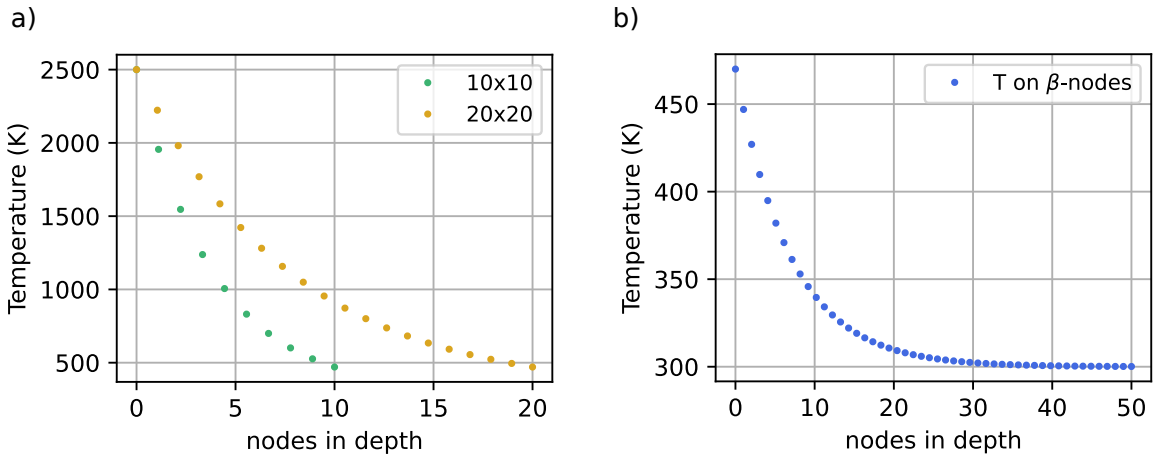

Figure 4.20 – a) Temperature distribution on the λ-nodes of the two different crystallites 10x10 and 20x20. The temperature is 2500 K on the photo-excited surface of the pellet and 470 K at the end the strain-transformed domains in depth. b) Temperature distribution on the β-nodes.

In this case, we assume that upon the strain propagation, there can be a collective excitation of the whole crystallite. The temperature distribution on the λ-nodes within a crystallite follows an exponential decrease in depth with a surface temperature of 2500 K. The rate of temperature decay have been chosen differently in the smaller and bigger crystallite such that at the grain boundary the temperature is 470 K. The temperature

profiles on the λ node for different grainsizes have been shown in Fig. 4.20a and that on the β nodes in Fig. 4.20b.

The dynamics in this case of whole crystallite transformed have been observed for different set of thermal exchange coefficients across the grains and grain boundaries.

Dynamics with B = 1 The intragrain and intergrain thermal exchange coefficients are kept equal. This means there is no effect of polycrystallinity in the dynamics. All other coefficients like $c_{i,air}$ and $c_{i,bulk}$ have the same values as in Table 4.1.

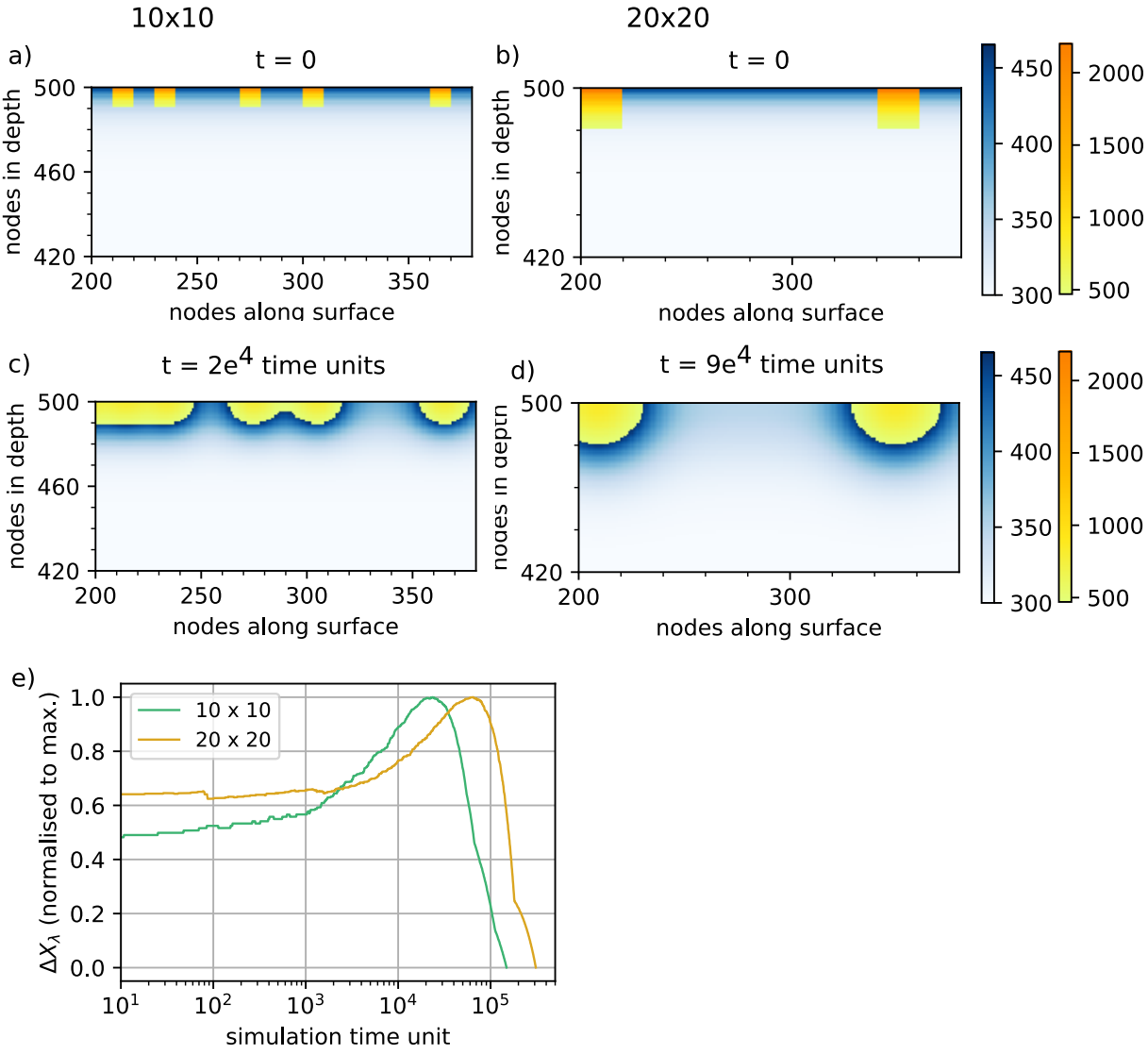

Figure 4.21 – a) to d)Spatial distribution of the λ and β phases at the initial state (a and b) and at the peak position (c and d) respectively for grainsizes 10x10 and 20x20. e) The evolution of the λ phase fraction with delays. The fraction is normalised to the maximum value to compare the peak shift only.

Dynamics with B = 10: The large ratio B between the intergrain and intragrain coefficients will make the heat diffusion slower across the grain boundaries compared to within the grains. All other coefficients like $c_{i,air}$ and $c_{i,bulk}$ have the same values as in Tab. 4.1.

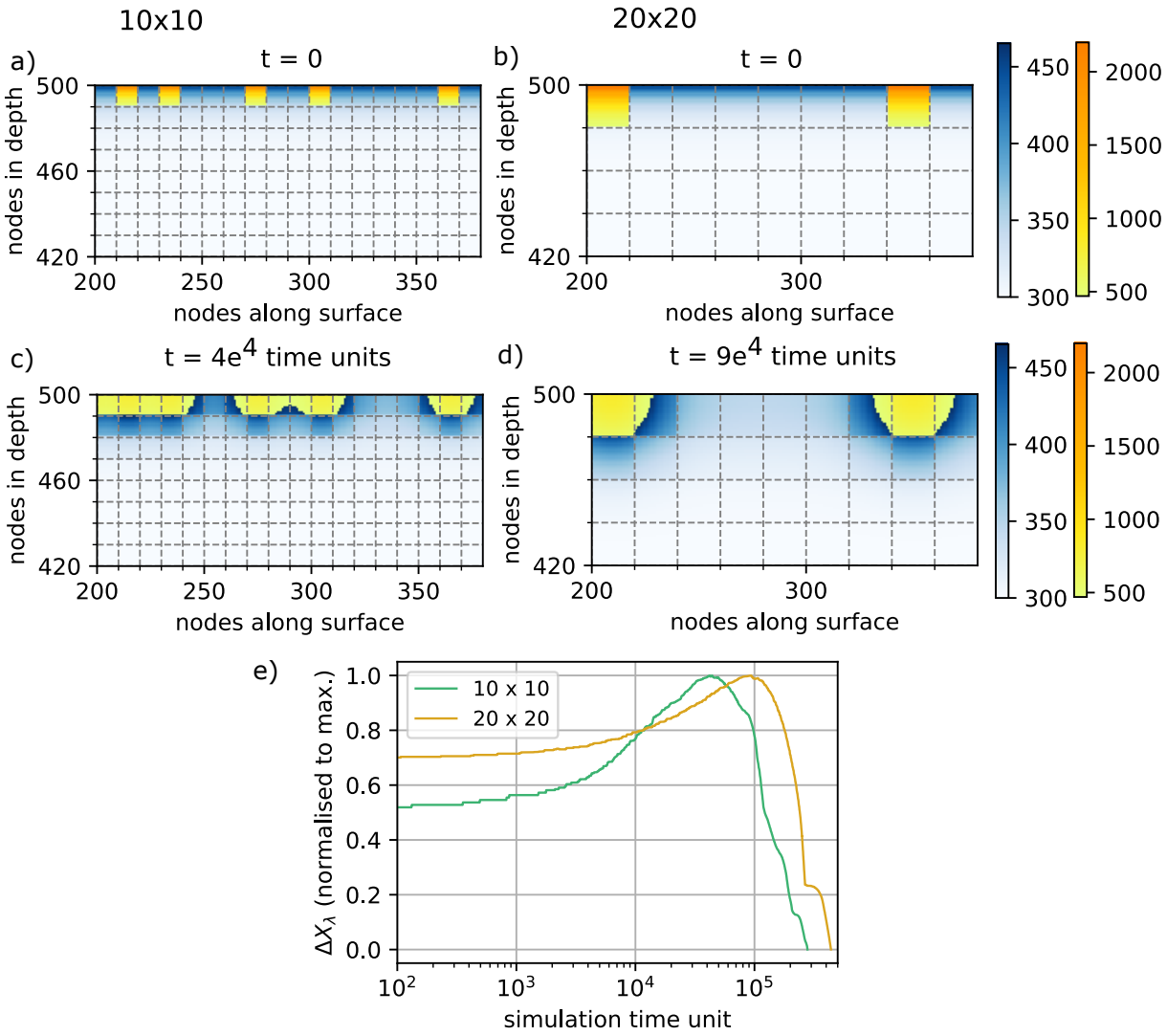

Figure 4.22 – a) to d)Spatial distribution of the λ and β phases at the initial state (a and b) and at the peak position (c and d) for the grains sizes 10x10 and 20x20 respectively. The dashed lines indicate the grain boundaries. e) The evolution of the λ phase fraction for both the grain sizes with delays. The fraction is normalised to the maximum value to compare the peak shift only.

For any set of parameters chosen, we see that the relative peak shift is such that the bigger crystallite relaxes later than the smaller crystallite. This trend is opposite to that have been observed in the experimental data.

4.4.2 Excitation in the form of domains on excited surface but limited by laser penetration depth

The initial pattern assumes an excitation of a an entire crystallite on the surface with a limitation in depth by the laser penetration. The temperature distribution on the strain transformed λ-nodes within a crystallite follows a exponential decrease in depth with a surface temperature of 2500 K and is same for both the smaller and bigger crystallites. The temperature profiles on the λ nodes is shown in Fig. 4.23e and that on the β is kept the same as in Fig. 4.20b.

The trend in the peak shift is opposite to what has been observed in the experimental results.

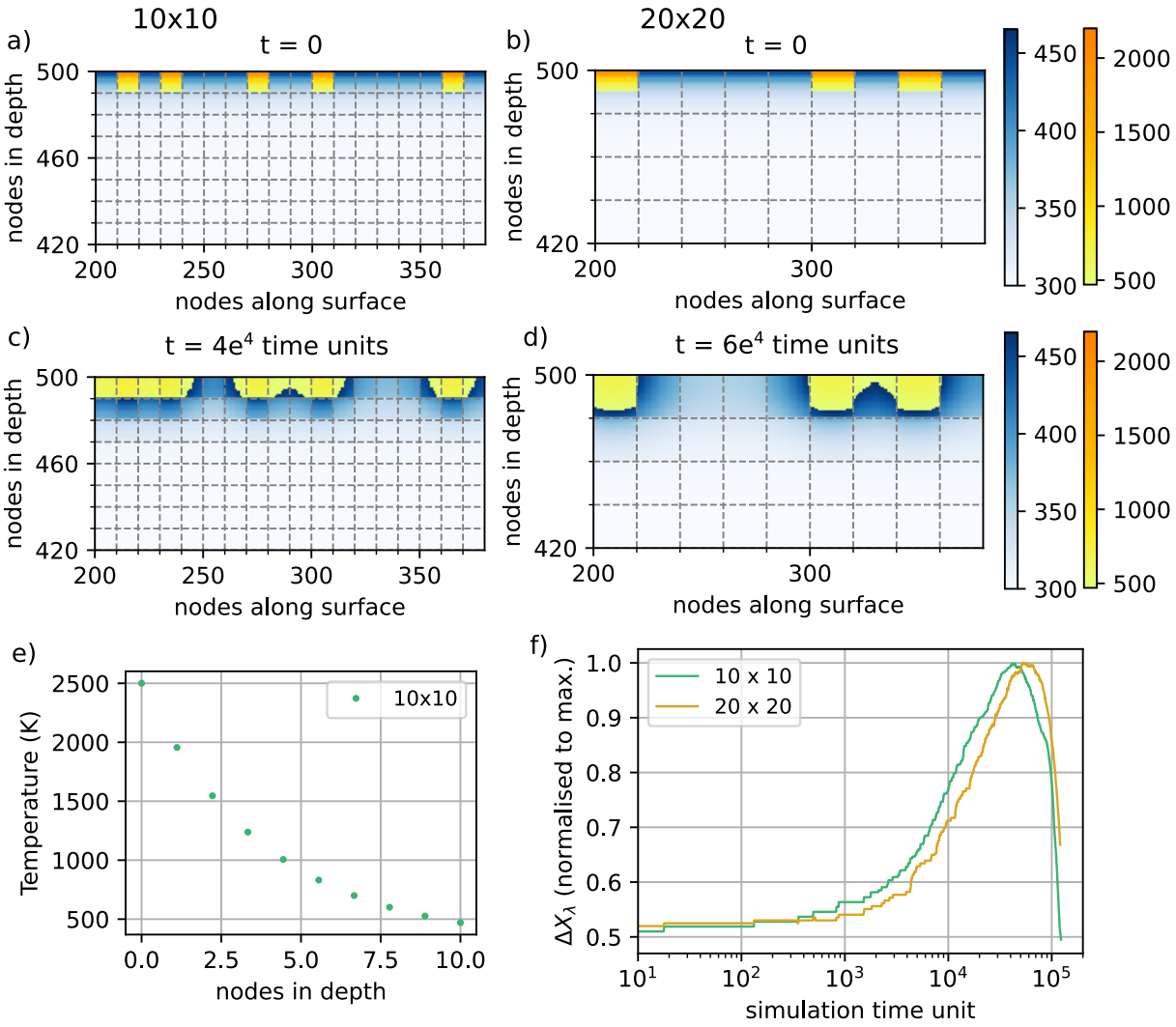

Figure 4.23 – a) to d)Spatial distribution of the λ and β phases at the initial state (a and b) and at the peak position (c and d) for the grains sizes 10x10 and 20x20 respectively. e) The temperature profile on the λ nodes at the initial state. The same profile is used for both the grain sizes. f) The evolution of the λ phase fraction (normalised to the maximum value) for both the grain sizes with delays.

4.4.3 Excitation in the form of domains limited by the laser penetration depth

In this case, the excitation is in the form of domains of few nodes on surface and limited in depth by the laser penetration. The temperature profiles on the λ nodes is shown in Fig. 4.23e and that on the β is kept the same as in Fig. 4.20b.

There is a relative peak shift between the ΔX_λ for the two grain sizes. However, the relative λ-phase content at the peak with respect to the initial λ-phase content remain exactly the same for the two sizes, which is not the behaviour observed experimentally.

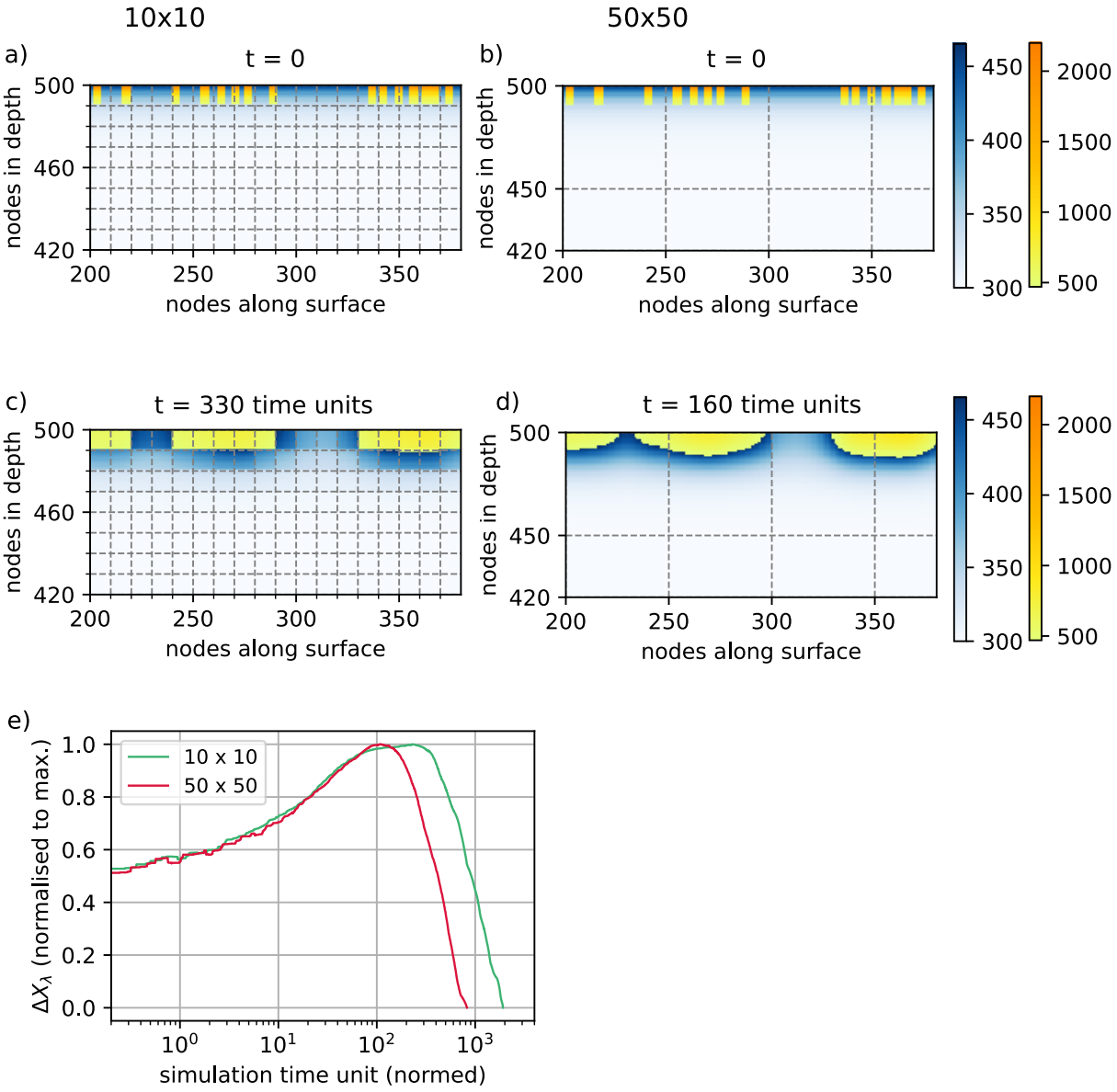

Figure 4.24 – Spatial distribution of the lambda phase domains at the initial state of the 500x500 system with a) 10x10, b) 50x50 grainsize. c and d shows the state of the system at the peak position for the two grains respectively. e) Evolution of the λ-phase fraction (normalised to its maximum value) with delays for the two different grain sizes. The simulation time unit is also normed to the peak position of the experimental dynamics of "flake-type" Ti_3O_5

4.4.4 Domains limited by the crystallite size

The initial temperature on each filament are defined exponentially decreasing with depth in the crystallite from the surface temperature of 2500 K as shown in Fig. 4.25e.

Dynamics with B = 1: In this condition, there is no difference between the thermal exchange coefficients inside the crystallites and across the grain boundaries. We observe only the effect of initial patterning in the system. Fig. 4.25f shows that there is a relative peak shift between the grain sizes of 10x10 and 50x50. However, the magnitude of shift is much smaller compared to that noticeable in the experimental curves.

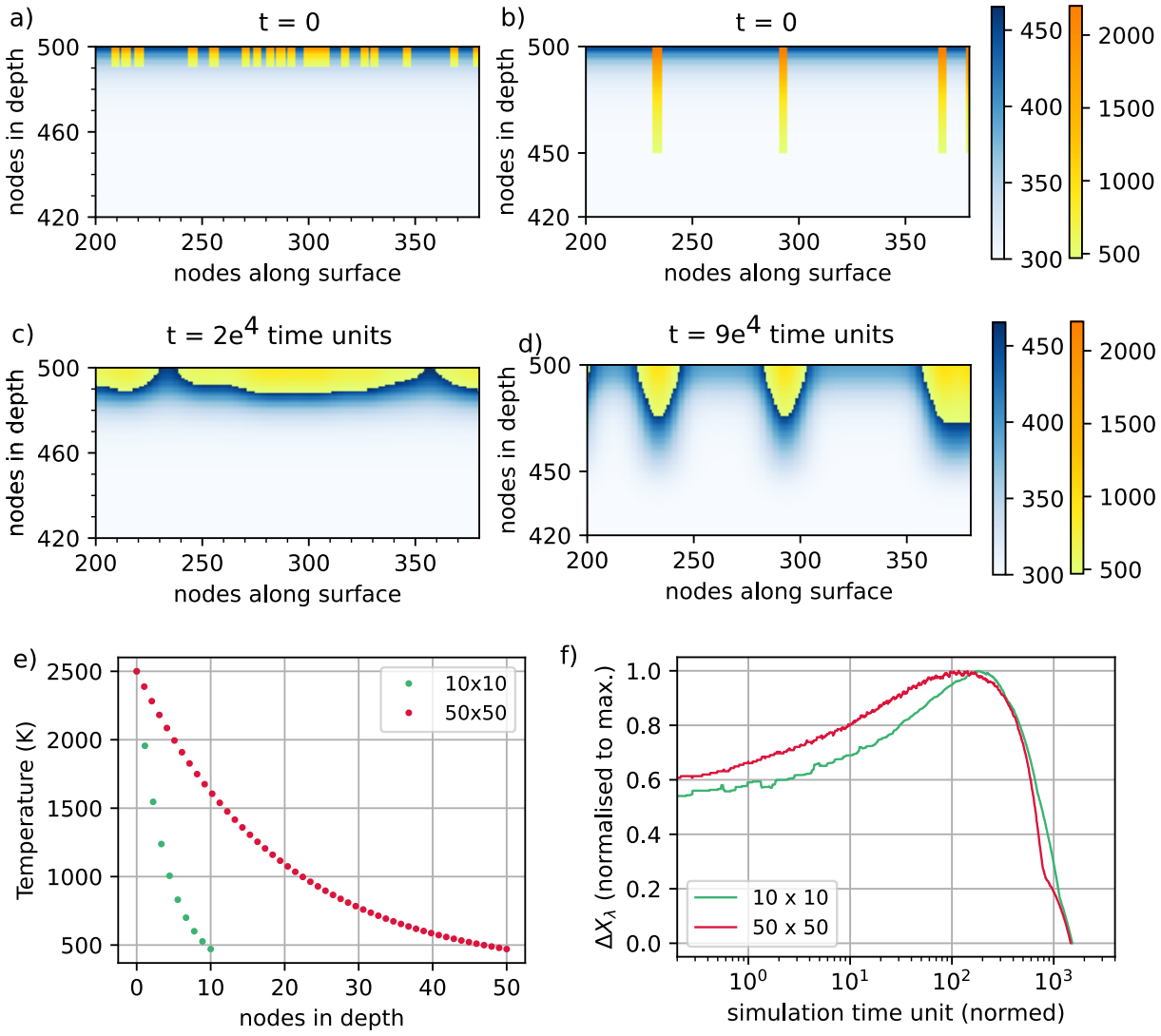

Figure 4.25 – a) to d)Spatial distribution of the λ and β phases at the initial state (a and b) and at the peak position (c and d). e) The temperature profile on the λ nodes at the initial state. f) The evolution of the λ phase fraction (normalised to the maximum value) for both the grain sizes with delays. The simulation time unit is also normalised to match the peak position of the experimental dynamics of "flake-type" Ti_3O_5

Dynamics with B = 10: The large ratio B between the intergrain and intragrain coefficients will make the heat diffusion slower across the grain boundaries compared to within the grains.

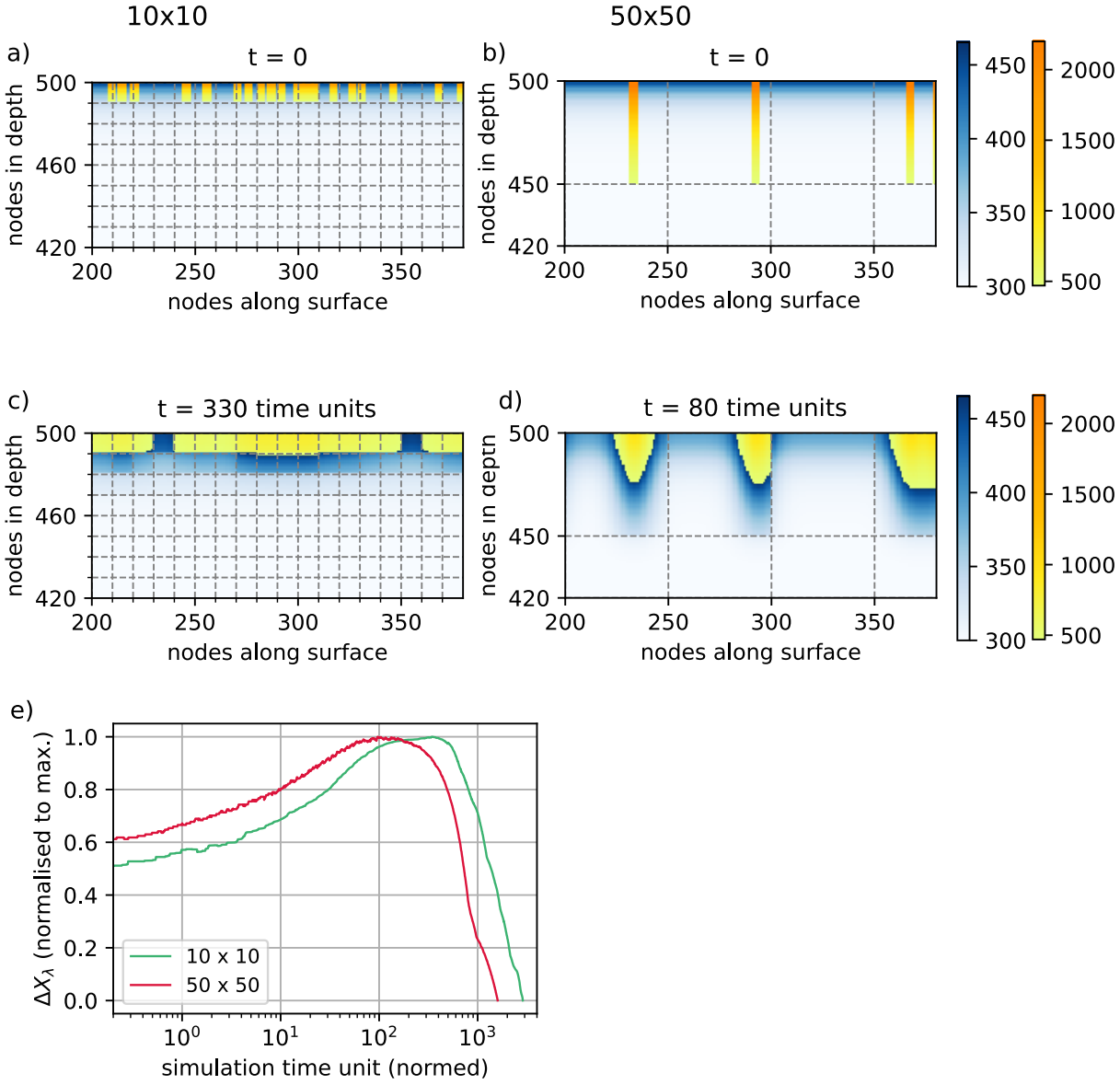

Figure 4.26 – a) to d)Spatial distribution of the λ and β phases at the initial state (a and b) and at the peak position (c and d) for the grains sizes 10x10 and 50x50 respectively. e) The evolution of the λ phase fraction (normalised to the maximum value) for both the grain sizes with delays. The simulation time unit is also normalised to match the peak position of the experimental dynamics of "flake-type" Ti_3O_5

The evolution of λ phase fraction have been extracted for the two different grainsizes:

10x10 and 50x50. The λ-phase fraction reaches its maximum at different simulation time units (about 300 numerical unit time in the smaller system and 80 numerical unit time in the bigger system) and the trend in peak shift is in the same order as our experimental results. So, the difference in the intra- and inter-grain coefficient along with the initial strain transformed domains results in the experimentally observed peak shift as well as the variation in the relative amplitude of this peak. A more complicated shapes of phase separation were not tried.

4.5 Conclusion

In this study the experiments were set up in order to explore the effect of experimental parameters on the photo-induced transition in Ti_3O_5 pellets of different crystallite sizes. In any situation, the overall dynamics reveal an early step on the picosecond timescale, followed by a slower transformation peak at about 10 - 100 nanosecond and a relaxation on microsecond timescale. The first step is convoluted with X-ray pulse duration($\sim$ 100 ps), but its origin and dynamics are known[55]. So in my thesis, I have focused on the later dynamics on the nanosecond timescale. The magnitudes of observed changes are not directly comparable between the three samples, because each experiment was subject to uncertainty on pump-probe spatial overlap. However, the ratio of the thermal transformation peak to the early plateau, and the relative shifts of the peak with delays can be reliably compared.

One conclusion from the TR-XRD measurements is that the larger the crystallite size, the faster it takes to reach the maximum transformation through heat diffusion. Besides, the fact that this peak appears at the same time delay for each type of Ti_3O_5 pellet irrespective of the incident laser wavelengths indicates that the dynamics is independent of the laser penetration depth. Another striking observation is that the nature of transition at the strain transformed part is quite different from that due to heat diffusion.

Using a rather simple heat diffusion model based on finite difference method, the trends of thermal transition peak in different samples have been successfully reproduced. The initial state of the model has been assumed to be that of a system after strain propagation. It has been observed that the results of the model are strongly dependent on the choice of the initial conditions. However, the initial condition that best reproduces the experimental trend is the one with the initial state containing randomly distributed and filament shaped domains of the λ-phase in the otherwise β-phase system. The filaments have lateral size scaling with laser excitation and length of the crystallite. The exact shape of such filament was not tested, because for simplicity of calculation we retained a regular one. Since the crystallites are randomly oriented in the polycrystalline powder, and there is acoustic impedance mismatch at the grain boundaries, we assume that the phase boundary for this early mechanism is located at the end of the grain. The filaments, or rather the phase front, do not end randomly within the crystallite or spill onto the neighbouring grains.

The dynamics span very different time-scales hence they obey different regimes, coherent or thermal. But, we can conclude that the outcome of the early dynamics, i.e the fast transition driven by propagating strain, has a strong effect on the slower transition. A 2D model was applied to rationalise this, so direct comparison with the experimental results should be done with caution. Nevertheless, we have been able to reproduce and explain the most striking experimental feature: the transformation dynamics on the nanosecond time-scale in a nano-structured sample.

Chapter 5

Photo-induced insulator-to-metal transition in V_2O_3 thin films

In the previous chapter, we have studied the photo-induced phase transition in a correlated electronic system Ti_3O_5, which exhibits a significant volume increase during the semiconductor-metal transition, followed by nanosecond timescale structural dynamics. In this chapter, we have explored the strain wave mechanism in another correlated system : V_2O_3. Unlike Ti_3O_5, V_2O_3 undergoes volume contraction during its insulator-metal transition, resulting in the establishment of compressive stress upon laser irradiation. In addition to the volume change, the AFI-PM transition in V_2O_3 is also associated with symmetry breaking. Our objective is to investigate whether compressive strain is as effective as tensile strain in establishing long range electronic and structural order in the system and the role of symmetry breaking in it.

This chapter focuses on exploring the out-of-equilibrium states that emerge following photo-excitation with femtosecond laser pulses on V_2O_3 thin films, by performing time-resolved X-ray diffraction. The TR-XRD experiments were carried out at the FemtoMAX beamline, MAXIV Laboratory and ID09 beamline, ESRF in collaboration with the research group from IMN, University of Nantes.

5.1 State of the art

The rich phase diagram of V_2O_3 often translates into rich non-equilibrium behavior. Several studies have been reported in the past years on the photoinduced phase transition in V_2O_3 with the help of different techniques. Abreu et.al.[1] [2] have studied the photo-induced transition of epitaxial V_2O_3 thin films with optical pump and THz probe pulse. It was observed that the insulator to metal conductivity dynamics depend on the incident laser fluence and temperature. A threshold laser fluence was also observed below which no transition was observed in the films.

In 2018, Singer et.al.[95] studied the insulator metal transition in epitaxial films of V_2O_3 using the time resolved X-ray diffraction and microscopy experiments. The transition was observed to have an out-of-equilibrium pathway.The results show that the coherence length of the ferroelastic domains increase within about 2 ps however, the transition from AFI to PM phase occurs over a time period of 100 ps.

Another study[80] on thin films of V_2O_3 showed the growth of the monoclinic domains, upon laser excitation, using photo-emission electron microscopy (PEEM) and tr-

spectroscopy measurements. All of these studies have claimed a nucleation and growth of the nanodomains of the metallic phase in the otherwise insulating AFI phase.

However, these studies were performed at a temperature close to the transition temperature of the AFI to PM phase, so we cannot exclude the fact that the transition is mostly thermal in origin.

5.2 Steady-state study of the pressure induced insulator to metal transition at low temperature

To achieve an understanding of the non-equilibrium states arising upon photo-excitation, it is crucial to posses a clear picture of the equilibrium phases attained through transitions under pressure or temperature (phase diagram in Fig. 3.12). The thermal transitions in V_2O_3 have been studied extensively[56][57] and the evolution of cell parameters across the AFI to PM transition is shown in Fig. 5.1. However, the structural distortions around transition lines in pressure are not well described in literature.

During AFI-to-PM transition under temperature, the lattice parameter c decreases with an increase of a and b parameters, inducing an overall unit cell volume contraction of $\Delta V/V \sim 1.5\%$ [56]. In addition to this, there is also thermal dilation in the high temperature PM phase. No thermal dilation was detected in the low temperature AFI phase.

A temperature-volume phase diagram (Fig. 5.1d) was constructed[56] using the fact that the effect of pressure on the volume jump at the AFI-PM transition is equivalent to the Cr-doping of V_2O_3. The shaded area in the figure is the predicted volume change at the transition at different temperatures. Around 10 K, the volume change $(-\Delta V/V)$ during the phase transition from AFI to PM phase is estimated to be $\sim$ 3% which is twice larger than the volume change upon thermal transition at ambient conditions.

In order to understand the effect of pressure on the lattice parameters, we performed X-ray diffraction measurements at low temperature (far from transition under ambient pressure) at the CRISTAL beamline, SOLEIL synchrotron radiation facility using the Diamond Anvil Cell setup (Section 2.6.3).

XRD images were collected from single crystals of V_2O_3 at various pressures from ambient pressure(0.1 MPa) to $\sim$ 5 GPa at a temperature of 20 K. The 2D images at 0.68 GPa (below the transition) and 4.5 GPa (after the transition) have been shown in Fig. 5.2a and b respectively.

Fig. 5.2c shows the shift in (110) peak for the two pressure points after azimuthal integration. The q of this peak at pressure 0.68 GPa and 4.5 GPa are 2.5137 $Å^{-1}$ and 2.5335 $Å^{-1}$ respectively. Therefore the volume change upon transition can be estimated as described below.

The volume of a hexagonal unit cell is :

$$V = \vec{a}.\vec{b} \times \vec{c} = a^2 c \, sin60^\circ \tag{5.1}$$

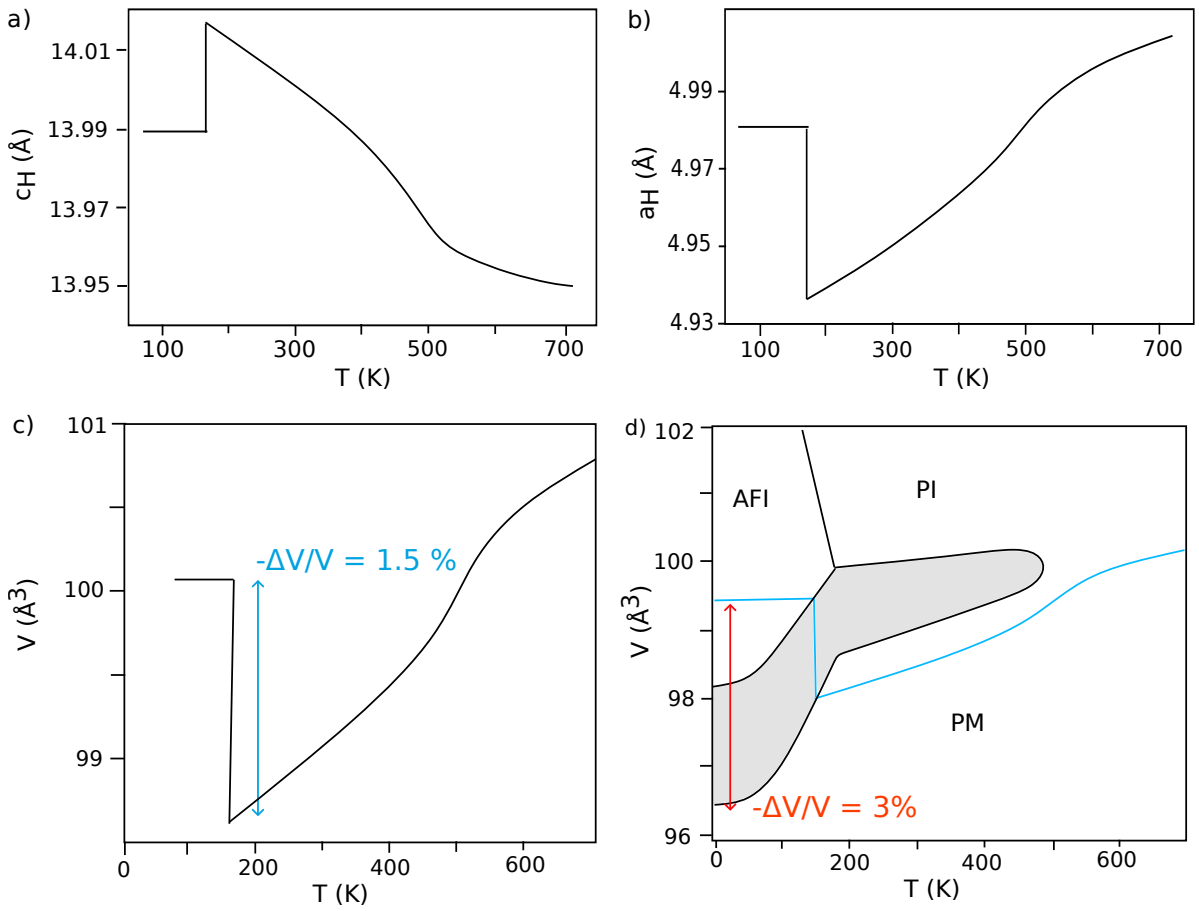

Figure 5.1 – Temperature evolution of the cell parameters a) $\vec{c}$, b) $\vec{a}$ and c)unit cell volume. d) The predicted volume phase diagram of V_2O_3. The thermal pathway is shown by the blue line and the volume change in the compression pathway is shown with the red arrow. The grey shaded area is a forbidden area in the phase diagram (Adapted from [56])

Therefore, change in volume of a hexagonal lattice:

$$\frac{\Delta V}{V} = 2\frac{\Delta a}{a} + \frac{\Delta c}{c} \tag{5.2}$$

In the hexagonal unit cell, the relation between d-spacing d and the miller indices h, k and l with cell parameters a and c is :

$$\frac{1}{d^2} = \frac{4}{3}\frac{h^2 + hk + k^2}{a^2} + \frac{l^2}{c^2} \tag{5.3}$$

Therefore using h = 1, k = 1 and l = 0 for the peak (110), we get d-spacing as:

$$d = a/2 \tag{5.4}$$

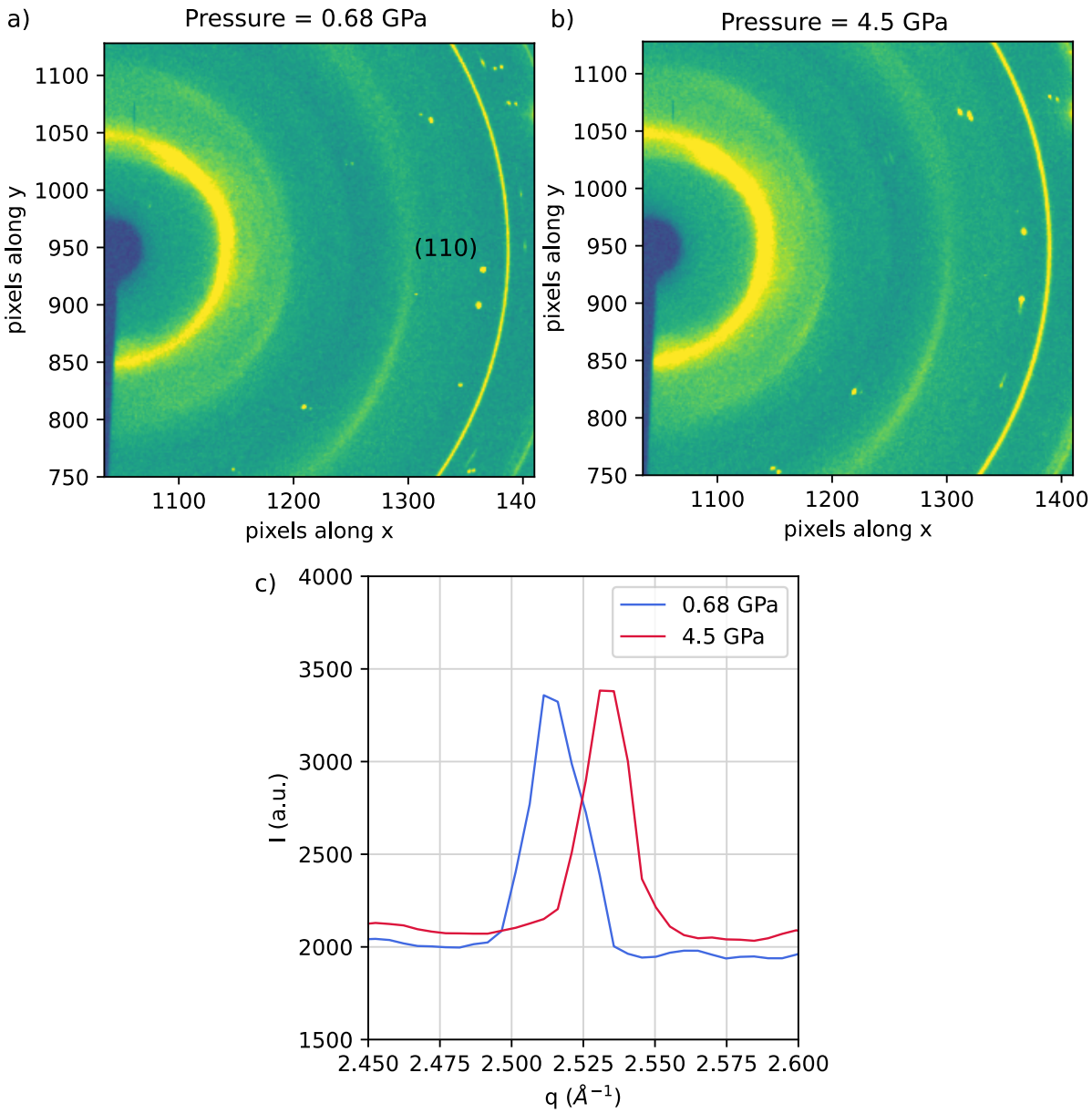

Figure 5.2 – Single crystal diffraction images at the pressure of a) P = 0.68 GPa and b) P = 4.5 GPa showing the peak (110). c) The azimuthal integrated patterns of two diffracted images showing the shift in peak (110).

Using Eqn. 5.4 and the fact that d = $\frac{2\pi}{q}$,

$$\frac{\Delta V}{V} = 2\frac{\Delta a}{a} = -2\frac{\Delta q}{q} \tag{5.5}$$

Therefore a volume change of 1.57% is estimated from the positions of (110) peak before

and after the transition as:

$$\Delta V/V = -2\frac{2.5137 - 2.5335}{2.5237} = 0.0157 \tag{5.6}$$

Data reduction was performed using the lattice parameters of the AFI phase for both states before and after transition with CrysalisPro software[23]. However, it is very difficult to refine the structures from single crystal diffraction images. First of all, the orientation of the crystal remains fixed inside the Diamond Anvil Cells(DAC). Secondly, the opening angle of the DAC is small, allowing few Bragg peaks to be detected in the diffraction images. So, the XRD measurements were also done on polycrystalline powder of V_2O_3. The diffraction images at two pressures P = 0.685 GPa in the AFI phase and P = 4.01 GPa in the PM phase are shown in Fig. 5.3a and b respectively. As we have observed from the simulated diffraction patterns in Chapter 3 (Fig. 3.14), the two or three peaks in the AFI phase merge into single peaks in the PM phase. This is also evident from the 1D diffraction patterns obtained by azimuthal integration as in Fig. 5.3c.

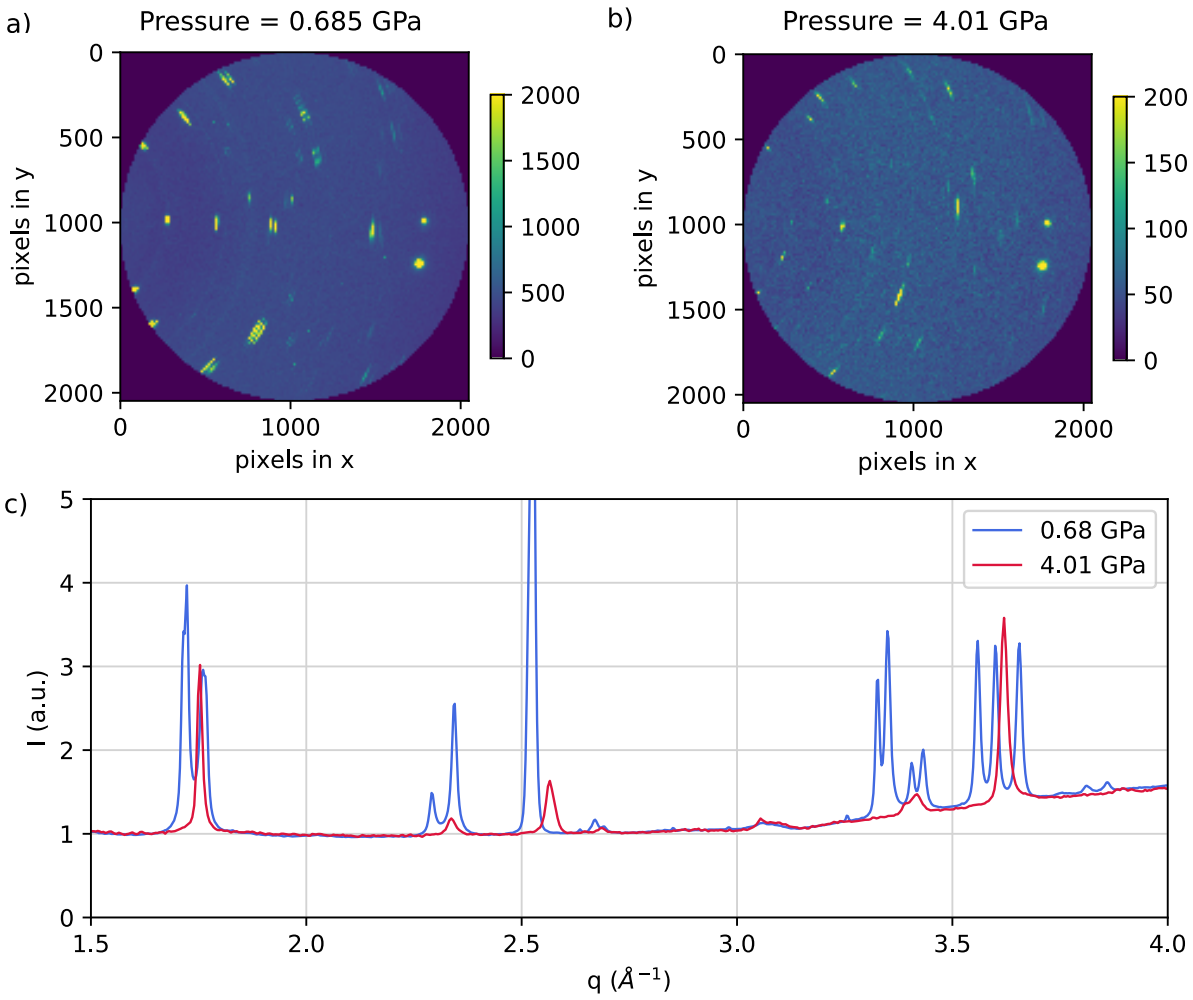

Figure 5.3 – The diffraction images of the powder sample at two different pressure a) P = 0.685 GPa and b) P = 4.01 GPa. c) The 1D diffraction patterns as obtained at the two pressure points showing distinct features in the AFI and PM phases as in Fig. 3.14

The values for cell parameters a, b and c and the unit cell volume, obtained after the refinement of the powder patterns, are plotted in Fig. 5.4. The evolution of the unit cell volume and b parameter have been plotted reliably from the single crystal data. The lattice parameters exhibit a discontinuity at the transition pressure of $\sim$ 2.3 GPa. The change in unit cell volume at the transition from AFI to PM phase at a constant temperature of 20 K $\sim$ 1.5% as can be observed from Fig. 5.4a.

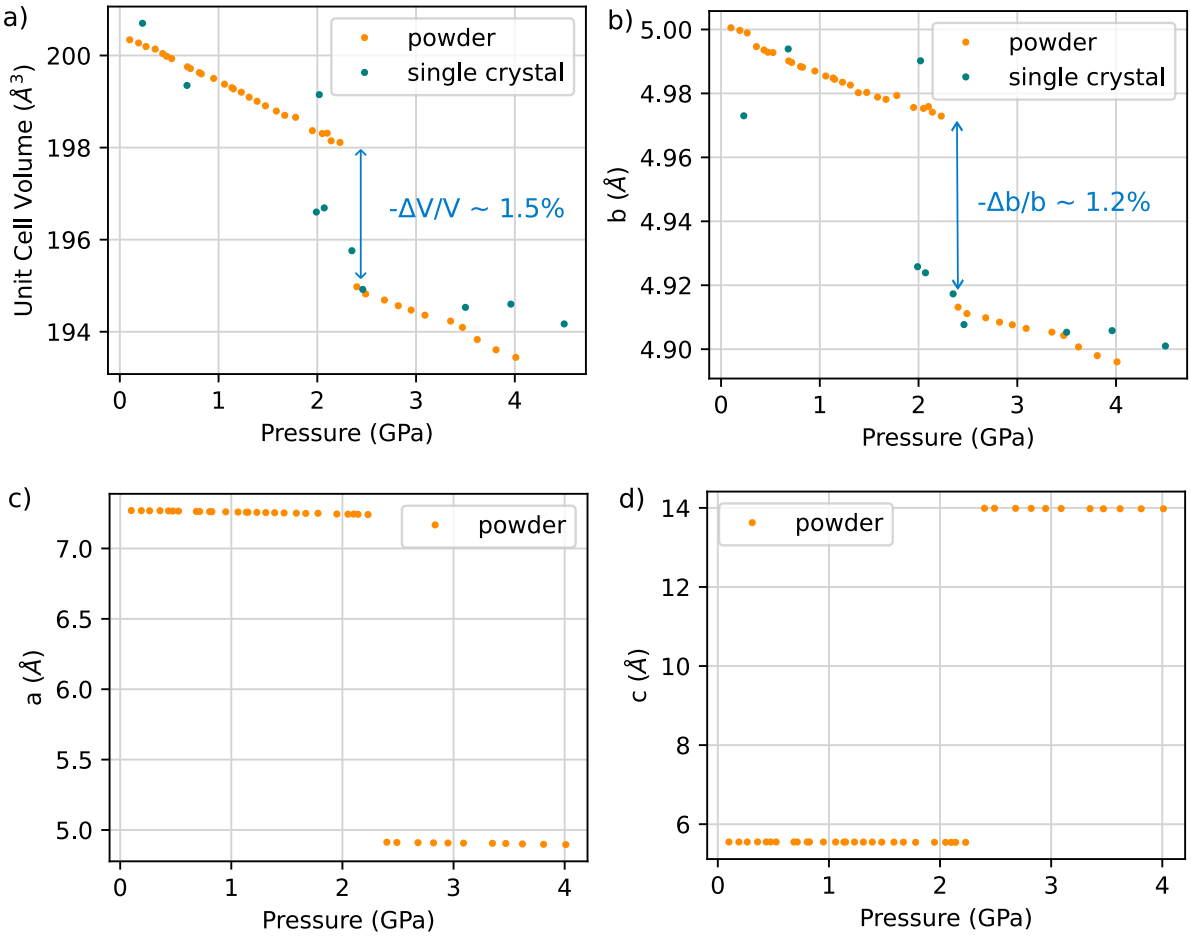

Figure 5.4 – Evolution of the cell parameters a) unit cell volume, b) lattice parameter b, c) a and d) c with pressure. The transition pressure is about 2.3 GPa with the low pressure phase in AFI and high pressure phase in PM.

5.3 Dynamics of the photo-induced structural changes in V_2O_3 thin films with TR-XRD measurements

To explore whether strain waves can facilitate the propagation of the insulator-to-metal phase transition upon photo-excitation in the correlated electronic system of V_2O_3, TR-XRD measurements were conducted on the polycrystalline thin films. The measurements were performed in the reflection geometry with configurations as described in Chapter 3.

Fig. 5.5 and 5.6 show the 1D diffraction patterns from the 100 nm thin film of V_2O_3 measured with the pink beam at FemtoMAX and monochromatic beam at ID09 respectively (Table 2.3). The diffraction patterns from the 270 nm thin film measured with the pink beam at FemtoMAX have been plotted in Fig. 5.7. The subfigures a) show the absolute patterns and b) show the differential patterns calculated by subtracting the "laser-off" pattern from all patterns at several delays.

From the absolute patterns, it can be observed that some of the peaks, such as (104), (012) and (116), show narrowing because of the merging of peaks at positive delays, indicating the symmetry change from AFI to PM phase. Furthermore, there is an overall shift of peaks to higher q values, suggesting a contraction in the unit cell volume. The peaks (110) and (300) show only a shift in q value due to volume contraction and hence the differential signal is bipolar in nature(Fig. 5.5c). A tripolar signal is observed for the peaks showing narrowing, with an asymmetry because of the overall peak shifts toward lower q.

It is important to note here that the significant background signal in Fig. 5.6a arises from the diffraction of ice, formed by the condensation of water vapour on the cold ($T \sim 85$ K) samples. Nevertheless, the signal from ice does not affect the photo-induced signal from V_2O_3 around the peaks (110) and (116) on which we follow the signal.

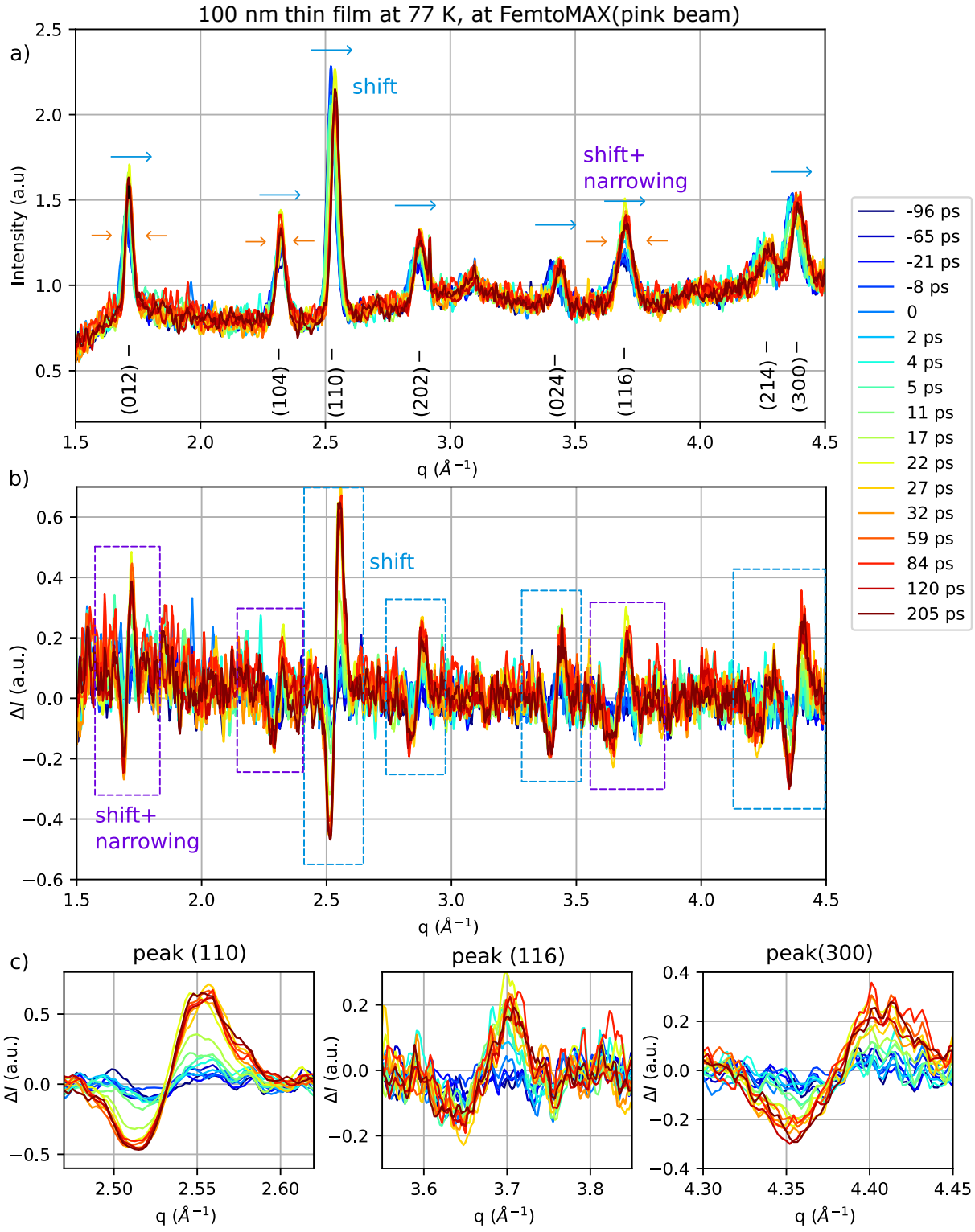

Figure 5.5 – a) The 1D diffraction patterns and b) the differential signal, calculated with respect to the "laser-off" pattern, are plotted for different delays with a pump fluence of 11 mJ/cm^2 at temperature of 77 K. c) A zoomed differential signal on the three peaks (110), (116) and (300) (from left to right) showing the bipolar signal on (110) and (300) and asymmetric tripolar signal on (116).

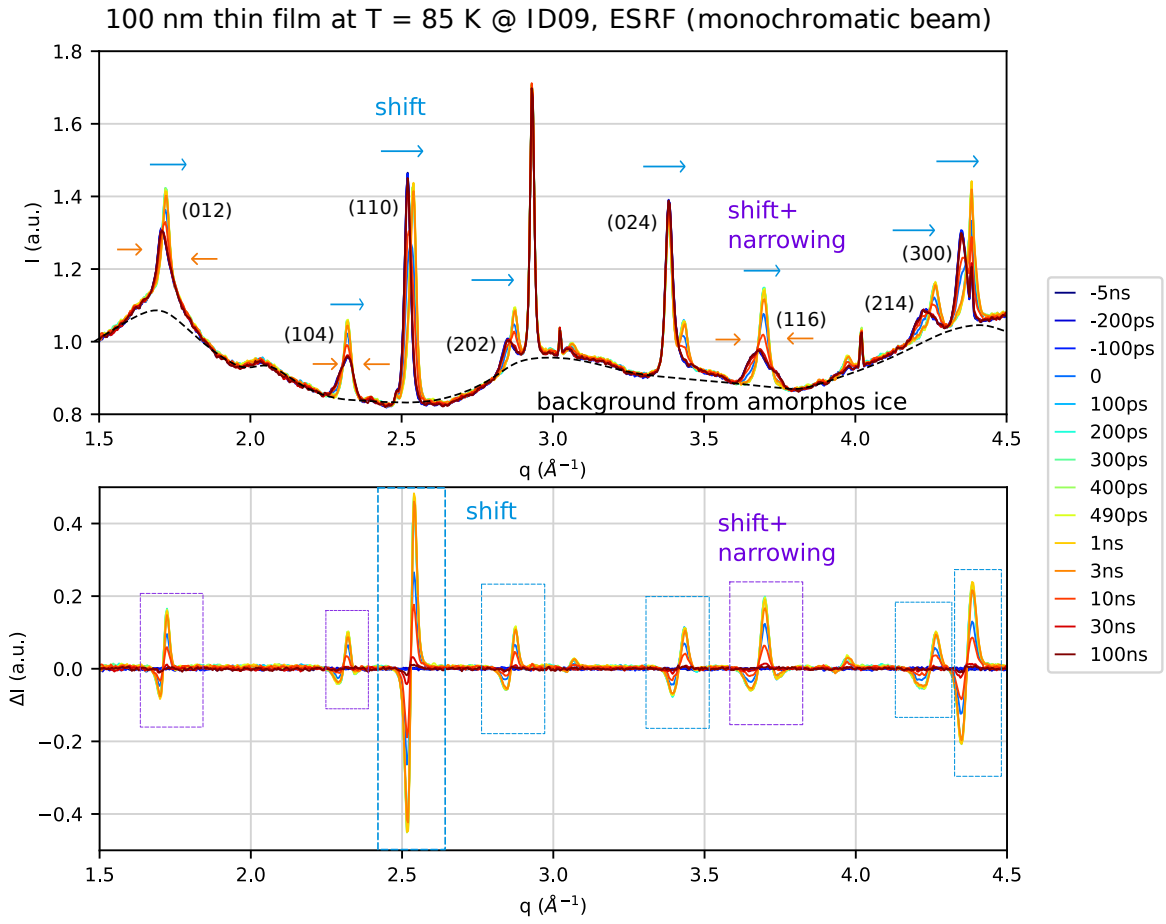

Figure 5.6 – (top) The absolute patterns of TR-XRD on thin film of thickness 100 nm measured at 85 K using a X-ray monochromatic probe beam. The background signal is mostly from amorphous ice condensed on the thin film surface.(bottom)The differential signal plotted from the absolutes by subtracting the reference pattern at -5 ns.

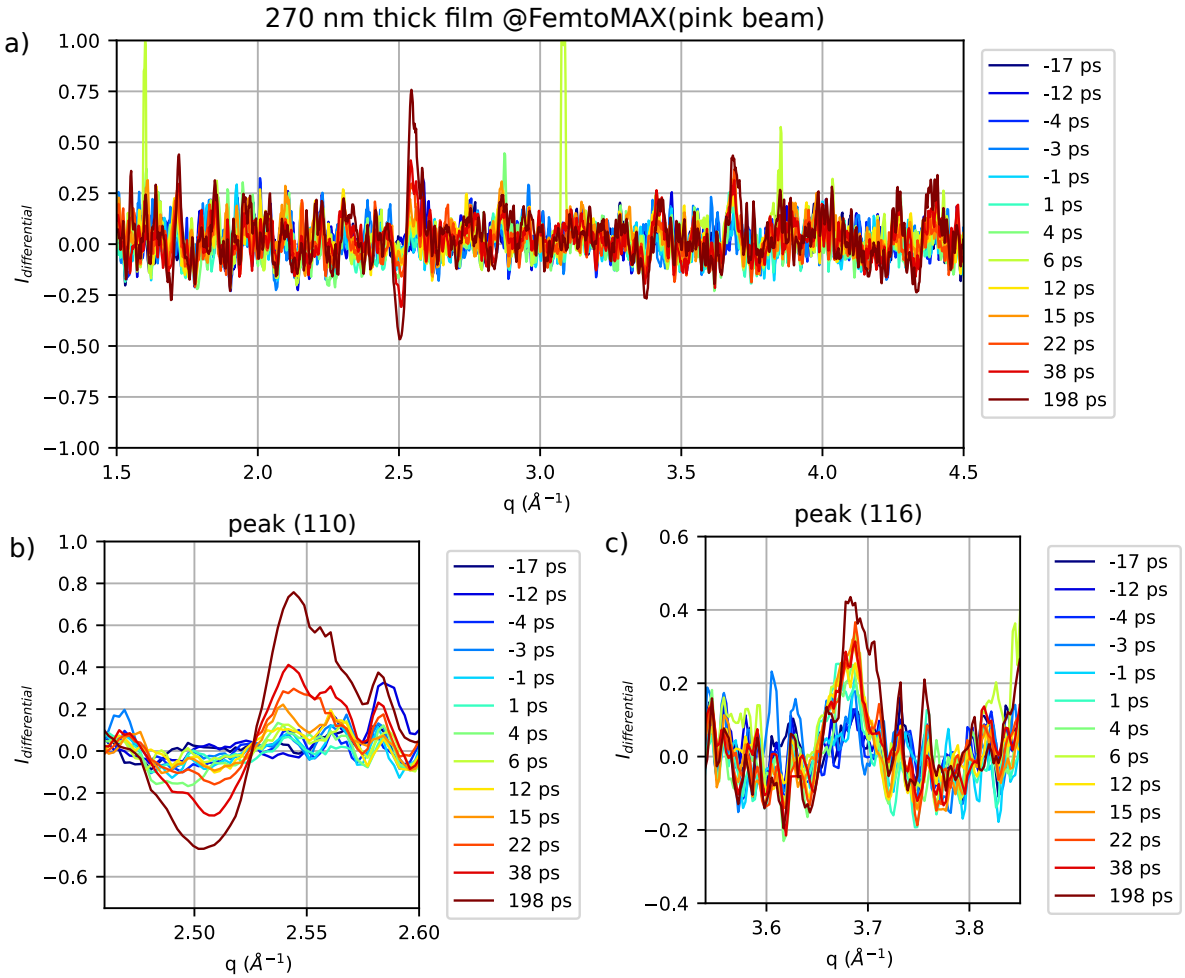

Figure 5.7 – a) The differential signal measured on the 270 *nm* thick film of V_2O_3 with a laser fluence of 11 mJ/cm^2 b) A zoom on bipolar differential signal of the peak (110) and c) tripolar signal of the peak (116).

The integrated values of the absolute differential signal are calculated at different delays to show the transient changes with time. The overall changes in the signal for the peak (110) are shown in Fig. 5.8. Upon photo-irradiation, there is a sharp increase of the signal around time zero. Around 100 ps (the time resolution at the ID09, ESRF), the signal already saturates and remains constant till about 3 ns. Following this, a subsequent phase of relaxation occurs within 100 ns.

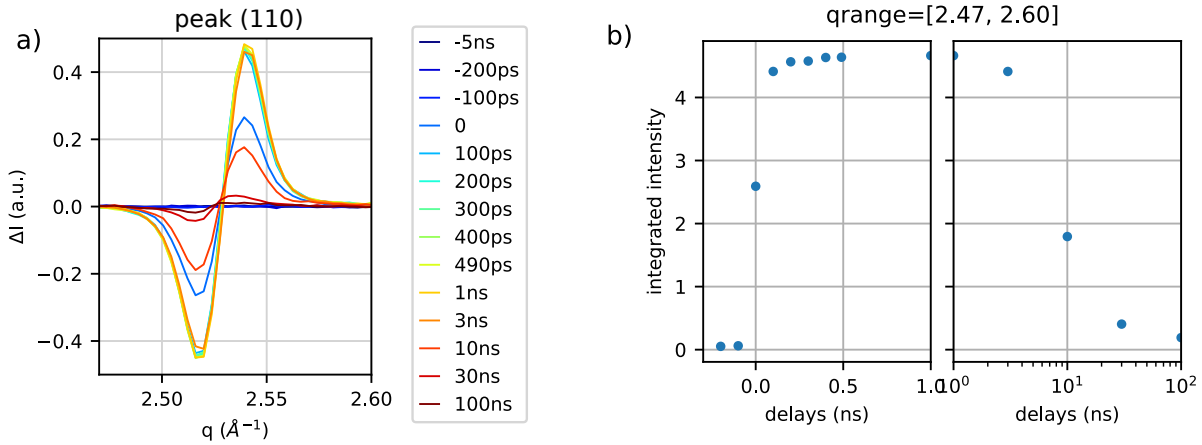

Figure 5.8 – a) Differential signal of the peak (110) for the 100 nm thin film of V_2O_3. b) The integrated signal of peak (110) plotted as a function of delays giving an overall photo-induce dynamics.

With a better time resolution of a few ps at FemtoMAX, we find that the increase of the photo-induced signal occurs much earlier than 100 ps. The delay, in which signal reaches its maximum value depends a lot on the thickness of the thin films. The integrated signal is plotted in Fig. 5.9 for peaks (110), (300) and (116) for both 100 nm and 270 nm thick films of V_2O_3.

In case of 100 nm thin film, the observed transient changes start around time zero and reach maximum values around 25 ps for both the peaks of (110) and (300) and then saturate. Notably, the peak (116) exhibits a slightly different behavior, with the changes saturating earlier than the other two peaks.

Comparable dynamics are observed in the transient signal for the 270 nm thick V_2O_3 film. The integrated signal for peaks (110) and (300) reaches saturation at a later delay of about 50 ps. The change in peak (116) reaches saturation much earlier.

These observations shed light on the temporal evolution of the transient changes upon photo-excitation in the thin and thick films, highlighting the distinctions in their response across different Bragg peaks.

One feature of the tripolar signal is that it is asymmetric. This is because the peaks that show symmetry breaking, for example (116), show both peak shift and narrowing upon transition. Therefore, the integrated differential signal takes into account the contributions from both peak width changes as well as the peak shift. In order to disentangle

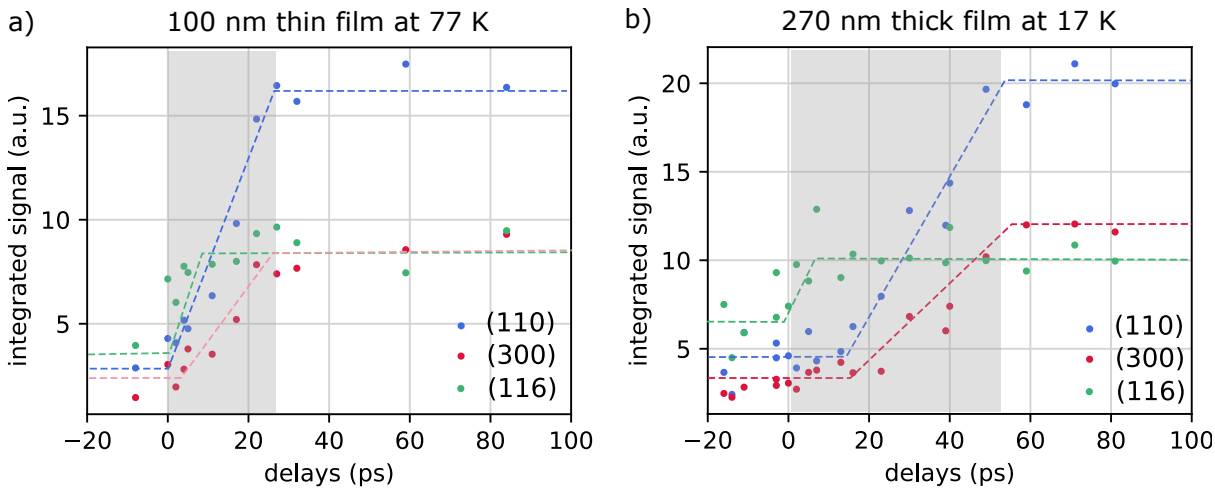

Figure 5.9 – The integrated signal plotted for three different peaks (110), (116) and (300) for a) 100 nm thin film and b) 270 nm thick film of V_2O_3. The dynamics of the peak (116), showing symmetry breaking, is similar in both the films. The volume changing peaks (110) and (300) show a dynamics dependent on the film thickness. The grey shaded region shows the delay range within which the integrated intensity changes. The dashed lines are drawn for guides to the eyes.

the effects, the individual peaks were fitted with a Gaussian profile, which allowed us to extract the position and width of the peaks.

5.3.1 Propagation of the volume contraction associated with AFI-PM phase transition

In order to extract the evolution of the volume contraction, we followed the position of Bragg peaks with zero component along the c^* reciprocal axis. Indeed, Bragg peaks with indices (hk0), for instance, peaks (110) and (300), are hardly affected by the symmetry change. So these peaks only exhibit peak shift without any change in the peak width.

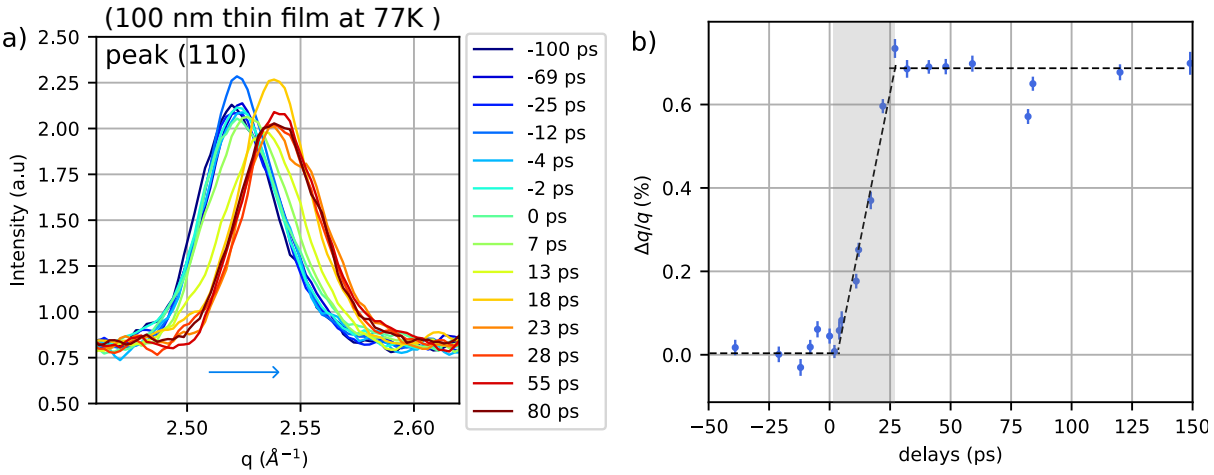

Figure 5.10 – a)The (110) peak position plotted for different negative and positive delays b) Time evolution of the change in the (110) peak position showing the shift takes place within $\sim$ 25 ps (indicated by the grey shaded area). The dashed lines are drawn as guides to the eyes.

The shift in peak position of (110) towards higher q values is evident from Fig. 5.10a and this shift can provide a direct estimation of the volume change as observed from Equation 5.5. With this aim, the peak at each delay is fitted with a Gaussian profile to extract the center at all delays. The change in the center with respect to a "laser off" pattern has been plotted in Fig. 5.10b. This shows that the change in the peak position for (110) starts at a later time than zero and saturates around 25 ps. This peak shift dynamics is similar to that of the integrated signal.

The volume change, evaluated from Equation 5.5, has been extracted for the two thin films of thickness 270 nm and 100 nm and plotted with delays in Fig. 5.11. It is observed that the volume change sets off at about 9 ps after the laser excitation and reaches the maximum change at different delays depending on the film thickness. From the onset of the volume contraction to the saturation, the time required is 16 ps for the thinner film of 100 nm and 40 ps for the thick film of 270 nm. The total volume change is -1.4% irrespective of the thickness of the films. The value of the change is similar to that observed under equilibrium phase transition with either temperature or pressure and this indicates a complete transition from the AFI to PM phase of the whole film.

The propagation times of the longitudinal strain wave through the thickness of the

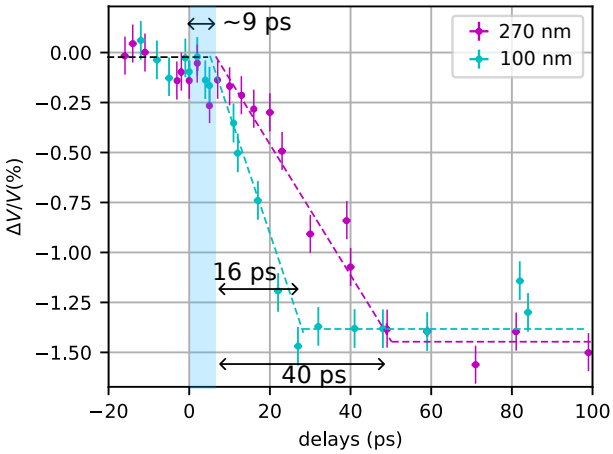

Figure 5.11 – Comparison of the volume change upon photo-excitation in the two V_2O_3 films of different thicknesses of 100 nm and 270 nm. The blue shaded area indicates a latent time of about 9 ps for the advent of the volume change. The error bars are estimated from the dispersion of measurements to account for the experimental drifts and the error in analysis. The dashed lines are guides to the eyes.

films can be obtained from the acoustic velocity in the V_2O_3 film. The acoustic velocity is 7-7.3 nm/ps[119][91]. Therefore time to travel in the thin film of 100 nm:

$$t = \frac{100\,nm}{7\,nm/ps} = 14.2\,ps \tag{5.7}$$

and in the thicker film of 270 nm:

$$t = \frac{270\,nm}{7\,nm/ps} = 38.6\,ps \tag{5.8}$$

The propagation times are in agreement with the experimental values shown in Fig. 5.11.

5.3.2 Propagation of the shear related to AFI-PM symmetry change

In order to follow the evolution of the symmetry change, we then focused on Bragg peaks with large component along the c^* reciprocal axis. Amongst them, the peak (116) has high intensity and is strongly affected by the symmetry change, with the three peaks in AFI (low temperature phase) merging into one peak in PM phase. Since, the q -resolution of the experiments is not enough to distinguish individual peaks, we can only track the width of the peak (116) as a signature of symmetry change.

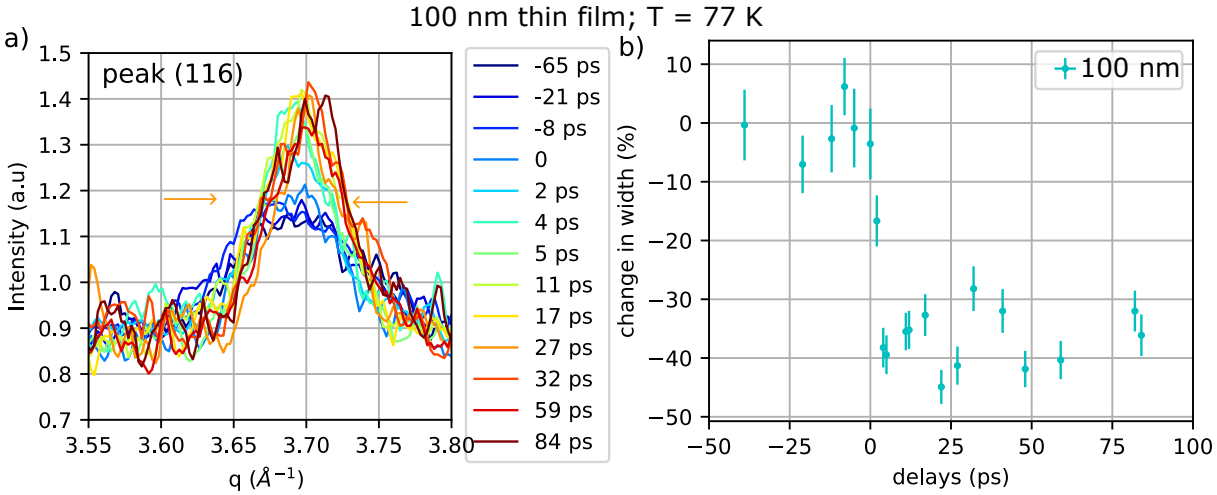

Figure 5.12 – a) Variation of intensity of the peak (116) around q = 3.7 Å^{-1} with few selected delays. The orange arrows indicate the narrowing of the peak at positive delays. b) The percentage change of width of the peak (116) with delays.

From Fig. 5.12, we can observe that the width of the peak (116) for the 100 nm thin film of V_2O_3 starts to decrease at time zero and after $\sim$ 2 ps, the width becomes constant. The peak at each delay is fitted with a Gaussian profile and the width change is plotted as a function of delays in Fig. 5.12b. The change in width of roughly 40% occurs from time 0 to 2 ps. On the other hand, for the 270 nm thick film of V_2O_3, we observe the decrease in width of the peak (116) to about 30 % around time zero.

The change in width of peak (116) occurs within same delay in both the films irrespective of the film thickness (Fig. 5.14). The average size of the monoclinic domains in both the films is 20 nm as was estimated from the peak profiles measured at ESRF. Therefore, the expected time required for the strain wave to propagate in the domains with the transverse acoustic velocity of 4 nm/ps[119].

$$t = \frac{10\,nm}{4\,nm/ps} \sim 2.5\,ps \tag{5.9}$$

which is in agreement with the experimental time delay for the monoclinic to hexagonal transition.

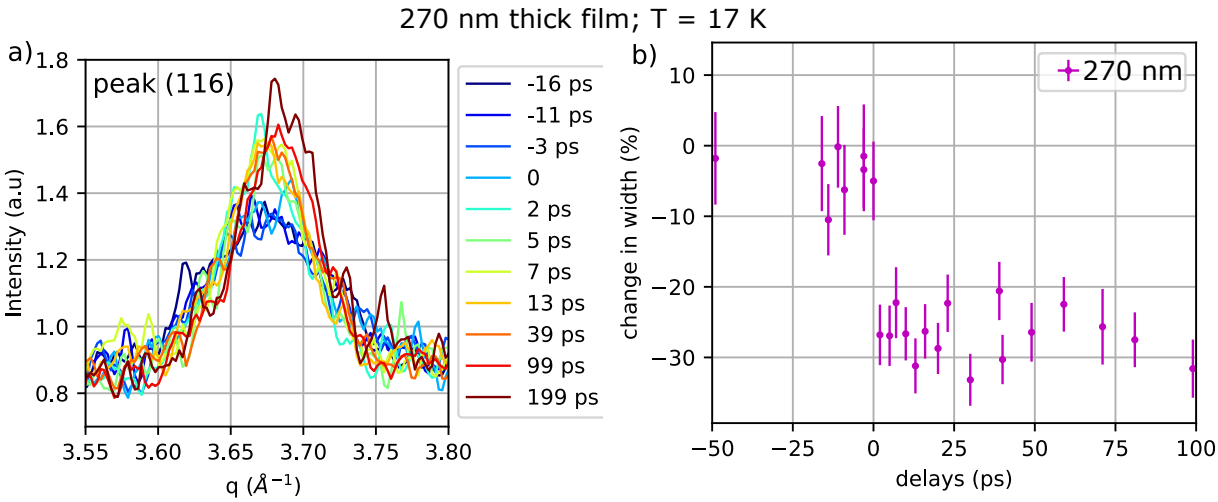

Figure 5.13 – a) Variation of intensity of the peak (116) around q = 3.7 Å^{-1} for thick film of 270 nm. b) The percentage change of width of the peak (116) with delays.

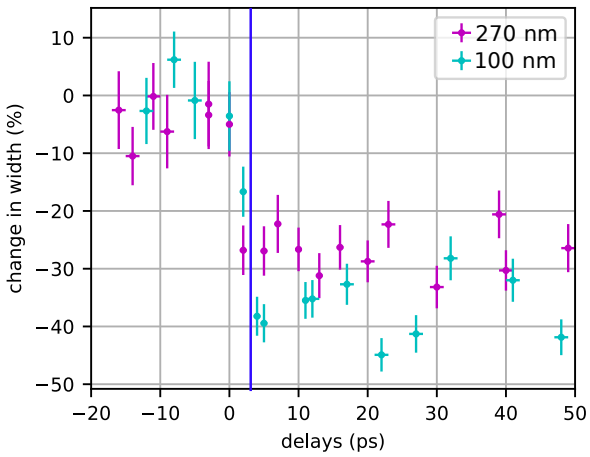

Figure 5.14 – Comparison of the change in width of peak (116) in two different thin films of thickness of 270 nm and 100 nm. The symmetry change occurs within 2-3 ps (indicated by blue solid line).

5.4 Effect of incident laser power on the Photo-induced structural changes

The study of the photo-induced changes with the variation of the incident laser fluence gives us important information on the mechanism of phase transition in the system. The V_2O_3 thin film with thickness of 100 nm was photo-excited with different laser fluences ranging from 1 mJ/cm^2 to 11 mJ/cm^2. The differential patterns at 200 ps taken on this film have been plotted in Fig. 5.15 for different incident laser fluences. The transient signal on all the peaks shows an increase with the increasing laser fluence.

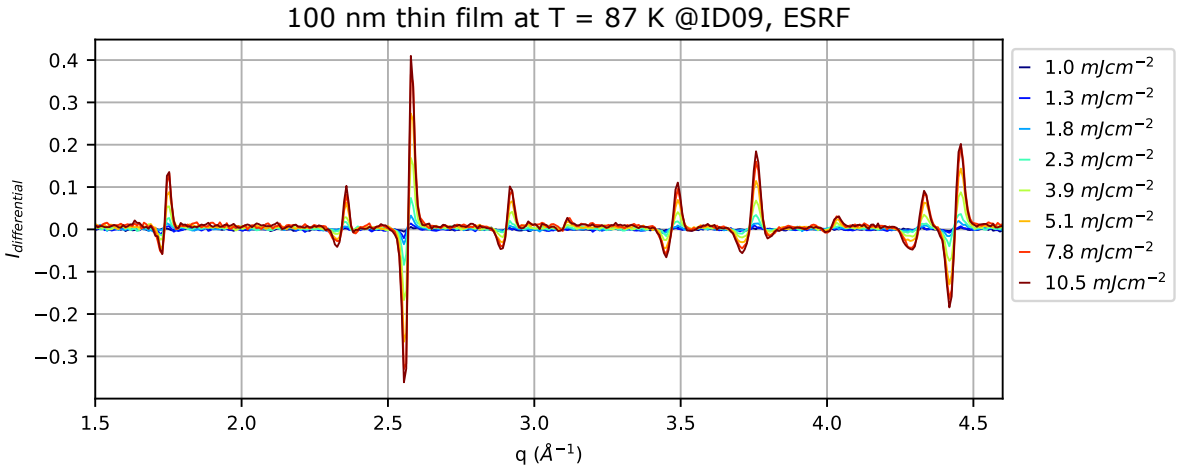

Figure 5.15 – The differential signal of thin film of thickness 100 *nm* at 200 ps for different incident laser fluences.

The integrated intensity of the absolute differential signals at a delay of 200 ps is plotted as a function of fluence. From Fig. 5.16 of the peak (110) and Fig. 5.17 of the peak (116), we observe that there is a threshold fluence of $\sim$ 1 mJ/cm^2 below which there is neither volume change nor symmetry breaking. Both the phenomena have a nonlinear response for fluences $>$ 1 mJ/cm^2 until they reach a saturation at around 8 mJ/cm^2. The threshold fluence indicates that a minimum laser power is required to initiate a phase transition on a macroscopic scale.

At the intermediate fluence of 3.9 mJ/cm^2 (Fig. 5.18), there is partial conversion from the monoclinic(AFI) to the hexagonal(PM) phase even at the delay of 200 ps. So, for these intermediate fluences, there is a phase separation in the thin film. At the fluence of 10.5 mJ/cm^2, there is complete conversion to the hexagonal(PM) phase at 200 ps.

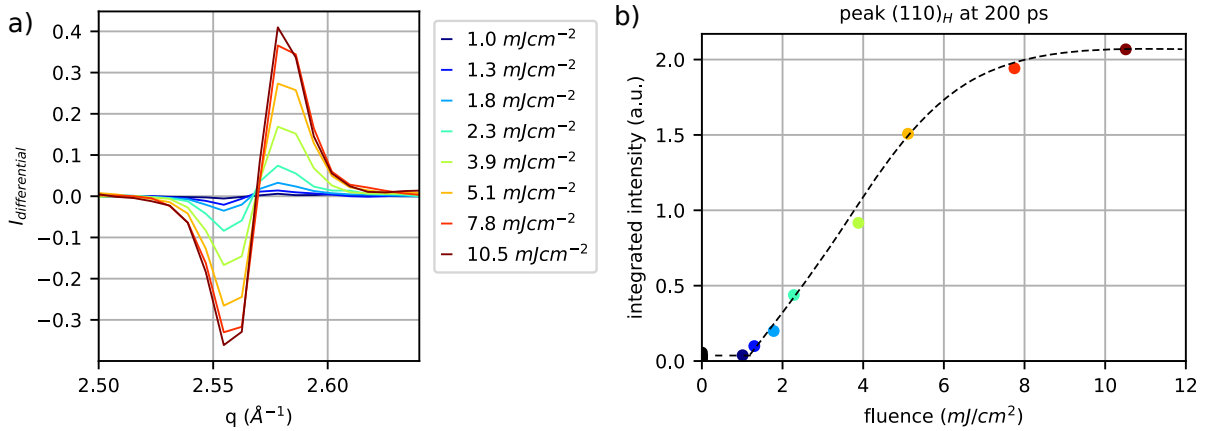

Figure 5.16 – a) The differential signal zoomed on the peak (110) at 200 ps upon photo-excitation with different laser fluences. b) The integrated signal plotted as a function of fluence showing the non-linear behavior with a threshold fluence of $\sim$ 1 mJ/cm^2 and saturation above 8 mJ/cm^2. The dashed lines are the guides to the eye.

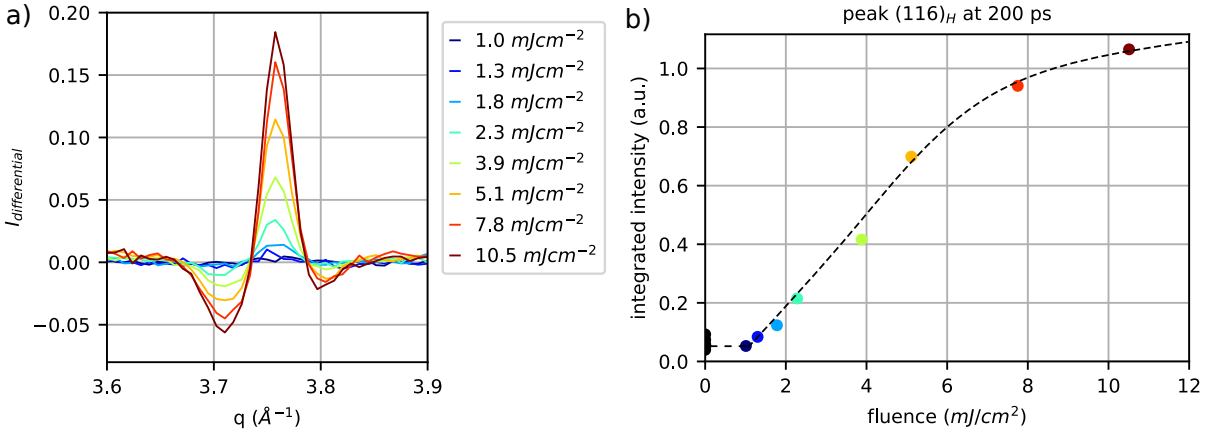

Figure 5.17 – a) The differential signal zoomed on the peak (116) at 200 ps with the variation of incident laser fluence. b) The integrated signal plotted as a function of fluence showing the non-linear behavior with a threshold fluence of $\sim$ 1 mJ/cm^2. The dashed lines are the guides to the eye.

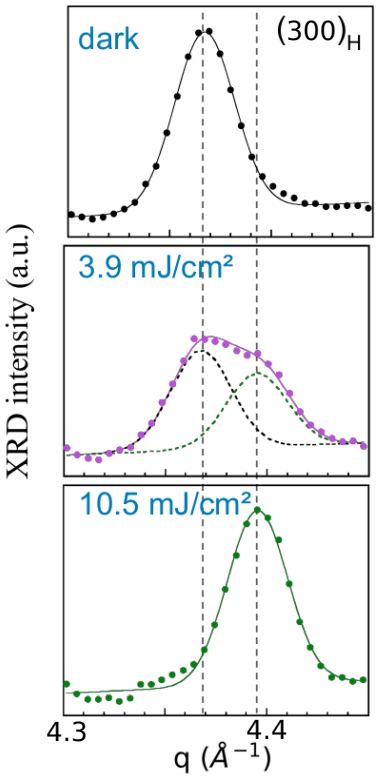

Figure 5.18 – Evolution of the peak (300) with fluence is plotted at "laser-off", at laser fluences of 3.9 mJ/cm^2 and 10.5 mJ/cm^2 (from top to bottom) at a delay of 200 ps. The "laser off" pattern is in AFI phase (black dotted line is measured and the solid line is fitted). The peak (300) at an intermediate fluence of 3.9 mJ/cm^2 is plotted in violet dotted line(measured) and solid line(fitted). The peak is plotted in green dotted and solid line at higher fluence of 10.5 mJ/cm^2 in PM phase.

Estimation of the maximum temperature rise in the thin films

To ensure that the AFI to PM phase transition in V_2O_3thin films does not occur solely by heating from the laser pulse, we have performed the TR-XRD measurements at 17 K, well below the transition temperature of $\sim$ 150 K. The total energy deposited on the surface of V_2O_3 thin film by the incident laser fluence of 1 mJ/cm^2 can be calculated using Equation 1.1.

$$W(z=0) = (1-0.21) \times \frac{1\, mJ/cm^2}{500\, nm} = 1.74 \times 10^8 J/m^3 \tag{5.10}$$

where R is the reflectivity of the V_2O_3 thin film (R = 0.21 [107]) and μ is the laser penetration depth of 500 nm. This gives a temperature rise on the surface of the film

$$\Delta T = \frac{W(z=0)}{C} \sim 49\, K \tag{5.11}$$

with a specific heat per unit volume (C) of 0.325×10^6 J K^{-1}m^{-3}. The temperature is maximum of 65 K on the surface and decreases exponentially with depth. So, the incident laser power is not enough to heat the film from 15 K to the transition temperature Tc $\sim$150 K. Hence we can conclude that the insulator-metal transition upon photo-excitation is not just due to laser heating in the films.

5.5 Conclusion

Two phenomena are evident from the results of the TR-XRD measurements. Firstly, V_2O_3 undergoes the symmetry change from the monoclinic AFI phase (I2/a) to a rhombohedral phase ($R\bar{3}c$) within few ps. The monoclinic distortion occurs within the ferroelastic domains and hence the dynamics scales with the domain size, which was same in films of different thicknesses. Secondly, a shift of the Bragg peaks towards higher q values was observed, indicating the volume contraction in the hexagonal phase and the amount of change (-1.5 %) is in agreement with the AFI-PM phase transition under equilibrium[57]. Moreover, we observe that the symmetry change is completed before the onset of the volume change. The volume dynamics sets off at about 9 ps after the laser excitation and the sonic propagation thereof is complete at the time scaling with the film thickness.

The corresponding delays indicate that upon photo-excitation of the V_2O_3 thin films, both longitudinal and transverse strain waves are launched from the film surface and propagate in the depth with the respective acoustic velocities. The structural changes such as the volume contraction and the symmetry breaking follow the strain wavefront. Timewise, the delayed volume dynamics may be due to the coupling of the volumic strain and the shear strain, however, a complete description requires further investigation. Structure-wise, the photo-induced transition follows a pathway of : Monoclinic phase at Low temperature $\rightarrow$ hexagonal phase (higher symmetry) with higher volume $\rightarrow$ hexagonal phase(higher symmetry) with a lower volume.

In addition, the TR-XRD results show that both the volume and shear dynamics take place above a threshold fluence. Hence, a minimum amount of laser power is required to establish microscopic structural order in the films. For high fluences, the whole X-ray probed regime gets converted to the PM phase upon laser excitation, whereas for the intermediate fluences there exists a phase co-existence between the AFI and PM phase in the probed volume within the thin film. The non-thermal origin of this process is supported with measurements at 15 K, that is sufficiently far from the phase transition temperature and phase coexistence regime, and with infrared excitation just above the electronic band gap of the insulating phase to reduce thermal effects.

Therefore, the photo-induced insulator-metal transition in V_2O_3 follows the propagation of volume change unlike in systems where the local dynamics is governed by a slow thermal activation [109]. Moreover, the observation of the threshold proved the existence of a critical value of electronic excitation which triggers the long range stabilisation of the new phase in V_2O_3. The results also highlight the role of sample morphology in establishing the long range structural order.

In addition to the TR-XRD measurements, optical transient reflectivity experiments are done in collaboration with Tatsuya Amano and Shinichiro Iwai from the University of Tohoku. The reflectivity measurements done under same temperature and laser excitation energy shows that there is persistence of the bandgap up to 5 ps. the onset of metallicity starts from 5 ps to complete 25 ps (in thin film) and 49 ps (in the thick film). So, it can be concluded that metallicity follows the volume dynamics.

Chapter 6

Conclusion

Correlated electron systems include a large class of materials and their photo-induced transitions have tremendous potential for application in modern day technologies, like ultra-fast sensors, energy storage or memory devices. The focus of this research was to deepen our understanding of the out-of-equilibrium thermodynamics of these materials, particularly when a phase transition occurs. Additionally, for improved efficiency of photo-induced transitions in mind, it is important to explore the various experimental factors that affect such transitions.

The first results in the manuscript concern the photo-induced phase transition in polycrystalline pellets of Ti_3O_5(Chapter 4). This transition represents a prototype of isostructural phase transition involving only the volume change. It is a multiscale process with a fast dynamics ($\sim$ 20 ps) and the slower dynamics around 100 ns [55]. The former is primarily driven by propagating strain waves, the latter is caused by heat diffusion in the pellets.

During my PhD, I have mostly focused on the phase transition at the nanosecond time scales governed by heat diffusion. We have explored the effect of various experimental parameters and also sample morphology on this thermal transformation. With TR-XRD experiments at ID09 (ESRF) and numerical simulations of heat diffusion, we established the set of rules by which the transition dynamics in laser excited nanocrystallites of Ti_3O_5 are likely to evolve in space and time. Our investigations highlight the role of causality in determining the spatio-temporal patterns of phase separation. Even though the dynamics evolving on very different time-scales obey different regimes, coherent or thermal, we show that the outcome of the fast driven transition predetermines that of the slower transition. The results show the impact of nanoscale morphology of the sample on the mechanism of macroscopic transformation triggered by laser excitation.

In order to see directly the effect of experimental parameters on the strain wave pathway, we utilised a laser pump X-ray probe setups with affording picosecond temporal resolution. Because the coherent pathway is complete within 100 ps (time resolution at the synchrotrons), the quest for a better time resolution led us to explore the characteristics of the so-called Picoswitch, discussed in Chapter 2. The Picoswitch is effective in producing 20 ps long X-ray pulses, but unfortunately, the flux was too low for tracking the small photo-induced changes (of about 10 %) in the pellets of Ti_3O_5.

In Chapter 5, we have investigated the photo-induced transformation pathway in thin films of V_2O_3, the phase transition of which involves both volume and symmetry change. The time resolved experiments at FemtoMAX (MAX IV) were performed at very low temperature, well below the transition temperature at ambient conditions. The pump-

ing energy was close to the band gap which limits the contribution of the incoherent phonon population, thereby reducing the lattice heating and excluding the possibility of thermal phase transition. Both the volume and symmetry dynamics occur within ps timescales after the photo-irradiation suggesting the ultra-fast coherent pathway for the phase transition. The study also highlights the role of sample morphology in this strain wave pathway.

The study of two different transition metal oxides on timescales varying from pico- to microseconds provides a comprehensive understanding of the multiscale nature of photo-induced phase transitions. In the case of V_2O_3, we observed the phase transition concurrent with the propagation of the strain wave, while in the Ti_3O_5, we analyzed how the phase distribution at ultrafast timescales influences the slower dynamics primarily governed by heat diffusion. Investigating both the ultrafast electron-phonon coupling and the slower heat diffusion processes is crucial for harnessing the photoinduced phase transitions. This approach allows for a better control of the parameters influencing phase transitions. Extraordinary capabilities opened by ultrabright and ultrashort X-ray sources have made these studies possible. Future studies could revolve around resolving the local precursor phenomena by using advanced crystallographic techniques at X-ray Free Electron Lasers. Another exciting direction is to track structural changes at the level of a singular object, such as isolated nanocrystallite, by using ultrafast electron diffraction or ultrafast electron microscopy.

Bibliography

[1] Elsa Abreu et al., « Dynamic conductivity scaling in photoexcited V 2 O 3 thin films », *in*: *Physical Review B* 92.*8* (2015), p. 085130.

[2] Elsa Abreu et al., « Ultrafast electron-lattice coupling dynamics in VO 2 and V 2 O 3 thin films », *in*: *Physical Review B* 96.*9* (2017), p. 094309.

[3] Tatsuya Amano et al., « Propagating insulator-to-metal transition in the wake of photoinduced strain waves in a Mott material », *in*: (2023).

[4] Sten Andersson et al., « Phase analysis studies on the titanium-oxygen system », *in*: *Acta chem. scand* 11.*10* (1957), pp. 1641–1652.

[5] Akifumi Asahara et al., « Ultrafast dynamics of photoinduced semiconductor-to-metal transition in the optical switching nano-oxide Ti 3 O 5 », *in*: *Physical Review B* 90.*1* (2014), p. 014303.

[6] Stig Åsbrink and Arne Magnéli, « Crystal structure studies on trititanium pentoxide, Ti3O5 », *in*: *Acta Crystallographica* 12.*8* (1959), pp. 575–581.

[7] Giannis Ashiotis et al., « The fast azimuthal integration Python library: pyFAI », *in*: *Journal of Applied Crystallography* 48 (2015), pp. 510–519, DOI: 10.1107/S1600576715004306, URL: https://hal.science/hal-01572879.

[8] Danylo Babich, « Electron-lattice coupling at the Mott transition driven by electric and/or by light pulse », PhD thesis, Nantes, 2020.

[9] P Babilotte et al., « Physical mechanism of coherent acoustic phonons generation and detection in GaAs semiconductor », *in*: *Journal of Physics: Conference Series*, vol. 92, 1, IOP Publishing, 2007, p. 012019.

[10] Matias Bargheer et al., « Recent progress in ultrafast X-ray diffraction », *in*: *Chemphyschem: a European journal of chemical physics and physical chemistry* 7.*4* (2006), pp. 783–792.

[11] DN Basov, RD Averitt, and D Hsieh, « Towards properties on demand in quantum materials », *in*: *Nature materials* 16.*11* (2017), pp. 1077–1088.

[12] Roman Bertoni et al., « Elastically driven cooperative response of a molecular material impacted by a laser pulse », *in*: *Nature materials* 15.*6* (2016), pp. 606–610.

[13] Davide Boschetto and Antoine Rousse, « Coherent Optical Phonons in Bismuth Crystal », *in*: *Coherence and Ultrashort Pulse Laser Emission*, IntechOpen, 2010.

[14] Azzedine Bousseksou et al., « Molecular spin crossover phenomenon: recent achievements and prospects », *in*: *Chemical Society Reviews* 40.*6* (2011), pp. 3313–3335.

[15] CH Brian et al., « Phase relationships and electrical properties of Ti 3 O 5, CrTi 2 O 5 and the pseudobrookite-type systems Mg x Ti 3–x O 5 and Li x Ti 3–x O 5 », *in*: *Journal of Materials Chemistry* 2.*12* (1992), pp. 1249–1256.

[16] Hervé Cailleau et al., « PIPT from the Beginning to Future », *in*: *Acta Physica Polonica A* 121.*2* (2012), pp. 297–306.

[17] Marco Cammarata et al., « Chopper system for time resolved experiments with synchrotron radiation », *in*: *Review of scientific instruments* 80.*1* (2009), p. 015101.

[18] Yunteng Cao et al., « Bistable structures for advanced functional systems », *in*: *Advanced Functional Materials* 31.*45* (2021), p. 2106231.

[19] Andrea Cavalleri et al., « Femtosecond structural dynamics in VO 2 during an ultrafast solid-solid phase transition », *in*: *Physical review letters* 87.*23* (2001), p. 237401.

[20] Samuel Chen et al., « The effects of titanium or chromium doping on the crystal structure of V2O3 », *in*: *Journal of Solid State Chemistry* 44.*2* (1982), pp. 192–200.

[21] Alan A Coelho, « TOPAS and TOPAS-Academic: an optimization program integrating computer algebra and crystallographic objects written in C++ », *in*: *Journal of Applied Crystallography* 51.*1* (2018), pp. 210–218.

[22] Eric Collet et al., « Laser-induced ferroelectric structural order in an organic charge-transfer crystal », *in*: *Science* 300.*5619* (2003), pp. 612–615.

[23] CrysAlisPro, « Data collection and data reduction software package », *in*: *Agilent Technologies* (2015), http://www.selectscience.net/products/crysalispro/?prodID=197116.

[24] PD Dernier and M Marezio, « Crystal structure of the low-temperature antiferromagnetic phase of V 2 O 3 », *in*: *Physical Review B* 2.*9* (1970), p. 3771.

[25] Henrik Enquist et al., « FemtoMAX–an X-ray beamline for structural dynamics at the short-pulse facility of MAX IV », *in*: *Journal of Synchrotron Radiation* 25.*2* (2018), pp. 570–579.

[26] Hazhir Fatahi, Jérôme Claverie, and Sébastien Poncet, « Thermal Characterization of Phase Change Materials by Differential Scanning Calorimetry: A Review », *in*: *Applied Sciences* 12.*23* (2022), p. 12019.

[27] Manfred Fiebig et al., « Visualization of the local insulator-metal transition in Pr0. 7Ca0. 3MnO3 », *in*: *Science* 280.*5371* (1998), pp. 1925–1928.

[28] Martin C Fischer et al., « Invited review article: pump-probe microscopy », *in*: *Review of Scientific Instruments* 87.*3* (2016).

[29] RWL Fong et al., « A Differential Scanning Calorimetry (DSC) Study of Phase Changes in an As-Received Zr-2.5 Nb Pressure Tube Material during Continuous Heating and Cooling », *in*: *Materials Science Forum*, vol. 706, Trans Tech Publ, 2012, pp. 853–858.

[30] Mizuho Fushitani, « Applications of pump-probe spectroscopy », *in*: *Annual Reports Section" C"(Physical Chemistry)* 104 (2008), pp. 272–297.

[31] Peter Gaal et al., « Ultrafast switching of hard X-rays », *in*: *Journal of synchrotron radiation* 21.*2* (2014), pp. 380–385.

[32] T Garl et al., « Birth and decay of coherent optical phonons in femtosecond-laser-excited bismuth », *in*: *Physical Review B* 78.*13* (2008), p. 134302.

[33] IE Grey, C Li, and IC Madsen, « Phase equilibria and structural studies on the solid solution MgTi2O5-Ti3O5 », *in*: *Journal of Solid State Chemistry* 113.*1* (1994), pp. 62–73.

[34] Philipp Gütlich, Andreas Hauser, and Hartmut Spiering, « Thermal and optical switching of iron (II) complexes », *in*: *Angewandte Chemie International Edition in English* 33.*20* (1994), pp. 2024–2054.

[35] Kristoffer Haldrup et al., « Observing solvation dynamics with simultaneous femtosecond X-ray emission spectroscopy and X-ray scattering », *in*: *The journal of physical chemistry B* 120.*6* (2016), pp. 1158–1168.

[36] Philipp Hansmann et al., *Mott–Hubbard transition in V2O3 revisited*, 2013.

[37] Muneaki Hase et al., « Ultrafast dynamics of coherent optical phonons and nonequilibrium electrons in transition metals », *in*: *Physical review B* 71.*18* (2005), p. 184301.

[38] « https://gitlab.esrf.fr/levantin/txs », *in*: ().

[39] Congliang Huang, Xin Qian, and Ronggui Yang, « Thermal conductivity of polymers and polymer nanocomposites », *in*: *Materials Science and Engineering: R: Reports* 132 (2018), pp. 1–22.

[40] Nolwenn Huby et al., « Photoinduced spin transition probed by x-ray diffraction », *in*: *Physical Review B* 69.*2* (2004), p. 020101.

[41] Anatoly Alexandrovich Ischenko et al., « Ultrafast electron diffraction and electron microscopy: present status and future prospects », *in*: *Physics-Uspekhi* 57.*7* (2014), p. 633.

[42] S Iwai et al., « Coherent control of charge and lattice dynamics in a photoinduced neutral-to-ionic transition of a charge-transfer compound », *in*: *Physical review letters* 96.*5* (2006), p. 057403.

[43] K Kadoya, N Matsunaga, and A Nagashima, « Viscosity and thermal conductivity of dry air in the gaseous phase », *in*: *Journal of physical and chemical reference data* 14.*4* (1985), pp. 947–970.

[44] H Kambe, K Horie, and T Suzuki, « Investigations of solid phase transitions of low molecular organic compounds by differential scanning calorimetry », *in*: *Journal of thermal analysis* 4 (1972), pp. 461–469.

[45] J Kieffer et al., « New tools for calibrating diffraction setups », *in*: *Journal of synchrotron radiation* 27.*2* (2020), pp. 558–566.

[46] Jérôme Kieffer and Dimitrios Karkoulis, « PyFAI, a versatile library for azimuthal regrouping », *in*: 425.*20* (2013), p. 202012.

[47] Erik B Knudsen et al., « FabIO: easy access to two-dimensional X-ray detector images in Python », *in*: *Journal of Applied Crystallography* 46.*2* (2013), pp. 537–539.

[48] Shinya Koshihara et al., « Challenges for developing photo-induced phase transition (PIPT) systems: from classical (incoherent) to quantum (coherent) control of PIPT dynamics », *in*: *Physics Reports* 942 (2022), pp. 1–61.

[49] Ewelina Kubacka and Piotr Ostrowski, « Influence of Composite Structure on Temperature Distribution—An Analysis Using the Finite Difference Method », *in*: *Materials* 16.*14* (2023), p. 5193.

[50] J-P Pollina Lebasque, « Low-alpha operation for the SOLEIL storage ring », *in*: (2012).

[51] Rui Liu, Jia-Xiang Shang, and Fu-He Wang, « Electronic, magnetic and optical properties of β-Ti3O5 and λ-Ti3O5: A density functional study », *in*: *Computational materials science* 81 (2014), pp. 158–162.

[52] P Loubeyre et al., « Equation of state and phase diagram of solid He 4 from single-crystal x-ray diffraction over a large P-T domain », *in*: *Physical review letters* 71.*14* (1993), p. 2272.

[53] Clare F Macrae et al., « Mercury 4.0: From visualization to analysis, design and prediction », *in*: *Journal of applied crystallography* 53.*1* (2020), pp. 226–235.

[54] Giorgio Margaritondo, « A primer in synchrotron radiation: everything you wanted to know about SEX (Synchrotron Emission of X-rays) but were afraid to ask », *in*: *Journal of synchrotron radiation* 2.*3* (1995), pp. 148–154.

[55] Céline Mariette et al., « Strain wave pathway to semiconductor-to-metal transition revealed by time-resolved X-ray powder diffraction », *in*: *Nature communications* 12.*1* (2021), p. 1239.

[56] DB McWhan and JP Remeika, « Metal-insulator transition in (V 1- x Cr x) 2 O 3 », *in*: *Physical Review B* 2.*9* (1970), p. 3734.

[57] DB McWhan et al., « Metal-insulator transitions in pure and doped V 2 O 3 », *in*: *Physical Review B* 7.*5* (1973), p. 1920.

[58] Mirko Mikolasek et al., « Complete set of elastic moduli of a spin-crossover solid: Spin-state dependence and mechanical actuation », *in*: *Journal of the American Chemical Society* 140.*28* (2018), pp. 8970–8979.

[59] Keiichirō Nasu, *Photoinduced phase transitions*, World Scientific, 2004.

[60] Stefan Nolte, Frank Schrempel, and Friedrich Dausinger, « Ultrashort pulse laser technology », *in*: *Springer Series in Optical Sciences* 195 (2016), p. 200.

[61] Shin-ichi Ohkoshi et al., « Light-induced spin-crossover magnet », *in*: *Nature chemistry* 3.*7* (2011), pp. 564–569.

[62] Shin-ichi Ohkoshi et al., « Low-pressure-responsive heat-storage ceramics for automobiles », *in*: *Scientific reports* 9.*1* (2019), pp. 1–8.

[63] Shin-ichi Ohkoshi et al., « Synthesis of a metal oxide with a room-temperature photoreversible phase transition », *in*: *Nature chemistry* 2.*7* (2010), pp. 539–545.

[64] H Okamoto, « O-Ti (oxygen-titanium) », *in*: *Journal of Phase Equilibria and Diffusion* 32.*5* (2011), pp. 473–474.

[65] H Okamoto et al., « Photoinduced phase transition in tetrathiafulvalene-p-chloranil observed in femtosecond reflection spectroscopy », *in*: *Physical Review B* 70.*16* (2004), p. 165202.

[66] Y Okimoto et al., « Ultrasonic propagation of a metallic domain in Pr 0.5 Ca 0.5 CoO 3 undergoing a photoinduced insulator-metal transition », *in*: *Physical review letters* 103.*2* (2009), p. 027402.

[67] Masashige Onoda, « Phase transitions of Ti3O5 », *in*: *Journal of Solid State Chemistry* 136.*1* (1998), pp. 67–73.

[68] Amine Ould-Hamouda et al., « Single-shot time resolved study of the photoreversible phase transition induced in flakes of Ti3O5 nanoparticles at room temperature », *in*: *Chemical Physics Letters* 608 (2014), pp. 106–112.

[69] Vinh Ta-Phuoc, « Temperature and pressure-driven dimerized insulator to metal transitions in Ti3O5 polymorphs evidenced by optical spectroscopy », *in*: (), [submitted].

[70] RS Potember, TO Poehler, and RC Benson, « Optical switching in semiconductor organic thin films », *in*: *Applied Physics Letters* 41.*6* (1982), pp. 548–550.

[71] Clemens Prescher and Vitali B Prakapenka, « DIOPTAS: a program for reduction of two-dimensional X-ray diffraction data and data exploration », *in*: *High Pressure Research* 35.*3* (2015), pp. 223–230.

[72] P Prigent et al., « Progress on the femto-slicing project at the synchrotron SOLEIL », *in*: *Journal of Physics: Conference Series*, vol. 425, 7, IOP Publishing, 2013, p. 072022.

[73] PL Privalov and VV Plotnikov, « Three generations of scanning microcalorimeters for liquids », *in*: *Thermochimica acta* 139 (1989), pp. 257–277.

[74] M Querré et al., « Non-volatile resistive switching in the Mott insulator (V1- xCrx) 2O3 », *in*: *Physica B: Condensed Matter* 536 (2018), pp. 327–330.

[75] Madec Querré et al., « Metal–insulator transitions in (V1-xCrx) 2O3 thin films deposited by reactive direct current magnetron co-sputtering », *in*: *Thin Solid Films* 617 (2016), pp. 56–62.

[76] Rakesh Rana et al., « Nonthermal nature of photoinduced insulator-to-metal transition in NbO 2 », *in*: *Physical Review B* 99.*4* (2019), p. 041102.

[77] Sylvain Rat et al., « Solvatomorphism and structural-spin crossover property relationship in bis [hydrotris (1, 2, 4-triazol-1-yl) borate] iron (II) », *in*: *CrystEngComm* 19.*24* (2017), pp. 3271–3280.

[78] Gerald W Recktenwald, « Finite-difference approximations to the heat equation », *in*: *Mechanical Engineering* 10.*01* (2004).

[79] Karl Ridier et al., « Finite size effects on the switching dynamics of spin-crossover thin films photoexcited by a femtosecond laser pulse », *in*: *Advanced Materials* 31.*25* (2019), p. 1901361.

[80] A. Ronchi et al., « Early-stage dynamics of metallic droplets embedded in the nanotextured Mott insulating phase of V_2O_3 », *in*: *Phys. Rev. B* 100 (7 Aug. 2019), p. 075111, DOI: 10.1103/PhysRevB.100.075111, URL: https://link.aps.org/doi/10.1103/PhysRevB.100.075111.

[81] Antoine Rousse, Christian Rischel, and Jean-Claude Gauthier, « Femtosecond x-ray crystallography », *in*: *Reviews of Modern Physics* 73.*1* (2001), p. 17.

[82] Patrick Rozier, Alicja Ratuszna, and Jean Galy, « Comparative Structural and Electrical Studies of V2O3 and V2—xNixO3 (0¡ x¡ 0.75) Solid Solution », *in*: *Zeitschrift für anorganische und allgemeine Chemie* 628.*5* (2002), pp. 1236–1242.

[83] Pascal Ruello and Vitalyi E Gusev, « Physical mechanisms of coherent acoustic phonons generation by ultrafast laser action », *in*: *Ultrasonics* 56 (2015), pp. 21–35.

[84] Takuo Saiki et al., « Selection rule for the photoinduced phase transition dominated by anisotropy of strain in Ti 3 O 5 », *in*: *Physical Review B* 105.*7* (2022), p. 075134.

[85] T Saito, O Matsuda, and OB Wright, « Picosecond acoustic phonon pulse generation in nickel and chromium », *in*: *Physical Review B* 67.*20* (2003), p. 205421.

[86] M Sander et al., « Characterization of an ultrafast Bragg-Switch for shortening hard x-ray pulses », *in*: *Journal of Applied Physics* 120.*19* (2016), p. 193101.

[87] Mathias Sander et al., « Demonstration of a picosecond Bragg switch for hard X-rays in a synchrotron-based pump–probe experiment », *in*: *Journal of synchrotron radiation* 26.*4* (2019), pp. 1253–1259.

[88] David Sands, « Pulsed laser heating and melting », *in*: *Heat Transfer-Engineering Applications* (2011), pp. 47–70.

[89] Daniel Schick et al., « Ultrafast lattice response of photoexcited thin films studied by X-ray diffraction », *in*: *Structural dynamics* 1.*6* (2014).

[90] Krystyna Schneider, « Optical properties and electronic structure of V2O5, V2O3 and VO2 », *in*: *Journal of Materials Science: Materials in Electronics* 31.*13* (2020), pp. 10478–10488.

[91] Md Motin Seikh et al., « A Brillouin study of the temperature-dependence of the acoustic modes across the insulator–metal transitions in V2O3 and Cr-doped V2O3 », *in*: *Solid state communications* 138.*9* (2006), pp. 466–471.

[92] Roberta Sessoli et al., « Magnetic bistability in a metal-ion cluster », *in*: *Nature* 365.*6442* (1993), pp. 141–143.

[93] Victoria Shalabaeva et al., « Vacuum deposition of high-quality thin films displaying spin transition near room temperature », *in*: *Journal of Materials Chemistry C* 5.*18* (2017), pp. 4419–4425.

[94] Guoyin Shen and Ho Kwang Mao, « High-pressure studies with x-rays using diamond anvil cells », *in*: *Reports on Progress in Physics* 80.*1* (2016), p. 016101.

[95] Andrej Singer et al., « Nonequilibrium phase precursors during a photoexcited insulator-to-metal transition in V 2 O 3 », *in*: *Physical review letters* 120.*20* (2018), p. 207601.

[96] Klaus Sokolowski-Tinten et al., « Femtosecond X-ray measurement of coherent lattice vibrations near the Lindemann stability limit », *in*: *Nature* 422.*6929* (2003), pp. 287–289.

[97] K Syassen, « Ruby under pressure », *in*: *High Pressure Research* 28.*2* (2008), pp. 75–126.

[98] Ryusei Takahama et al., « Structural, magnetic, transport, and thermoelectric properties of the pseudobrookite AlTi 2 O 5- Ti 3 O 5 system », *in*: *Physical Review Materials* 4.*7* (2020), p. 074401.

[99] Guray Tas and Humphrey J Maris, « Electron diffusion in metals studied by picosecond ultrasonics », *in*: *Physical Review B* 49.*21* (1994), p. 15046.

[100] Kelin R Tasca et al., « Time-Resolved X-Ray Powder Diffraction Study of Photoinduced Phase Transitions in Ti3O5 Nanoparticles », *in*: *ChemPhysChem* 18.*10* (2017), pp. 1385–1392.

[101] Naoyuki Tateiwa and Yoshinori Haga, « Evaluations of pressure-transmitting media for cryogenic experiments with diamond anvil cell », *in*: *Review of Scientific Instruments* 80.*12* (2009).

[102] GA Thomas et al., « Observation of the gap and kinetic energy in a correlated insulator », *in*: *Physical review letters* 73.*11* (1994), p. 1529.

[103] C Thomsen et al., « Surface generation and detection of phonons by picosecond light pulses », *in*: *Physical Review B* 34.*6* (1986), p. 4129.

[104] Hiroko Tokoro et al., « External stimulation-controllable heat-storage ceramics », *in*: *Nature communications* 6.*1* (2015), p. 7037.

[105] Do H Tomboulian and PL Hartman, « Spectral and angular distribution of ultraviolet radiation from the 300-Mev Cornell synchrotron », *in*: *Physical Review* 102.*6* (1956), p. 1423.

[106] Renske M Van Der Veen et al., « Single-nanoparticle phase transitions visualized by four-dimensional electron microscopy », *in*: *Nature chemistry* 5.*5* (2013), pp. 395–402.

[107] I Lo Vecchio et al., « Optical properties of V 2 O 3 in its whole phase diagram », *in*: *Physical Review B* 91.*15* (2015), p. 155133.

[108] Alix Volte, « Photo-induced cooperativity in bistable volume-changing materials », PhD thesis, Rennes 1, 2020.

[109] Alix Volte et al., « Dynamical limits for the molecular switching in a photoexcited material revealed by X-ray diffraction », *in*: *Communications Physics* 5.*1* (2022), p. 168.

[110] Jincheng Wang and Chunlei Guo, « Effect of electron heating on femtosecond laser-induced coherent acoustic phonons in noble metals », *in*: *Physical Review B* 75.*18* (2007), p. 184304.

[111] Mingzhe Wang et al., « Phase evolution and formation of λ phase in Ti3O5 induced by magnesium doping », *in*: *Journal of Alloys and Compounds* 774 (2019), pp. 1189–1194.

[112] Daniel Wegkamp and Julia Stähler, « Ultrafast dynamics during the photoinduced phase transition in VO2 », *in*: *Progress in Surface Science* 90.*4* (2015), pp. 464–502.

[113] BA Welt et al., « Explicit finite difference methods for heat transfer simulation and thermal process design », *in*: *Journal of Food Science* 62.*2* (1997), pp. 230–236.

[114] Philip Willmott, *An introduction to synchrotron radiation: techniques and applications*, John Wiley & Sons, 2019.

[115] OB Wright and VE Gusev, « Acoustic generation in crystalline silicon with femtosecond optical pulses », *in*: *Applied physics letters* 66.*10* (1995), pp. 1190–1192.

[116] Oliver B Wright and VE Gusev, « Ultrafast acoustic phonon generation in gold », *in*: *Physica B: Condensed Matter* 219 (1996), pp. 770–772.

[117] Oliver B Wright and Vitalyi E Gusev, « Ultrafast generation of acoustic waves in copper », *in*: *IEEE Transactions on ultrasonics, ferroelectrics, and frequency control* 42.*3* (1995), pp. 331–338.

[118] Bo Yang et al., « Flatband λ-Ti3O5 towards extraordinary solar steam generation », *in*: *Nature* (2023), pp. 1–8.

[119] WB Yelon and JE Keem, « The elastic constants of V2O3 in the insulating phase », *in*: *Solid State Communications* 29.*11* (1979), pp. 775–777.

[120] Kenji Yonemitsu and Keiichiro Nasu, « Theory of photoinduced phase transitions in itinerant electron systems », *in*: *Physics reports* 465.*1* (2008), pp. 1–60.

[121] Ahmed H Zewail, « Femtochemistry: atomic-scale dynamics of the chemical bond using ultrafast lasers (Nobel Lecture) », *in*: *Angewandte Chemie International Edition* 39.*15* (2000), pp. 2586–2631.

[122] Qian Zhang, Xiang Wu, and Shan Qin, « Pressure-induced phase transition of V2O3 », *in*: *Chinese Physics Letters* 29.*10* (2012), p. 106101.

COLLEGE SCIENCES DE LA MATIERE
DOCTORAL DES MOLECULES
BRETAGNE ET MATERIAUX

Université de Rennes

Titre : Étude de diffraction des rayons X en temps résolu de la dépendance en taille des changements de phase photoinduits dans des oxydes de métaux de transition.

Mot clés : Transition de phase photoinduite, Dynamique ultrarapide, Systèmes électroniques corrélés

1 **Résumé :** Ces dernières années, avec le développement du laser ultrarapide et intense, des opportunités sans précédent sont apparues pour modifier les propriétés macroscopiques des matériaux de maniere efficace et ultra-rapide. Les techniques d'analyse avancées, en particulier la diffraction des rayons X en temps résolue, permettent de sonder la structure des materiaux photo-excités avec les résolutions temporelles adéquates, des échelles de temps sous-ps a la microseconde et au-delà. Cette etude se focalise principalement sur les systèmes électroniques corrélés, les composes de Ti_3O_5 et V_2O_3. Il a été démontré recemment que la transformation macroscopique dans des matériaux photo-excitables a changement de volume suit l'onde de deformation. Ici, nous avons cherché à comprendre ce mécanisme d'ondes de déformations dans les systèmes électroniques corrélés en étudiant deux systèmes présentant des changements de volume de différents types au cours de la transition de phase. La transition de phase semi-conducteur (β) à métal (λ) dans Ti_3O_5 est associée à un changement de volume significatif. V_2O_3, d'autre part, subit à la fois une contraction de volume et un changement de symétrie lors de la transition isolant (AFI) - métal (PM).

Une partie de ce travail de doctorat est consacrée au mécanisme de commutationá l'échelle de la nanoseconde dans Ti_3O_5. Sur ces échelles de temps, la transition de la phase β- à λ se propage à l'intérieur et à travers les joints de grains (entre les nanocristaux). Nous montrons que cette dynamique depend de la taille des nanocristaux. Nous étudions cette croissance de la phase photoinduite lors de la dissipation de la chaleur et recherchons des corrélations entre ce processus lent et les la forme des domaines nanoscopiques resultant de la transition induite par l'onde de deformation, se produisant sur une échelle de temps ultra-rapide. Les résultats sont rationalisés par une simulation numérique basée sur un modéle 2D de diffusion de chaleur, qui cartographie la distribution de phase dans ces échantillons polycristallins. Dans V_2O_3, la dynamique ultrarapide est régie par la propagation des déformations longitudinales dans l'épaisseur du film et par les déformations de cisaillement au sein des cristallites. Grâce a la morphologie des échantillons et a la photo-excitation homogene, aucune réponse lente n'est observé dans ce cas. Notre étude structurale à un delai de 100 ps après la photo-excitation montre une séparation de phase à une fluence laser au delà d'une fluence seuil, et une transformation complète au delà de la fluence de saturation.

Title: Time-resolved XRD study of size dependence in the photoinduced phase change in transition metal oxides

Keywords: Photoinduced phase transition, Ultrafast dynamics, Correlated electron systems,

1 **Abstract:** In recent years with the development of ultrafast and intense laser, unprecedented opportunities have emerged to modify macroscopic properties of materials in ultrafast and efficient manner. Advanced probing technique, in particular time-resolved X-ray diffraction, allows to probe the structure of photo-excited materials with relevant time resolutions, from sub-ps to us and beyond. This study primarily focuses on correlated electron systems, namely Ti_3O_5 and V_2O_3 compounds. It has been recently demonstrated that strain wave is the pathway for macroscopic transformation in photo-excitable volume changing materials. Here, we sought to understand this strain wave mechanism in correlated electron systems by studying two systems with contrasting volume changes across phase transitions. The semiconductor (β-) to metal (λ-) phase transition in Ti_3O_5 is associated with a significant volume expansion. V_2O_3, on the other hand, undergoes both volume contraction and symmetry breaking during the insulator (AFI) to metal (PM) transition.

A part of this work is dedicated to the switching mechanism on the nanosecond times scale in Ti_3O_5. On these time-scales, the transition from β- to λ-phase propagates within and across grain boundaries (between nanocrystals). We show that this dynamics depends of the size of the nanocrystals. We monitor how the photo-induced phase grows upon dissipating heat, and seek correlations of this slow process with nanoscopic patterns left by strain driven transition occurring on the ultrafast timescale. The results are rationalised with numerical simulation based on a 2D-model of heat diffusion, which maps the phase distribution of the polycrystalline samples. In V_2O_3, the ultrafast dynamics are governed by the longitudinal strain propagation within the film thickness and shear strain within the crystalittes. Thanks to the morphology of the sample and homogeneous photo-excitation, no late response was observed in this case. The study shows an evidence of phase separation at intermediate laser fluence and complete transformation at saturating fluence at 100 ps time delay after photo-excitation.

Title: Étude par diffraction des rayons X en temps résolu de la dépendance en taille des changements de phase photoinduits dans des oxydes de métaux de transition

Summary:
Ces dernières décennies, les progrès technologiques concernant les impulsions lasers intenses et ultra-rapides ont révolutionné le domaine de la science des matériaux, offrant des opportunités sans précédent pour la manipulation efficace et ultra-rapide des propriétés macroscopiques des matériaux. Ces progrès technologiques ont mené à un nombre croissant de publications montrant l'impact profond de l'excitation laser sur les ordres électroniques et structuraux dans les matériaux, influençant par la suite leur fonctionnalité. Notamment, la dynamique des réarrangements électroniques ou structuraux locaux se déroule sur des échelles de temps femto ou picoseconde, ces échelles de temps étant dictées par des interactions microscopiques. Les observations en temps réel de ces processus sont devenues possibles grâce à l'émergence de techniques de sonde ultra-rapides telles que la spectroscopie optique, les rayons X ou la diffraction électronique.

Le manuscrit est structuré en six chapitres, chacun avec un objectif spécifique. Le chapitre 1 fournit une introduction aux transitions de phase photo-induites et discute de l'utilisation de techniques pompe-sonde pour étudier ces phénomènes hors-équilibre. Le chapitre 2 propose une introduction générale à la diffraction des rayons X(DRX) et à la technique expérimentale de DRX résolue en temps pour surveiller les changements structuraux en temps réel. En outre, il discute les performances de diverses sources de DRX ultra-rapides aujourd'hui disponibles et il détaille des méthodes d'analyse de diffraction utilisées au cours de ce travail. Le chapitre 3 décrit les systèmes électroniques corrélés à changement de phase (Ti_3O_5 et V_2O_3) étudiés au cours de cette thèse. Enfin, les chapitres 4 et 5 présentent les résultats de mesures DRX résolues dans le temps sur des pastilles polycristallines de Ti_3O_5 et des films minces de V_2O_3, respectivement. Le chapitre 6 sert de conclusion, résumant les résultats et discutant de leur signification plus large dans le contexte des transitions de phase photo-induites.

Lorsqu'un matériau semi-conducteur est excité par une impulsion lumineuse ultra-brève, les électrons sont excités de la bande de valence (VB) à la bande de conduction, laissant derrière eux un trou dans VB. Peu de temps après, l'électron se désexcite en transmettant de l'énergie au réseau grâce au couplage électron-phonon. L'absorption des photons donne lieu à un stress électronique résultant de la création de paires d'électrons et de trous et à un stress phononique dû à la redistribution de l'énergie vers le bain de phonons [Thomsen 1986]. En conséquence, la contrainte générée dans la zone excitée par le laser induit une onde de déformation qui se

propage depuis la surface vers l'intérieur avec une vitesse acoustique[Schick 2014]. Une partie de l'énergie excédentaire va à la population de phonons incohérentes, augmentant ainsi la température globale du système. Tous ces processus se produisent à différentes échelles temporelles et spatiales après la photo-excitation. Aucune équation maîtresse n'est capable de décrire tous ces processus.

Souvent, la photo excitation peut conduire le système vers un nouveau paysage énergétique, qui relaxe ensuite vers une nouvelle phase [Koshihara 2022]. Il est reconnu que l'interaction entre différents degrés de liberté, tels que les électrons, les magnons, les polarons, les polaritons, les excitons, jouent un rôle important dans l'établissement de la phase photoinduite [Basov 2017]. Au cours de ce travail, nous nous sommes concentrés sur un nouveau type de coopérativité, la propagation des ondes de déformation, qui peut renforcer l'efficacité de la commutation aux échelles de temps courts , en premier lieu dans les matériaux montrant un changement de volume significatif lors d'une transition de phase à l'équilibre thermodynamique.

Les techniques expérimentales de type pompe-sonde sont typiquement utilisées pour étudier en temps réel les changements de structure ou de propriétés électroniques au cours de tels processus ultra-rapides. Ces techniques utilisent deux impulsions: l'impulsion de pompe et l'impulsion de sonde. L'impulsion de pompe (le plus souvent laser) est intense et courte, elle initie des changements électroniques ou structuraux dans le système, le portant loin de l'équilibre thermodynamique. L'impulsion de sonde peut être choisie en fonction de la propriété que l'on souhaite étudier. Par exemple, les propriétés structurales peuvent être étudiées par diffraction des rayons X (DRX) ou par diffraction électronique (ED), les propriétés électroniques par mesures de réflectivité ou d'absorption optique, par des techniques de spectroscopie d'absorption ou d'émission des rayons X, etc… La résolution de ces mesures dépend de la durée de l'impulsion de la pompe et de la sonde ainsi que de la corrélation entre les deux impulsions. Au cours de travail de mon doctorat, nous avons principalement étudié les changements structuraux photo-induits en utilisant comme sonde des impulsions laser comme impulsion de pompe et des impulsions de rayons X ultra-brèves comme impulsion de sonde. La plupart des expériences ont été réalisées sur des grandes infrastructures des s sources de rayons X pulsés et intenses : l'ESRF (ligne de lumière ID09 [Cammarata 2009]) et le laboratoire MAXIV (ligne de lumière FemtoMAX [Enquist 2018]). A l'ESRF, le flux de rayons X est assez élevé (10^9 phonons/impulsion) et a une résolution temporelle de 100 ps, limitée par la durée de l'impulsion de rayons X. La ligne de lumière FemtoMAX de l'installation MAXIV offre une meilleure résolution temporelle de 200 fs. Le flux est comparativement plus faible (10^7 phonons/impulsion), mais suffisant pour nos mesures de diffraction sur des couches minces inorganiques polycristallines au prix de temps cependant de temps d'acquisition plus longs.

Au cours de cette thèse, nous avons étudié les transitions de phase photo-induites dans deux oxydes de métaux de transition, le pentoxyde de trititane (Ti_3O_5) et le trioxyde de vanadium (V_2O_3), qui présentent tous deux un changement de volume significatif lors de la transition en température à l'équilibre thermodynamique. Ti_3O_5 a été sélectionné en raison de sa transition isostructurale semi-conducteur-métal associée à un saut de volume substantiel (~ 6%) résultant du couplage entre les paramètres de réseau et l'état électronique [Åsbrink 1959]. Dans Ti3O5, nous avons la preuve que la transition semi-conducteur-métal suit l a propagation de l'onde de déformation [Mariette 2021]. Cette transition est un processus multi-échelle avec une dynamique rapide (~ 20 ps) et une dynamique plus lente autour de 100 ns. La première est principalement due à la transition qui suit la propagation des ondes de déformation et la dernière étape est induite par l'homogénéisation de la température par diffusion de chaleur dans le volume sondé.

Au cours de ma thèse, nous nous sommes principalement concentrés sur la transition de phase à l'échelle de la nanoseconde régie par la diffusion de chaleur. Nous avons exploré l'effet de divers paramètres expérimentaux ainsi que la morphologie de l'échantillon sur la dynamique de changement de phase autour de la nanoseconde . Grâce aux expériences pompe/sonde de diffraction des rayons X en temps résolu, combinées aux simulations numériques de diffusion de chaleur, nous avons établi le schéma suivi parles nanocristallites Ti3O5 excités par laser. Nos investigations mettent en évidence la séparation de phases dans l'espace et dans le temps. Même si les dynamiques évoluant à des échelles de temps très différentes obéissent à des régimes différents, cohérents ou thermiques, nous montrons que l'issue de la transition rapide prédétermine celle de la transition plus lente. Les résultats montrent l'impact de la morphologie à l'échelle nanométrique des systèmes électroniques corrélés sur le mécanisme de transformation macroscopique déclenché par l'excitation laser.

Au chapitre 5, nous avons étudié les mécanismes de transformation photo-induite dans des films minces de V_2O_3, dont la transition de phase de l'isolant antiferromagnétique (AFI) à la phase métallique paramagnétique (PM) implique à la fois un changement de volume et de symétrie [McWhan 1970]. Les expériences en temps résolu ont été réalisées à très basse température, bien en dessous de la température de transition à pression ambiante. L'énergie de photons du laser de pompe est proche de la largeur de la bande interdite, ce qui limite la contribution de la population de phonons incohérents issue du couplage électrons-phonons, réduisant ainsi l'échauffement du réseau et excluant la possibilité de transition de phase d'origine purement thermique.

Les résultats montrent que la dynamique du volume et de la symétrie se produit dans des délais ps après la photo-irradiation, suggérant une voie cohérente ultra-rapide pour la transition de phase. Le changement de symétrie se produit dans les domaines monocliniques de 20 nm et ne dépend pas de l'épaisseur du film. Cependant, la dynamique du volume évolue avec l'épaisseur du film. La symétrie et la dynamique du volume sont en accord avec la propagation des ondes de déformation avec respectivement des vitesses acoustiques longitudinale et transversale. L'étude met en évidence le rôle de la morphologie de l'échantillon sur les transitions ainsi induites. Par ailleurs, nous avons également observé la présence d'un seuil de puissance laser en dessous duquel il n'y a pas de transition vers la phase métallique. Il existe également une fluence saturante de 10 mJ/cm^2 au-delà de laquelle on obtient 100 % de conversion du film. À toutes les fluences intermédiaires, une coexistence de phases a été observée entre les phases AFI et PM.

Les études menées à des échelles de temps très différentes sur les systèmes discutés permettent de mieux comprendre la nature multi-échelle des transitions de phase photo-induites. Dans le cas de V_2O_3, nous observons la transition de phase concomitante à la propagation de l'onde de déformation, tandis que dans l'enquête Ti_3O_5, nous analysons comment la distribution de phase à des échelles de temps ultrarapides influence la dynamique plus lente est principalement régie par la diffusion de la chaleur. L'étude du couplage ultrarapide électron-phonon et des processus de diffusion de chaleur plus lents est cruciale pour comprendre la dynamique multi-échelles se produisant à différentes échelles de temps et d'espace. Cette approche permettra de mieux contrôler les paramètres influençant les transitions de phase photo-induites hors-équilibre. Il est important de souligner, que les progrès des sources de rayons X pulsés ont grandement facilité l'étude de ces divers mécanismes structuraux en jeu suite à la photoexcitation. L'étude hors-équilibre d'objets individuels, tels que des nanocristallites uniques, en utilisant des techniques expérimentales alternatives aujourd'hui disponibles telles que la diffraction électronique ou la microscopie électronique ultrarapide, sera nécessaire afin de mieux comprendre les facteurs qui influencent la structuration à plus petite échelle encore. .

Les références:

[Thomsen 1986] Thomsen, C., et al. "Surface generation and detection of phonons by picosecond light pulses." *Physical Review B* 34.6 (1986): 4129.

[Schick 2014] Schick, Daniel, et al. "Ultrafast lattice response of photoexcited thin films studied by X-ray diffraction." *Structural dynamics* 1.6 (2014).

[Koshihara 2022] Koshihara, Shinya, et al. "Challenges for developing photo-induced phase transition (PIPT) systems: from classical (incoherent) to quantum (coherent) control of PIPT dynamics." *Physics Reports* 942 (2022): 1-61.

[Basov 2017] Basov, D. N., R. D. Averitt, and D. Hsieh. "Towards properties on demand in quantum materials." *Nature materials* 16.11 (2017): 1077-1088.

[Cammarata 2009] Cammarata, Marco, et al. "Chopper system for time resolved experiments with synchrotron radiation." *Review of scientific instruments* 80.1 (2009).

[Enquist 2018] Enquist, Henrik, et al. "FemtoMAX–an X-ray beamline for structural dynamics at the short-pulse facility of MAX IV." *Journal of Synchrotron Radiation* 25.2 (2018): 570-579.

[Mariette 2021] Mariette, Céline, et al. "Strain wave pathway to semiconductor-to-metal transition revealed by time-resolved X-ray powder diffraction." *Nature communications* 12.1 (2021): 1239.

[Volte 2022] Volte, Alix, et al. "Dynamical limits for the molecular switching in a photoexcited material revealed by X-ray diffraction." *Communications Physics* 5.1 (2022): 168.

[Åsbrink 1959] Åsbrink, Stig, and Arne Magnéli. "Crystal structure studies on trititanium pentoxide, Ti3O5." *Acta Crystallographica* 12.8 (1959): 575-581.

[McWhan 1970] McWhan, D. B., and J. P. Remeika. "Metal-insulator transition in (V 1− x Cr x) 2 O 3." *Physical Review B* 2.9 (1970): 3734.